Single crystal growth and neutron scattering studies of novel quantum materials

Von der Fakultät für Georessourcen und Materialtechnik der
Rheinisch-Westfälischen Technischen Hochschule Aachen

zur Erlangung des akademischen Grades eines

Doktors der Naturwissenschaften

genehmigte Dissertation

vorgelegt von

Xiao Wang M. Eng.
aus
Henan, China

Berichter: **Univ.-Prof.Dr.rer. nat. Georg Roth**
Univ.-Prof.Dr.rer. nat. Thomas Brückel
Tag der mündlichen Prüfung: 23.02.2021

Abstract

The recent development of theoretical and experimental study of emergent phenomena, such as anomalous Hall effects, topological electronic band structures as well as quantum spin liquid states in condensed matter physics have evoked tremendous research interest in the search and study of novel quantum materials. High quality single crystal samples of the quantum materials, which serve as a key prerequisite to study the novel properties are of great importance in the study of quantum materials. In this PhD work, employing two cutting-edge methods: molten flux and chemical vapour transport, series of novel quantum material single high quality crystal samples have been grown, such as CeSb, PrSb, NdSb, α-RuCl$_3$, Mn$_3$Sn, Sr$_2$IrO$_4$, Cr$_2$Ge$_2$Te$_6$, Cr$_2$Si$_2$Te$_6$, CeZn$_3$As$_3$, PrZn$_3$As$_3$, PtBi$_2$, ZrTe$_5$, which have been studied intensively in this PhD work as well as other cooperators.

The second important part of this PhD thesis is to study the correlation among crystal structure, magnetic structure and physical properties in two novel quantum materials: Mn$_3$Sn and α-RuCl$_3$ by comprehensive characterization methods.

Mn$_3$Sn, which is proposed to be a candidate of magnetic Weyl semimetal has been studied by a combination of polarised and unpolarised neutron diffraction techniques in this work. Single crystals of topological semimetal Mn$_3$Sn have been grown by Sn self-flux method. The magnetic susceptibility and electronic resistivity showed a magnetic phase transition at 285 K and below that, the anomalous Hall effects at room temperature disappeared completely. With a combination of unpolarised and polarised neutron study, the crystal structure and magnetic structure at low temperature have been determined and a novel double-**q** magnetic ground state is found. As a result of breaking symmetry, AHE could not be realised in this kind of magnetic structure but the double-**q** magnetic structure has offered a rare case to study the non coplanar order in materials with kagomé lattice.

α-RuCl$_3$, which is a candidate to realise Kitaev quantum spin liquid, is a layered two dimensional materials bonded with the weak Van der Weals force. Growing high quality samples of α-RuCl$_3$ single crystals has been a big challenge since the stacking faults will be introduced inevitably. In this thesis, single crystals up to 700 mg were successfully grown by optimising the crystal growth conditions. Based on the high quality single crystals, the low temperature crystal structure of α-RuCl$_3$ has been proved to be $R\overline{3}$ instead of $C2/m$ by single crystal neutron diffraction which demonstrates that α-RuCl$_3$ maybe a perfect candidate to study Kitaev physics without lattice distortion. Besides, with spherical polarised neutron analysis the ordered magnetic moment direction of Ru^{3+} has been precisely determined which will help to reveal the microscopic interaction in Kitaev quantum spin liquids physics. In addition, the phase diagram of α-RuCl$_3$ under isostatic pressures has also been determined by single crystal neutron diffraction. The results reveal the magnetic order in α-RuCl$_3$ could be effectively suppressed with increase of external hydrostatic pressure. However, a pressure induced structural phase transition occurs when the pressure is higher than 0.15 GPa. Despite that the quantum spin liquid state is not realised in α-RuCl$_3$ by the isostatic pressure, this result has proved that the pressure could change the transition temperature in Kitaev materials explicitly and will shed lights on the pressure tuning magnetic order in similar materials.

Zusammenfassung

Experimentelle und theoretische Untersuchungen über "emergent phenomena", wie der anomale Hall-Effekt (AHE), topologische Bandstrukturen und Quantenspinflüssigkeiten wecken immer mehr Interesse für die Forschung an Quantenmaterialien. Um diese neuartigen Effekte untersuchen zu können werden Einkristalle von hoher Qualität benötigt, weshalb ein Fokus dieser Doktorarbeit die Entwicklung und Implementierung von Methoden zum Kristallwachstum in unserem Labor ist. Mithilfe von zwei nmodernen Methodenwurden, Schmelzfluss und chemischer Dampftransport, wurden viele Einkristalle neuartiger Quantenmaterialien für unsere Gruppe und Kooperationspartner gezüchtet, wie etwa CeSb, PrSb, NdSb, α-$RuCl_3$, Mn_3Sn, Sr_2IrO_4, $Cr_2Ge_2Te_6$, $Cr_2Si_2Te_6$, $CeZn_3As_3$, $PrZn_3As_3$, $PtBi_2$, $ZrTe_5$. Ein anderer wichtiger Teil dieser Doktorarbeit ist eine umfassende Studie zweier Materialien um das Zusammenspiel von Kristallstruktur, magnetischer Ordnung und physikalischen Eigenschaften zu untersuchen. Mn_3Sn ist ein möglicher Kandidat eines magnetischen Weyl Halbmetalls und zeigt einen starken AHE bei 300 K und α-$RuCl_3$ ist eine mögliche Kitaev Quantenspinflüssigkeit. Einkristalle des topologischen Halbmetalls Mn_3Sn wurden mit der Sn Selbstflussmethode gezüchtet. Die magnetische Suszeptibilität und elektrische Widerstand zeigen einen magnetischen Phasenübergang bei 285 K und der anomale Hall-Effekt, sichtbar bei 300 K, verschwindet komplett. Die Kristallstruktur und magnetische Struktur für niedrige Temperatur wurde durch eine Kombination von unpolarisierten und polarisierten Neutronenmessungen bestimmt und ein neuartiger doppel-**q** magnetischer Grundzustand ermittelt. Durch einen Symmetriebruch kann der AHE in dieser magnetischen Struktur zustande kommen nicht und die magnetische doppel-**q** Struktur eröffnet die seltene Möglichkeit eine nicht-koplanare Struktur in Materialien mit Kagomé Struktur zu untersuchen. Da α-$RuCl_3$ ein zweidimensionales Van-der-Waals Material ist, ist das Wachstum von hochqualitativen Einkristallen eine große Herausforderung, weil Stapelfehler zwangsläufig auftreten werden. Durch viele Versuche wurden die Wachstumsbedingungen für α-$RuCl_3$ bestimmt und Einkristalle bis zu 700 mg gezüchtet. Neutronendiffraktion an diesen Einkristallen führte zur Bestimmung der $R\overline{3}$ Kristallstruktur bei niedrigen Temperaturen, nicht $C2/m$, was α-$RuCl_3$ zu einem idealen Kandidaten macht um Kitaev Physik ohne Gitterverzerrung zu untersuchen. Außerdem konnte durch Sphärische Polarisierte Neutronen Analyse die Ordnung der magnetischen Momente von Ru^{3+} präzise bestimmt werden, was helfen wird die mikroskopischen Interaktionen in Kitaev Quantenspinflüssigkeiten zu ermitteln. Zusätzlich haben wir auch das Phasendiagram von α-$RuCl_3$ bei isostatischen Drücken am D10 Instrument am ILL gemessen. Die Resultate zeigen, dass externe hydrostatische Drücke die magnetischer Ordnung in α-$RuCl_3$ unterdrücken können und dass sich die Kristallstruktur für Drücke über 0.15 GPa ändert. Quantenspinflüssigkeitszustand in α-$RuCl_3$ durch hydrostatische Drücke nicht realisiert werden konnte, zeigen unsere Resultate dass Druck die Übergangstemperatur von Kitaev Materialien ändern kann und sie werden helfen den Einfluss von Druck auf die magnetischer Ordnung in ähnlichen Materialien zu verstehen.

Contents

1

Introduction

In the current trends in condensed matter physics research, there has been a rapidly growing interest in collective phenomena where the many-body physics, commonly known as strongly correlated electrons in solids, gives rise to a variety of emergent phenomena, like unconventional superconductivity, quantum Hall effect (QHE), anomalous Hall effect (AHE), novel phases and exotic magnetic excitations [1–3]. The interpretation of such emergent physics calls for quantum effects to be brought into in view of facts that they cannot be approximated by a classical description at a macroscopic level, leading to the come-to-being of the concept of **Quantum Materials**. Topology, one of the significant concepts in the understanding of electronic states in quantum materials characterizes the non-trivial nature of topological superconductivity, topological insulator and topological semimetal [4–20]. For instance, a topological insulator band inversion observed in materials with strong spin-orbit coupling is identified by the non-trivial gapless Dirac cone-like surface states inside the bulk band gap [11, 12]. Topological surface states could also be realized in the so-called Weyl semimetals when the spatial inversion or the time-reversal symmetry is further broken, and this surface state is characterised by the topological Fermi arcs [14]. It comes to the conclusion that Weyl semimetals may only be realised in materials with specific symmetries, for instance in non-centrosymmetric or magnetically ordered materials. This draws the attention to the important roles of crystal structure and magnetic order in the search for novel quantum materials.

Another important concept that is strongly related to the crystal structure in the study of quantum materials is magnetic frustration, which happens in the materials where the localized magnetic moments, or spins in magnetic materials which interact through the competing exchange interactions that cannot be simultaneously satisfied, causing a large degeneracy of the system ground state. Geometric frustration occurs in spin systems that involve triangular lattices where the three spins cannot all be antiparallel with antiferromagnetic nearest-neighbour interactions, while competing exchange frustration arises in materials where two magnetic ions are connected by several competing interaction exchange paths. In this regard, a large class of materials with magnetic ions occupying in a face-centre cubic pyrochlore lattice, triangular lattice, kagomé lattice, square lattice and honeycomb lattice with Kitaev exchange paths have been extensively explored and investigated as the potential playground for the study of magnetic frustration. Therefore, revealing the relationship among novel properties, crystal structure and magnetic order is of great importance in the study of quantum materials.

The strong interplay among charge, spin, orbital, lattice degrees of freedom and topology constitute the fundamental attributes of quantum materials, which often leads to emergent quantum phenomena and novel functionalities. To shed light on the coupling between topology, magnetic order and lattice in novel quantum materials, high quality single crystals have benn prepared in this word via cutting-edge crystal growth techniques, and physical properties measurement, crystal structure determination and magnetic structure solution were also performed with diverse techniques.

The goal of this thesis is to obtain a better understanding of the interplay among physical properties, crystal structure and magnetic order by carefully performing experiments such as in-house characterisations, non-polarised and polarised neutron scattering under ambient conditions as well as isostatic pressures on high quality single crystals.

It is organized as the following chapters:

Chapter 1 introduces a general summary of the study motivation, goal and structure of this PhD work.

Chapter 2 presents a short introduction to the basic concepts of topological materials, AHE and magnetic frustration.

Chapter 3 gives a summary of crystal growth methods, neutron scattering theory and principles as well as approaches of magnetic structure determination from neutron diffraction data.

Chapter 4 presents the crystal growth of the topological Weyl semimetal Mn_3Sn, phase transition studied by various neutron scattering techniques. The magnetic structure of the modulated phase at 225 K and the reasons for the incommensurate magnetic order as well as the absence of AHE.

Chapter 5 is dedicated to the crystal structure and magnetic structure studies of the Kitaev quantum spin liquid candidate α-$RuCl_3$. In addition, the phase diagram of α-$RuCl_3$ under hydrostatic pressures is also reported.

Chapter 6 summarizes the important results described in this thesis and discuss the outlook of future studies of those fascinating compounds.

2

Scientific Background: Quantum Materials

The search for emergent phenomena and novel functionalities in condensed matter has been an active field that is being expanded beyond strongly correlated electron systems, giving rise to the emergent concept of quantum materials [21].

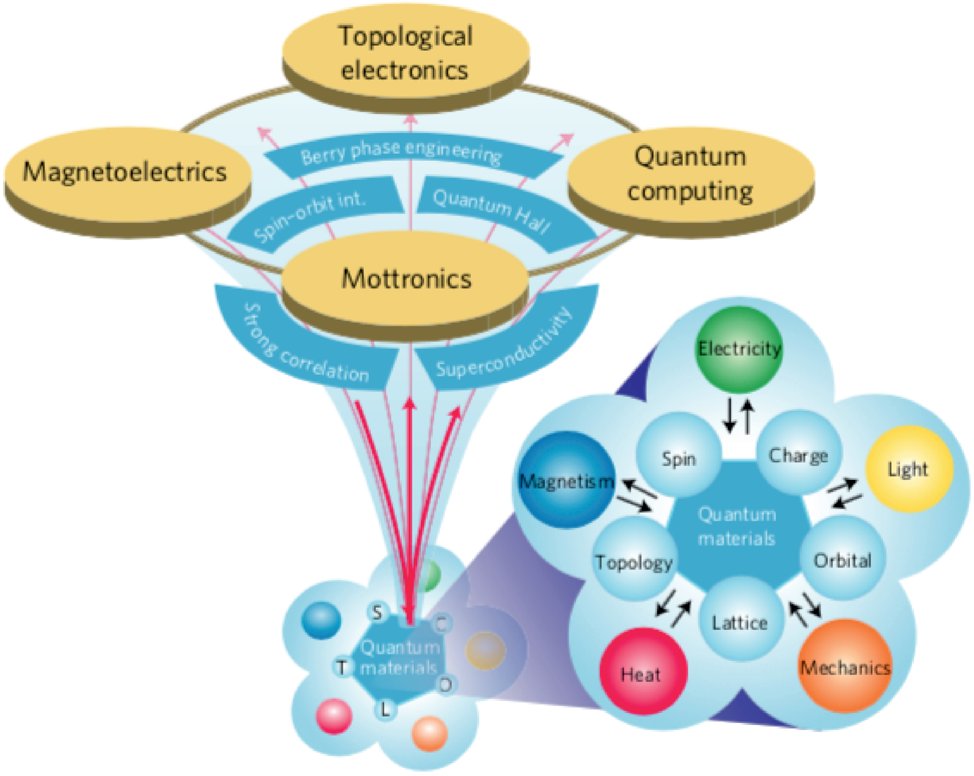

Figure 2.1: Various degrees of freedom of strongly correlated electrons in solids, which respond to external stimuli. These strong couplings lead to the emergent functions with the cross correlations among different physical observables and to the developments towards the potential applications of emergent functions such as Mottronics, magnetoelectrics, topological electronics, and quantum computing (taken from Ref.[2]).

The study of quantum materials has included but is not limited the following topics: topological insulators, Weyl semimetals, AHE, anomalous quantum Hall effects and quantum spin liquids etc., with particular focus on the strong interplay among various degrees of freedom, such as spin, charge, orbital, topology and lattice. These strong couplings lead to the emergent functions with the cross correlations among different physical properties and to the developments towards the potential applications of emergent functions such as Mottronics, magnetoelectrics, topological electronics, and quantum computing [2]. A brief introduction to the concepts of topological materials, AHE and quantum spin liquid that are related to this PhD study will be introduced in the next sections.

2.1 Topological materials

2.1.1 Topological insulators

An insulating behaviour in solid-state materials can often be explained due to the presence of the large energy gap between conduction and valence electronic energy bands. Topological insulators are a class of materials that has a finite energy gap in the bulk but possessing non-trivial gapless surface states. This emergent state of matter is mainly due to the strong spin-orbit coupling interaction, and its non-trivial surface state is topologically protected since spin-orbit coupling preserves the time-reversal symmetry. Similar to unconventional superconductivity and other emergent phenomena, the exotic physical properties in topological insulators may harbour potential application in the development of new generation topological spintronics devices, and may also provide a novel platform for future quantum technologies. Topological insulators have already been found in many materials, such as A_2X_3 (A = Bi,Ab and X = S,Se,Te) family [12, 22–24] and so on.

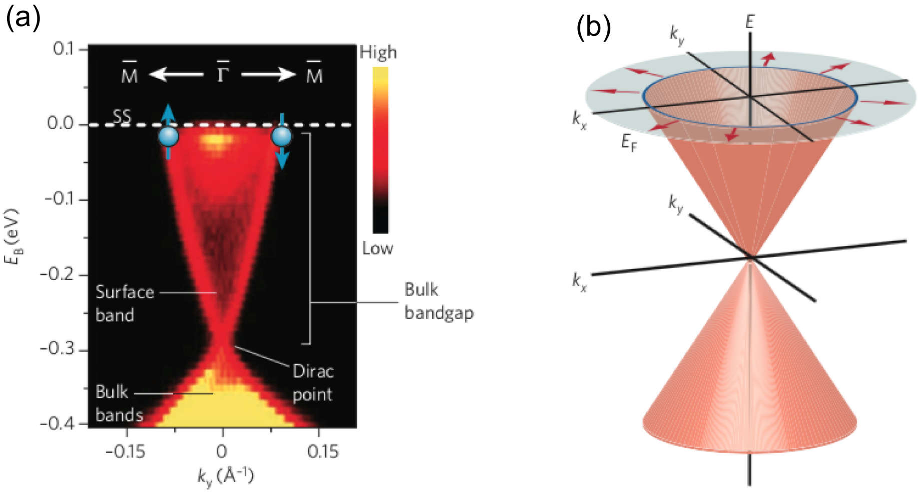

Figure 2.2: Surface states in the topological insulator Bi_2Se_3. (a) Electronic band structure was obtained from angle-resolved photoemission spectroscopy (ARPES) experiment. E_B is the measured electron energy. $\overline{\Gamma}$, $\overline{M}$ are the respective symbols for Brillouin-zone centre and Brillouin-zone boundary in the reciprocal space. Dirac point at $\overline{\Gamma}$ is regarded as the proof for topological insulator. (b) Theoretical calculation of the electronic band structure of Bi_2Se_3, showing the rotation of the spin degree of freedom (red arrows) as an electron (with energy E) moves around the Fermi surface (taken from Ref.[25]).

Fig.2.2 illustrates the electronic band structure of topological insulators Bi_2Se_3 from angle-resolved photoemission spectroscopy (ARPES) experiment [12]. A Dirac-cone shape linearly dispersive band due to topologically non-trivial surface states is clearly observed in Fig.2.2(a), in which the opposite direction of the electron spin is marked.

A current study focus in topological insulators is to combine topology and electronic correlation for instance by looking into systems with the presence of magnetism, especially ferromagnetism. This has led to the new theoretical frameworks and the recent discoveries of magnetic topological insulators [20, 26–28]. In such magnetic topological insulators, as illustrated in Fig.2.3, the time-reversal symmetry breaking, which will lead to the opening of an energy gap at the Dirac point, giving rise to the emergence of quantum anomalous Hall effect (QAHE), a quantized Hall effect that occurs at zero magnetic field. The QAHE manifests itself as a chiral edge mode, the direction of which not only depends on the sign of the Chern number, a number that describes the topological invariant and could be calculated from the surface integral of the Berry flux, but also the direction of magnetization (shown in Fig.2.3(c) and (d)). The realisation of magnetic topological insulators has been achieved in the magnetic ions (for instance Mn, Cr or V) doped topological insulators and in some thin films. The recent discovery of $MnBi_2Te_4$ with ferromagnetic arrangement of Mn-atoms in each layer has already stimulated considerable interests in the study of magnetic topological insulators [29–31].

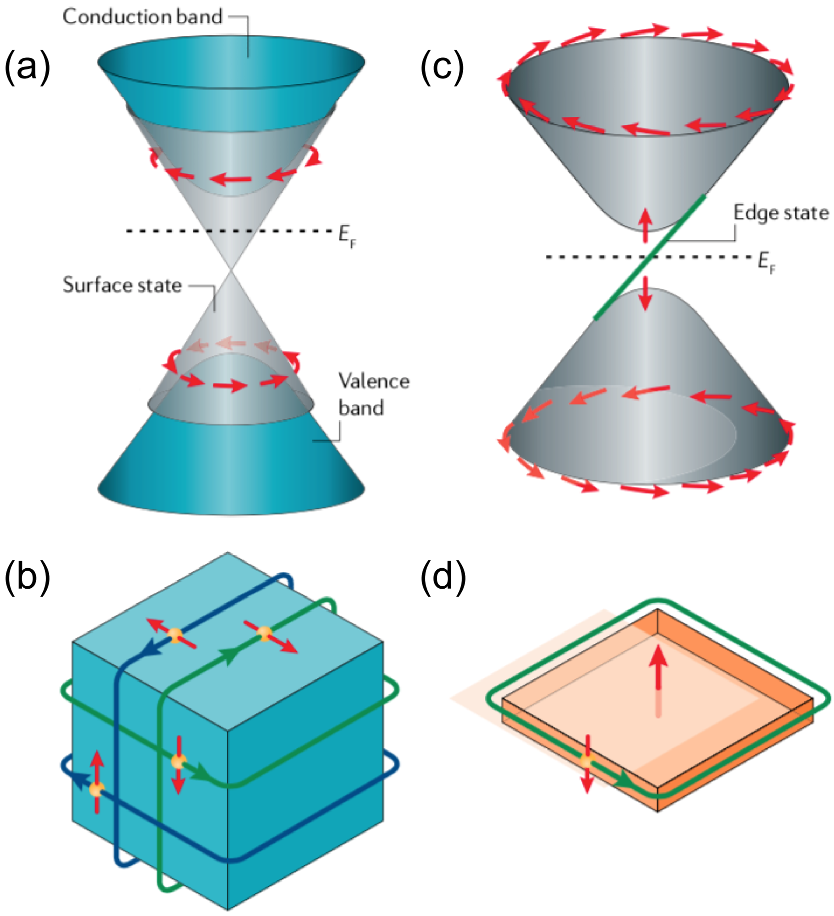

Figure 2.3: Comparison of the electronic band structure of topological insulators and magnetic topological insulators in the momentum space and real space. (a) and (b): A Dirac cone shape dispersion of the surface state in a topological insulator and electrons with opposite spins move in the opposite directions in the real space. (c) and (d): The gapless Dirac dispersion is gapped in magnetic topological insulators and the chiral edge mode appears if the Fermi level E_F is located in the gap induced by the magnetic exchange interaction (taken from Ref.[20]).

2.1.2 Topological semimetals

Another large class of intriguing topological materials that has attracted tremendous research attention is topological semimetal, for instance Weyl semimetal that is manifested by the topological Fermi arcs that connect two so-called Weyl points in the Fermi surface [14–16, 32]. The Weyl points in Weyl semimetals refer to the nodes where the energy bands disperse linearly in momentum space. In Fig.2.4, the bulk and surface energy band structures of the topological materials are summarised. Similar to topological insulators, a band inversion happens as a result of large spin-orbit coupling effects as shown in Fig.2.4. If the time-reversal symmetry and spatial inversion symmetry persist in the materials, a Dirac semimetal appears with a pair of Weyl points, otherwise it degenerates to Weyl semimetals as shown in Fig.2.4(b).

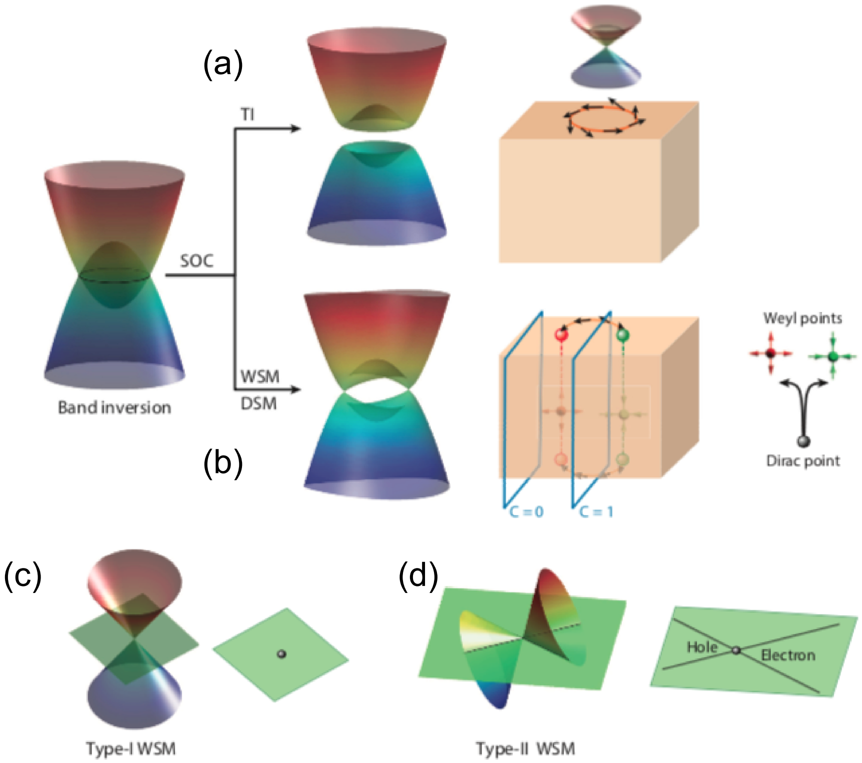

Figure 2.4: The bulk and surface band structures in topological materials. The topologies of topological insulators and a Weyl or Dirac semimetal require band inversion with large spin-orbit coupling. (a) The spin-orbit coupling opens a full gap after the band inversion in a topological insulator, giving rise to metallic states on the surface. (b) In a Weyl or Dirac semimetal, due to the topology of the bulk bands, topological states appear on the surface and form exotic Fermi arcs. In a Dirac semimetal all bands are doubly degenerated, whereas in a Weyl semimetal, the degeneracy is lifted owing to the breaking of the inversion symmetry or time-reversal symmetry or both. (c) The type-I Weyl semimetal. The Fermi surface shrinks to zero at the Weyl points when the Fermi energy is sufficiently close to the Weyl points. (d) The type-II Weyl semimetal. Due to the strong tilting of the Weyl cone, the Weyl point acts as the touching point between electron and hole pockets in the Fermi surface (taken from Ref.[32]).

In summary, the emergence of Weyl fermions in materials require the breaking of time-reversal symmetry and spatial inversion symmetry. Berry curvature, which describes the topological entanglement between conduction and valence band, plays an essential role for the understanding of the topological properties such as quantum Hall effect, AHE and becomes singular at Weyl points [32]. The pair of Weyl points has different chirality acting as monopoles in momentum space, which means it could be a source or a sink of Berry curvature connected by the unclosed lines of the Fermi arcs that start from one Weyl point and end at other with opposite chirality. The Fermi arcs are considered to be a robust and reliable experimental evidence for the identification of Weyl semimetals as displayed in Fig.2.5.

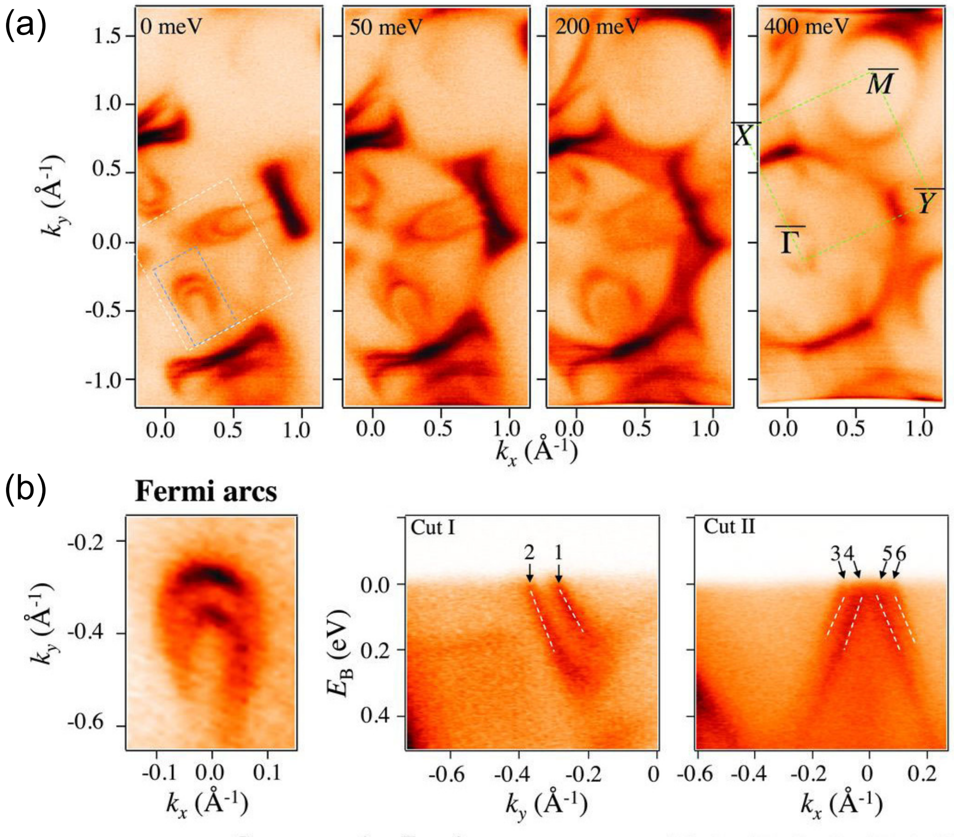

Figure 2.5: Topological Fermi arc surface states on the (001) surface of TaAs observed by ARPES. (a) ARPES Fermi surface map and constant–binding energy contours measured with incident photon energy of 90 eV. (b) High-resolution ARPES Fermi surface map of the crescent Fermi arcs (taken from Ref.[15]).

Weyl semimetals can be further classified into type I and type II. In type I Weyl semimetals, the Fermi surface shrinks to zero at Weyl points when the Fermi energy is sufficiently close to the Weyl points, while in type II Weyl semimetals, the Weyl cones can be either the electron or hole pockets in the Fermi surface at Weyl points as shown in Fig.2.4 (c) and (d). The experimental discovery of Weyl fermions was achieved very recently in TaAs family [15, 33–35] after the theoretical prediction [36, 37]. In addition to the TaAs family, $Y_2Ir_2O_7$ [38], $HgCr_2Se_4$ [39], WTe_2 [40], $MoTe_2$ [41], $Co_3Sn_2S_2$ [42] have also been proved to be Weyl semimetal candidates and Na_3Bi [43], Cd_3As_2 [44] to be Dirac semimetal candidates. Another candidate, Mn_3Sn [45], in which large AHE generated by the Berry curvature is observed, has been an active research topic for the potential application in the novel spintronics devices and has been studied comprehensively in this work.

2.2 Anomalous Hall effect

The interpretation of the AHE has become a standing issue that has puzzled theoretical and experimental scientists for more than a century since it was reported in ferromagnetic irons by Edwin Hall [46]. The early semi-empirical relation of the Hall resistivity ρ_{xy}, magnetic field H_z and magnetization M_z [47, 48] is

$$\rho_{xy} = R_0 H_z + R_s M_z, \tag{2.1}$$

where R_0 and R_s depend on the density of carriers and specific materials. This formula is derived from the results of ferromagnets and applies to many materials over a broad range of external fields. Recent theoretical and experimental achievements have unveiled the key role of the time-reversal symmetry breaking for the emergence of AHE. The discovery of the quantum Hall effect (QHE) and its successful explanation by the topological properties of electronic wave functions have a great impact on the understanding of the origin of the intrinsic AHE [49, 50]. The adoption of the Berry phase concepts in the intrinsic AHE has established a link between the AHE and the topological nature of the Hall currents [51, 52].

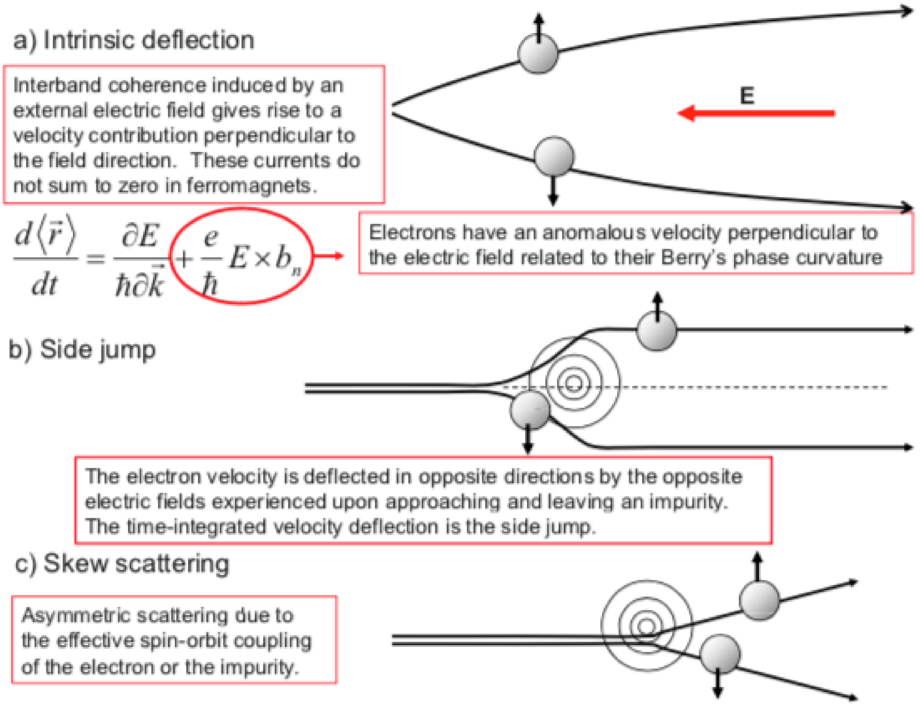

Figure 2.6: Illustration of the three main mechanisms that can give rise to an AHE. In a real material all of these mechanisms can act to influence the electron motion (taken from Ref.[53]).

In order to understand the deep physics in AHE, three mechanisms were introduced as shown in Fig.2.6:(i) intrinsic mechanism, which is dependent only on the band structure of perfect crystals [54]. The intrinsic contribution to AHE from Berry curvature in momentum space could be regarded as "unquantized" version of QHE. The other two originate from the scattering process: (ii): the skew scattering, which comes from the asymmetric scattering caused by the spin-orbit coupling effects [55, 56]; (iii) the side jump, which is a sudden shift of electron coordinates during scattering [57]. Therefore, the anomalous Hall conductivity could be expressed by

$$\sigma_{xy}^{AH} = \sigma_{xy}^{AH-int} + \sigma_{xy}^{AH-skew} + \sigma_{xy}^{AH-sj}, \tag{2.2}$$

where σ_{xy}^{AH-int}, $\sigma_{xy}^{AH-skew}$, σ_{xy}^{AH-sj} are contributions from the intrinsic mechanism, skew scattering and side jump to AHE, respectively. On the experimental front, various new experimental studies of the AHE in transition metals, transition metal oxides, such as spinels, pyrochlores helped to establish a systematic understanding of this phenomenon. These two developments, in concert with first-principles electronic structure calculations, strongly favour the dominance of an intrinsic Berry-phase-related AHE mechanism in metallic ferromagnets with moderate conductivity. The intrinsic AHE can be expressed in terms of the Berry-phase curvatures and it is therefore an intrinsic quantum-mechanical property of a perfect crystal [53]. Since the intrinsic AHE is linked to the topological properties of the materials and it has deep relationship with the structure in materials, we will discuss further about this in the next sections.

2.2.1 Intrinsic anomalous Hall effect

The pioneer work done by Karplus and Luttinger (KL) [54] has laid the foundation of understanding of the intrinsic AHE in ferromagnets. KL showed that when an external electric field was applied to a solid, electrons acquired an additional contribution to their group velocity. KL's anomalous velocity was perpendicular to the electric field and therefore could contribute to the Hall effects. In the case of ferromagnetic conductors, the sum of the anomalous velocity over all occupied band states could be non-vanishing. Because this contribution depends only on the band structure and is largely independent of scattering, it has recently been referred to as the intrinsic contribution to the AHE. When the conductivity tensor is inverted, the intrinsic AHE yields a contribution $\rho_{xy} \approx \sigma_{xy}/\sigma_{xx}^2$. The current development of theory [58–60] in the topological nature of the intrinsic AHE has shown that the intrinsic contribution to AHE can be calculated by

$$\sigma_{xy}^{A-int} = e^2\hbar \sum_{n\neq n'} \int \frac{dk}{(2\pi)^2} \left[f\left(\varepsilon_n(k)\right) - f\left(\varepsilon_{n'}(k)\right)\right] \operatorname{Im} \frac{\langle n,\boldsymbol{k}\left|v_x(\boldsymbol{k})\right| n',\boldsymbol{k}\rangle \langle n',\boldsymbol{k}\left|v_y(\boldsymbol{k})\right| n,\boldsymbol{k}\rangle}{\left(\varepsilon_n(\boldsymbol{k}) - \varepsilon_{n'}(\boldsymbol{k})\right)^2} \tag{2.3}$$

for an ideal lattice, given the eigenstates $|n,\boldsymbol{k}\rangle$ and eigenvalues $\varepsilon_n(\boldsymbol{k})$ of a Bloch Hamiltonian H, where the velocity operator $\boldsymbol{v}(\boldsymbol{k})$ is defined using $\boldsymbol{k}$-dependent Hamiltonian $[H(\boldsymbol{k})]$ by

$$\boldsymbol{v}(\boldsymbol{k}) = \frac{1}{i\hbar}[\boldsymbol{r}, H(\boldsymbol{k})] = \frac{1}{\hbar}\boldsymbol{\nabla}_k H(\boldsymbol{k}). \tag{2.4}$$

Eq.2.3 is directly linked to the topological properties of Bloch states. Specially it is proportional to the integration of Berry phases over the Fermi surface segments. Thus, it can be further reduced as

$$\sigma_{ij}^{AH-int} = -\varepsilon_{ij\ell}\frac{e^2}{\hbar}\sum_n \int \frac{d\boldsymbol{k}}{(2\pi)^d} f\left(\varepsilon_n(\boldsymbol{k})\right) b_n^{\ell}(\boldsymbol{k}) \tag{2.5}$$

where $\boldsymbol{b}_n(\boldsymbol{k})$ is the Berry phase curvature. In case $\boldsymbol{a}_n(\boldsymbol{k}) = i \langle n, \boldsymbol{k} \left| \boldsymbol{\nabla}_k \right| n, \boldsymbol{k} \rangle$ is the Berry phase connection, the Berry phase curvature can also be expressed as:

$$\boldsymbol{b}_n(\boldsymbol{k}) = \boldsymbol{\nabla}_k \times \boldsymbol{a}_n(\boldsymbol{k}). \tag{2.6}$$

The Berry phase curvature $\boldsymbol{b}_n(\boldsymbol{k})$ is regarded as a "fictitious" magnetic flux acting on electrons with the state $|n, \boldsymbol{k}\rangle$. In the presence of an electric field, an electron can acquire an anomalous velocity proportional to the Berry curvature of the band. The formula for the velocity in a given state becomes

$$v_n(k) = \frac{1}{\hbar}\frac{\partial \varepsilon_n(k)}{\partial k} - \frac{e}{\hbar}\boldsymbol{E} \times \boldsymbol{b}_n(\boldsymbol{k}). \tag{2.7}$$

Eq.2.7 reveals that the anomalous velocity in the second term is transverse to the magnetic field and thus gives rise to the anomalous Hall current.

2.2.2 Symmetry conditions for the intrinsic anomalous Hall effect

Actually, in many experiments the observed AHE can be well described by the semi-empirical Equ.2.1. In materials with the co-existence of time-reversal symmetry and spatial inversion symmetry, the Berry curvature vanishes throughout the Brillouin zone. Therefore a comprehensive description of the AHE in relation to the symmetry, especially the magnetic symmetry in magnetically ordered materials is essential for the understanding of this effect in quantum materials.

In Eq.2.7, considering the magnetic symmetry elements in a given magnetic material, the transformation properties could be derived since symmetry-operation of $v_n(\boldsymbol{k})$, $\varepsilon_n(\boldsymbol{k})$, $\boldsymbol{b}_n(\boldsymbol{k})$ and $\boldsymbol{k}$ are known. For instance, the Berry curvature $\boldsymbol{b}_n(\boldsymbol{k})$ is invariant under the translational symmetry operation. Besides, it is transformed in the same way as an ordinary vector under the rotational symmetry operation in momentum space and the space inversion brings $\boldsymbol{b}_n(\boldsymbol{k})$ to $\boldsymbol{b}_n(-\boldsymbol{k})$. In this case, the Berry curvature acts as an axial vector in momentum space and as might be expected, we will have $\boldsymbol{b}_n(\boldsymbol{k})$ transferred to $-\boldsymbol{b}_n(-\boldsymbol{k})$ for the time-reversal symmetry. Therefore, for any materials possessing both time-reversal symmetry and spatial inversion symmetry, it will readily prove $\boldsymbol{b}_n(\boldsymbol{k}) = -\boldsymbol{b}_n(\boldsymbol{k}) = 0$, resulting in $\boldsymbol{b}_n(\boldsymbol{k}) = 0$.

Tab.2.1 surveys the symmetry constraint on the Berry curvature in momentum space for some representative symmetries, where $B^{\alpha}(\boldsymbol{k})$ refers to the Berry curvature along one of the three x, y, z Cartesian coordinate directions. Based on the symmetry properties of $\boldsymbol{b}_n(\boldsymbol{k})$ in momentum space, one can easily derive the symmetry properties of the intrinsic AHE. For instance, if the Berry curvature satisfies the condition $B^{\alpha}(R\boldsymbol{k}) = -B^{\alpha}(\boldsymbol{k})$ (R is the rotation operator) due to a magnetic symmetry, the corresponding AHE must be zero since the Berry curvature at $\boldsymbol{k}$ and $R\boldsymbol{k}$ are cancelled out by integration of the whole Brillouin zone. Besides, for any n-fold rotation symmetry operator, the components of σ_{xy}^{AH-int} that perpendicular to the n-fold symmetry should vanish.

Table 2.1: Constraint on the Berry curvature $\boldsymbol{b}_n(\boldsymbol{k})$ in momentum space for some representative symmetries. Here, x, y, z express the Cartesian coordinates. $C_{n\mu}$ indicates the n-fold rotation operator along the μ axis, P is the spatial inversion operator, and T is the time-reversal operator. The mirror operation whose mirror plane is normal to the μ axis corresponds to $PC_{2\mu}$ (taken from Ref.[61]).

Unitary	operators	Antiunitary	operators
C_{2z}	$B^x\left(-k_x,-k_y,k_z\right)=-B^x\left(k_x,k_y,k_z\right)$	TC_{2z}	$B^x\left(k_x,k_y,-k_z\right)=B^x\left(k_x,k_y,k_z\right)$
	$B^y\left(-k_x,-k_y,k_z\right)=-B^y\left(k_x,k_y,k_z\right)$		$B^y\left(k_x,k_y,-k_z\right)=B^y\left(k_x,k_y,k_z\right)$
	$B^z\left(-k_x,-k_y,k_z\right)=B^z\left(k_x,k_y,k_z\right)$		$B^z\left(k_x,k_y,-k_z\right)=-B^z\left(k_x,k_y,k_z\right)$
PC_{2z}	$B^x\left(k_x,k_y,-k_z\right)=-B^x\left(k_x,k_y,k_z\right)$	TPC_{2z}	$B^x\left(-k_x,-k_y,k_z\right)=B^x\left(k_x,k_y,k_z\right)$
	$B^y\left(k_x,k_y,-k_z\right)=-B^y\left(k_x,k_y,k_z\right)$		$B^y\left(-k_x,-k_y,k_z\right)=B^y\left(k_x,k_y,k_z\right)$
	$B^z\left(k_x,k_y,-k_z\right)=B^z\left(k_x,k_y,k_z\right)$		$B^z\left(-k_x,-k_y,k_z\right)=-B^z\left(k_x,k_y,k_z\right)$
$C_{2\vert 1\bar{1}0]}$	$B^x\left(-k_y,-k_x,-k_z\right)=-B^y\left(k_x,k_y,k_z\right)$	$TC_{2[1\bar{1}0]}$	$B^x\left(k_y,k_x,k_z\right)=B^y\left(k_x,k_y,k_z\right)$
	$B^y\left(-k_y,-k_x,-k_z\right)=-B^x\left(k_x,k_y,k_z\right)$		$B^y\left(k_y,k_x,k_z\right)=B^x\left(k_x,k_y,k_z\right)$
	$B^z\left(-k_y,-k_x,-k_z\right)=-B^z\left(k_x,k_y,k_z\right)$		$B^z\left(k_y,k_x,-k_z\right)=B^z\left(k_x,k_y,k_z\right)$
$PC_{2[1\bar{1}0]}$	$B^x\left(k_y,k_x,k_z\right)=-B^y\left(k_x,k_y,k_z\right)$	$TPC_{2[1\bar{0}]}$	$B^x\left(-k_y,-k_x,-k_z\right)=B^y\left(k_x,k_y,k_z\right)$
	$B^y\left(k_y,k_x,k_z\right)=-B^x\left(k_x,k_y,k_z\right)$		$B^y\left(-k_y,-k_x,-k_z\right)=B^x\left(k_x,k_y,k_z\right)$
	$B^z\left(k_y,k_x,k_z\right)=-B^z\left(k_x,k_y,k_z\right)$		$B^z\left(-k_y,-k_x,-k_z\right)=B^z\left(k_x,k_y,k_z\right)$
$C_{3[111]}$	$B^x\left(k_z,k_x,k_y\right)=B^y\left(k_x,k_y,k_z\right)$	$TC_{3[111]}$	$B^x\left(-k_z,-k_x,-k_y\right)=-B^y\left(k_x,k_y,k_z\right)$
	$B^y\left(k_z,k_x,k_y\right)=B^z\left(k_x,k_y,k_z\right)$		$B^y\left(-k_z,-k_x,-k_y\right)=-B^z\left(k_x,k_y,k_z\right)$
	$B^z\left(k_z,k_x,k_y\right)=B^x\left(k_x,k_y,k_z\right)$		$B^z\left(-k_z,-k_x,-k_y\right)=-B^x\left(k_x,k_y,k_z\right)$
$PC_{3[111]}$	$B^x\left(-k_z,-k_x,-k_y\right)=B^y\left(k_x,k_y,k_z\right)$	$TPC_{3[111]}$	$B^x\left(k_z,k_x,k_y\right)=-B^y\left(k_x,k_y,k_z\right)$
	$B^y\left(-k_z,-k_x,-k_y\right)=B^z\left(k_x,k_y,k_z\right)$		$B^y\left(k_z,k_x,k_y\right)=-B^z\left(k_x,k_y,k_z\right)$
	$B^z\left(-k_z,-k_x,-k_y\right)=B^x\left(k_x,k_y,k_z\right)$		$B^z\left(k_z,k_x,k_y\right)=-B^x\left(k_x,k_y,k_z\right)$

A complete list of relations between symmetry operators and forbidden components of intrinsic AHE is shown in Tab.2.2. For simplicity, we denote the intrinsic AHE component as σ^{ℓ} for x, y, z Cartesian coordinates. For a given magnetic material, if the magnetic structure is known, one can analyse the possible AHE component by taking into account the magnetic symmetry elements.

Table 2.2: Complete list of the symmetry operators which are forbidden if the intrinsic anomalous Hall conductivity (AHC) components is non-vanishing. The translational part of the operators, which does not affect the results, is not shown. All the superscripts of the AHC are explicitly written such as $\sigma_{ij}^{\ell} \equiv \sigma^{\ell} = \sigma_{ij} (i, j, \ell = x, y, z)$. The integer in parentheses shows the number of O_h (D_{6h}) magnetic point group elements (taken from Ref.[61]).

AHE component	Unitary operators	Antiunitary operators
	Cubic	
σ_{ij}^{k}	$C_{n(ij)}, PC_{n(ij)}(n = 2, 4)(16)$	$TC_{nk}, TPC_{nk}(n = 0, 2, 4)(16)$
$\sigma^{[111]}$	$C_{2[1\bar{1}0]}, C_{2[01\bar{1}]}, C_{2[\bar{1}01]},$	$TC_{n[111]}, TPC_{n[111]}(n = 0, 3)(6)$
	$PC_{2[1\bar{\mathrm{I}}0]}, PC_{2[01\bar{\mathrm{I}}]}, PC_{2[\mathrm{I}\tilde{\bar{0}}1]}(6)$	
	Hexagonal	
σ_{xy}^{z}	$C_{2(xy)}, PC_{2(xy)}(12)$	$TC_{nz}, TPC_{n_z}(n = 0, 2, 3, 6)(12)$
σ_{yz}^{x}	$C_{nz}, PC_{nz}(n = 2, 3, 6)$	$TC_{nz}, TPC_{nz}(n = 0, 3, 6)$
	$C_{2y}, PC_{2y}(12)$	$TC_{2x}, TPC_{2x}(12)$
σ_{zx}^{y}	$C_{nz}, PC_{nz}(n = 2, 3, 6)$	$TC_{nz}, TPC_{nz}(n = 0, 3, 6)$
	$C_{2x}, PC_{2x}(12)$	$TC_{2y}, TPC_{2y}(12)$

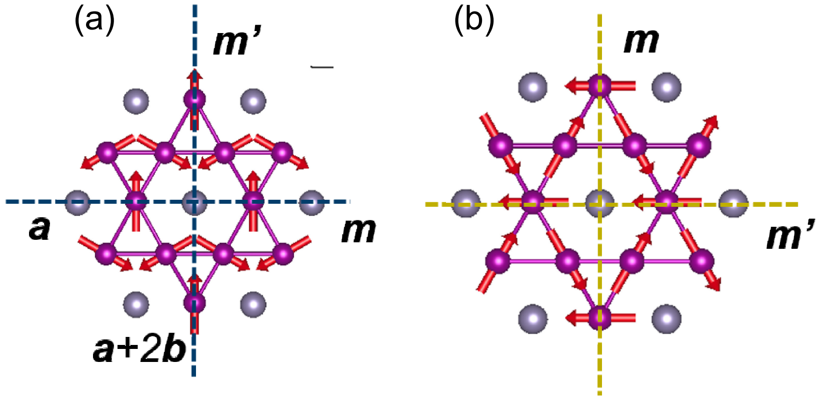

Figure 2.7: Illustration of the magnetic symmetry operators in the hexagonal *ab* basal plane of Mn_3Sn for (a) *Cm′cm′* and (b) *Cmc′m′* magnetic structure models, respectively, where ***m*** and ***m***′ refer to the mirror symmetry and time-reversal mirror symmetry, respectively. ***a*** and ***b*** are the crystallographic axes in a hexagonal setting. The two magnetic structure models can be converted from one to another by rotating the direction of the magnetic moments by 90°. Magnetic structure model is plotted by Vesta [62].

The application of such analysis can be shown in the novel topological Weyl semimetal antiferromagnet Mn_3Sn, which has an inverse-triangle antiferromagnetic structure and experiences a large AHE at room temperature [63–66]. The magnetic space group model is proposed to be either *Cm′cm′* or *Cmc′m′*, despite the true magnetic structure of Mn_3Sn is still under debate [67]. Both of them follow the same irreducible representation and there is a unitary mirror symmetry to preserve the finite in-plane Berry curvature by breaking the time-reversal symmetry. The magnetic symmetry elements in *ab* basal plane have been illustrated in Fig.2.7 for (a) $Cm'cm'$ or (b) $Cmc'm'$ magnetic structure models. Based on symmetry analysis results in Tab.2.2, we can predict the possible AHE component in Mn_3Sn for each magnetic structure model and the result is summarised in Tab.2.3. Indeed a large AHE has been observed experimentally in Mn_3Sn in the *ab* basal plane. In the experiment of measuring Hall effect, both σ^x and σ^y are observed because the magnetic moments in Mn_3Sn can be easily rotated with a small magnetic field [65].

Table 2.3: Intrinsic AHC components in Mn_3Sn based on magnetic symmetry analysis. $M_iT(i = x, y, z)$ is the time-reversal mirror plane along three orthogonal directions. That is, x is along **a** direction, y is along $(\boldsymbol{a} + 2\boldsymbol{b})$ direction and z is along **c** direction, where $\boldsymbol{a}$, $\boldsymbol{b}$, $\boldsymbol{c}$ are three crystallographic axes in the hexagonal setting.

Structure models	Symmetry operators	Berry curvature	AHE components
	M_xT	$B^x = -B^x$	$\sigma^x = 0$
$Cm'cm'$	M_y	$B^y = B^y$	$\sigma^y \neq 0$
	M_zT	$B^z = -B^z$	$\sigma^z = 0$
	M_x	$B^x = B^x$	$\sigma^x \neq 0$
$Cmc'm'$	M_yT	$B^y = -B^y$	$\sigma^y = 0$
	M_zT	$B^z = -B^z$	$\sigma^z = 0$

2.2.3 Scalar spin chirality and topological Hall effect

The AHE could be also observed in the systems with non-trivial spin textures like Skyrmions due to spin-orbit coupling interactions, which is so-called "topological Hall effect" (THE) [52]. The scalar spin chirality defined as $\chi = S_i \cdot (S_j \times S_k)$, where S_i, S_j, S_k are magnetic moments as shown in Fig.2.8 is strongly linked to the topological properties originating from the Berry phase or the associated "fictitious" magnetic field. When the magnetic structure is of coplanar type, such as commensurate collinear or incommensurate spiral structures, the scalar spin chirality is vanished as imposed by the symmetry. Therefore, only a non-coplanar magnetic structure could lead to a finite scalar spin chirality which is linked to the Berry curvature and generates factious magnetic flux proportional to the scalar spin chirality as the spin-orbit interaction does in ferromagnetic materials [61, 68–71]. The emergence of THE is considered as the signature of topological textures, for instance Skyrmions as shown in Fig.2.9. It should be noted here that in some cases, even if the non-coplanar magnetic structure is realized, the scalar spin chirality still could be zero due to the symmetry and no THE is therefore expected. For instance, in a single-**k** incommensurate magnetic structure, there is a global time-reversal symmetry at the half of the period and the scalar spin chirality will vanish.

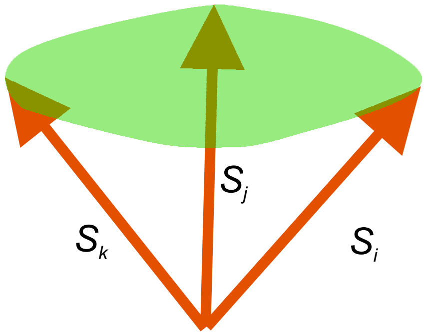

Figure 2.8: Noncoplanar magnetic moments and generation of scalar spin chirality. The scalar spin chirality can be calculated by $\chi = S_i \cdot (S_j \times S_k)$, where S_i, S_j and S_k are magnetic moments.

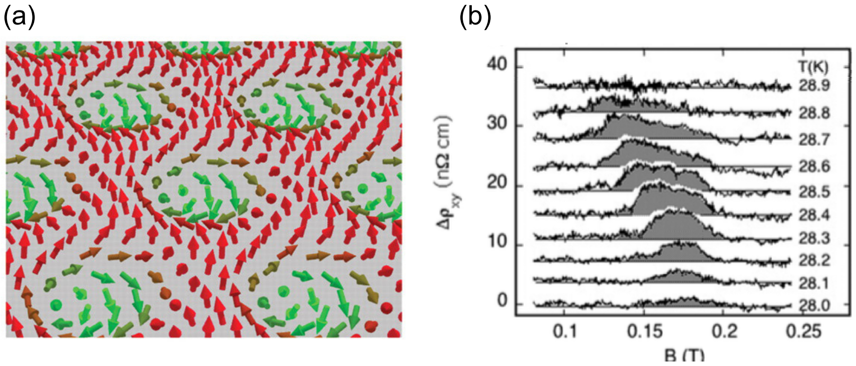

Figure 2.9: Skyrmion and topological Hall effect in MnSi. (a) Illustration of real space depiction of the spin arrangement in the Skyrmion phase (taken from Ref.[72]). (b) Topological Hall effect $\Delta\rho_{xy}$ in the Skyrmion phase. Data are shifted vertically for better visibility (taken from Ref.[69]).

2.3 Frustrated magnets and exotic states of matter

Frustrated magnets are a class of magnetic materials in which the localized magnetic moments interact through competing exchange interactions that cannot be simultaneously satisfied, giving rise to a large degeneracy of the system ground states [73]. An easy-to-understand example is geometry frustration that arises from an equilateral triangular lattice of magnetic ions with dominant Ising type (the Ising type referring to the spins can be only allowed to point up ↑ or down ↓) antiferromagnetic exchange interactions as shown in Fig.2.10(a) [74–77]. If only the nearest-neighbour antiferromagnetic coupling is brought into consideration, an antiparallel arrangement can not be simultaneously achieved for all nearest-neighbour spins in an equilateral triangle. As a result of this magnetic frustration, instead of the two ground states due to Ising symmetry (↑ and ↓), there are six possible ground states as illustrated in Fig.2.10(a). The lack of long-range magnetic order and the persistence of a large degeneracy in the ground state are two hallmarks of frustrated magnets. In addition to triangular lattice, a kagomé lattice formed by the star of David which has six corner-sharing triangles is another prominent two dimensional (2D) motif that possesses geometrical frustration. In three dimensional (3D) cases, a tetrahedral lattice with corner-occupying magnetic ions is the basic unit shown in Fig.2.10(b). Such tetrahedra could be found in pyrochlore or spinels with face centred structure.

Magnetic frustration can also arise from the competing interactions from $J_1 - J_2$ Ising model in a square lattice as depicted in Fig.2.10(c) [78]. Assuming the nearest-neighbour coupling is J_1 and the next-nearest-neighbour coupling is J_2. The exchange Hamiltonian is

$$H_{J_1-J_2} = J_1 \sum_{NN} S_i \cdot S_j + J_2 \sum_{NNN} S_i \cdot S_j, \quad S_i, S_j \ = \uparrow \mathit{and} \downarrow, \tag{2.8}$$

where S_i, S_j are spins in the corner of the square lattice and NN, NNN denote the nearest and next nearest spins. If the strength of J_1 and J_2 are comparable, a simple antiparallel arrangement of spins between all possible nearest-neighbour sites cannot be satisfied simultaneously. In this case, the ground state of the model depends on the relative strength of the competing interactions J_1/J_2. By varying the value of J_1/J_2, novel ground states could be realised in the square lattice models. Another exchange frustration example is the well-known Kitaev model with competing bond-direction dependent exchange interactions in a honeycomb lattice or a face centred lattice, which will be discussed in next section. In the view point of experiment, an empirical formula is introduced to the magnetic frustration, which is

$$f = \left|\theta_{CW}\right| / T_{tran}, \tag{2.9}$$

where θ_{CW} is the Curie-Weiss temperature fitted from the magnetic susceptibility at high temperature and T_{tran} is the transition temperature to an ordered ground state. Frustration is an important source for the emergence of many exotic states of matter, such as "monopole" excitation in a spin ice system and "spinon" excitations in the quantum spin liquid system.

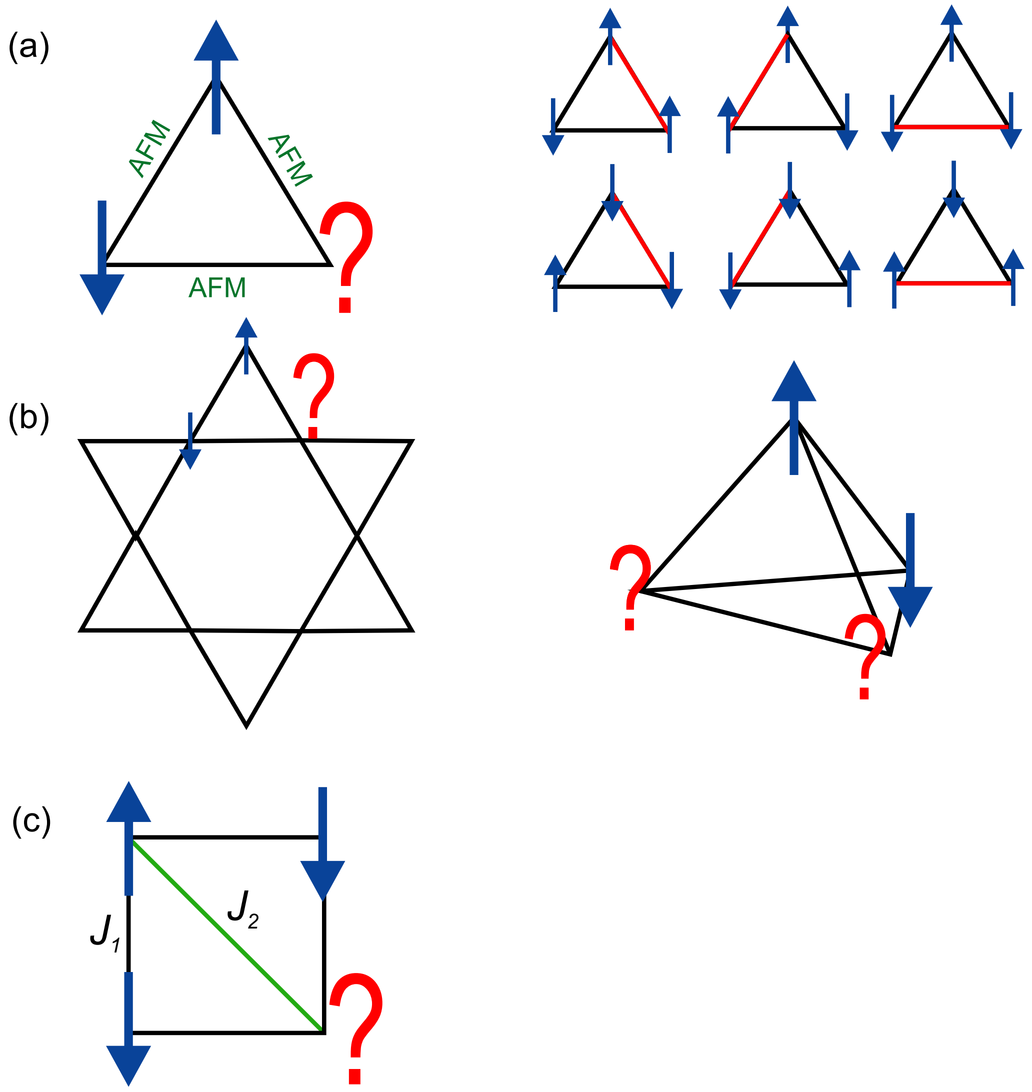

Figure 2.10: Magnetic frustrations in various lattices. (a) Geometry frustration in an equilateral triangle with antiferromagnetic Ising spins gives rise to six possible ground states. (b) A David′ star with six triangles in the two dimensional (2D) kagomé lattice (left) and three dimensional (3D) tetrahedral lattice with four non-coplanar triangles (right). (c) In a square lattice with competing antiferromagnetic interactions of nearest-neighbour coupling J_1 and next-nearest-neighbour coupling J_2 of Ising spins, if the strength of J_1 and J_2 are comparable, a simple antiparallel arrangement of spins between all possible nearest-neighbour sites cannot be satisfied simultaneously.

2.3.1 Quantum spin liquid states

Quantum spin liquid (QSL) is an exotic state of matter with a variety of unusual features arising from its intrinsic topological character [79]. Despite the fact that it is difficult to give a clear-cut definition of QSL, an essential ingredient of quantum spin liquids is not the lack of order, but the presence of an anomalously high degree of entanglement, or massive quantum superposition [80]. As a highly entangled quantum matter, QSL is proposed to be a possible platform for decoherence-free quantum computing. In the past decades, a number of materials were identified as possible QSL candidates by various experimental techniques in which neutron scattering is one of the most powerful probes.

The study of QSL could be dated back to 1973 when Anderson's famous "resonating valence bond" (RVB) state was put forward [81–83]. In Anderson's original RVB model, spins with $S = \frac{1}{2}$ pair with each other and form a singlet state with $S = 0$ as a result of nearest-neighbour antiferromagnetic interaction as shown in 2.11(a). If all the spins are formed into singlet pairs and could be partitioned into specific valence bonds, it comes to the "valence bond" state, which is non-magnetic and has spin-0. When considering the quantum fluctuation effects, the pairing of valence bonds are not static and the real ground state is a superposition state of different pairs in 2.11(b) and (c), which is the "RVB" state.

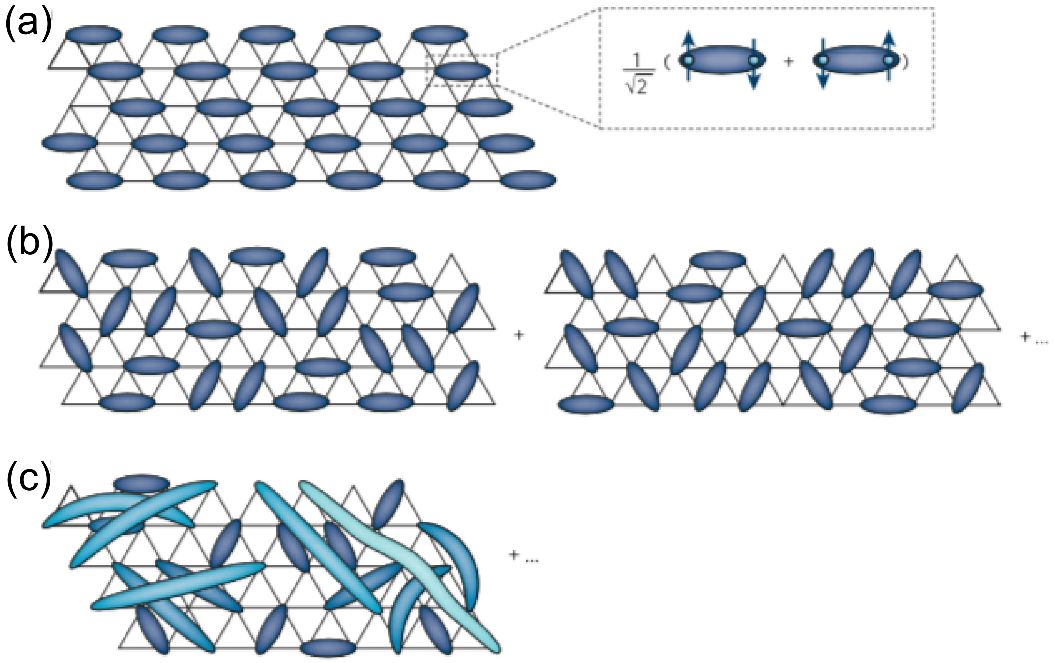

Figure 2.11: Valence-bond states of frustrated antiferromagnets. In a VBS state: (a) a specific pattern of entangled pairs of spins-the valence bonds is formed. Entangled pairs are indicated by ovals that cover two points on the triangular lattice. By contrast, in a RVB state, the wavefunction is a superposition of many different pairings of spins. The valence bonds may be short range (b) or long range (c). Spins in longer-range valence bonds (the longer, the lighter the colour) are less tightly bound and are therefore more easily excited into a state with non-zero spin (taken from Ref.[73]).

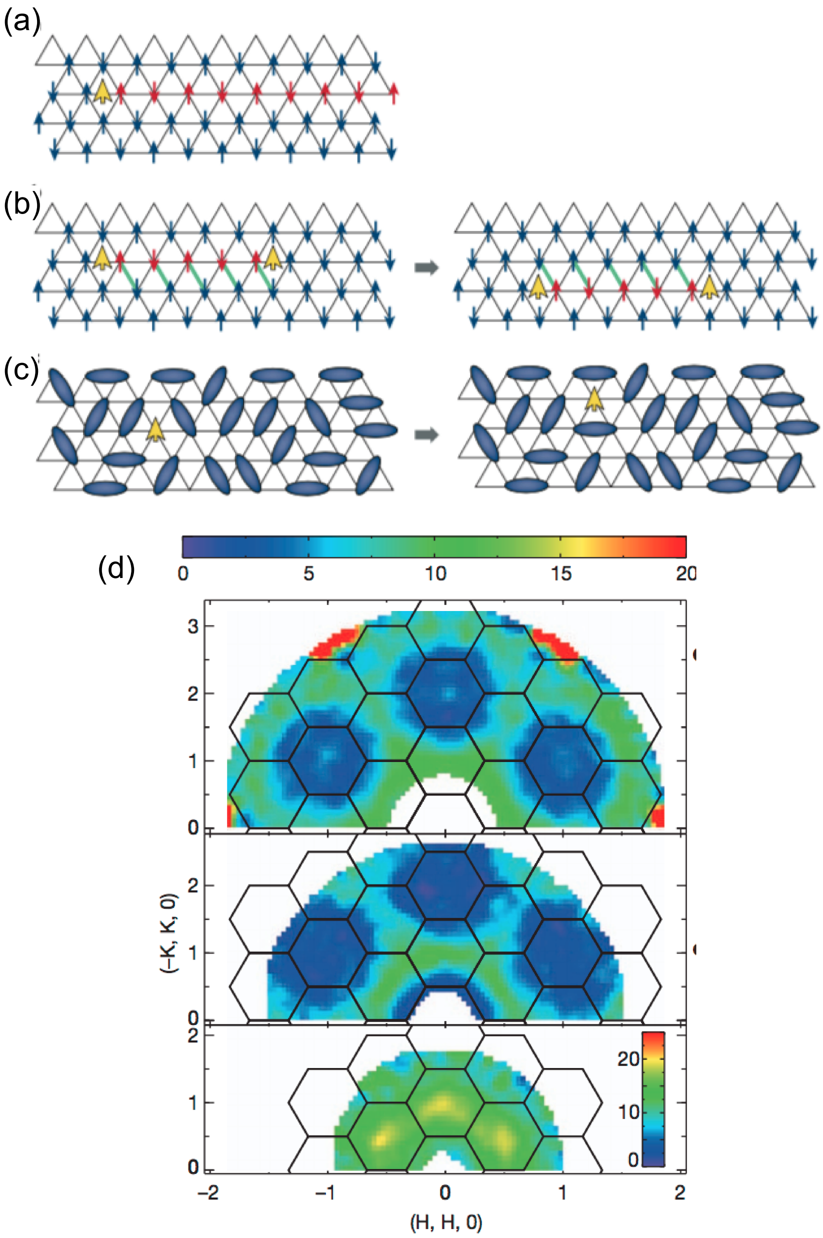

Figure 2.12: Excitations of quantum antiferromagnets (taken from Ref.[73, 84]). (a) In a quasi-1D system (such as the triangular lattice), 1D spinons are formed as a domain wall between the two antiferromagnetic ground states. Creating a spinon (yellow arrow) thus requires the flipping of a semi-infinite line of spins along a chain, shown in red. The spinon cannot hop between chains, because to do so would require the coherent flipping of an infinite number of spins, in this case all of the red spins and their counterparts on the next chain. (b) A bound pair of 1D spinons forms a triplon. Because a finite number of spins are flipped between the two domain walls (shown in red), the triplon can coherently move between chains, by the flipping of spins along the green bonds. (c) In a 2D quantum spin liquid, a spinon is created simply as an unpaired spin, which can then move by locally adjusting the valence bonds. (d) An example of spinon excitation measured from single crystal $ZnCu_3(OD)_6Cl_2$. The experiment was performed at 1.6 K and the dynamic structure factor is plotted for $\hbar\omega$ = 6 meV, 2 meV and 0.75 meV.

In the RVB sate, the distribution of the valence bonds is much broader and there is no preference for any specific valence bonds, so this state could be regarded as a "liquid" state. A true QSL state will not break the lattice symmetry but it has long range quantum entanglement.

Based on the nature of the excitation energy gap, QSL could be loosely classified into two different classes. For instance, a topological QSL is characterised by the global topological structure of their ground state wave functions and has an energy gap, while a Kitaev QSL has a gapless excitation spectrum.

One of the most intriguing exotic excitations of QSL is the "spinon" excitation shown in Fig.2.12. To understand a "spinon", considering a spin string in a one dimensional system in Fig.2.12(a), by flipping a semi-infinite string of spins, a spinon is created, similar to the antiferromagnetic domain walls. In one dimensional system, the boundary of strings is its end point, so the string is guaranteed to cost only a finite energy from its boundary, while in higher dimensions, the boundary of a string extends to its full length. A string is expected to have a tension, which means there is an energy proportional to its length. In a true two dimensional or three dimensional QSL, the string associated with a spinon remains tensionless down to 0 K, as a result of quantum fluctuation. This can be understood from the quantum superposition principle: rearranging the spins along the string simply reshuffles the various spin or valence-bond configurations that are already superposed in the ground state.

2.3.2 Kitaev materials

The celebrated Kitaev model that is an exactly solvable quantum spin model on a two dimensional honeycomb lattice with spin-$\frac{1}{2}$ moments was firstly put forward in 2006 [85]. This model has attracted tremendous research interests not only because it is solvable but also because the spins in the Kitaev model could fractionalize into Majorana fermions and its ground state is QSL. The Hamiltonian involving only pure Kitaev terms may be expressed as:

$$H = \sum_{x} K_x s_i^x s_j^x + \sum_{y} K_y s_i^y s_j^y + \sum_{z} K_z s_i^z s_j^z, \tag{2.10}$$

where three types of bonds are labelled by x, y and z in the honeycomb lattice as shown in Fig.2.13(a). The summation is taken over all the nearest-neighbour spins S_i, S_j of x, y and z bonds. This Hamiltonian indicates that the interaction of spins are bond dependent and the bond related interaction K_x, K_y, K_z could be different due to the symmetry. The orthogonal anisotropies of the three nearest-neighbour bonds of each spin conflict with each other, leading to frustration and large ground state degeneracies.

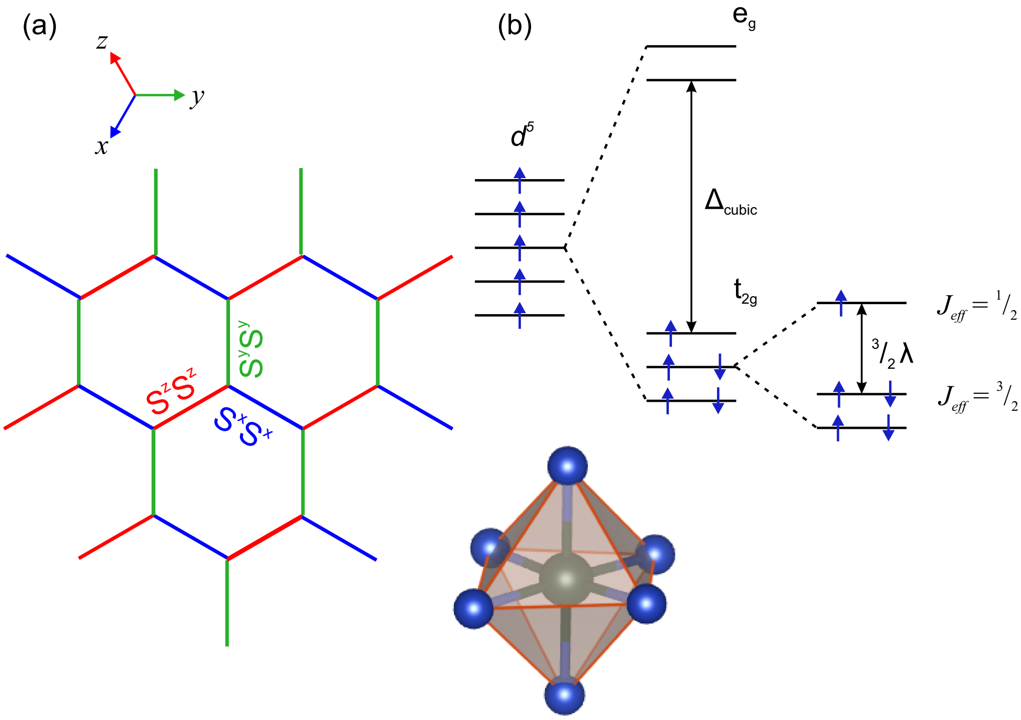

Figure 2.13: Kitaev model and its realisation in $4d^5$ or $5d^5$ compounds. (a) The spin-$\frac{1}{2}$ magnetic ions on the corner of the honeycomb lattice with bond dependent Ising interactions. The bonds in blue, green and red which have easy axes parallel to the x, y and z directions in a local xyz Cartesian frame are labelled by **x**, **y** and **z** in the honeycomb lattice. These bonds are directed along $\frac{y-z}{\sqrt{2}}$, $\frac{z-x}{\sqrt{2}}$ and $\frac{x-y}{\sqrt{2}}$, respectively. (b) Splitting of five-fold degenerate d levels of d^5 in Ir^{4+} and Ru^{3+} into the doublet e_g and the triplet t_{2g} in a cubic crystal field Δ_{cubic} of O_6 or Cl_6 octahedra. As a result of spin-orbit coupling interaction, t_{2g} manifold further splits into $J_{eff} = \frac{1}{2}$ doublet and $J_{eff} = \frac{3}{2}$ quartet.

In magnetic ions with $4d^5$ or $5d^5$ electronic configuration, such as Ru^{3+} and Ir^{4+}, the cubic crystal field splitting is very large, which overcomes Hund's first rule favouring the high spin state, leading to all five d electrons accommodated in the triply degenerate t_{2g} manifold that comprise d_{xy}, d_{yz} and d_{zx} orbitals [86–88]. Then the spin-orbit coupling breaking further splits the electronic states into $J_{eff} = \frac{1}{2}$ doublet and $J_{eff} = \frac{3}{2}$ quartet. Experimental evidences of the formation of $J_{eff} = \frac{1}{2}$ states in Ir^{4+} and Ru^{3+} have been found by angle-resolved photoemission, optical conductivity, and x-ray absorption measurements recently. Several candidate Kitaev materials of Ir^{4+} and Ru^{3+} have already been found and are summarized in tab.2.4.

Table 2.4: Summary of the candidate materials to study Kitaev physics and their basic physical properties.

Electronic configuration	Materials	Crystal structure	T_N	Magnetic ground state
$5d^5$	Na_2IrO_3	$C2/m$	15 K	Zigzag
	α-Li_2IrO_3	$C2/m$	15 K	Spiral
	β-Li_2IrO_3	$Fddd$	38 K	Spiral
	γ-Li_2IrO_3	$Cccm$	39.5 K	Spiral
	$H_3LiIr_2O_6$	$C2/m$	No	Spin liquid
$4d^5$	α-$RuCl_3$	$C2/m$ or $R\overline{3}$	6.5-8 K	Zigzag

As an important part of this PhD work, the single crystal growth, crystal structure and magnetic structure determination, and magnetic order under magnetic fields or hydrostatic pressure of α-$RuCl_3$ have been studied intensively. High quality and large α-$RuCl_3$ single crystal samples have been successfully prepared in this PhD work for the study of the crystal structure and magnetic structure by a combination of various techniques in Chapter.5. The current research progress and the important results of α-$RuCl_3$ are shown in Fig.2.14. In Fig.2.14(a), inelastic neutron scattering experiment of single crystals of α-$RuCl_3$ has already been performed by the time-of-flight spectrometry. Two sharp branches of antiferromagnetic spin waves along with a broad continuum excitation were observed at 0 T in the magnetically ordered state. At 8 T, the sharp magnetic peaks from spin waves in the zigzag phase disappeared, leaving only the continuum. The continuum was temperature independent up to well above 100 K and was considered as the signature of fractionalised excitations in this proximate Kitaev QSL material.

In addition, a half-integer thermal Hall conductance plateau was found in α-$RuCl_3$ shown in Fig.2.14(b). This half-integer quantization of the thermal Hall conductance in a bulk material was a signature of the topologically protected chiral edge currents of charge-neutral Majorana fermions (particles that are their own antiparticles), which had half the degrees of freedom of conventional fermions [89]. The measurement was carried on a tilted α-$RuCl_3$ single crystal, for which the magnetic field along ab plane $H_{\parallel}$ could suppress magnetic order and the magnetic field perpendicular to ab plane $H_{\perp}$ could induce thermal Hall effects.

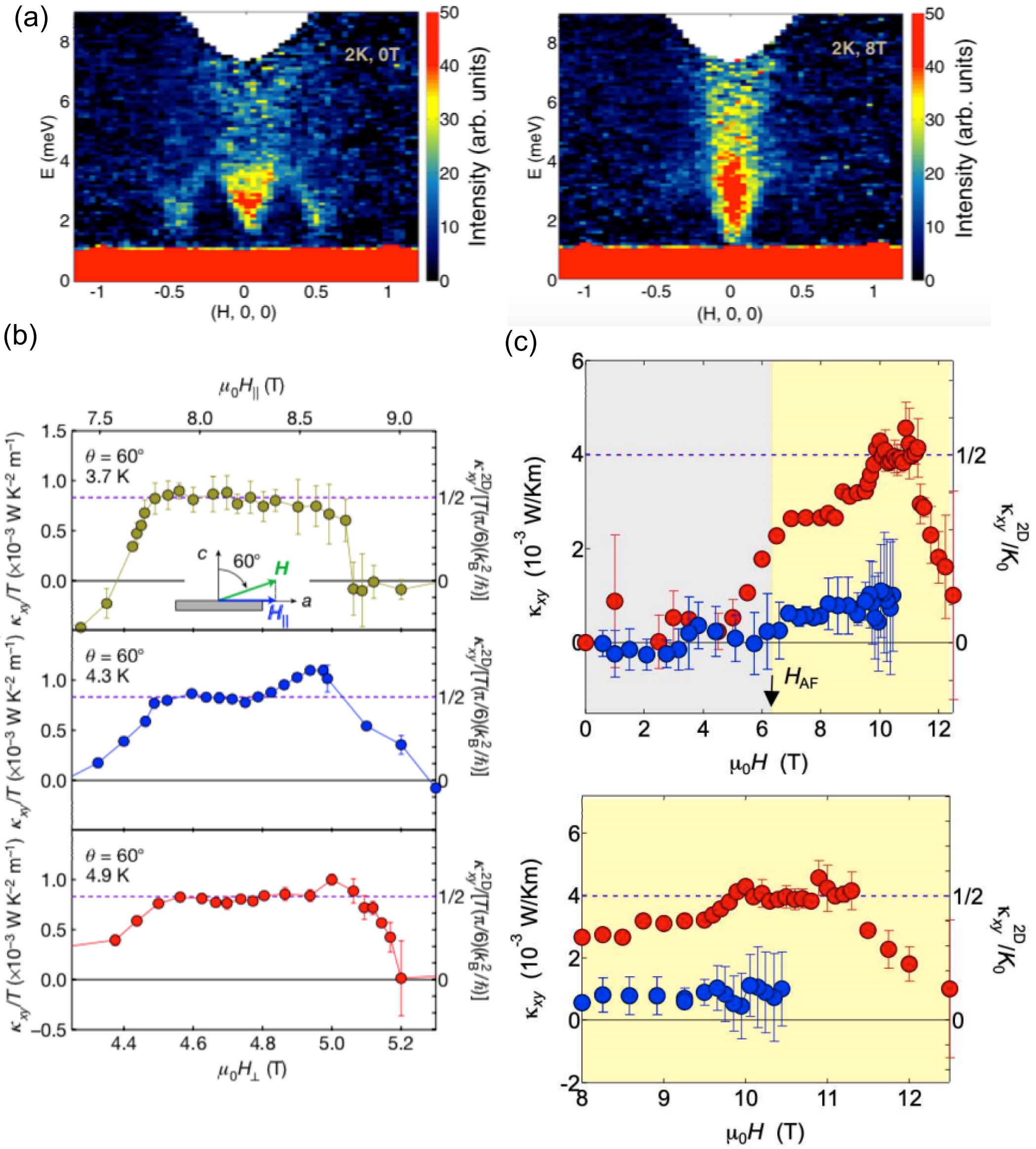

Figure 2.14: Key data of the Kitaev QSL candidate α-RuCl$_3$. (a) Inelastic neutron scattering was measured at T = 2 K along the reciprocal [H, 0, 0] (r.l.u.) direction in a zero external magnetic field and in a field of 8 T in the honeycomb plane, where the zigzag magnetic order was suppressed (taken from [90]), leaving only the continuum. (b) Half-integer thermal Hall conductance plateau: Half-integer thermal Hall conductance plateau was observed in the thermal Hall conductivity κ_{xy}/T in a field tilted at θ = 60° from ab plane plotted as a function of $H_{\perp}$. The top axes show the parallel field component, $H_{\parallel}$. The right scales represent the 2D thermal conductivity κ_{xy}^{2D}/T, in units of $(\pi/6)\left(k_B^2/\hbar\right)$. Violet dashed Hall conductivity represent the half-integer thermal Hall conductance $\kappa_{xy}^{2D}/\left[T(\pi/6)\left(k_B^2/\hbar\right)\right] = \frac{1}{2}$ (taken from [91]). (c) Half-integer quantized anomalous thermal Hall: thermal Hall conductivity κ_{xy} in the antiferromagnetic (grey shaded area) and spin liquid (yellow) states for $H \parallel a$ axis (red circles) and $H \parallel b$ axis (blue circles) at 4.8 K. In the right axis, thermal Hall conductance per 2D layer κ_{xy}^{2D} is plotted in units of the quantum thermal conductance $K_0 = \left(\pi^2/3\right)\left(k_B^2/h\right)T$. The small but finite κ_{xy} experimentally observed for $H \parallel b$ is likely attributed to a misalignment of the magnetic field direction from the b axis.

This observation of a half-integer anomalous thermal Hall effect firmly establishes that the Kitaev interaction is primarily responsible and that the non-Abelian topological order associated with fractionalization of the local magnetic moments persists even in the presence of non-Kitaev interactions in α-RuCl$_3$.

Despite that many exciting results have been found in the study of α-RuCl$_3$, there are some fundamental questions which are pending for answers. One is the exact crystal structure at low temperature (below 100 K). Due to stacking faults in the sample, the crystal structure of α-RuCl$_3$ has been reported to be $C2/m$, $P3_112$ or $R\overline{3}$ from different samples. Therefore to prepare high quality samples with less stacking faults density is of great importance to solve the crystal structure.

3
Experimental Techniques and Theory

3.1 Single crystal growth

3.1.1 An overview

Single crystal samples are of great importance and serve as the prerequisite for the study of physical properties of materials. Not only do they offer the opportunities to reveal the anisotropic properties in the study of dispersive collective excitations, electric and thermal transport, but also the high quality single crystal samples are a prerequisite to eliminate the influence from the grain boundaries, size effects in powder samples. This situation is particularly true in the research of the emergent phenomena in quantum materials since the novel phenomena that condensed matter physicists are interested in are always the results of a dedicate balance of many subtle effects. For example, the external pressure or magnetic field plays a crucial role in the tuning of quantum criticality in quantum materials with the presence of the competing phases. In single crystal samples, one will have more options to study their anisotropic properties when the external pressures or magnetic fields are applied along the different crystallographic directions. Besides, in the study of two-dimensional frustrated layered magnetic materials, the weak Van der Waals interlayer coupling may have profound influence on the magnetic order since the stacking faults will be introduced inevitably. For instance, in the Kitaev quantum spin liquid candidate α-$RuCl_3$, for sample with AB stacking sequence, it antiferromagnetically orders at 14 K; while in the sample with ABC stacking sequence, its magnetic transition temperature is reduced to 8 K [92]. In single crystal samples the mixture of AB and ABC stacking sequences is very common as a result of the nature of Van der Waals materials, which could be seriously misleading in the understanding of the intrinsic nature of α-$RuCl_3$.

Among a variety of quantum materials, topological materials, two-dimensional materials and frustrated magnets stand out because of their fascinating physical properties and huge potential in the application of spintronics and quantum technologies. The crystal growth of novel quantum materials is an activity encompassing both theoretical and experimental study and calling for a broad knowledge of material science, solid-state chemistry, physics, crystallography and engineering. Two cutting-edge methods: molten melt flux and chemical vapour transport are employed in the PhD work to grow single crystal samples. In the next sections, several most commonly used crystal growth methods for the synthesis of quantum materials as well as their realisation in this PhD work will be introduced. Furthermore, a list of the crystal growth experiments that have been carried out during the PhD study is given in Appendix A.1.

3.1.2 Crystal growth methods

A crystal growth process involves the well controlled transformation of the state or phase to a solid [93–95]. This may happen from liquid or vapour states to solid states, or from a solid state to a solid state. The last mentioned case is the solid-solid phase transition, which is usually unwanted in the process of crystal growth. Based on the states transformation in the crystal growth [96–108], there are therefore three major methods available for the single crystal growth: (a) growth of crystals from solutions; (b) growth of crystals from vapours; (c) growth of crystals from melts.

(a) Growth of crystals from solutions

This kind of method provides the possibilities that crystals can be grown in the temperature range that is much lower than the melting point, provided there is a suitable solvent and has the unique advantage that crystals could be grown even if they melt incongruently. The use of this method is widespread in preparation of water soluble compounds (also known as hydrothermal method), oxides, halides and intermetallics.

In the hydrothermal method, the lower-solubility crystals are successfully grown in a high-pressure (above ambient pressure) autoclave. The starting materials and suitable water based solvents are loaded in the autoclave at ambient condition firstly. Then the autoclave is put in a precisely temperature controlled incubator. Under the high temperature and high pressure condition, chemical reactions happen and give rise to the crystallization of the desired component. This process may take from several days to several weeks and crystals grown from the hydrothermal method are usually too small for neutron scattering experiment and have to be co-aligned together to enhance the signals.

Crystal growth of oxides or intermetallics from solutions (molten flux methods) needs much higher temperature compared to hydrothermal method. The common working temperature for this "flux method" is in the range of 100-1200 ° C, and this temperature range could be easily reached by a laboratory furnace. This method is perhaps most generally applicable in almost every laboratory for the growth of crystals because of the following advantages: (i) the target compound melts incongruently so it is difficulty to grow it by an optical floating zone furnace or a Bridgman furnace; (ii) the target compound or the starting materials have very high melting point, but the growth temperature may be substantially decreased by using a flux; (iii) flux could help to decrease the loss of volatile constituents and to eliminate the potential risk caused by the high vapour pressure. In the flux growth, the starting materials are dissolved in a solvent: salt (for oxides) or metal (for intermetallics) with relatively low melting point firstly. The crystals nucleate and grow at a much lower temperature than the melting point at normal condition and grow continuously with the decreasing of the temperature. A list of the desired properties that an ideal solvent should have is in Tab.3.1.

Table 3.1: Desired properties for an ideal solvent (taken from Ref.[109]).

1.	High solubility for the crystal constituents.
2.	The crystal phase required should be the only stable solid phase.
3.	Appreciable change of solubility with temperature.
4.	Viscosity in the range of 1 to 10 centipoise.
5.	Low melting point.
6.	Low volatility at the highest applied temperature.
7.	Low reactivity with the container material.
8.	Absence of elements which are incorporated into the crystal.
9.	Ready availability in high purity at low cost.
10.	Density appropriate for the mode of growth.
11.	Ease of separation from the grown crystal by chemical or physical means.
12.	Low tendency of the solvent to "creep" out of the crucible.
13.	Low toxicity.

Naturally, there is no solvent that fulfils all the requirements and a compromise has to be made in a real case, depending on the requirement of the size and quality of the crystals. For instance, the growth of oxides, the solvents that are widely used are listed in Tab 3.2. Crystal growers have to consider all the possible reactions between the solvents and the starting materials and make the best decision. Lead compounds are still widely used and the most important attribute of them is the high solubility of refractory oxides owing to the strong polarization of the Pb^{2+} ions, and the reaction among staring materials with the lead based solvents will form the complex ionic species. The solubility of bismuth based compounds is relatively lower compared to lead based compounds, but in many cases the bismuth compounds can be used to replace the lead compounds since Pb is not very environmentally friendly. One exception is the growth of crystals containing rare earth elements, in which the trivalent Bi^{3+} ions tends to replace the rare earth ions.

When it comes to the growth of intermetallic compounds, there are more information for reference, for instance the database for binary phase diagrams. Before choosing a suitable flux, the binary phase diagram is a powerful tool to help to make the decision. The use of metals with relatively low melting points and high boiling points are widespread and a summary of metallic fluxes commonly used is listed in Tab.3.3.

Table 3.2: Properties of the solvents commonly used for the growth of oxides (taken from Ref.[109]).

Type of solvent	Solvent	Melting point/°C	Boiling point/°C	Solubility of solvent	Remarks
Lead and bismuth based compounds	PbO	888	1472	Hot HNO_3-H_2O	Environmentally unfriendly; Corrodes Pt above 1300 °C
	PbF_2	855	1293	Hot HNO_3-H_2O	
	$PbCl_2$	498	954	Hot H_2O or acid	
	Bi_2O_3	820	1890	Hot HNO_3-H_2O	
	Bi_2O_3-B_2O_3	620-720	–	Hot HNO_3-H_2O	
	BiF_3	727	1027	Hot HNO_3-H_2O	
Borates	B_2O_3	460	1860	HF-H_2O	
	$K_2B_4O_7$	815	–	Hot H_2O or acid	
	$BaBO_4$	1105	–	Hot HNO_3-H_2O	
Halides	LiF	842	1676	Hot H_2O	
	LiCl	610	1382	Hot H_2O	
	NaF	988	1695	H_2O	
	KF	856	1502	H_2O	
	NaCl	801	1413	H_2O	
	KCl	772	1407	H_2O	
Hydroxides	NaOH	318	1390	H_2O	
	KOH	360	1320	H_2O	

Table 3.3: Properties of the solvents commonly used for the growth of intermetallics.

Solvent	Melting point/°C	Boiling point/°C	Separation of fluxes	Remarks
Sn	232	2270	Centrifugation; Ga; HCl-H_2O	
Ga	30	2430	Centrifugation; I_2-DMF	Ref.[110]
In	157	2080	Centrifugation; Ga	
Bi	271	1560	Centrifugation;	
Pb	327	1740	Centrifugation;	
Al	660	2467	Centrifugation; NaOH-H_2O	
Sb	631	1635	Centrifugation	
Te	450	990	Centrifugation; Evaporation	

After the crystal growth, the separation between crystals and flux is the last but most important step. Decanting and centrifuging are two widely used methods, while the drawback of them is self-evident: this process may cause large stress in the crystals from the abrupt thermal shock and the large centrifugal force may break the crystals. Separating flux at very high temperature is often accompanied by a thermal quenching of the crystal and will thus introduce the thermal shock and internal strain in the crystals inevitably, which may cause serious problems in the investigation of their physical properties. Yet for all that, many laboratories choose the centrifuge because they are easily operated and suitable for plenty of different compounds. A complication of methods to separate the specific flux from crystals has already been listed in Tab 3.2 and Tab.3.3, and some general techniques that could be considered for the designing the experiment for the flux separation are shown in Tab.3.4. The experimental approach and the equipment used (including the tube furnace, centrifugal machine and a sealed ampoule) for the crystal growth experiments using the flux method in this PhD thesis are as shown in Fig. 3.1 and in Fig. 3.2, respectively. The Al_2O_3 crucible with raw materials is sealed in a quartz ampoule and then it is put in a tube furnace. After it experiences the setted temperature history, the quartz ampoule is transferred to the centrifugal machine quickly and the flux is separated from the crystals.

Table 3.4: An overview of the flux separation techniques (taken from Ref.[110]).

Flux separation in the liquid state	Czochralski method
	Top-seeded solution growth (TSSG)
	Centrifugation, spinning off
	Pouring out, decanting
	Soaking up, ceramic sponge
Flux separation in the solid state	Drilling
	Etching (acids, bases, water, ...)
	Evaporation (Mg, Yb, Hg, Zn, ...)
	Isopropanol route
	Alloying (with Hg, Ga)
	I_2-DMF route

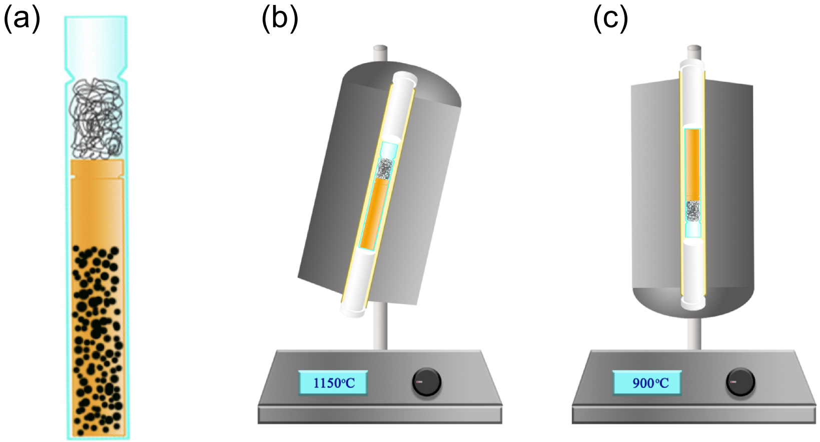

Figure 3.1: Sketch of the crystal growth from the flux method in this PhD work. The raw materials are firstly loaded in an Al_2O_3 crucible, and then sealed in the silica ampoule with argon atmosphere. When the growth of crystals finishes, the furnace is rotated by 180 ° around a horizontal axis (as shown in the figure). After that, the ampoule is transferred to the centrifuge to separate the crystals from the flux.

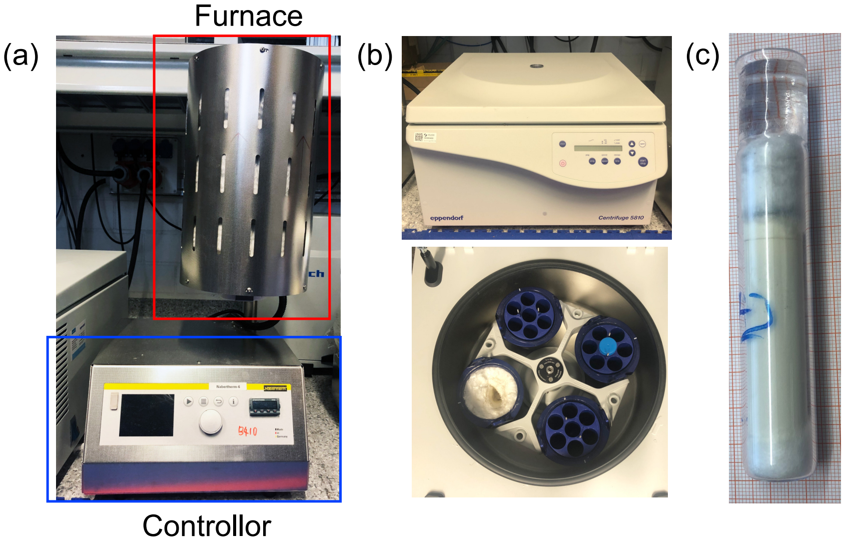

Figure 3.2: Equipments of the crystal growth from the flux method in this PhD work. (a) Tube furnace with working temperature from room temperature to 1200 °C manufactured by Nabertherm. (b) Centrifuge. (c) A sealed silica ampoule with samples inside.

(b) Growth of crystals from vapours

The growth of crystals from vapour involves the formation of vapour, cycling of transport agents and the deposition of crystals [111]. The term chemical vapour transport (CVT) itself summarizes a variety of reactions that share the following features in common: solid phases as the reactants and resultants, the presence of one or more intermediate reactants in gas form. A schematic picture of the crystal growth by CVT is illustrated in Fig.3.3, where the raw materials are transferred from the hot end (T_1) to the cold end (T_2) along with the formation and growth of crystals.

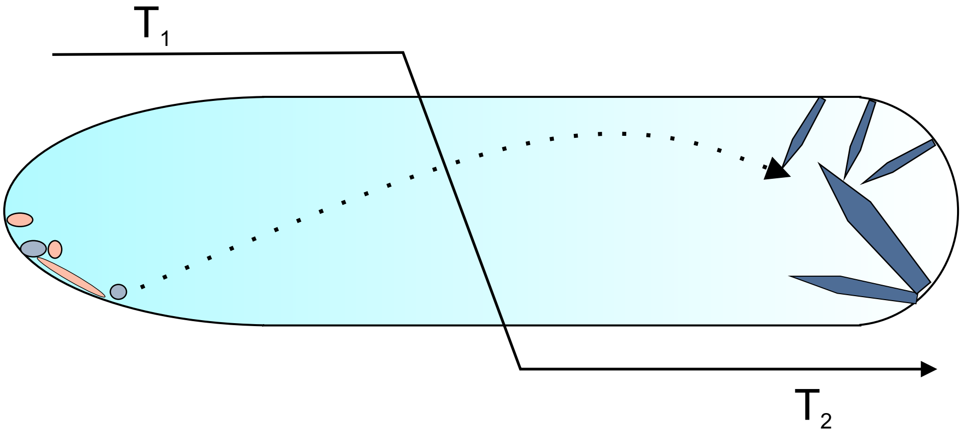

Figure 3.3: Sketch of the chemical vapour transport method. The ampoule is put in the furnace with a temperature gradient. During the crystal growth, the raw materials in the hot end (T_1) are transferred to the cold end (T_2) along with the formation and growth of the crystals.

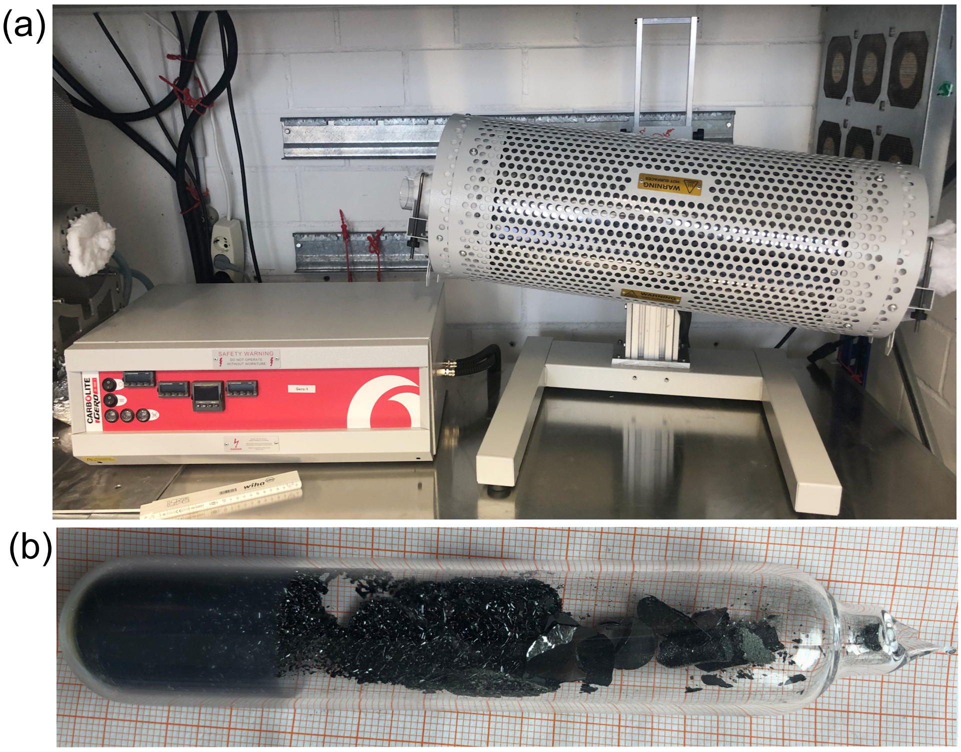

Figure 3.4: Equipments of the crystal growth from CVT method in this PhD work. (a) Three zone tube furnace for the crystal growth from CVT in this PhD work (Carbolite Gero). (b) A silica ampoule with α-$RuCl_3$ single crystals after growth inside.

A well-known experiment reported by H. Schäfer in 1956 emphasizes an interesting case that the migration of iron (III) oxide in the presence of hydrogen-chloride under a temperature gradient for the first time. The starting material and transport agent are sealed in quartz ampoules and this method is still commonly used up to now [112, 113]. The reactions in the sealed ampoules can be described in a general equation:

$$iA(\mathrm{s}) + kB(\mathrm{g}) \rightarrow jC(\mathrm{g}) + \ldots \tag{3.1}$$

where $A(\mathrm{s})$, $B(\mathrm{g})$ and $C(\mathrm{g})$ are resultants in solid (s) and gaseous (g) form and i, j, k are coefficients. It characterises the fundamental features in a CVT experiment that gaseous products are transferred from a condensed phase and a gaseous transport agent. The transport rate can be further calculated by *Schäfer's transport equation*:

$$\dot{n}(A) = \frac{n(A)}{t'} = \frac{i}{j} \cdot \frac{\Delta p(C)}{\Sigma p} \cdot \frac{\bar{T}^{0.75} \cdot q}{s} \cdot 0.6 \cdot 10^{-4} \left(\mathrm{mol} \cdot \mathrm{h}^{-1}\right) \tag{3.2}$$

$\dot{n}(A)$ Transport rate $\left(\mathrm{mol} \cdot \mathrm{h}^{-1}\right)$
i, j Stoichiometric coefficients in the transport equation
$\Delta p(C)$ Partial pressure difference of the transport effective species C (bar)
$\bar{T}$ Mean temperature along the diffusion path (K)
q Cross section of the diffusion path (cm^2)
s Length of the diffusion path (cm)
t' Duration of the transport experiments (h)

The equation can be used in a pressure range between 10^{-4} and 0.3 kPa to estimate the transport rate in a closed environment. The most important thing for a real experiment is to choose a suitable transport agent and a proper temperature gradient. There are some popularly used transport agents: $\mathrm{I_2}$, $\mathrm{Cl_2}$, $\mathrm{Br_2}$, $\mathrm{AlCl_3}$, $\mathrm{TeCl_4}$, HCl. It must be mentioned here that these transport agents are dangerous at high temperature, thus a rather precise estimation of the possible vapour pressure in the ampoule at high temperature is necessary. The sealed ampoule is usually put in a temperature-controlled two or three zone furnace, and in each zone of the furnace, the temperature can be set independently. The aim of crystal growth for neutron scattering experiment by CVT is to grow large high quality single crystal. Sadly, it is a pity that the crystals grown by CVT are normally in millimetre sizes and it takes a very long time for a growth experiment, so it is better to consider other methods first.

The picture of the three zone furnace and one ampoule with α-$\mathrm{RuCl_3}$ inside after the crystal growth is illustrated in Fig. 3.4. There are three independent temperature controlling systems in the furnace, allowing one to set the temperature gradient depending on the experiment. In the ampoule, some shiny plate-shape α-$\mathrm{RuCl_3}$ crystals can be seen after growth at the end of the ampoule.

(c) Growth of crystals from melts

The biggest advantage of this method is that crystals grown by this method are usually large in size, very suitable for neutron scattering experiment, while the drawback is that the crystal needs to melt congruently and they should not undergo a solid state phase transition during

cooling. There are three commonly used techniques for growing crystals from the melt:
Czochralski pulling technique: Firstly the starting materials are molten at high temperature in a crucible. The melt is kept at high temperature and a seed crystal is maintained just below its melting point. Then in the next step, the seed is brought into contact with the liquid. The temperatures of the seed and melt are adjusted so that the seed could grow slowly. By pulling the seed slowly, the crystal could grow along the opposite direction of the pulling.
Bridgman technique: This method needs to maintain the hot zone above the melting point of the material homogeneously usually by electric induction method. The crucible with materials inside is slowly moved out of the hot zone, and sometimes a small seed can also be loaded at the initial point of the growth. The usage of a seed crystal can improve the size of the crystal and the growth rate can be controlled by the rate of the crucible movement. If there is no seed, the grain with preferred orientation will be grown by weeding out other grains.
Optical floating zone technique: Crystal growth using this technique has been extensively used in the preparation of samples, particularly of multiferroics and pyrochlore compounds for neutron scattering during the past decades. The main part of the optical floating zone furnace is the ellipsoidal or parabolic mirrors to help focus infrared light onto the sample. The working temperature of the furnace depends on the lamps, and there are two kinds of lamps that are commonly used: halogen or xenon lamps. The crystal growth procedure is similar to Bridgman, and the one of the big advantages in the optical floating zone furnace is that by controlling the focus of the light the heating zone is much smaller, which helps control the crystal growth precisely. Besides, this technique is suitable for both conducting and insulating materials. Choosing a suitable crystal growth method is highly dependent on the aim of experiment. For physical properties measurement, like electric transport or thermal transport, millimetre size crystals will be enough and for neutron diffraction, a small and high quality sample is necessary, but for inelastic neutron scattering experiments, especially in order to observe continuous excitations in quantum spin liquid systems, the requirement for the quantity of the samples is always in several grams. In these experiments, co-aligning many pieces of small crystals is the most effective way to enhance the weak signals. Therefore, in order to decide a suitable method for the crystal growth, the available equipments, safety regulations, the temperature of separation, the mechanical robustness, the chemical stabilities and the targeted experiments for the crystals will have to be taken into account.

3.2 Neutron scattering theory

Neutron scattering is a powerful tool that can help to gain a microscopic understanding of many unique properties in condensed matter. Based on the basic properties of neutrons, such as spin-$\frac{1}{2}$, electrical neutrality, neutrons can penetrate deeply into the sample and come close to the nuclei without overcoming any Coulomb force. In addition, neutron can interact with magnetic dipole fields due to the unpaired electrons in an atom since it is spin-$\frac{1}{2}$, it thus can provide the information on the arrangement of electron spins and magnetization density maps in magnetic materials. Neutrons can also be employed to study light elements like hydrogen or oxygen and distinguish the different isotopes of a element due to their distinct scattering powers. Moreover, by inelastic neutron scattering, neutrons can detect the dynamics in condensed matter because the energies and wavelengths of neutrons match well to the time and length scales of many collective excitations in condensed matter. In this section, a brief description of the general neutron scattering theory [114, 115] will be given.

In a neutron scattering experiment, it is convenient to say the incident neutrons from the moderator with temperature T have the energy:

$$E = k_{\mathrm{B}}T, \tag{3.3}$$

where k_B is the Boltzmann constant and the de Broglie wavelength of a neutron with velocity v is

$$\lambda = \frac{h}{mv}, \tag{3.4}$$

where h is the Plank constant. The wave vector k and the momentum of the neutron are defined as

$$\mathbf{k} = \frac{2\pi}{\lambda}, \tag{3.5}$$

$$\boldsymbol{p} = \hbar\boldsymbol{k}. \tag{3.6}$$

Thus, it is easy to obtain the kinetic energy of neutrons given by

$$E = k_{\mathrm{B}}T = \frac{1}{2}mv^2 = \frac{h^2}{2m\lambda^2} = \frac{81.81}{\lambda^2}. \tag{3.7}$$

In the above equations, λ is in Å, T is in K, v is in km·s^{-1} and E is in meV. According to the energy of a neutron beam, the neutron source for experiments can be divided into three types: cold (0.1-10 meV), thermal (5-100 meV) and hot (100-500 meV).

3.2.1 General neutron scattering theory

For an incident neutron beam with incident wave vector $\boldsymbol{k}_i$ as shown in Fig. 3.5, the partial differential cross-section obtained from Fermi' Golden Rule is

$$\left(\frac{d^2\sigma}{d\Omega dE'}\right)_{\lambda_i\to\lambda_f} = \frac{1}{N}\left(\frac{m}{2\pi\hbar^2}\right)^2 \frac{\boldsymbol{k}_f}{\boldsymbol{k}_i}\sum_{\lambda_i,\sigma_i} p_{\lambda_i}p_{\sigma_i}\left|\left\langle \boldsymbol{k}_f\sigma_f\lambda_f|V(\mathbf{r})|\boldsymbol{k}_i\sigma_i\lambda_i\right\rangle\right|^2\cdot\delta\left(\hbar\omega+E_{\lambda_f}-E_{\lambda_i}\right), \tag{3.8}$$

where wave vector $\boldsymbol{k}_i$, spin state σ_i, energy E_{λ_i} represent the sates for an incident neutron, and after scattering by the interaction potential $V(\mathbf{r})$, the state of neutron becomes $\boldsymbol{k}_f$, σ_f, E_{λ_f}, and the quantum numbers λ_i, λ_f denote the initial and finial states of the scattering system. The δ function describes the law of energy conservation in the scattering system. In addition, a possible change in energy of the scattering system $\hbar\omega$ and the probability p_j for the system or the neutron of being in the quantum state j are also considered. This master formula can be further applied on neutron scattering of the nuclear with specific interaction potential $V(\mathbf{r})$ upon some assumptions.

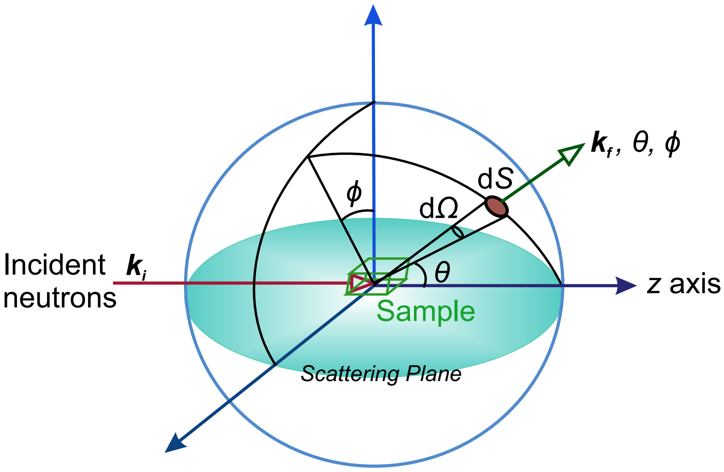

Figure 3.5: A sketch of the scattering cross-section, where the incident neutron beam with wave vector $\boldsymbol{k}_i$ changes to $\boldsymbol{k}_f$ after scattering at the sample.

The neutron interacts with the nuclei of the sample by short range nuclear forces, which is much smaller than the typical neutron wavelength. In this regard, the interaction potential of a crystalline sample can be treated as the point-like potential. The interaction potential can be described by Fermi pseudo-potential for the nuclear scattering:

$$V(\mathbf{r}) = \frac{2\pi\hbar^2}{m}\sum_j b_j\delta(\mathbf{r}-\mathbf{R}_j). \tag{3.9}$$

Here $\mathbf{R}_j$ denotes the position of the j^{th} scattering nuclei in the sample, and ($\mathbf{r}$ - $\mathbf{R}_j$) provides the distance between the incident neutron and the j^{th} nuclei. b_j is the nuclear scattering length, which characterises the scattering magnitude of the elements. The momentum transfer is defined as $\mathbf{Q} = \boldsymbol{k}_f - \boldsymbol{k}_i$, as the spatial variable instead of the neutron wave vectors. The differential cross sections for coherent and incoherent nuclear scattering can be further are derived as

$$\left(\frac{d^2\sigma}{d\Omega dE'}\right)_{coh} = \frac{1}{N}\frac{\sigma_{coh}}{4\pi}\frac{1}{2\pi\hbar}\frac{k_f}{k_i}\sum_{j,j'}\int_{-\infty}^{\infty}\left\langle e^{-i\mathbf{QR}_j(0)}e^{i\mathbf{QR}_{j'}(t)}\right\rangle e^{i\omega t}dt \tag{3.10}$$

and

$$\left(\frac{d^2\sigma}{d\Omega dE'}\right)_{inc} = \frac{1}{N}\frac{\sigma_{inc}}{4\pi}\frac{1}{2\pi\hbar}\frac{k_f}{k_i}\sum_{j}\int_{-\infty}^{\infty}\left\langle e^{-i\mathbf{QR}_j(0)}e^{i\mathbf{QR}_{j}(t)}\right\rangle e^{-i\omega t}dt, \tag{3.11}$$

where

$$\sigma_{\text{coh}} = 4\pi(\bar{b})^2, \quad \sigma_{\text{inc}} = 4\pi\left\{\overline{b^2} - (\bar{b})^2\right\} \tag{3.12}$$

account for the value for the coherent and incoherent scattering length. The coherent scattering depends on the correlation between the positions of the same nucleus. Therefore it gives the interference effects and results in the Bragg scattering with a characteristic **Q**-dependence of the scattered intensity. The pair correlation function $S(\mathbf{Q},\omega)$ can be used to describe the correlations and concludes the momentum and the energy transfers in a scattering system with integrating all the correlations in space and time, is the aim for a neutron experiment.

$$S(\mathbf{Q},\omega) = \frac{1}{N}\frac{1}{2\pi\hbar}\sum_{j,j'}\int_{-\infty}^{\infty}\left\langle e^{-i\mathbf{QR}_j(0)}e^{i\mathbf{QR}_{j'}(t)}\right\rangle e^{i\omega t}dt. \tag{3.13}$$

Neutron scattering from crystalline samples

Here the elastic neutron scattering without any energy transfer where the incident and scattered neutrons have the same energy is only discussed. In a crystalline sample, the lattice vector is given as $\mathbf{d} = l_1\boldsymbol{a}_1 + l_2\boldsymbol{a}_2 + l_3\boldsymbol{a}_3$ if the three basis vectors of the unit cell are denoted as $\boldsymbol{a}_1$, $\boldsymbol{a}_2$, $\boldsymbol{a}_3$ and l_1, l_2, l_3 are integers. Considering the displacement of atom d from its equilibrium position j caused by thermal oscillations $\mathbf{u}_d(j,t)$, the position of atom d can be expressed as

$$\mathbf{R}_{j,d} = \mathbf{j} + \mathbf{d} + \mathbf{u}_d(j,t). \tag{3.14}$$

Therefore, the differential cross section for elastic scattering with invariant incident and scattered energy can be deduced by substituting $\mathbf{R}_{j,d}$ in Equ.3.13.

$$\left(\frac{d\sigma}{d\Omega}\right)_{coh}^{el} = \frac{(2\pi)^3}{v_0}\sum_{\tau}|F_N(\mathbf{Q})|^2 \times \delta(\mathbf{Q}-\tau), \tag{3.15}$$

where $|F_N(\mathbf{Q})|^2$ is the structure factor, which is defined as

$$F_N(\mathbf{Q}) = \sum_d \bar{b}_d e^{i\mathbf{Qd}} e^{-W_d(\mathbf{Q})}, \tag{3.16}$$

in which exp(-$W_d(\mathbf{Q})$) is the Debye-Waller factor, which accounts the mean square displacement of each atom and further reduces the scattered intensity. The $|F_N(\mathbf{Q})|^2$ is the Fourier transform of the scattering density within the unit cell. It is very important in the determination of structures and actually is the quantity results measured from a neutron diffraction experiment since it contains the structure information of the scattered sample.

Magnetic neutron scattering

For magnetic neutron scattering, the incident neutron interacts with magnetization densities by unpaired electrons by magnetic dipole interactions with the spin of the neutrons. The interaction potential between a neutron in spin state $S(\mathbf{Q}, \omega)$ and a moving electron of momentum $\mathbf{p}$ and spin $\mathbf{s}$ is

$$\mathbf{V}_M(\mathbf{r}) = -\gamma \mu_N^2 \mu_B \boldsymbol{\sigma} \cdot \left[\mathrm{curl} \left(\frac{\mathbf{s} \times \hat{\mathbf{R}}}{R^2} \right) + \frac{1}{\hbar} \frac{\mathbf{p} \times \hat{\mathbf{R}}}{R^2} \right], \tag{3.17}$$

where γ is 1.9132 representing the gyromagnetic ratio, and μ_N, μ_B are the nuclear and the Bohr magneton. Furthermore, by introducing this potential in Equ.3.8 will give the magnetic scattering expression:

$$\left(\frac{d^2\sigma}{d\Omega dE'} \right)_{mag} = \frac{(\gamma r_0)^2}{\hbar} \frac{k_f}{k_i} \sum_{\alpha,\beta} \left(\delta_{\alpha,\beta} - \frac{Q_\alpha Q_\beta}{Q^2} \right) S^{\alpha,\beta}(\mathbf{Q}, \omega), \tag{3.18}$$

where r_0 is the classic electron radius and α, β are spatial coordinates with $\alpha, \beta \in [\, x,y,z \,]$. The corresponding correlation function for magnetic neutron scattering can be interpreted as

$$S^{\alpha,\beta}(\mathbf{Q}, \omega) = \frac{1}{2\pi} \int_{-\infty}^{\infty} \sum_{j,d} \frac{1}{2} g_d f_d(\mathbf{Q}) e^{-W_d(\mathbf{Q})} e^{i\mathbf{Q}(\mathbf{j}+\mathbf{d})} \left\langle S_0^\alpha(0) S_{j+d}^\beta(t) \right\rangle e^{-i\omega t} dt, \tag{3.19}$$

in which $f_d(\mathbf{Q})$ is the atomic form factor of atom d in the unit cell j, g is the Landé factor.

Polarised neutron scattering

The spin of neutrons has provided a unique and invaluable tool to study magnetism in condensed matter. There are several ways to create polarised neutrons, and the use of He^3 gas cells, super-mirrors, Bragg scattering from a crystal monochromator are widespread [116–120]. The definition of the polarisation of a neutron beam is based on the quantization of the numbers with neutron in spin up and spin down states, which is written as

$$P = \frac{n_\uparrow - n_\downarrow}{n_\uparrow + n_\downarrow}. \tag{3.20}$$

Based on the Blume-Maleyev equation, the polarised neutron scattering differential cross section is described with four terms, which are as

$$\left(\frac{d\sigma}{d\Omega} \right) = N^* N + \mathbf{M}_\perp^* \cdot \mathbf{M}_\perp + (N \mathbf{M}_\perp^* + N^* \mathbf{M}_\perp) \cdot \mathbf{P_i} + i \left(\mathbf{M}_\perp^* \times \mathbf{M}_\perp \right) \cdot \mathbf{P_i}; \tag{3.21}$$

$$\mathbf{M}_\perp = (\mathbf{Q} \times \mathbf{F_M} \times \mathbf{Q}), \tag{3.22}$$

where N, $\mathbf{M}_\perp$ are the structure factor and the magnetic interaction vector, and $\mathbf{P_i}$ is the polarisation of the incident beam. The first and second term N^*N, $\mathbf{M}_\perp{}^* \cdot \mathbf{M}_\perp$ are pure nuclear contribution and magnetic contribution respectively. The third term comes from the interference between the nuclear and the magnetic signals, and the last one is the chiral magnetic term. The direction and the magnitude of the beam polarisation is also dependent on the scattering process. Considering the scattered neutrons have the polarisation $\mathbf{P_f}$, there is

$$\begin{aligned}\mathbf{P}_\mathrm{f}\left(\frac{d\sigma}{d\Omega}\right) &= N^*N\mathbf{P}_\mathrm{i} \\ &- \left(\mathbf{M}_\perp{}^* \cdot \mathbf{M}_\perp\right)\mathbf{P_i} + \left(\mathbf{P_i} \cdot \mathbf{M}_\perp{}^*\right)\mathbf{M}_\perp + \left(\mathbf{P_i} \cdot \mathbf{M}_\perp\right)\mathbf{M}_\perp{}^* \\ &+ \left(N\mathbf{M}_\perp{}^* + N^*\mathbf{M}_\perp\right) - i\left(N\mathbf{M}_\perp{}^* - N^*\mathbf{M}_\perp\right) \times \mathbf{P_i} \\ &- i\left(\mathbf{M}_\perp{}^* \times \mathbf{M}_\perp\right).\end{aligned} \tag{3.23}$$

The first line gives the terms parallel to $\mathbf{P}$ which do not rotate the polarisation and the second line gives those which produce rotation towards the interaction vector

$$\mathbf{M}_\perp = < \mathbf{M} \times \mathbf{Q} \times \mathbf{M} > . \tag{3.24}$$

Obviously, the nuclear scattering do not change the polarisation while the effect of non chiral magnetic terms is a precession of the incident polarisation by 180° around $\mathbf{M}_\perp$. The third term contributes to the polarisation when magnetic and nuclear signal are in phase and the chiral term creates polarisation along the scattering $\mathbf{Q}$ if it exists. Thus, the scattered neutron spin $\mathbf{P}_f$ has the following tensor relationship with incident neutron spin

$$\mathbf{P}_f = \mathcal{P}\mathbf{P}_i + \mathbf{P}', \tag{3.25}$$

where $\mathcal{P}$ is a tensor to describe the rotation of the polarisation and $\mathbf{P}'$ is the polarisation created.

In experiment, three polarisation directions are defined in a right-handed orthogonal coordinated system, where polarisation direction x is along scattering vector $\mathbf{Q}$, polarisation direction z is parallel to the scattering plane and polarisation direction y can be found by right-hand rule. By combining the spin states of the incident or accident states of the polarised neutron, nine different terms are generated, namely xx, xy, xz, yx, yy, yz, zx, zy and zz, in which xx, yy, and zz are diagonal terms, which are used for XYZ polarisation analysis.

$$\begin{pmatrix} p_{fx}\frac{p_{ix}\left(N^2-\mathbf{M}^2\right)-J_{yz}}{I_x} & p_{fx}\frac{-p_{iy}J_x-J_{yz}}{I_y} & p_{fx}\frac{p_{iz}J_{ny}-J_{yz}}{I_z} \\ p_{fy}\frac{p_{ix}J_{nz}+R_{ny}}{I_x} & p_{fy}\frac{p_{iy}\left(N^2+\mathbf{M}^2_{\perp y}-\mathbf{M}^2_{\perp z}\right)+R_{ny}}{I_y} & p_{fy}\frac{p_{iz}R_{yz}+R_{ny}}{I_z} \\ p_{fz}\frac{-p_{ix}J_{ny}+R_{nz}}{I_x} & p_{fz}\frac{p_{iy}R_{yz}+R_{nz}}{I_y} & p_{fz}\frac{p_{iz}\left(N^2-\mathbf{M}^2_{\perp y}+\mathbf{M}^2_{\perp z}\right)+R_{nz}}{I_z} \end{pmatrix} \tag{3.26}$$

with

$$
\begin{aligned}
&N^2 = NN^*; \\
&R_{ni} = 2\,\mathrm{Re}\left(N\mathbf{M}^*_{\perp i}\right); \qquad && R_{ij} = 2\,\mathrm{Re}\left(M_{\perp i}M^*_{\perp j}\right); \\
&J_{ni} = 2\,\mathrm{Im}\left(N\mathbf{M}^*_{\perp i}\right); && J_{ij} = 2\,\mathrm{Im}\left(\mathbf{M}_{\perp i}M^*_{\perp j}\right); \\
&I_x = N^2 + \mathbf{M}^2_{\perp y} + \mathbf{M}^2_{\perp z} + p_{ix}J_{yz}; \\
&I_y = N^2 + \mathbf{M}^2_{\perp y} + \mathbf{M}^2_{\perp z} + p_{iy}R_{ny}; \\
&I_z = N^2 + \mathbf{M}^2_{\perp y} + \mathbf{M}^2_{\perp z} + p_{iz}R_{nz},
\end{aligned}
$$

where N is nuclear structure factor, $\mathbf{M}_{\perp y}$ and $\mathbf{M}_{\perp z}$ are the magnetic components perpendicular to $\mathbf{Q}$ along polarised y or z direction, thus $\mathbf{M}_{\perp} = \mathbf{M}_{\perp y} + \mathbf{M}_{\perp z}$. p_{ix}, p_{ix}, p_{ix} are the incident neutron beam polarisation. For a pure magnetic reflection, there are $N = R_{ny} = R_{nz} = J_{ny} = J_{nz} = 0$. In case of p_{ix} = p_{ix} = p_{ix} = p_0 and p_{fx} = p_{fx} = p_{fx} = 1, the polarisation matrix can be further reduced as

$$
\begin{pmatrix}
\frac{p_0\mathbf{M}^2_{\perp} - J_{yz}}{I_x} & \frac{-J_{yz}}{I_y} & \frac{-J_{yz}}{I_z} \\
0 & \frac{p_0\left(\mathbf{M}^2_{\perp y} - \mathbf{M}^2_{\perp z}\right)}{I_y} & \frac{p_0 R_{yz}}{I_z} \\
0 & \frac{p_0 R_{yz}}{I_y} & \frac{p_0\left(-\mathbf{M}^2_{\perp y} + \mathbf{M}^2_{\perp z}\right)}{I_z}
\end{pmatrix}. \tag{3.27}
$$

For each term in the matrix 3.26, the results of the polarisation analysis experiment could be expressed in terms of generalised cross-sections I_{ij}. The indices i and j each refer to one of the three orthogonal directions defined by the experiment: the second superscript gives the direction of polarisation and the first the direction of analysis. They are related to the general polarisation equation by

$$
\mathcal{P}_{ij} = \frac{I^{ij} - I^{-ij}}{I^{ij} + I^{-ij}}. \tag{3.28}
$$

3.3 Neutron scattering instruments

DNS (Diffuse scattering neutron time of flight spectrometer)

DNS is a powerful and versatile diffuse scattering cold neutron time-of-flight spectrometer with polarisation analysis [121, 122]. Based on the XYZ-polarisation analysis technique, DNS could separate the nuclear coherent, spin incoherent and magnetic scattering unambiguously and cover a large scattering $\mathbf{Q}$ range in reciprocal space. A sketch picture of DNS is illustrated in Fig. 3.6. Three directions are defined in the DNS as shown in Fig.3.7, where the polarisation x direction is parallel to the average directions of the scattering vector $\mathbf{Q}$, polarisation z direction is perpendicular to the scattering plane and polarisation y direction can be determined by a right-hand rule.

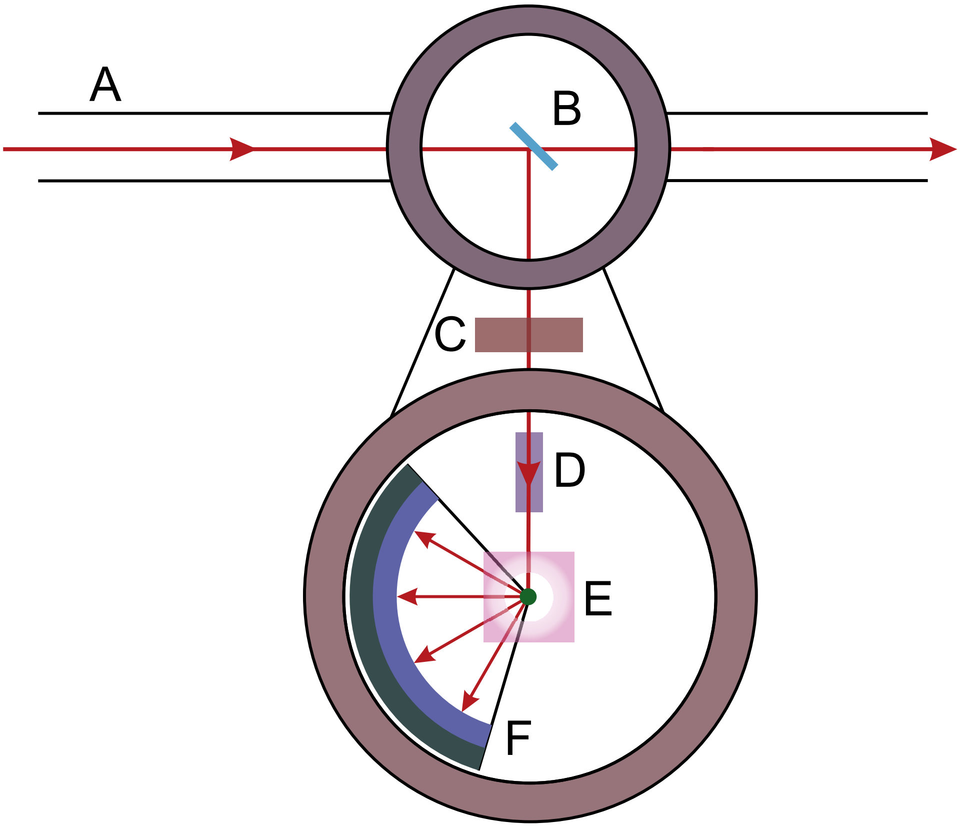

Figure 3.6: Sketch of the DNS instrument. A: Neutron guide NL6-S; B: Monochromator; C: Chopper; D: Polariser; E: Sample space with XYZ coils; F: Detector banks with polarisation analyser. Figure replotted from `https://mlz-garching.de/dns`.

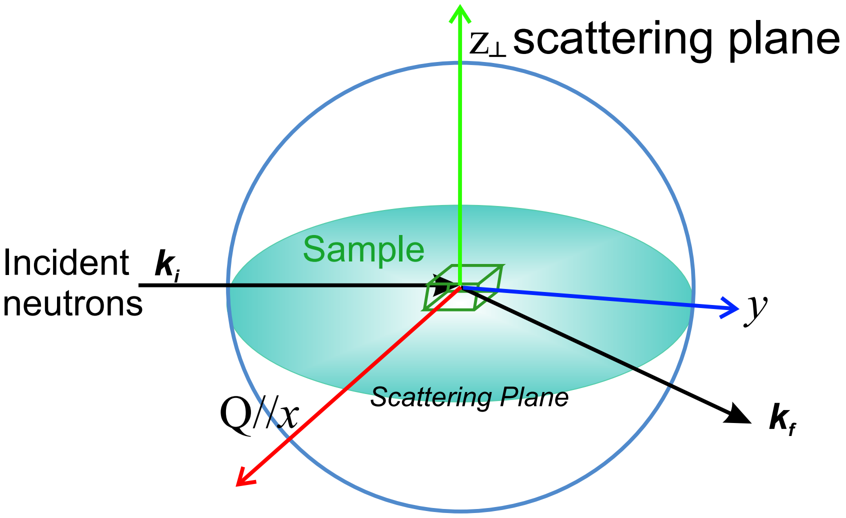

Figure 3.7: Definition of the x, y, z direction in a polarised scattering experiment.

The scattering intensity measured in each XYZ-polarisation channel in DNS follows the below rules:

Table 3.5: The scattering intensities measured in different channels at DNS.

Polarisation	Spin-flip	Non Spin-flip
$\mathbf{P} \parallel x \parallel \mathbf{Q}$	$\frac{2}{3}\frac{d\sigma}{d\Omega_{inc}} + bg + \frac{d\sigma^{\mathbf{M}_y^{\perp}}}{d\Omega_{mag}} + \frac{d\sigma^{\mathbf{M}_z^{\perp}}}{d\Omega_{mag}}$	$\frac{d\sigma}{d\Omega_{coh}} + \frac{1}{3}\frac{d\sigma}{d\Omega_{inc}} + bg$
$\mathbf{P} \parallel z \perp \mathbf{Q}$	$\frac{2}{3}\frac{d\sigma}{d\Omega_{inc}} + bg + \frac{d\sigma^{\mathbf{M}_y^{\perp}}}{d\Omega_{mag}}$	$\frac{d\sigma}{d\Omega_{coh}} + \frac{1}{3}\frac{d\sigma}{d\Omega_{inc}} + bg + \frac{d\sigma^{\mathbf{M}_z^{\perp}}}{d\Omega_{mag}}$

where $\mathbf{P}$, x, y, z, $\mathbf{Q}$, $\frac{d\sigma}{d\Omega_{inc}}$, $\frac{d\sigma}{d\Omega_{mag}}$, bg denote neutron beam polarisation, x, y, z neutron polarisation directions, scattering vector, incoherent cross section, magnetic cross section and background. The most important separating rule at DNS is when $\mathbf{P} \parallel x \parallel \mathbf{Q}$, if the background and incoherent scattering is ignored, the intensity in x-spin-flip channel is pure magnetic scattering while the intensity in x-non-spin-flip channel only measures the nuclear contributions.

Single crystal diffractometer

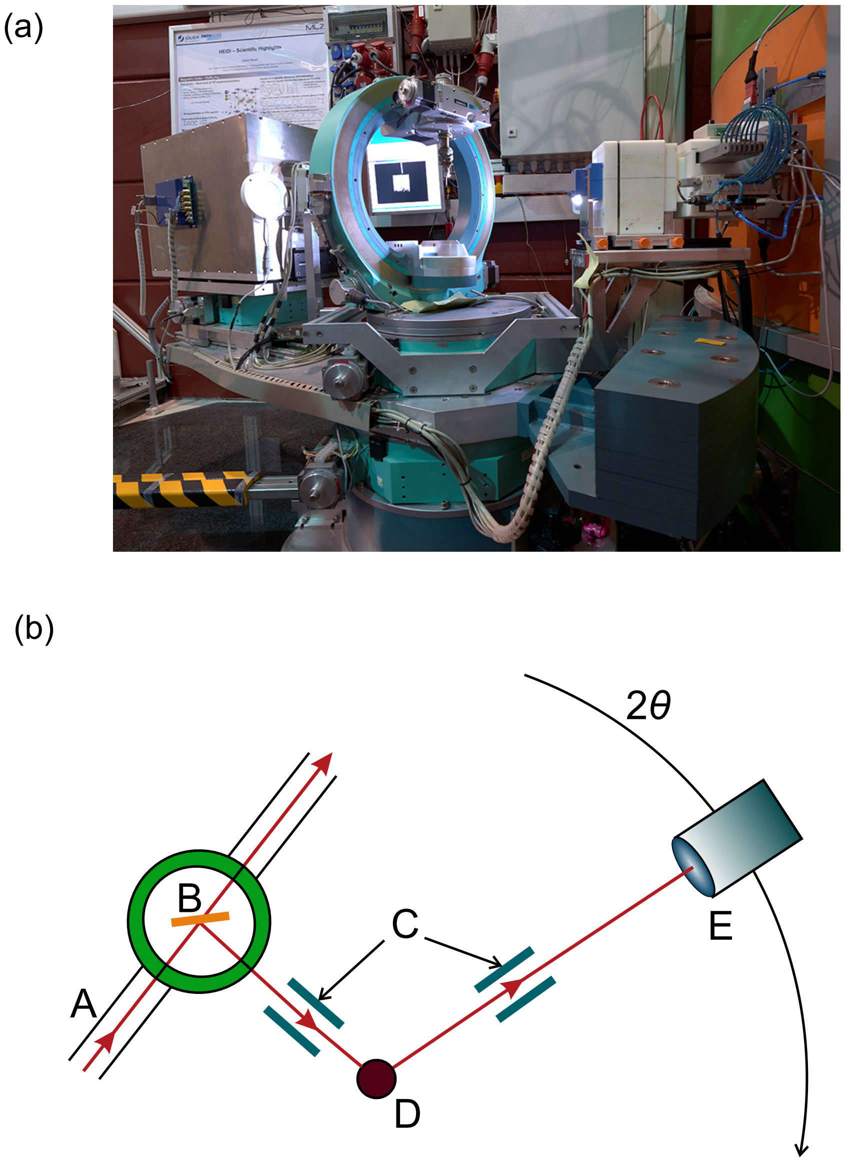

Figure 3.8: Pictures of the four cycle diffractometer instrument. (a) A picture of HEiDi. Source: `https://mlz-garching.de/heidi`. (b) Sketch of horizontal scattering plane of the diffraction: A: Neutron guide; B: Monochrometer; C: Slits or collimators before and after sample. D: Sample space; E: Detector.

D10 (Institut Laue-Langevin, Grenoble) and HEiDi (MLZ, Garching) are both typical constant wavelength four circle single crystal diffractometers [123, 124]. The sketch of D10 is shown in Fig. 3.8(b), where the scattering plane is the horizontal plane when the Orange Cryostat is used . To start a neutron diffraction experiment at such instrument requires the pre-knowledge of lattice parameters of the samples and the rough orientation of the crystallographic axes. A typical neutron diffraction experiment normally lasts 3-10 days depending on the number of measured (hkl) reflections. In order to measure a (hkl) reflection, the detector is moved to the calculate 2θ position , and then rotate the sample about a vertical axis to right position to collect intensities. After collecting the data, neutron data normally needs to be corrected for the refinement.

3.4 Physical properties measurement

Magnetization (DC), heat capacity and electrical resistivity measurements are performed on Quantum Design Physical Properties Measurement Systems (PPMS) (shown in Fig.3.9) by standard procedure. PPMS uses the thermal relaxation method to measure the heat capacity, which measures the response of the sample after a heat perturbation. A flat-plate-shaped sample with a smooth surface is mounted on the micro-calorimeter platform linked by four threads with thermal conductance to the cryostat (Bath). Apiezon N grease is used to increase the thermal conductivity between the micro-calorimeter platform and the sample. The puck with an appropriate amount of the grease has to be measured separately and subtracted from the raw data of the sample measurements to obtain the absolute heat capacity of the sample. The measurement of longitudinal electrical resistivity and Hall resistivity employs the standard four points method with ETO option of PPMS on a commercial sample pack from quantum design. Magnetic susceptibility is measured under both field cooling and zero field cooling conditions on a standard procedure at PPMS.

Figure 3.9: Picture of quantum design PPMS system. Source: www.qdusa.com/products/ppms.html

3.5 Magnetic structure determinations from neutron diffraction

The magnetic structures of crystalline samples determined form neutron scattering experiments are mainly solved by two crystallographic approaches: magnetic space groups (Shubnikov groups) and group representation theory applied to conventional crystallographic space groups [125–133]. The magnetic space group approach is widespread used to describe the invariance symmetry properties and commensurate magnetic configurations, while the representation analysis is more general and can be applied to all kinds of magnetic structures [134]. By extending the magnetic space group to the magnetic superspace groups, one can describe the incommensurate magnetic structures successfully, which has the advantage of understanding the macroscopic properties derived from the spin configurations [131]. This section will introduce fundamental knowledge of magnetic symmetry and the application of group representation in the magnetic structure determination.

3.5.1 Magnetic space groups

Considering the magnetic group **M**, which is the subgroup of the direct product crystallographic group **G** and the time-reversal group **G**:

$$\mathbf{M} \subset \mathbf{G} \otimes \mathbf{R} \tag{3.29}$$

where $\mathbf{R} = \{1, 1'\}$ and 1, $1'$ are identity and time-reversal symmetry, respectively [128, 129]. The magnetic groups derived from the crystallographic group **G** can be constructed considering the index 2 subgroups **H** of **G** as constituting the unprimed elements and the rest of operators, $(\mathbf{G} - \mathbf{H})$, those that are multiplied by the time-reversal operator. The magnetic group is then expressed as

$$\mathbf{M} = \mathbf{H} + (\mathbf{G} - \mathbf{H})1'. \tag{3.30}$$

The International Table of Crystallography, Volume A (ITA) has summarised the subgroups of index 2 for all the space groups.

Following Eq.3.30, one can construct the magnetic point groups. There are 32 trivial magnetic point groups, 32 paramagnetic groups and 58 black-white point groups. However, only 31 magnetic point groups are *admissible*, in which the ordered magnetic structure could be realised. For instance, if the point group is $\mathbf{G} = 4/m$, the magnetic point groups are

$$\{4/m, 4/m', 4'/m', 4'/m\}$$

derived from Eq.3.30. If there is a magnetic moment **S** is put at the origin pointing along arbitrary direction and applying the operator, the magnetic moment **S** should vanish. Similarly, if the magnetic moment is put along the four fold symmetry or lies in the mirror plane, the magnetic moment also vanishes. This proves that not all the magnetic point groups are *admissible*. The primitive Bravais lattices could be constructed by the linear combination of three non coplanar basis vectors $\{\mathbf{a_1}, \mathbf{a_2}, \mathbf{a_3}\}$:

$$\mathbf{T}_P = \{\mathbf{t} \mid \mathbf{t} = l_1\mathbf{a}_1 + l_2\mathbf{a}_2 + l_3\mathbf{a}_3, l_i \in \mathbb{Z}\},$$

where $l_i, i = 1, 2, 3$ are integers. In the centre lattice , the centre vectors are added $\mathbf{t}_i^C, i = 1, ..n_c$:

$$\mathbf{T}_C = \left\{ \mathbf{t} \mid \mathbf{t} = l_1\mathbf{a}_1 + l_2\mathbf{a}_2 + l_3\mathbf{a}_3 + n_1\mathbf{t}_1^C + n_2\mathbf{t}_2^C \ldots + n_{n_c}\mathbf{t}_{n,l}^C, l_i \in \mathbb{Z}, n_i \in \{0, 1\} \right\}.$$

The translation group can always be described using a primitive cell but, in order to simplify the expressions of the symmetry operators a centred basis is often more convenient. Following the previous procedure one can construct the different magnetic Bravais lattices. A total number of 1651 types of magnetic space groups are derived and among them 230 magnetic space groups have the form $\mathbf{P} = \mathbf{G} + \mathbf{G}'$ (paramagnetic or "grey" groups) and 1191 magnetic space groups are "black-white" groups with the form $\mathbf{M} = \mathbf{H} + (\mathbf{G} - \mathbf{H})1'$. In the last groups, the translation subgroup contains "anti-translations" (pure translations combined with the time-reversal operator).

In the magnetic space groups, the first kind the subgroup of translations is the same as that of the parent space group, and in other words, the magnetic unit cell is the same as the crystallographic unit cell. In the second kind there are some translations associated with time-reversal operator, so that the “primitive magnetic unit cell” is bigger than the primitive crystallographic unit cell.

In order to refine the magnetic structure from neutron diffraction data by the magnetic space group approach, one has several choices. Jana2006 has integrated the magnetic space groups and the magnetic superspace groups options for users [135]. When input the neutron diffraction data and propagation vector, Jana2006 could calculate the symmetry allowed magnetic space groups models and users could refine the data in different models and find the best solution [135]. Besides, Fullprof also supports the refinement by magnetic space groups, and the corresponding profile controlling file (PCR) could be generated from online crystallographic tools "Bilbao crystallography server" [136].

3.5.2 Group representation analysis of magnetic structure

The group representation theory is a very useful tool to describe and classify magnetic order in materials [137–141]. The matrices $\Gamma(g)$ ascribed to each element g for which the same multiplication rules as for the group $\mathbf{G}$ holds is termed a representation of group $\mathbf{G}$:

$$\Gamma = \{\Gamma(g) \mid g \in \mathbf{G}\}, \quad \Gamma(g_1 g_2) = \Gamma(g_1)\Gamma(g_2). \tag{3.31}$$

A new matrix system which is similar to $\mathbf{G}$ could be generated by similarity transformation by the unitary matrix U:

$$U\Gamma(g)U^{-1} = \widetilde{\Gamma}(g), \tag{3.32}$$

which is also a representation of the group $\mathbf{G}$.

If a representation Γ of group $\mathbf{G}$ could be portioned so that it has the form

$$\widetilde{\Gamma}(g) = \begin{pmatrix} \Gamma_{11}(g) & \Gamma_{12}(g) \\ \mathbf{0} & \Gamma_{22}(g) \end{pmatrix}, \tag{3.33}$$

for each $g \in \mathbf{G}$, then the matrices $\Gamma_{11}(g)$ and $\Gamma_{22}(g)$ are also representations of group $\mathbf{G}$. A representation of a group $\mathbf{G}$ is said to be *reducible* if it could be written in form of Eq.3.33,

otherwise it is said to be "*irreducible*", known as irreducible representations ("*irreps*").
A reducible representation can be expressed as the direct sum of *irreps*:

$$\Gamma = \sum_{\oplus\nu} n_\nu \Gamma^\nu = n_1\Gamma^1 \oplus n_2\Gamma^2 \oplus n_3\Gamma^3 \cdots \oplus n_m\Gamma^m, \tag{3.34}$$

where ν is the index of the representation with dimension l_ν. The number of irreducible representations of a group and their dimensionality are entirely determined by the structure of the group.
When Γ^ν_{ij} and Γ^μ_{lm} are the matrices of different irreducible representations, the orthogonality relation is

$$\sum_{g\in\mathbf{G}} \Gamma^{\nu *}_{ij}(g)\Gamma^\mu_{lm}(g) = \frac{n(\mathbf{G})}{l_v}\delta_{il}\delta_{jm}\delta_{\mu\nu}, \tag{3.35}$$

where $n(\mathbf{G})$ is the order of group $\mathbf{G}$. The traces of the representation matrix is the character of the element in group $\mathbf{G}$: $\chi(g) = tr(\Gamma(g)) = \sum_{j=1}^{n(\mathbf{G})} \Gamma(g)_{jj}$. The Equ.3.35 could be reduced to the orthogonality relation for the characters of the *irreps*

$$\sum_{g\in\mathbf{G}} \chi^{\nu *}(g)\chi^\mu(g) = n(\mathbf{G})\delta_{\mu\nu}. \tag{3.36}$$

The quantity n_ν, which describes the multiplicity of the νth *irreps* is given by

$$n_v = \frac{1}{n(\mathbf{G})}\sum_{g\in\mathbf{G}} \chi(g)\chi^{*\nu}(g). \tag{3.37}$$

If $\varphi_i(i = 1, 2, ...p)$ donates a set of physically relevant functions of the working space and the action of the operator $O(g)$ associated to a symmetry operator when applied to the function is given by

$$O(g)\varphi_j(\mathbf{r}) = \varphi'(\mathbf{r}) = \sum_i \Gamma_{ij}(g)\varphi_i(\mathbf{r}). \tag{3.38}$$

The general procedure obtained in the theory of representations for constructing the basis functions ψ of a given *irreps* of group $\mathbf{G}$ means having the so-called projection operator P act upon some starting function φ

$$\psi^v_i = P^\nu\varphi = \frac{1}{n(\mathbf{G})}\sum_{g\in\mathbf{G}} \Gamma^{*\nu}_{i[j]}(g)O(g)\varphi \quad (i = 1, \ldots l_\nu). \tag{3.39}$$

The pure translation group $\mathbf{T}$ is a subgroup of the space group, which is Abelian and hence, the *irreps* is all one-dimensional. Obviously, an element $\mathbf{T}(g)$ corresponding to some translation $\mathbf{t} = n_1\mathbf{t}_1 + n_2\mathbf{t}_2 + n_1\mathbf{t}_3$ can be represented in multiplication form:

$$\mathbf{T}(t) = [\mathbf{T}(t_1)]^{n_1}[\mathbf{T}(t_2)]^{n_2}[\mathbf{T}(t_3)]^{n_3}. \tag{3.40}$$

Considering the cyclic condition for a three dimensional finite crystal, the corresponding equation for the elements of the translational group can be written as

$$[\mathbf{T}(t_i)]^{N_i+1} = \mathbf{T}(t_i) \qquad (i = 1, 2, 3), \tag{3.41}$$

where N_i denotes the number of primitive cells of the crystal in the ith direction. Then the one dimensional representations representations satisfy the two requirements is

$$\mathbf{T}(t) \to \exp\left\{2\pi i\left(\frac{p_1 l_1}{N_1}+\frac{p_2 l_2}{N_2}+\frac{p_3 l_3}{N_3}\right)\right\}, \quad p_i, N_i \in \mathbb{Z}\&0 \leq p_i \leq N_i - 1. \tag{3.42}$$

There exist $N_1 N_2 N_3$ representations which could be expressed in the reciprocal vectors and the matrix of representation $\mathbf{k}$ corresponding to translation $\mathbf{t}$ is then

$$\Gamma^{\mathbf{k}}(t) = \exp\left\{2\pi i\left(\frac{p_1 l_1}{N_1}+\frac{p_2 l_2}{N_2}+\frac{p_3 l_3}{N_3}\right)\right\} = \exp\{2\pi i\mathbf{k}\mathbf{t}\}, \tag{3.43}$$

where $\mathbf{k} = \left(\frac{p_1}{N_1}, \frac{p_2}{N_2}, \frac{p_3}{N_3}\right) = \frac{p_1}{N_1}\mathbf{b}_1 + \frac{p_2}{N_2}\mathbf{b}_2 + \frac{p_3}{N_3}\mathbf{b}_3$ is reciprocal space vector and restricted to the first Brillouin zone. The basis functions of the *irreps* of the group of translations could be written in the Bloch functions

$$\psi^{\mathbf{k}}(\mathbf{r}) = u_{\mathbf{k}}(\mathbf{r})\exp\{-2\pi i\mathbf{k}\mathbf{r}\}, \tag{3.44}$$

where $u_{\mathbf{k}}$ denotes a periodic function with the periods of the non-inverted lattice.
Then the irreducible representations of the space group $\mathbf{G}$ and of their basis functions are constructed. The pure translations $\mathbf{T}(t)$ will transform the function $\psi^{\mathbf{k}}(\mathbf{r})$ into itself with the numerical phase factor exp($-i\mathbf{k}\mathbf{t}$). Under the action of other symmetry operators $O(g) = \{h|t_g\}$ (h and t_h denote rotation and translation parts) in the space group, the basis functions will be transformed into some other functions.

$$\{h|t_h\}\psi^{\mathbf{k}}(\mathbf{r}) = \psi'(\mathbf{r}). \tag{3.45}$$

Act the pure translation on the new function $\psi'(\mathbf{r})$, and there will be

$$O(\mathbf{t})\psi'(\mathbf{r}) = \exp\{2\pi i h\mathbf{k}\mathbf{t}\}\psi'(\mathbf{r}), \tag{3.46}$$

so that Bloch functions also serve as the basis functions. However, the *irreps* of the group $\mathbf{G}$ are not one-dimensional in general case. If it is assumed that the form

$$\{h|t_h\}\psi^{\mathbf{k}}(\mathbf{r}) = \psi^{h\mathbf{k}}(\mathbf{r}). \tag{3.47}$$

The set of non-equivalent $\mathbf{k}$ vectors obtained by applying the rotational part h of the symmetry operators of the space group constitutes the "star of $\mathbf{k}$" in case that $(\mathbf{H}+\mathbf{k})$ is equivalent to $\mathbf{k}$.

$$\{\mathbf{k}\} = \{h_1\mathbf{k}_1, h_2\mathbf{k}_1, h_3\mathbf{k}_1, h_4\mathbf{k}_1, \ldots\} = \left\{\mathbf{k}_1, \mathbf{k}_2, \ldots \mathbf{k}_{l_k}\right\}, \tag{3.48}$$

where $\mathbf{k}_i$ is called the "arm of the star". Since all vectors $\mathbf{k}$ start from the centre of Brillouin zone, the vectors $\mathbf{k}$ are not affected by translation. The set of symmetry element that leaves $\mathbf{k}$ unchanged is termed the wave vector group or the little group $\mathbf{G}_{\mathbf{k}}$, which is a subgroup of $\mathbf{G}$. The expansion of the group $\mathbf{G}$ in its subgroup $\mathbf{G}_{\mathbf{k}}$ is conveniently stated in cosets:

$$\mathbf{G} = \mathbf{G}_{\mathbf{k}} + g_2\mathbf{G}_{\mathbf{k}} + \cdots = \sum_{L=1}^{l_k} g_L\mathbf{G}_{\mathbf{k}}. \tag{3.49}$$

The arbitrary magnetic structure only taking translation symmetry into consideration could be expressed as Fourier series:

$$\mathbf{m}_{lj} = \sum_{\mathbf{k}} \mathbf{S}_{\mathbf{k}j} \exp\left(-2\pi i \mathbf{k}\mathbf{R}_l\right), \tag{3.50}$$

where the atom j in the unit cell has the lattice vector $\mathbf{R}_l$ and $\mathbf{k}$ is propagation vector of the magnetic structure. If $\mathbf{k} = (0,0,0) = 0$, there will be $\mathbf{m}_{lj} = \mathbf{S}_{\mathbf{0}j} \exp\left(-2\pi i \mathbf{0}\mathbf{R}_l\right) = \mathbf{m}_{\mathbf{0}j}$, which means the magnetic unit cell coincides with the crystal unit cell. The magnetic structure could not only be ferromagnetic, but also antiferromagnetic, collinear or non-collinear. This kind of magnetic structure could be described by one of the 230 monochrome or 674 black-white first kind magnetic space groups.

If $\mathbf{k} = \frac{1}{2}\mathbf{H}$ ($\mathbf{H}$ is a reciprocal lattice vector), there will be

$$\mathbf{m}_{lj} = \mathbf{S}_{\mathbf{k}j} \exp\left(-\pi i \mathbf{H}\mathbf{R}_l\right) = \mathbf{S}_{\mathbf{k}j}(-1)^{\mathbf{H}\mathbf{R}_f} = \mathbf{S}_{\mathbf{k}j}(-1)^{n_l} = \mathbf{m}_{0j}(-1)^{n_l},$$

which means the magnetic moments in the jth cell are either parallel or opposite to the *0*th cell. The magnetic structure is naturally antiferromagnetic and can be described by one of the 517 black-white magnetic space groups.

If $\mathbf{k}$ is not a special vector as in the two previous cases, there is no magnetic Shubnikov group. The general expression of Fourier coefficient for the atom j is given by:

$$\mathbf{m}_{lj} = \sum_{(\mathbf{k})} \left\{ \mathbf{R}_{\mathbf{k}j} \cos 2\pi \left[\mathbf{k}\mathbf{R}_l + \phi_{\mathbf{k}j}\right] + \mathbf{I}_{\mathbf{k}j} \sin 2\pi \left[\mathbf{k}\mathbf{R}_l + \phi_{\mathbf{k}j}\right] \right\}, \tag{3.51}$$

where $\left(\mathbf{R}_{\mathbf{k}j}, \mathbf{I}_{\mathbf{k}j}\right)$ are coefficients defined in (xyz) three directions. Incommensurate magnetic structures like helix or cycloid magnetic structures are expressed in this form.

Now taking Wyckoff positions into consideration, if the magnetic atom site j has equivalent atoms $js(j_1, j_2, ...j_{pj})$ under the symmetry operators of the little group $\mathbf{G}_{\mathbf{k}}$, then the magnetic representation matrix for the site j and propagation vector $\mathbf{k}$ can be calculated by applying the symmetry operator to the unit vectors of the working complex space, which has the dimension $n_j = 3 \times p_j$. The explicit components for the magnetic representation matrices are:

$$\Gamma_{Mag} \rightarrow \Gamma^{\mathbf{k}j}_{q\beta,s\alpha}(g) = e^{2\pi i \mathbf{k}\mathbf{a}^j_{gs}} \det(h) h_{\beta\alpha} \delta^j_{q,gs}, \tag{3.52}$$

where α, β = 1,2,3 or x, y, z and s, q denote equivalent positions. The δ symbol has value to 1 when the operator g transforms the atom s into atom q, and zero otherwise. By introducing the permutation representation by the axial representation of dimension 3, the magnetic representation is further expressed as

$$\Gamma_{\mathrm{Mag}} = \Gamma_{\mathrm{Perm}} \otimes \Gamma_{\mathrm{Axial}}. \tag{3.53}$$

The magnetic representation Γ_{Mag} can be decomposed in irreducible representations of the propagation vector group. The number of possible basis functions N_{BV} of the *irreps* of $\mathbf{G}_{\mathbf{k}}$ that describes possible magnetic structures can be calculated by $N_{BV} = n_\nu \times l_\nu$. And the basis functions of the irreps of $\mathbf{G}_{\mathbf{k}}$ can be calculated from the projection operator in Eq.3.39.

In addition, for symmetry analysis, when working with magnetic structure, the Fourier coefficient $\mathbf{S}_{\mathbf{k}js}$ in Eq.3.50 that describes magnetic structures of propagation vector $\mathbf{k}$ must be a linear combination of the basis functions of the $\mathbf{G_k}$ irreducible representations:

$$\mathbf{S}_{\mathbf{k}js} = \sum_{n\lambda} C_{ni}^{\mathbf{k}v} \mathbf{S}_{n\lambda}^{\mathbf{k}v}(js), \tag{3.54}$$

where ν demotes the active *irreps* Γ^{ν} of the little group $\mathbf{G_k}$; λ denotes the component corresponding to the dimension of the representaion Γ^{ν}; n is an additional index running between one and the number of times the representation Γ^{ν} is contained in the global magnetic representation Γ_{mag}.

This is the principal relation for magnetic symmetry analysis and the the magnetic structure determination. To refine or analyse the magnetic structure by the the representation approach, one can perform irreducible representation analysis by "BasIreps" or "SARAh" and obtain the basis functions of *irreps* [142, 143]. The magnetic structure could be refined by copying the basis functions to to the Fullprof input file (PCR) directly.

The general expression for the magnetic structure factor of neutron scattering at position $\mathbf{h} = \mathbf{H} + \mathbf{k}$ is

$$\mathbf{M}(\mathbf{h}) = p \sum_{j=1}^{n_a} O_j f_j(\mathbf{h}) e^{-B_j|h/2|^2} \sum_{s=1,\dots p_j} M_{js} \mathbf{S}_{\mathbf{k}j1} \exp\left\{2\pi i \left[(\mathbf{H}+\mathbf{k})\{h \mid \mathbf{t}\}_s \mathbf{r}_1^j - \psi_{\mathbf{k}js}\right]\right\}, \tag{3.55}$$

where $p = 0.2695$ is a constant; $f_i(\mathbf{h})$ is magnetic form factor; $e^{-B_j|h/2|^2}$ is isotropic thermal motion term; $\psi_{\mathbf{k}js}$ is the phase factor. The sum over j concerns the atoms of the magnetic asymmetric unit for the wave vector $\mathbf{k}$, so that j labels different sites. The sum over s concerns the symmetry operators of the wave vector group $\mathbf{G_k}$. The phase factor $\psi_{\mathbf{k}js}$ has two components:

$$\psi_{\mathbf{k}js} = \Phi_{\mathbf{k}j} + \phi_{\mathbf{k}js}, \tag{3.56}$$

where $\Phi_{\mathbf{k}j}$ is a phase factor that is not determined by symmetry and $\phi_{\mathbf{k}js}$ is a phase factor determined by symmetry. If there is more than one propagation vectors in the magnetic structure known as multiple $\mathbf{k}$ magnetic structures, and there is no strong coupling with the crystal lattice, it is not possible to determine unambiguously the spin configuration because the phase between the different Fourier components can not be determined by diffraction methods [131].

4

Mn_3Sn

4.1 Introduction

Anomalous Hall effect (AHE) signified by the transverse voltage jumps at zero magnetic field arises when an electric current is applied in ferromagnets [53]. Recent developments in the theory and experiment have proved that AHE can also be observed in certain antiferromagnetic materials when the time-reversal symmetry is broken [61, 68, 144–146]. For example, in a non-coplanar magnetic structure, the non-vanishing scalar spin chirality could give rise to AHE because its non-coplanar moments will break time-reversal symmetry with the spin rotation operator $R_S T$, while in a coplanar non collinear magnetic structure, the finite anomalous Hall effect can be explained with the intrinsic Hall effect concept induced by the non-vanishing Berry curvature in the momentum space when the time-reversal symmetry is broken (see Sec.2.2.1).

One famous case is the topological Weyl semimetal Mn_3A (A = Sn, Ge), which has been an active study topic since the discovery of the large anomalous Hall effect, large Nernst effect at room temperature, magnetic Weyl fermions, magnetic inverse spin Hall effects [40, 45, 63–66, 147–154]. Mn_3A (A = Sn, Ge) crystallizes in a hexagonal structure with space group $P6_3/mmc$ as shown in Fig.4.1. In every unit cell of Mn_3A, manganese atoms form a frustrated kagomé lattice in each $z = 1/4$ and $z = 3/4$ layers with tin or germanium atoms occupying the centre positions of the kagomé lattice. It has been already well proved that Mn_3Sn exhibits an antiferromagnetic (AFM) order below 420 K [155]. Early neutron experiment reveals that the magnetic structure has the propagation wave vector $\mathbf{k}$ = (0,0,0) with a so-called "inverse triangular magnetic structure", where for each Mn-triangles in the kagomé plane, it has the negative vector spin chirality [63] as illustrated in Fig.4.1. This kind of orthorhombic inverse triangular magnetic structure is stabilized by Dzyaloshinskii-Moriya (DM) interaction, along with the ordered manganese moments lying in the crystallographic *ab* basal plane along with the weak ferromagnetism also in *ab* plane [67, 156–158]. The magnetic structure space group model is proposed to either $Cm'cm'$ or $Cmc'm'$. Both of them follow the same irreducible representation and there is a unitary mirror symmetry in the magnetic structure to preserve the in-plane Berry curvature staying finite by breaking the time-reversal symmetry as discussed in Sec.2.2.2 [65, 147].

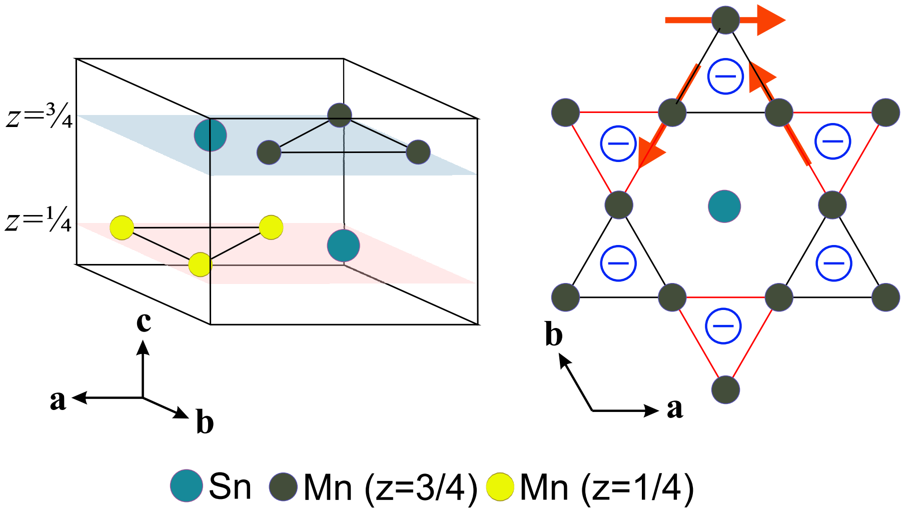

Figure 4.1: Crystal structure of Mn$_3$Sn. For each $z = 1/4$ and $z = 3/4$ layers, Mn-atoms form a frustrated kagomé plane. For each triangle in the kagomé plane, the vector spin chirality which is calculated by $V = S_iS_j + S_jS_k + S_kS_i$ where S_j, S_j, S_k are magnetic spins, is negative.

In samples prepared from Czochralski method, the AHE could persist to 50 K from room temperature [63, 149, 154, 159, 160]. However, in the as-grown samples synthesised from Sn-flux method, the AHE completely disappears after a magnetic phase transition around T_1 = ∽280 K. By annealing the samples prepared by the Bridgman method between 700-850 °C, a similar transition could also be observed at much lower temperature and neutron diffraction experiments in these samples revealed the emergence of two modulated phases, which were reported from the double in-plane helix magnetic structures at low temperature [155, 161]. Below this phase transition temperature in the flux grown single crystals, the large AHE vanishes dramatically as well as the weak ferromagnetism in the crystallographic *ab* plane, implying a significant change in the magnetic structure [154, 160]. In addition, a very recent report revealed that excess Mn in Mn$_3$Sn suppressed this magnetic phase transition between the triangular magnetic structure at room temperature and the modulated phases at low temperature, and introduced magnetic defects at low temperatures, leading to a glassy ferromagnetic phase in Mn-rich samples [162]. Thus, in order to understand the interplay between magnetic structure and AHE, high quality Mn$_3$Sn single crystals have been prepared from the molten flux method [154, 159, 160] and their physical properties and magnetic structures have been studied via comprehensive methods.

4.2 Single crystal growth

The Mn-Sn binary phase diagram [163] is shown in Fig.4.3 and it is evident that Mn$_3$Sn exists only with excess Mn presence in Mn$_3$Sn below 984 °C. This can explain why the real compositions of Mn$_3$Sn differ from samples to samples, since for different crystal growth methods, they have been prepared from different starting compositions and cooling speeds. Compared to crystals grown from other methods, for instance Bridgmann or Czochralski mehods, crystals grown by Sn self-flux methods have the advantage that samples could be separated from the melt by using a centrifuge and its composition is decided by the phase diagram. In the Sn self-flux grown method, 30 at.% of Sn and 70 at.% of Mn have been used as the starting material, which could help decrease the precipitation temperature of Mn_3Sn. In some batches, the centrifuging temperature has been set to be 800 °C for test, but the second phase Mn_2Sn will precipitate, which is ferromagnetic order at 230 K and have some effects on the characterization of sample properties.

High quality Mn_3Sn single crystals were grown from molten Sn self-flux methods [154, 159, 160]. Starting materials of Mn pieces (99.95%, Alfa Asear) and Sn Granules (99.99%, Chempur) with a molar ratio of 7:3 were loaded in an Al_2O_3 crucible with some quartz wools on the top of crucible as a filter and then the crucible was sealed in a quartz ampoule. The ampoule was heated to 1100 °C in 10 hours, dwelt at 1100 °C for 20 hours, and cooled down to 900 °C at a rate of 1 °C/hour. Finally, when the temperature decreased to 900 °C, the ampoule was transferred to a centrifuge quickly to separate crystals from the Sn flux. In some batches, crystals were not fully separated from flux and excess Sn flux could be removed mechanically easily from Mn_3Sn crystals. As-grown crystals are very shiny and there is no flux left on the samples. Typical pictures of as-grown crystals are shown in Fig.4.2.

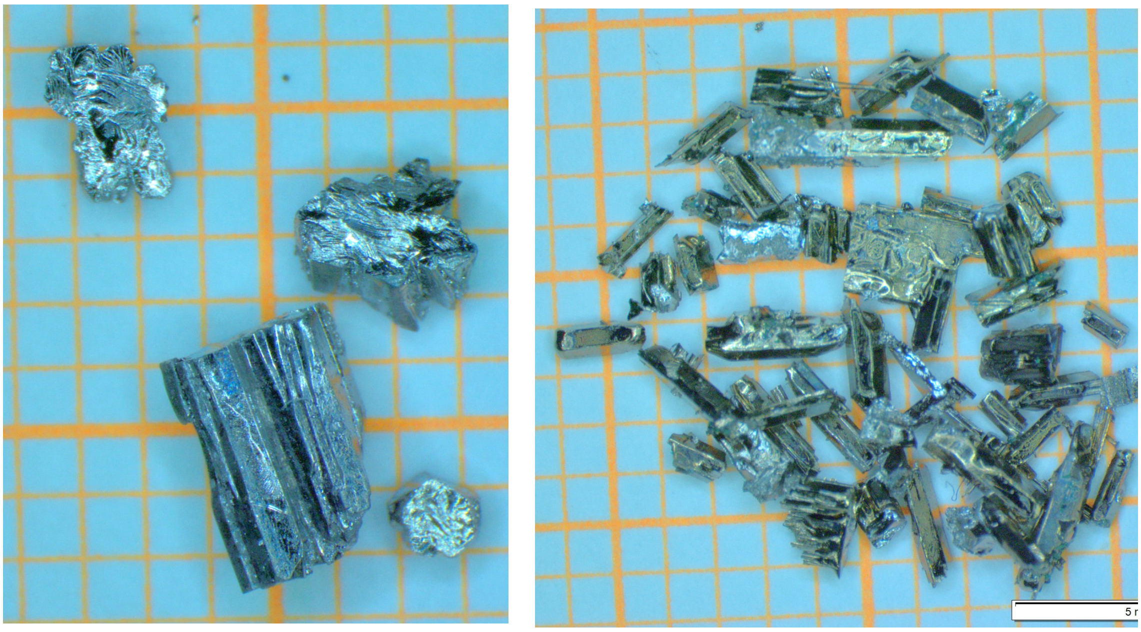

Figure 4.2: Picture of as-grown Mn_3Sn single crystals on the millimetre paper from batch WX098 (left) and batch WX100 (right).

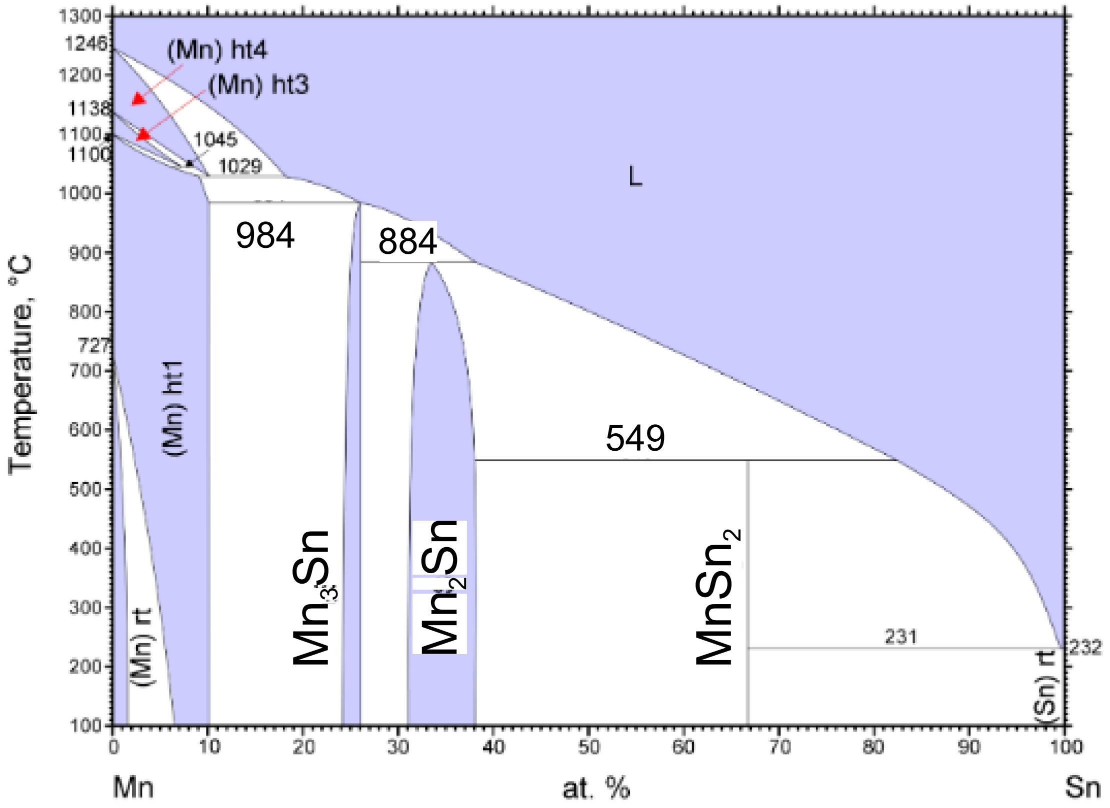

Figure 4.3: Mn-Sn binary phase diagram [163].

4.3 Chemical composition determination

The chemical composition of the as-grown samples was determined by EDX (Energy-dispersive X-ray spectroscopy) and neutron diffraction experiment. Based on the fundamental principle that each element has a unique atomic structure allowing a unique set of peaks on its electromagnetic emission spectrum, EDX is widespread used in the determination of material compositions in the materials science. Two batches of the samples were selected to be tested by EDX. As-grown single crystals from two batches WX098 and WX100 were picked for EDX measurement and the results are summarised in Tab.4.1. For each batch, five small pieces of crystals were glued on the surface of the conductive tape and the composition of Mn or Sn was determined by averaging different samples. The results in Tab.4.1 prove that the composition of the as-grown crystals is quite close to the stoichiometric sample and the excess of Sn in the sample may come from the Sn flux.

Table 4.1: EDX (Energy-dispersive X-ray spectroscopy) results for Mn_3Sn samples grown from Sn self-flux method with the starting molar ratio of 7:3 of Mn and Sn.

Batches	Mn (at.%)	Sn (at.%)	Mn_3Sn
WX098	74.37	25.63	$Mn_3Sn_{1.033}$
WX100	70.85	29.15	$Mn_3Sn_{1.234}$

Single crystal neutron diffraction was also carried out to determine the composition of Mn_3Sn at HEiDi at MLZ. It is well known that Mn has a negative scattering length while Sn has a positive scattering length, which creates a large contrast for the refinement. In this regard, the composition of Mn_3Sn could be decided very accurately by refining the single crystal neutron diffraction data.

Single crystal neutron diffraction experiment was performed on four circle neutron diffractometer HEiDi at MLZ at 210 K (reasons will discussed in Sec.4.4). 707 nuclear reflections were collected for the determination of the composition and crystal structure at 210 K. The refinement was conducted on the crystallographic computing system Jana 2006 [135]. The picture of refined square of structure factors versus calculated square of structure factors is shown in Fig.4.4 and the refined lattice parameters are shown in Tab.4.2. The refined weighted R_w is good, as small as 2.64 %, indicating there is no structural transition down 210 K. The refined occupation for Mn is 1.016(7) for the flux grown high quality crystal. If the excess manganese will occupy the positions of tin, the plausible composition is $Mn_{3.012}Sn_{0.988}$ assuming there is no vacancies in Sn sites in the sample. This result means only 1.2% of tin is replaced by manganese, proving that the sample is quite close to the stoichiometric sample and high quality.

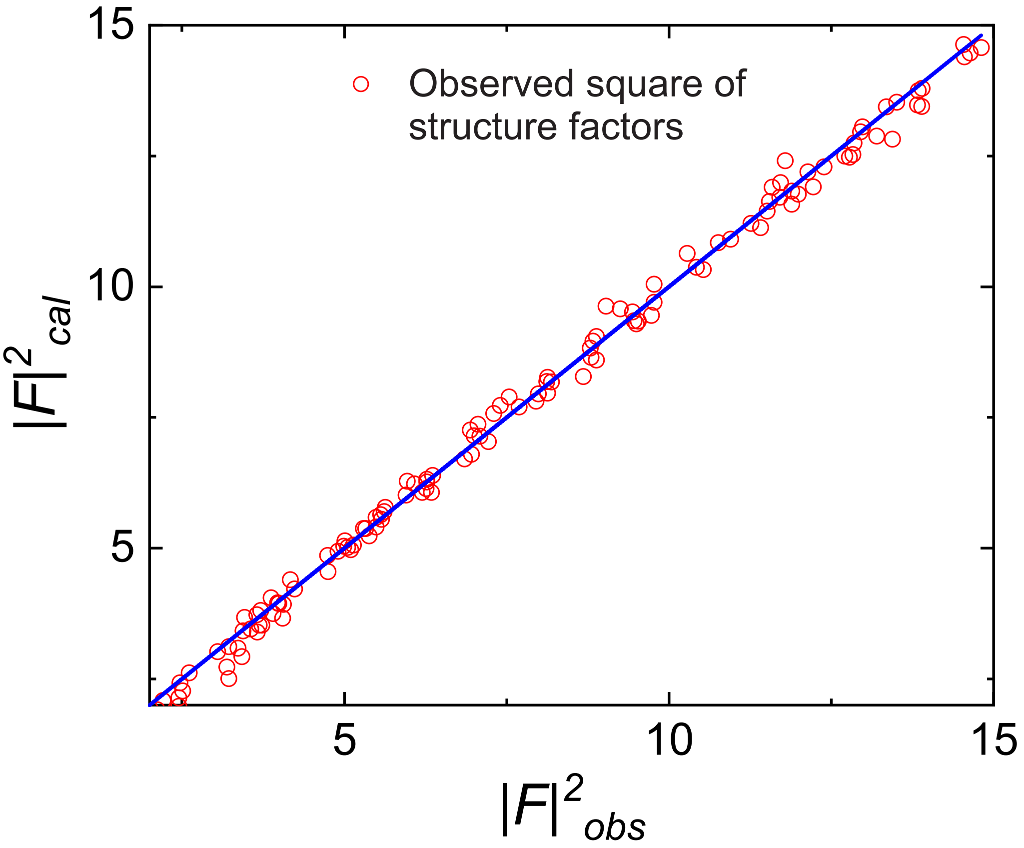

Figure 4.4: Refined square of structure factors versus calculated square of structure factors of the pure nuclear reflections for the Mn$_3$Sn from single crystal neutron diffraction data at 210 K collected at HEiDi at MLZ.

Table 4.2: Mn$_3$Sn nuclear structure refinement parameters from neutron single crystal diffraction data taken at 210 K.

Atom	Site	x	y	z	$Occ.$	U_{iso} (Å^2)
Mn	6h	0.8387(1)	0.6773(2)	0.25	1.016(7)	0.0073(2)
Sn	2c	0.3333	0.6667	0.25	0.3333	0.0064(3)

$Occ.$: atoms occupation

a=b=5.66(8) Å, c = 4.52(8) Å

$R(obs)$ = 2.30%, $R_w(obs)$ = 2.59%, $R_w(all)$ = 2.64%

4.4 Magnetic properties of Mn$_3$Sn

Firstly, to check the sample quality among different batches, three batches of the sample were measured by PPMS. All of the crystals showed the same magnetic phase transition at 280 K, proving the reproducibility of the sample preparation method as shown in Fig.4.5. WX098 and WX138 batches have the same starting compositions, which is Mn:Sn (7:3 in molar ratio) and the starting materials ratio for WX 100 batch is Mn:Sn (7.2:2.8 in molar ratio). Therefore the magnetic phase transition temperature in the sample from WX100 batch is a little different from WX0198 and WX139 batches. The different susceptibility behaviours below 260 K result from the contamination of Mn$_2$Sn in the samples , which orders ferromagnetically below 250 K [164, 165].

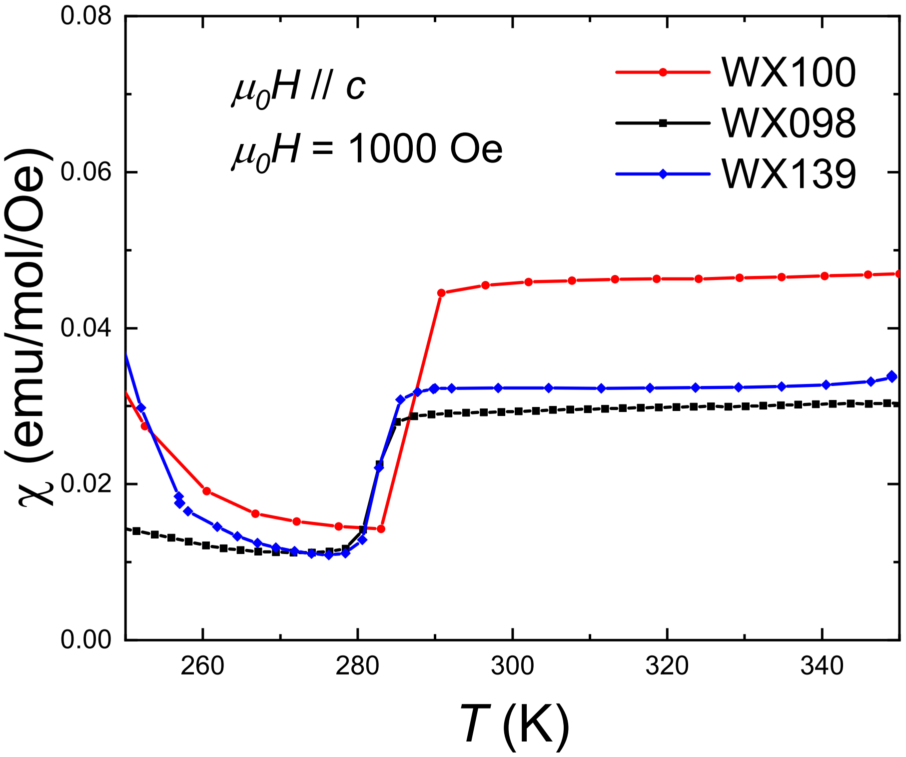

Figure 4.5: Comparison of magnetic susceptibility of Mn$_3$Sn from different batches measured for field along *c* direction under zero field cooling condition, where a phase transition is observed at ∽280 K.

Magnetic properties of an as-grown crystal (batch WX098) were further measured in the crystallographic *ab* plane and along *c* direction in various conditions as shown in Fig.4.6. Zero field cooling (ZFC) and field cooling (FC) susceptibility measured with 1000 Oe external field in *ab* plane are illustrated in Fig.4.6(a). The results prove the occurrence of a manifested phase transition around 280 K, which is expected for the magnetic phase transition from the triangular antiferromagnetic structure to the modulated phases. From 300 K to 280 K, ZFC and

FC susceptibilities well coincide with each other and at 280 K a conspicuous drop in magnetic susceptibility happens at T_1 = 280 K. After this drastic change in magnetic susceptibility, there is initially no difference between ZFC and FC susceptibilities, implying that this magnetic structure below T_1 is still antiferromagnetic. In the following temperature range, the magnetic susceptibility exhibits several kinks, the one at round ∼250 K comes from the contamination of Mn_2Sn [164, 165], which has a magnetic phase transition from the paramagnetic state to the ferromagnetic state. In addition, there is another kink at ∼200 K, which is reported to be the anisotropy change of double helix magnetic structures [159].

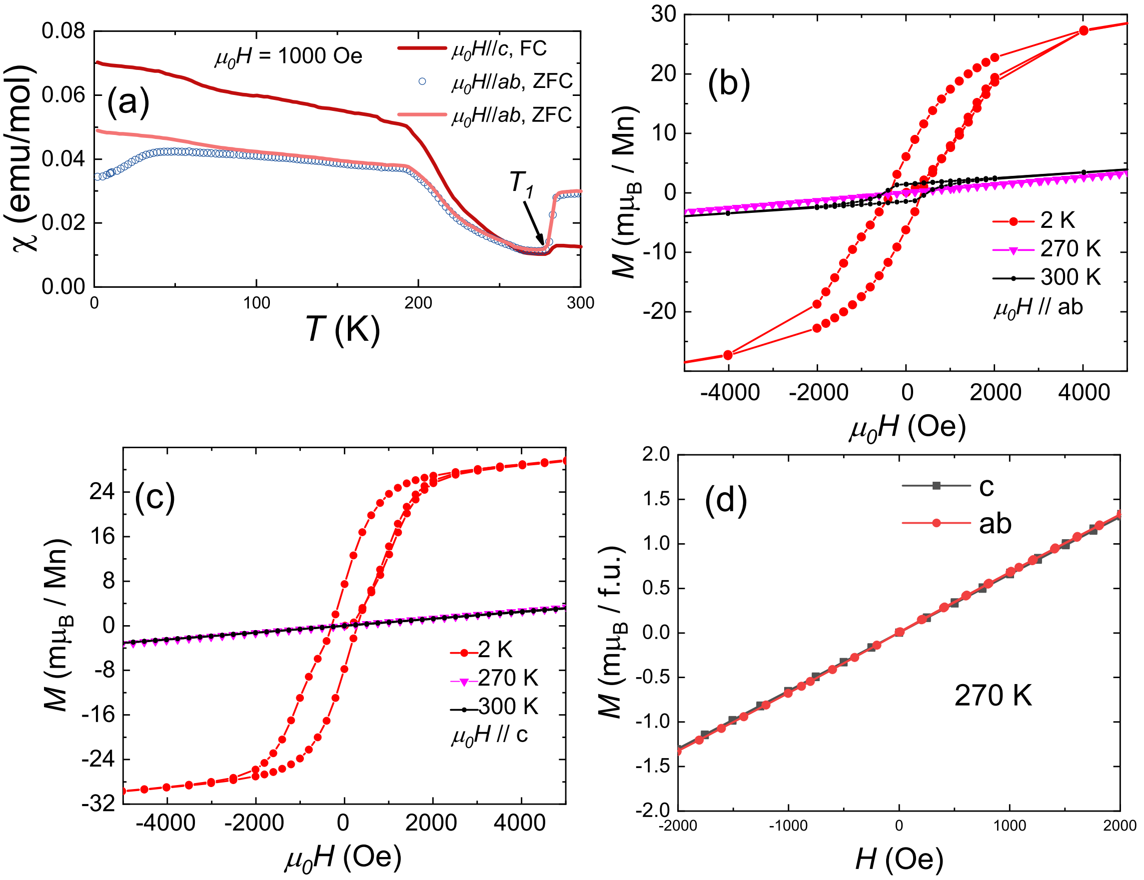

Figure 4.6: Magnetic properties of Mn_3Sn single crystals. (a) Temperature dependence of magnetic susceptibility measured in Mn_3Sn *ab* basal plane and *c* direction under a magnetic field of 1000 Oe in field cooling (FC) and zero field cooling (ZFC) conditions. (b) and (c) Isothermal magnetization of *ab* plane and *c* direction measured at 300 K, 270 K and 2 K. (d) Comparison of isothermal magnetization of *ab* plane and *c* direction at 270 K.

Below 45 K, a drop in ZFC susceptibility happens, which is considered to be a spin glass behaviour similar to that observed also in crystals grown from other methods. By comparison of magnetic susceptibility of *ab* basal plane and *c* direction measured under field cooling condition in Fig.4.6(a), it is obvious that above T_1 the magnitude of susceptibility for *ab* plane is about three times of that for *c* direction, while after the phase transition at T_1, the anisotropy between *ab* basal plane and *c* direction reverses, which is direct evidence for the change of magnetic anisotropy in Mn$_3$Sn. Isothermal magnetization data for both *ab* plane and *c* direction measured at 300 K, 270 K and 2 K are illustrated in Fig.4.6(b), respectively. At 300 K, it is clear that a weak ferromagnetic hysteresis loop can be found in *ab* plane with the remanence of B_r(300 K) = $\sim$5 mμ_B per Mn. Besides, this weak ferromagnetism is absent for *c* direction, which is similar to the previous report [63]. While at 270 K below phase transition at T_1, the magnetic hysteresis disappears completely in *ab* plane with no obvious change in *c* direction as shown in Fig.4.6(d).

4.5 Electrical transport properties of Mn$_3$Sn

Electrical resistivity and Hall effects were measured on an oriented as-grown single crystal from the same batch (WX098) with the magnetic susceptibility. Longitudinal resistivity ρ_{xx} was measured along [$\bar{1}$,2,0] and [0,0,1] directions from 300 K to 2 K at zero field, which are plotted in Fig.4.7. When temperature decreases to the base temperature, the resistivity demonstrates the metallic behaviour for both directions and a small but distinct resistivity jump can be seen at T_1 in [$\bar{1}$,2,0] direction, consistent with the magnetic phase transition temperature. The jump of resistivity in [$\bar{1}$,2,0] direction implies the decrease of electron density of states at Fermi surface, which could be explained as the open of energy gaps at the Fermi surface. By contrast, there is no such a jump in the resistivity of [0,0,1] direction.

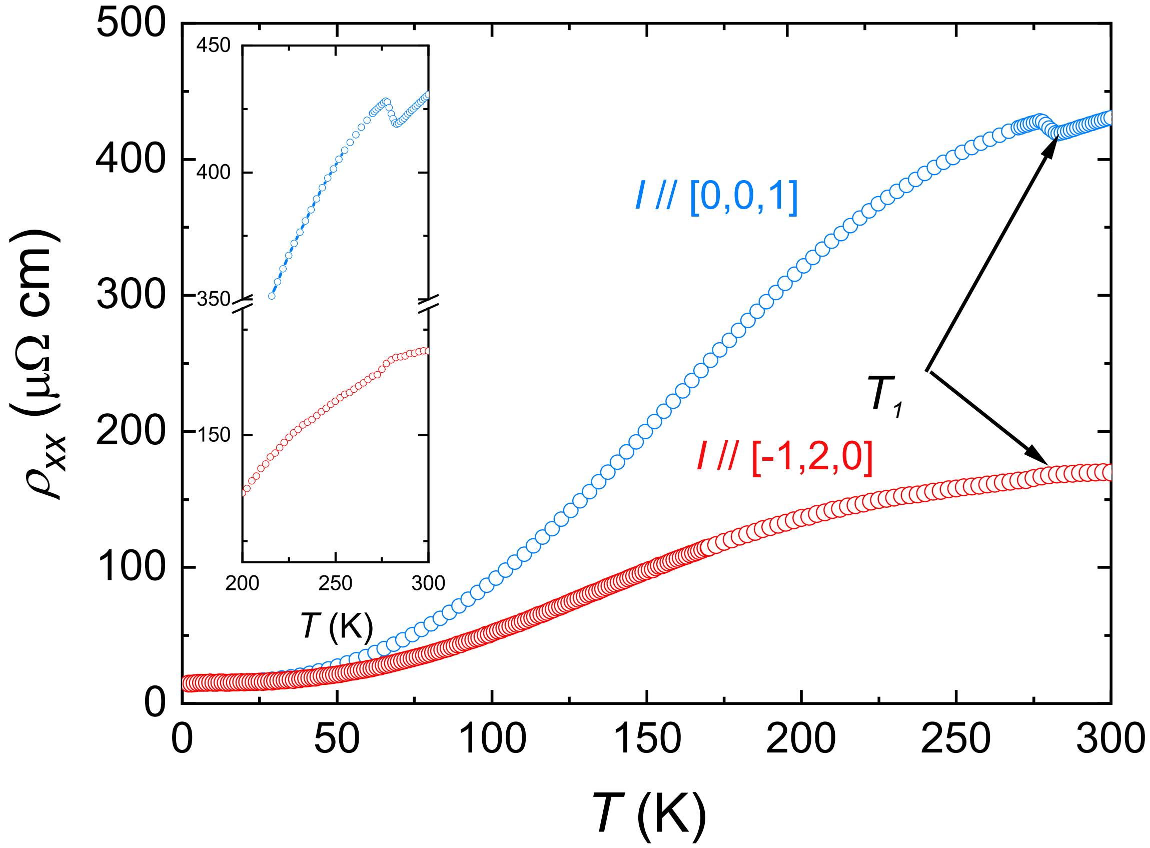

Figure 4.7: Temperature dependence of longitudinal electrical resistivity ρ_{xx} of the Mn$_3$Sn as-grown single crystal with current applied along [0,0,1] and [$\bar{1}$,2,0] at zero field.

Magnetic field dependence of Hall effects measured under various conditions are depicted in Fig.4.8. When the magnetic field $B \parallel$ [0,1,0], AHE arises at 300 K for $I \parallel$ [0,0,1] and $I \parallel$ [$\bar{1}$,2,0] as shown in Fig.4.8 (a) and (b) with the same magnitude as the samples prepared from other methods [63]. While when $B \parallel$ [0,0,1], no AHE is observed, indicating only an in-plane magnetic field could induce AHE in Mn$_3$Sn. This result is consistent with previous report because only the Berry curvature in *ab* plane is preserved by the symmetry. When temperature is below T_1, AHE disappears in all the directions and does not recover until 2 K, indicating significant change in the magnetic structure at T_1. It is concluded that the symmetry conditions for the non-vanishing of Berry curvature is broken in the magnetic structure since there is no structural phase transition at low temperature. Therefore, a systematic study of the magnetic structures in Mn$_3$Sn is essential to understand the disappearance of AHE in Mn$_3$Sn.

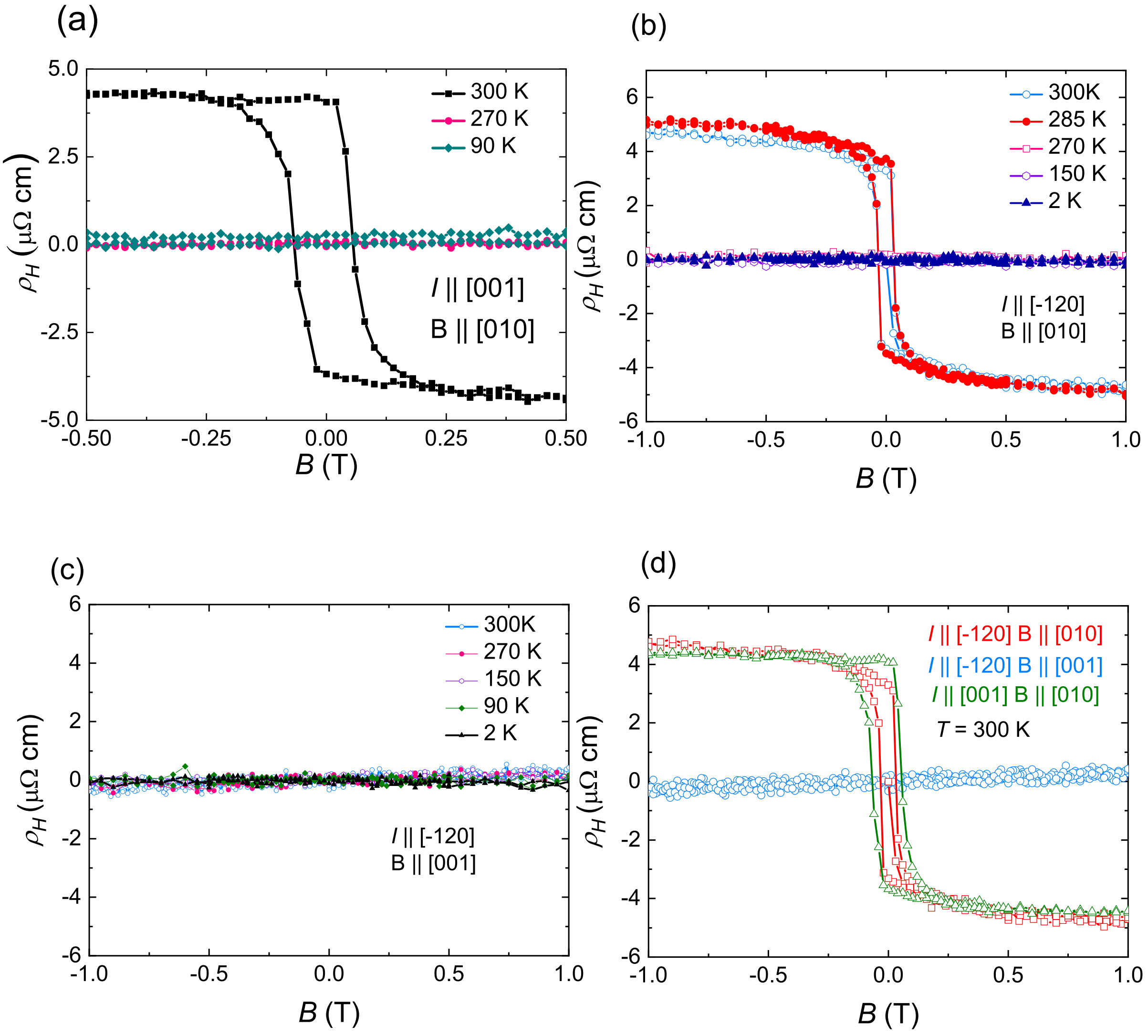

Figure 4.8: Magnetic field dependence of Hall effects in Mn$_3$Sn. (a) Measured with the electric current along [0,0,1] and magnetic field along [0,1,0] under various temperatures. (b) Measured with the electric current along [$\bar{1}$,2,0] and magnetic field along [0,1,0] under various temperatures. (c) Measured with the electric current along [0,0,1] and magnetic field along [0,0,1] under various temperatures. (d) Comparison of AHE among three above measured conditions at 300 K.

4.6 Neutron diffraction

Various neutron diffraction experiments have been performed to study the phase transition and magnetic structure of Mn$_3$Sn at low temperature:
DNS at MLZ for *xyz* polarisation analysis;
HEiDi at MLZ for crystal structure and magnetic structure determination;
D23 at Institut Laue-Langevin (ILL) for high resolution diffraction study;
IN12 at ILL for spherical polarisation analysis with Cryopad option.
With the combination of the results of these techniques, the magnetic structure at room temperature and especially the low temperature modulated phases are successfully and ambiguously solved.

4.6.1 Magnetic structure at room temperature

It has been already well proved that Mn$_3$Sn exhibits an antiferromagnetic (AFM) order around 420 K [155]. Early polarised neutron experiments revealed that the magnetic structure is **k** = (0,0,0) orthorhombic inverse triangular magnetic structure. The magnetic structure space group model is proposed to be either *Cm′cm′* or *Cmc′m′*. Both of them follow the same irreducible representation and there is a unitary mirror symmetry in them to preserve the inplane Berry curvature finite by breaking the time-reversal symmetry [65, 147] as shown in Fig.4.9. The only difference for the proposed magnetic structure models is the direction of ordered magnetic moments: in the *Cm′cm′* model, magnetic moments are parallel to $\langle 110 \rangle$ crystallographic directions while in *Cmc′m′* model, magnetic moments are parallel to $\langle 100 \rangle$ directions.
To further confirm the magnetic structure at 300 K, single crystal neutron diffraction experiment was carried out at single crystal neutron diffractometer HEiDi at MLZ at 300 K [123]. Irreducible representation analysis was performed by online crystallographic tools Bilbao crystallographic server [136]. For the **k** = (0,0,0) room temperature magnetic structure, the little group $\mathbf{G}_k$ can be decomposed as

$$\begin{aligned}&\mathbf{G}_k = \\ &mGM_{1-}^{(1)} \oplus mGM_{2+}^{(1)} \oplus mGM_{2-}^{(1)} \oplus mGM_{3+}^{(1)} \oplus mGM_{3-}^{(1)} \oplus mGM_{4+}^{(1)} \oplus mGM_{5+}^{(2)} \oplus 2mGM_{5-}^{(2)} \\ &\oplus 2mGMG_{6+}^{(2)} \oplus mGM_{6-}^{(2)}\end{aligned}$$

The active irreducible representation (*Irreps*) $mGM_{6+}^{(2)}$ is two dimensional and allows two magnetic space group models: $Cmc'm'$ and $Cm'cm'$ as shown in Fig.4.9 (a) and (c). 1350 reflections were refined by crystallographic computing system Jana2006 and the calculated structure factor versus observed ones for each the magnetic structure is shown in Fig.4.9. Both the calculated square of structure factors for the two models are quite consistent with the measured values and the refined ordered moment at 300 K is 2.54(8) μ_B and 2.53(10) μ_B for each model, close to 3.00(1) μ_B that was obtained by J. Brown at 200 K [67]. To separate the two models is quite challenging for the unpolarised neutron experiment because of the existence of the magnetic domains. In a recent spherical polarised neutron diffraction experiment on Mn$_3$Ge,

the magnetic structure model *Cm′cm′* has been determined to be the ground state at 1.5 K [166]. Ab initio calculation has demonstrated that the energy difference between these two magnetic structure models is in the calculation uncertainty [151, 152], thus a small perturbation may favour one of them.
As also marked in Fig.4.9 (a) and (c), the mirror symmetry in *Cmc′m′* and *Cm′cm′* is along x or y direction, respectively, which ensures the non-vanishing of Berry curvature in momentum space.

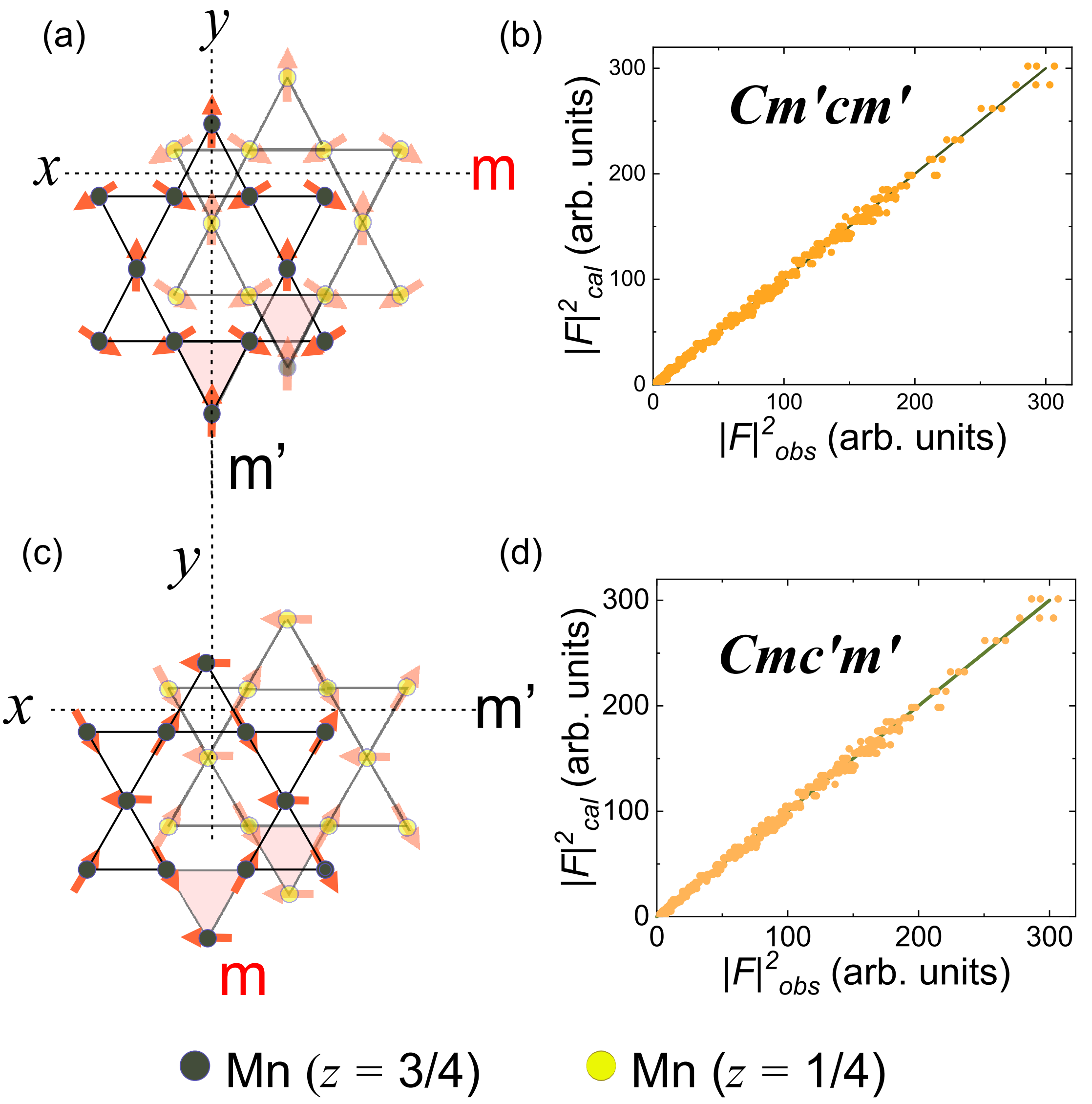

Figure 4.9: (a-d) Two magnetic structure models *Cm′cm′* ((a) and (b)), *Cmc′m′* ((c) and (d)) and the refined structure factors versus measured structure factors from single crystal neutron diffraction data collected at HEiDi at MLZ. Magnetic symmetry elements in *ab* plane are also marked, where x is parallel to crystallographic [1,0,0] direction and y is parallel to crystallographic [1,$\bar{2}$,0] direction. m is mirror plane symmetry and m' is mirror plane plus time-reversal symmetry. Single crystal neutron diffraction data was collected at HEiDi at MLZ at 300 K.

Table 4.3: Refined results for the magnetic structures of Mn$_3$Sn at 300 K with magnetic propagation vector **k** = (**0,0,0**) from single crystal neutron diffraction data collected at HEiDi at MLZ. The Wyckoff position used here is still from $P6_3/mmc$ space group.

Magnetic space group model 1: $Cm'cm'$						
Atom	Site	x	y	z	$Occ.$	U_{iso}(Å^2)
Mn1	6h	0.8387(1)	0.6775	0.25	1.016	0.00615(13)
Mn2	6h	-0.6775	0.1612(1)	0.25	1.016	0.00615(13)
Sn	2c	0.3333	0.6667	0.25	0.3333	0.00462(12)
$R(obs)$ = 2.27%, $R_w(obs)$ = 2.72%, $R_w(all)$ = 3.05%						
M_{Mn} = 2.54(8) μ_B						
Magnetic space group model 2: $Cmc'm'$						
Atom	Site	x	y	z	$Occ.$	U_{iso}(Å^2)
Mn1	6h	0.8386(1)	0.6773	0.25	1.016	0.00617(13)
Mn2	6h	-0.6773	0.1614(1)	0.25	1.016	0.00617(13)
Sn	2c	0.3333	0.6667	0.25	0.3333	0.00467(13)
$R(obs)$ = 2.30%, $R_w(obs)$ = 2.75%, $R_w(all)$ = 3.08%						
M_{Mn} = 2.53(10) μ_B						
a = b = 5.66(9) Å, c = 4.52(9) Å						

It should be mentioned here that for an ideal kagomé lattice formed by Mn-atoms, the six triangles have the same bond length. In Mn$_3$A materials, the Wyckoff position for Mn is 6h (x, 2x, 1/4), only when x = 5/6 (0.8333) the kagomé plane is perfect, otherwise it develops into the breathing type with unequal bond length between two nearest triangles. In Mn$_3$Sn, the refined x is 0.8386(1) in the flux grown crystal, close to a recent Bridgman grown crystal, where the refined x is 0.8385(1), which also shows a similar transition at $\sim$ 260 K [167]. The slight change in the atom positions of Mn-atoms results in a non-ignorable breathing amplitude as large as 0.18 Å with a 6.6% difference in ratio between two nearest triangles by contrast to that of 0.01 Å in a Czochralski method grown Mn$_3$Ge sample in Tab.4.4. The small difference in the structure between Mn$_3$Sn and Mn$_3$Ge may explain the phase transition in Mn$_3$Sn at 280 K.

Table 4.4: Crystal structure parameters for Mn$_3$Ge obtained from [168].

Atom	Site	x	y	z	$Occ.$
Mn	6h	0.833(1)	0.666(2)	0.25	1
Ge	2c	0.3333	0.6667	0.25	0.95
a = b = 5.338(1) Å, c = 4.3148(3) Å					

4.6.2 Polarised analysis of DNS

XYZ-polarisation analysis of Mn_3Sn was carried out at DNS as shown in Fig.4.10.

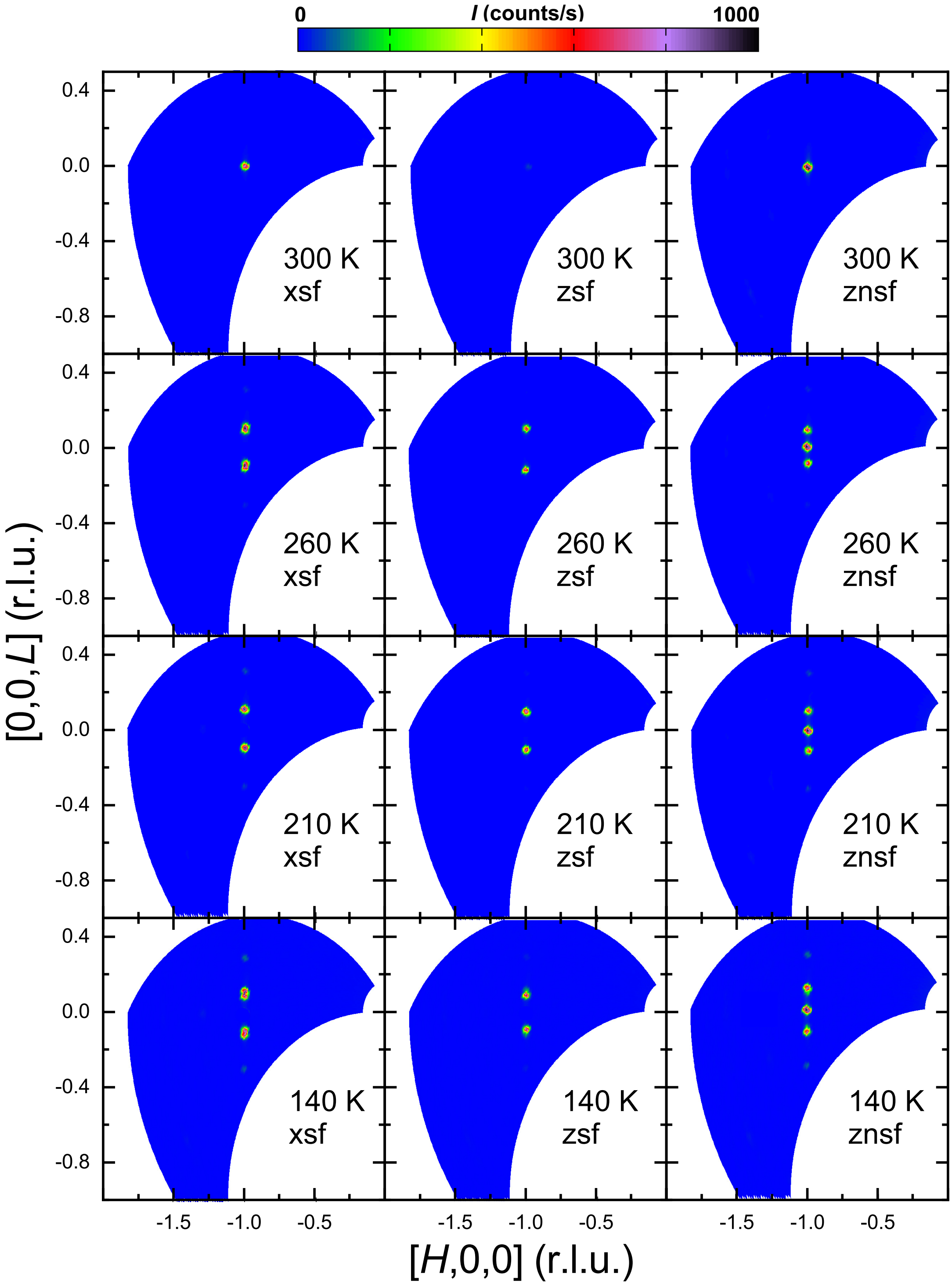

Figure 4.10: Contour maps of the measured neutron diffraction intensities in the (*h*0*l*) scattering plane of the Mn_3Sn as-grown single crystal under *x* spin-flip, *z* spin-flip and *z* non spin-flip channels measured at 300K, 260, 210 K and 140 K reconstructed from DNS-data, respectively.

For XYZ-polarisation analysis, the scattered intensity for each channel has been introduced in Sec.3.5. A high quality as-grown Mn$_3$Sn single crystal was aligned in ($h0l$) scattering plane and measured in x spin-flip (xsf), x non-spin-flip (xnsf), z spin-flip (zsf) and z non-spin-flip (znsf) channels at various temperatures.

The results are shown in Fig.4.10, in which $xnsf$ data is omitted since no magnetic reflections are measured in this channel. At 260 K below the magnetic phase transition, the magnetic reflection at ($\overline{1}$,0,0) in xsf channel vanishes completely along with the emergence of pairs of satellite reflections around ($\overline{1}$,0,$\pm$0.1) in xsf, zsf and $znsf$ channels. When temperature is reduced down from 260 K to 140 K, there is no evident change in all the channels.

The resulting cross section results cut (**Q**-scan calculated from the contour maps) from DNS contour maps at 260 K, 210K and 140 K are illustrated in Fig.4.11. It is evident that the antiferromagnetic peak ($\overline{1}$,0,0) for the inverse triangular magnetic structure disappears completely in *xsf* channel and there are two pairs of modulation peaks in xsf channel around ($\overline{1}$,0,$\pm$0.1) which could be well separated by zsf and $znsf$ channels surprisingly. The modulated reflections in $znsf$ and zsf channels are denoted as $\mathbf{q}_1$ and $\mathbf{q}_2$, respectively. When temperature is lowered to 210 K, in xsf channel there is only a single peak but it could still be separated into two reflections in $znsf$ and zsf channels, but they appear at the same position. At 140 K, the reflections in $znsf$ and zsf channels split again, but now the reflections $\mathbf{q}_1$ and $\mathbf{q}_2$ in $znsf$ and zsf exchange **Q** positions: the reflection in $znsf$ channel moves from low **Q** to high **Q**, while the reflection in zsf moves from high **Q** to low **Q**. The temperature dependent behaviour of the periods of the modulated phase proves that the low temperature magnetic structure is incommensurate.

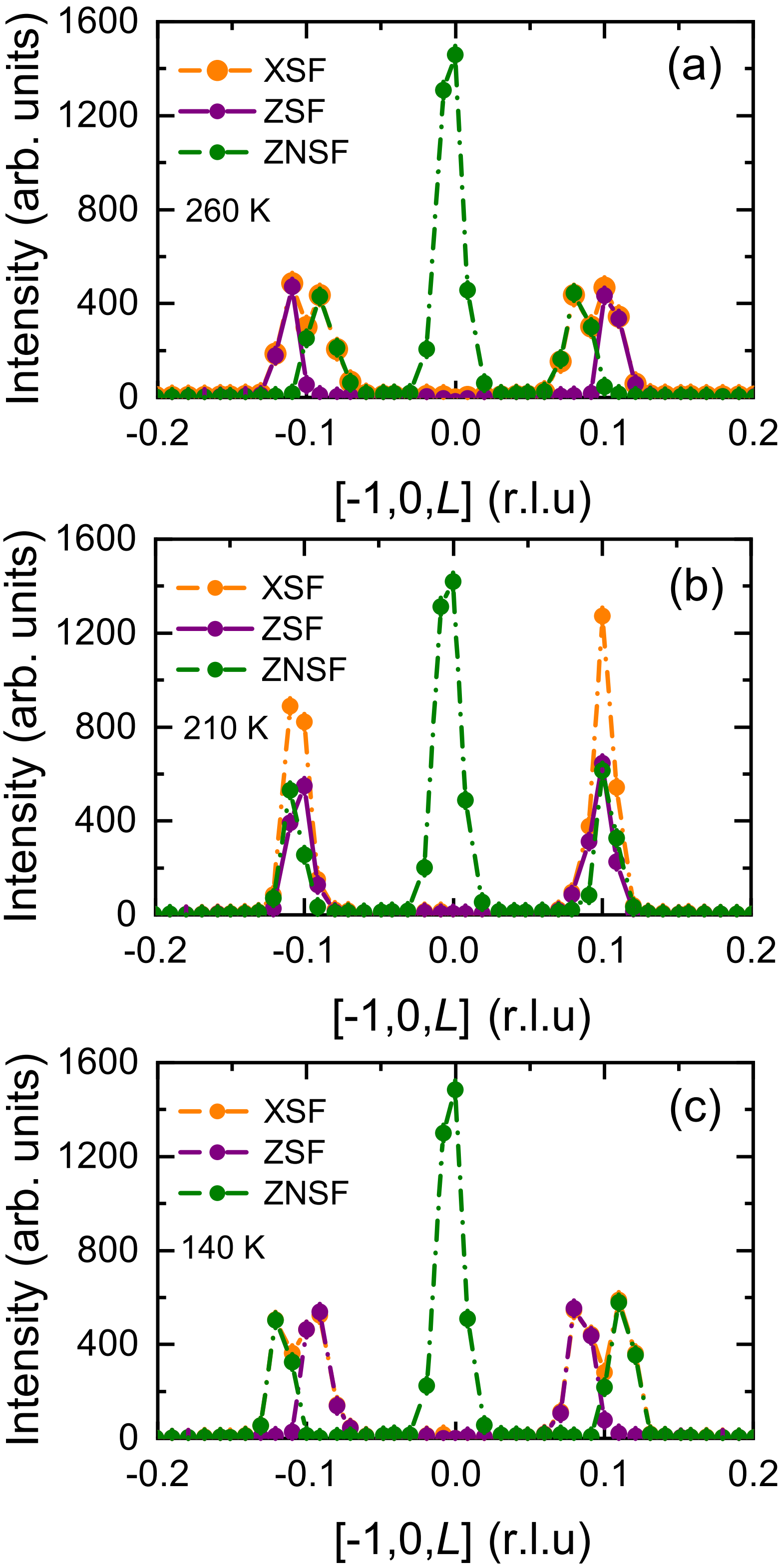

Figure 4.11: Q-scan along [$\bar{1}$,0,L] (r.l.u.) direction obtained from cutting along [$\bar{1}$,0,L] (r.l.u.) direction in DNS contour maps in *xsf*, *zsf* and *znsf* channels at (a) 260 K, (b) 210 K and (c) 140 K: two modulated reflections in *xsf* channel can be well separated in *zsf* and *znsf* channels.

To understand the polarisation analysis results from DNS, the scattering geometry for this experiments are discussed in Fig.4.12.

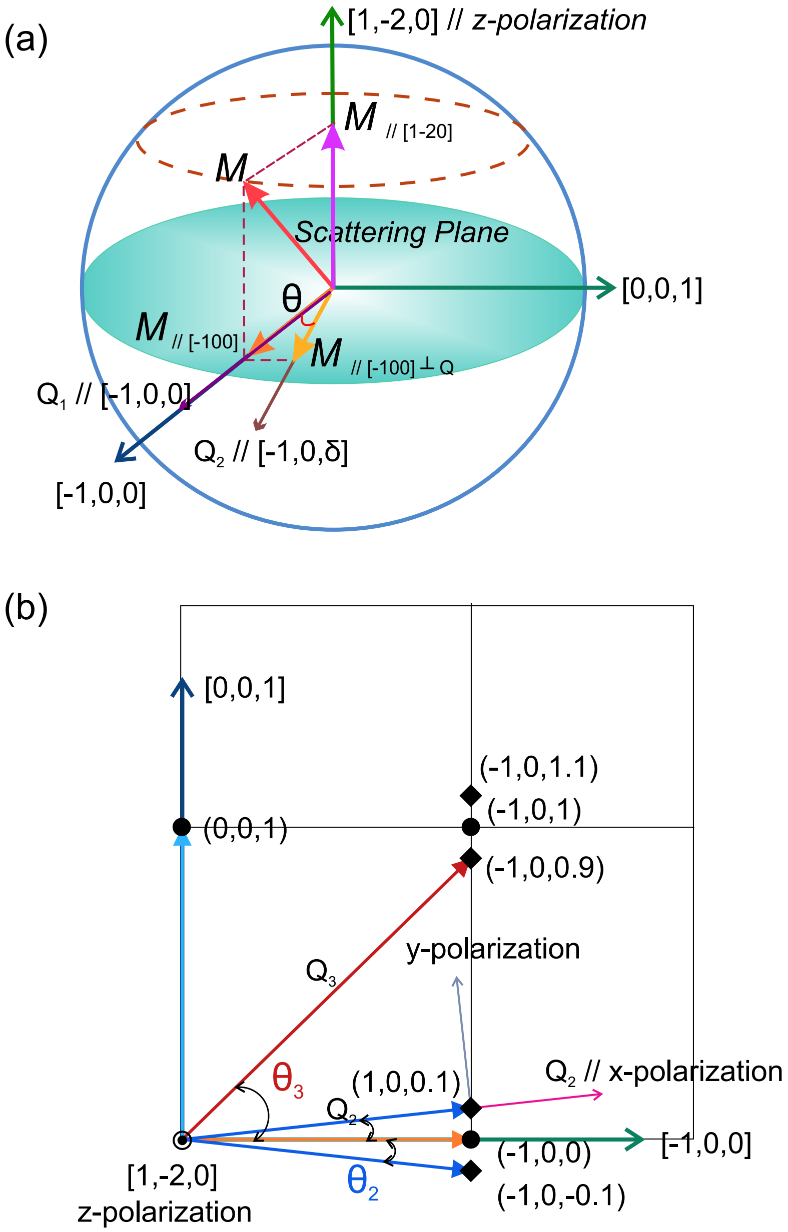

Figure 4.12: Scattering geometry of the experiments at DNS at MLZ. (a) The scattering plane is ($h0l$) plane where the magnetic moment $\mathbf{M}$ in ($hk0$) plane can be decomposed into $\mathbf{M}_{[1,\bar{2},0]}$ and $\mathbf{M}_{[\bar{1},0,0]}$ first. Then $\mathbf{M}_{[\bar{1},0,0]}$ can be further projected onto [0,0,1] direction $\mathbf{M}_{[\bar{1},0,0]\perp\mathbf{Q}}$. $\mathbf{Q}_1$ is the scattering vector for the reflection $[\bar{1},0,0]$ in crystallographic ab plane and $\mathbf{Q}_2$ is the scattering vector for modulated reflections. θ is the angle between scattering vector $\mathbf{Q}$ and ($hk0$) plane. (b) The ($h0l$) plane and the scattering vectors are depicted, where θ is shown.

According to the definition of XYZ directions at DNS, x polarised direction is parallel to the average scattering vectors $\mathbf{Q}$ in the experimental scattering ($h0l$) scattering plane, and the vertical direction perpendicular to the scattering plane is the z polarised direction which is always parallel to [1,$\bar{2}$,0] crystallographic direction in this experiment. It is clear that for the magnetic scattering, only the magnetic components $\mathbf{M}_{\perp\mathbf{Q}}$ are measured and they will be presented in xsf channel because of $\mathbf{Q} \parallel \mathbf{P}$. And for zsf channel and $znsf$ channels, the presence of magnetic peaks are practically dependent on the geometry relationships among $\mathbf{P}$, $\mathbf{Q}$ and the magnetic interaction vector $\mathbf{M}_{\perp\mathbf{Q}}$. When measuring at ($\bar{1}$,0,0) peak, the scattering vector $\mathbf{Q}_1$ is in ab basal plane along [$\bar{1}$,0,0] direction as depicted in Fig.4.12. In this geometry, there will not be any intensity contribution from ab basal plane to the zsf channel since $\mathbf{M}_{ab\perp\mathbf{Q}} \parallel z$, so all the intensities in zsf will measure only magnetic components along c direction. By contrast, except the nuclear reflection, $znsf$ channel will also measure the magnetic contribution along [1,$\bar{2}$,0] direction. Therefore, the magnetic contribution can be decomposed into two orthogonal parts for $\mathbf{Q}_1$: the magnetic moments lying in ab plane will be measured in $znsf$ channel and the magnetic moments along c direction will be measured in zsf channel. In the polarised analysis data at 300 K in Fig.4.10, magnetic reflections only appear in xsf and $znsf$ channels proving that all the magnetic moments well lie in the ab basal plane at 300 K, which is consistent with the neutron diffraction experiment at HEiDi.

When it comes to 260 K below T_1, the scattering vector $\mathbf{Q}_2$ for xsf channel is along [$\bar{1}$,0,δ] for each satellite peak. In this case, both magnetic components in and out of ab basal plane will be measured in zsf channel because the scattering vector $\mathbf{Q}_2$ is not in ab plane any longer. In zsf and $znsf$ channels, the intensity that have been measured can be written in the following formulas if the background and incoherent scattering are not considered:

$$\begin{aligned} \sigma_{zz}^{sf} &= \sigma_{xx}^{sf} - \sigma_{yy}^{sf} = \mathbf{M}_y^2 = \mathbf{M}_{[1,0,0]}^2 \sin^2\theta + \mathbf{M}_{[0,0,1]}^2 \cos^2\theta \\ \sigma_{zz}^{nsf} - \sigma_{xx}^{nsf} &= \sigma_{yy}^{sf} = \mathbf{M}_z^2 = \mathbf{M}_{[1,\bar{2},0]}^2 \end{aligned} \tag{4.1}$$

where σ_i^j, i = xx, yy, zz and j = sf, nsf are intensity in x, y or z channels in spin-flip channel or non-spin-flip channel. Assume that there is no magnetic component along c direction just as previously reported [161, 167], the contribution from magnetic components only in ab plane to the intensity in zsf channel can be estimated. Considering at $\mathbf{Q}$ position ($\bar{1}$,0,1/10) which is at the middle of two modulated reflections, the angle between $\mathbf{Q}_2$ and ab basal plane is about θ_2 = $tan^{-1}(((2\pi/c) * 0.1)/(2\pi/(\sqrt{3}a/2))$ = 6.22°. The magnetic moments projecting perpendicularly to $\mathbf{Q}_2$ from ab basal plane is as small as $\mathbf{M}_{//[\bar{1},0,0]\perp\mathbf{Q}} = \mathbf{M}_{//[\bar{1},0,0]} sin\theta_2 =$ $0.11\mathbf{M}_{//[\bar{1},0,0]}$, which means less than 1.2% magnetic moment will contribute to the observed intensities in zsf channel because of $I \propto {\mathbf{M}_{\perp\mathbf{Q}}}^2$. However, the magnetic modulated reflection observed in zsf channel is even stronger than that of $znsf$ channel, thus it can be deduced that there should be some contribution from the magnetic moments along c direction. As a result, the magnetic structure below 280 K has transformed from a non collinear coplanar inverse triangular magnetic structure to a modulated non-coplanar magnetic structure. This is a new result since in all the previous papers, the low temperature magnetic structure is considered as a double helix magnetic structure, but the polarised neutron analysis shows the emergence of out plane magnetic moment explicitly.

At DNS, the x spin polarisation direction is parallel to the average directions of scattering vector **Q** and in this case, the x spin flip channel could not be separated with y spin flip channel since for a specific scattering position x polarisation direction is not strictly parallel to **Q**. Polarised neutron diffraction experiment was also performed at the triple axis spectrometer IN12 at the ILL in Grenoble with the help of the Cryopad option [116], which ensured that the x polarisation direction is strictly perpendicular to the scattering vector **Q** and y is perpendicular to x direction and z direction. Two samples from different batches were aligned in the ($h0l$) and ($hk0$) scattering planes, respectively. The magnetic phase transition was firstly checked by following the intensity of (1,0,0) and (1,1,0) in xsf and $xnsf$ channels as shown in Fig.4.13. It is clear that both the magnetic reflections (1,0,0) and (1,1,0) completely disappear in the samples and the magnetic phase transition occurs at 280 K, consistent with the magnetic susceptibility and electrical resistivity results. Below the magnetic phase transition, the polarisation analysis was measured in six channels at 260 K and 178 K as shown in Fig.4.14. This result is consistent with DNS results but the modulated reflections are fully separated due to the high resolution at IN12.

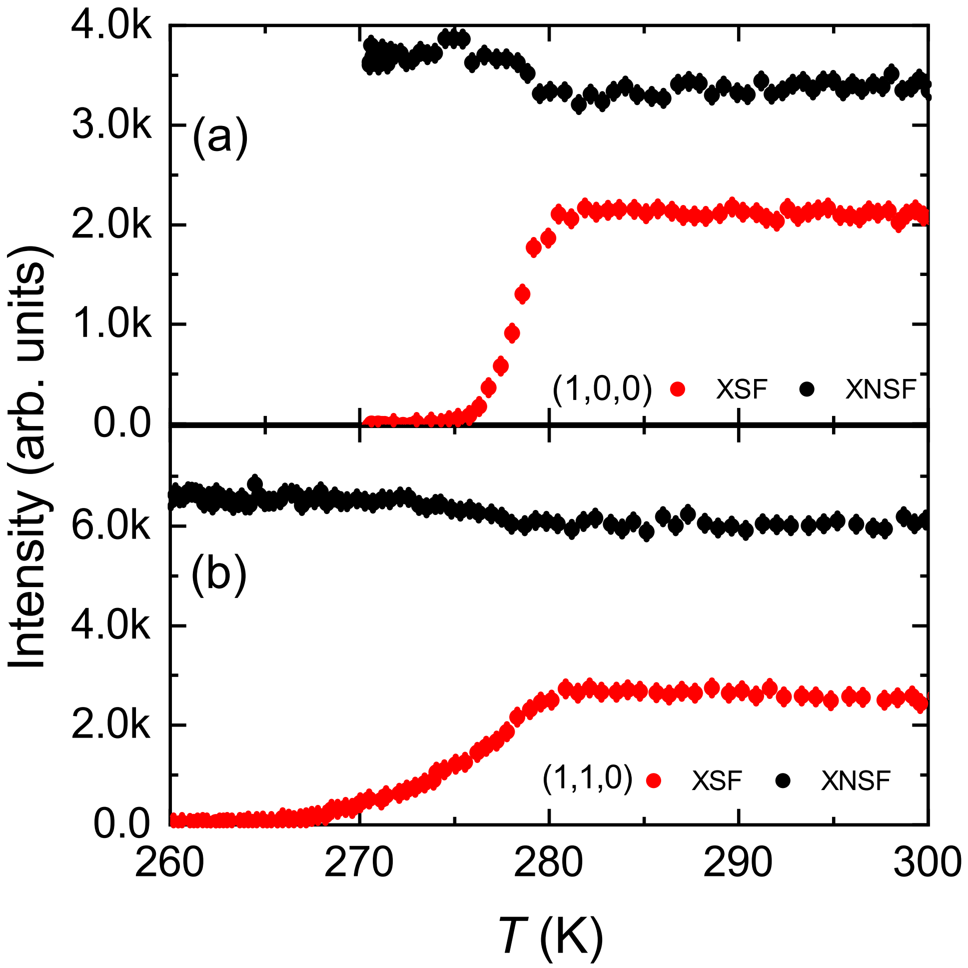

Figure 4.13: Temperature dependence of magnetic reflections: (a) (1,0,0) and (b) (1,1,0) measured in xsf and $xnsf$ channels at IN12 at ILL, respectively. The reflections (1,0,0) and (1,1,0) were measured on samples from two different batches.

Based on the equation 4.1, the square of magnetic components $|\mathbf{M}|^2_{[1,\bar{2},0]}$ and $|\mathbf{M}|^2_{[0,0,1]}$ could be calculated. As mentioned before, the angle between the scattering vector for satellite reflection and *ab* plane is as small as $\theta_2 = 6.22°$, thus in zsf channel, the contribution from $|\mathbf{M}|^2_{[1,0,0]}$ could be omitted. In this regard, the intensities in zsf and $znsf$ represent magnetic components along $|\mathbf{M}|^2_{[0,0,1]}$ and $|\mathbf{M}|^2_{[1,\bar{2},0]}$, which are plotted in Fig.4.14. This result is quite surprising because it means the magnetic components along *c* direction and in *ab* plane have different modulated wave vectors.

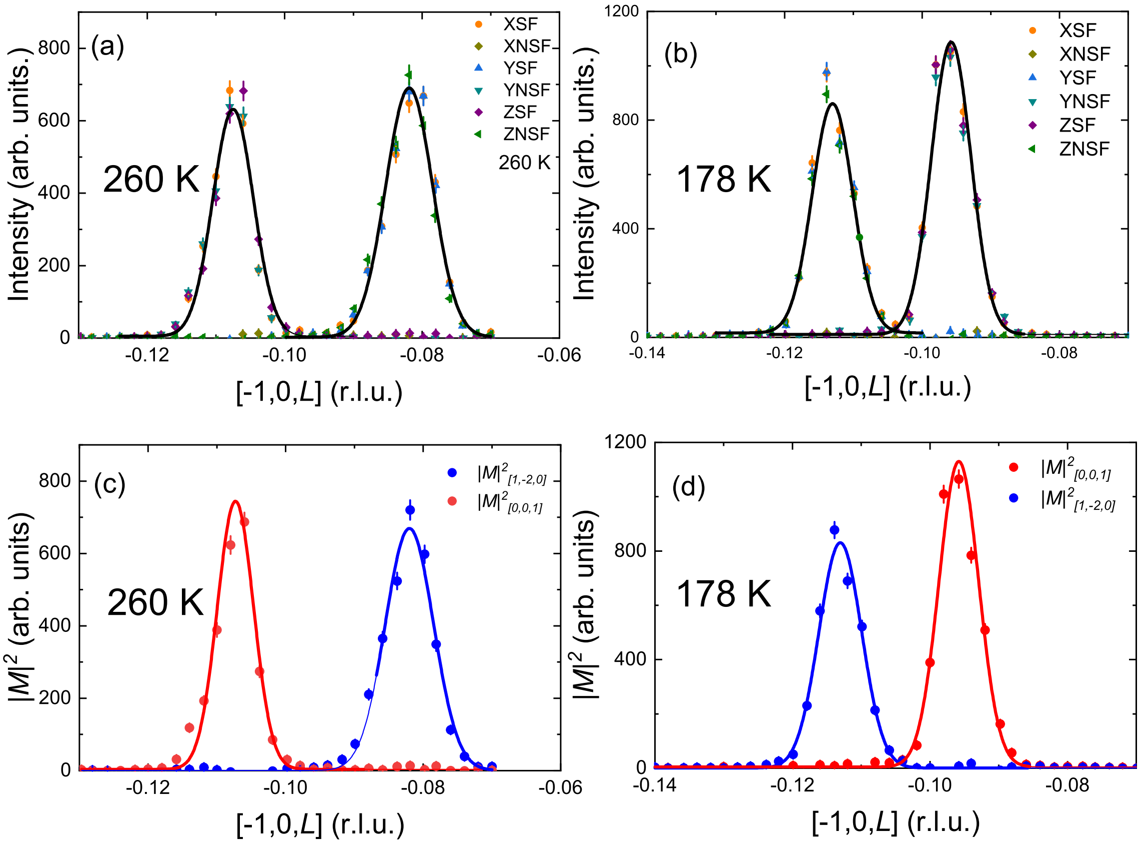

Figure 4.14: Polarised analysis results obtained at IN12 at ILL. (a-b) XYZ polarised analysis measured in six channels at 260 K and 178 K for satellite reflections. (c-d) Calculated square of magnetic components $|\mathbf{M}|^2_{[1,\bar{2},0]}$ and $|\mathbf{M}|^2_{[0,0,1]}$ from (a-b) at 260 K and 178 K.

4.6.3 High resolution neutron diffraction study of modulated phases

Due to the poor resolution at DNS, it is difficulty to separate the two modulated reflections completely. In this regard, high resolution unpolarised neutron diffraction data was also taken at D23 in ILL, Grenoble under various temperatures to study the temperature dependence behaviour of the modulated phases. The data has been plotted as a contour map and is illustrated in Fig.4.15. From the contour map, in the temperature range between 300 K and 2 K, the magnetic phases could be roughly classified into four regimes: (i) above 280 K, where the magnetic structure is $\mathbf{k}$ = (0,0,0) antiferromagnetic; (ii) between 280 K and 250 K, where the modulated wave vectors $\mathbf{q}_1 < \mathbf{q}_2$; (iii) between 250 K and 200 K, where the modulated wave vectors $\mathbf{q}_1 = \mathbf{q}_2$ and (iv) between 200 K and 2 K, where the modulated wave vectors $\mathbf{q}_1 > \mathbf{q}_2$. Single crystal neutron diffraction data was also collected at 225 K with propagation vector $\mathbf{k}$ = (0,0,1/10) to solve the magnetic structure since at this temperature $\mathbf{q}_1 = \mathbf{q}_2 = 0.1L(r.l.u)$.

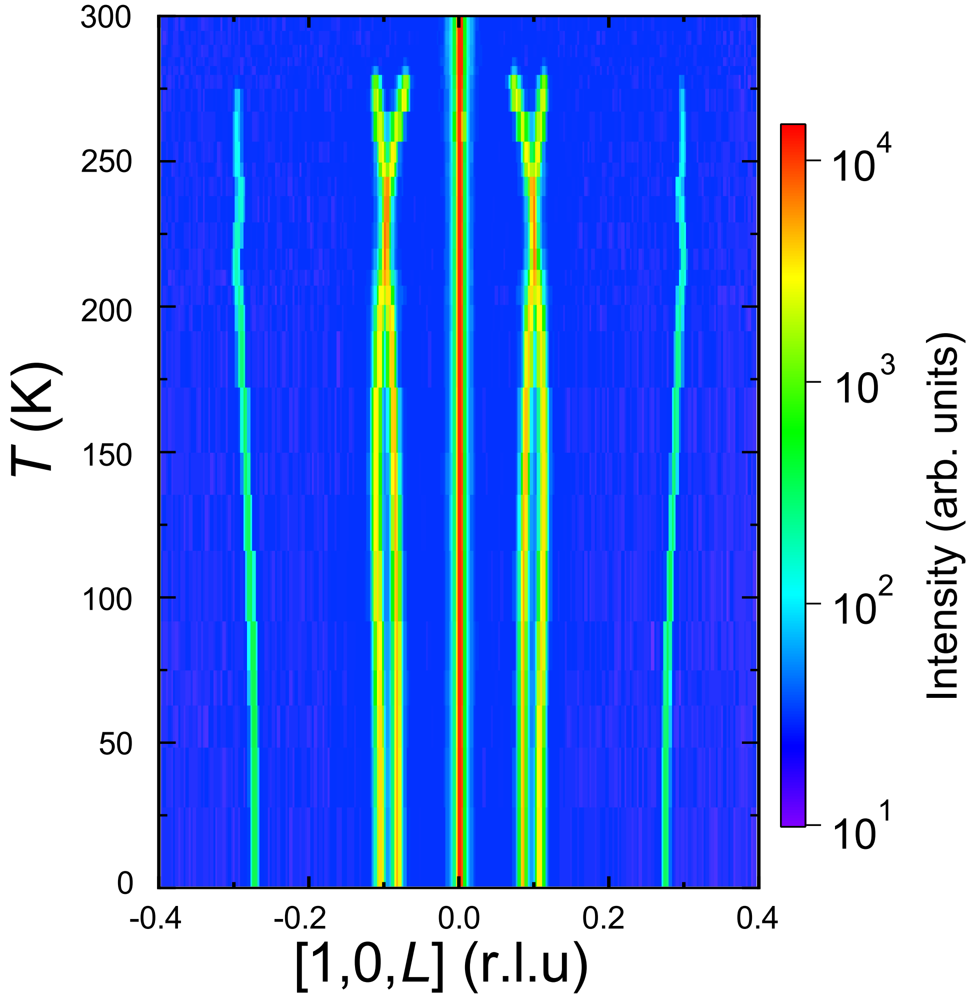

Figure 4.15: Contour map of temperature dependence of incommensurate phases in Mn$_3$Sn measured at the two-axis neutron diffractometer D23 at ILL.

In addition, the higher order harmonics $\mathbf{q}_3$ which are present around $(\bar{1},0,\pm0.3)$ are also very clear from the high resolution scan. By fitting each scan, one can obtain the fitted peak centres, which reflect the modulated wave vectors in Fig.4.16. From the polarisation analysis results, it is clear that the magnetic intensity in zsf channel comes from the magnetic components along c direction while the magnetic intensity in $znsf$ channel comes from the magnetic components in ab plane. The $\mathbf{q}_1$ in $znsf$ channel can be denoted as $\mathbf{q}_T$ which means the magnetic components are transverse with the wave vector that is along c direction and $\mathbf{q}_2$ in zsf channel as $\mathbf{q}_L$ as it propagates along the longitudinal direction of the wave vector. The higher order is to be indexed by calculating three times of $\mathbf{q}_T$ or $\mathbf{q}_L$ according to previous reports [156, 158], but this does not work as illustrated in Fig.4.16 (b). Then the third harmonic is indexed by the combination of $\mathbf{q}_T$ and $\mathbf{q}_L$. Surprisingly, the high order harmonic $\mathbf{q}_3$ could be successfully indexed by $(2\mathbf{q}_L + \mathbf{q}_T)$, which is a solid evidence of the emergence of a double-$\mathbf{q}$ magnetic modulation at low temperature in Fig.4.16 (c).

A spin density wave magnetic structure model could explain this double-$\mathbf{q}$ magnetic structure, which can be expressed as the combination of a helix with magnetic moments parallel to the ab plane and rotation axis perpendicular the ab-plane and a longitudinal sine-wave modulation along c direction with independent $\mathbf{q}$ wave vector. For the helix modulation in ab plane, it can be further decomposed into two orthogonal parts for each Mn($\boldsymbol{R}_l$):

$$(\mathbf{M}_{ab})_{[1,\bar{2},0]} = \mathbf{M}_{ab}cos(2\pi\mathbf{q}_T \cdot \boldsymbol{R}_l + \phi_{ab});$$

$$(\mathbf{M}_{ab})_{[\bar{1},0,0]} = \mathbf{M}_{ab}sin(2\pi\mathbf{q}_T \cdot \boldsymbol{R}_l + \phi_{ab})$$

and the observed intensity in $znsf$ channel is actually contributed from

$$(\mathbf{M}_{ab})_{[1,\bar{2},0]}.$$

The magnetic moments along c direction can only be modulated in their amplitudes:

$$\mathbf{M}_c cos(2\pi\mathbf{q}_L \cdot \boldsymbol{R}_l + \phi_c).$$

As a result, the moment for Mn in each layer is

$$\mathbf{M}_{Mn}(\boldsymbol{R}_l) = \mathbf{M}_{ab}(2\pi\mathbf{q}_T \cdot \boldsymbol{R}_l + \phi_{ab}) + \mathbf{M}_c(2\pi\mathbf{q}_L \cdot \boldsymbol{R}_l + \phi_c),$$

thus the total amplitude of Mn can be $\boldsymbol{l}$ independent only if

$$\mathbf{q}_T = \mathbf{q}_L.$$

This physical picture of spin density wave model is consistent with the electrical resistivity in Fig.4.7, where a sudden increase of the resistivity upon cooling is observed that corresponds to the formation of an energy gap around the magnetic phase transition at 280 K, which is a signature of the formation of the spin density wave.

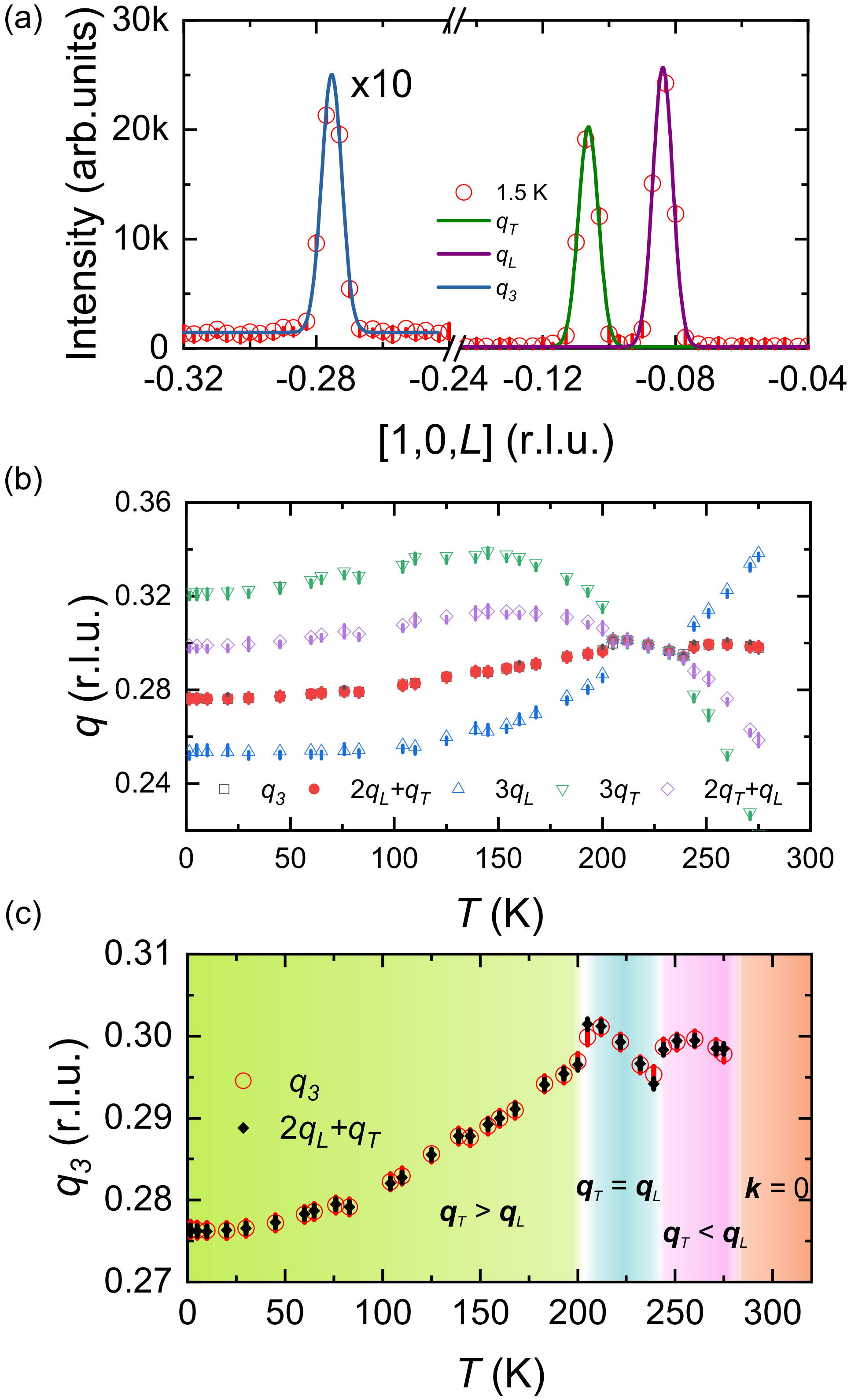

Figure 4.16: (a) The Q-scan measured from D23 at ILL could be well fitted by simple Gaussian functions for each peak. The higher order harmonic $\mathbf{q}_3$ has been scaled up by 10 times. (b) and (c) The index of the higher order harmonic $\mathbf{q}_3$. Only $(2\mathbf{q}_L + \mathbf{q}_T)$ could fit $\mathbf{q}_3$ very well, which is the direct evidence that the low temperature magnetic structure is a double-**q** magnetic structure.

4.6.4 Magnetic structure of Mn_3Sn at 225 K

When the modulation wave vectors $\mathbf{q}_T = \mathbf{q}_L = 0.1L(r.l.u.)$ between 250 K and 200 K, there is a single peak in xsf, zsf, $znsf$ channels. It has to be mentioned that this single peak measured at unpolarised neutron diffraction could still be well separated at DNS with two nearly equal intensity peaks in zsf and $znsf$ channels in Fig.4.10. The magnetic structure of this $\mathbf{q}_T = \mathbf{q}_L$ phase at 225 K was investigated by single crystal neutron diffraction at HEiDi in MLZ.

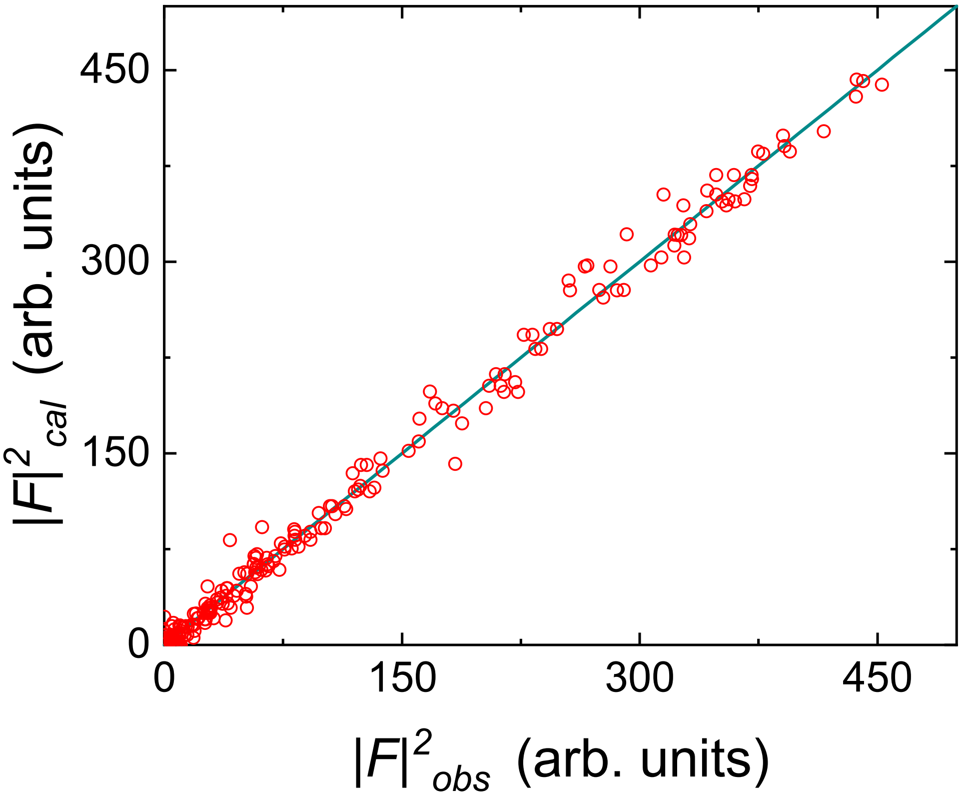

Figure 4.17: Refined square of structure factors versus calculated structure factors for magnetic structure of Mn_3Sn at 225 K from single crystal neutron diffraction data collected at HEiDi at MLZ.

362 reflections (168 main + 194 satellite) were collected with propagation wave vector $\mathbf{k}$ = (0,0,1/10) at 225 K and refined with the magnetic superspace approach by Jana2006 [135]. In the magnetic superspace approach, the magnetic moment of the atom μ can be expressed by a Fourier series of the type:

$$\begin{aligned}\mathbf{M}_\mu\left(\mathbf{k}\cdot\mathbf{r}_\mu\right) =& \mathbf{M}_{\mu,0} + \sum_m \left[\mathbf{M}_{\mu,ms}\sin\left(2\pi m\mathbf{k}\cdot\mathbf{r}_\mu\right)\right. \\ & \left. + \mathbf{M}_{\mu,mc}\cos\left(2\pi m\mathbf{k}\cdot\mathbf{r}_\mu\right)\right]\end{aligned}$$

where $\mathbf{M}_{\mu,0}$, $\mathbf{M}_{\mu,ms}$ and $\mathbf{M}_{\mu,mc}$ are the absolute value, amplitude of sine term and amplitude of the cosine term, respectively. The representation analysis and possible magnetic superspace symmetry analysis is performed automatically by Jana2006 [126]. By trials and errors, the best fitting magnetic superspace model is found, which is $P6_322.1'(00g)$-$h00s$ shown in Fig.4.17

with refined $R(obs) = 3.43\%$, $R_w(obs) = 5.27\%$, $R_w(all) = 5.49\%$ and the refined parameters are summarized in tab.4.5. As illustrated in Fig.4.18, this structure model is indeed a non-coplanar spin density wave where the phase and the amplitude of of the magnetic moment on the Mn atoms varies periodically, consistent with the polarised neutron analysis. The transverse magnetic components lying in ab plane is a helix and the magnetic components along$c$ direction is a longitudinal spin density wave.

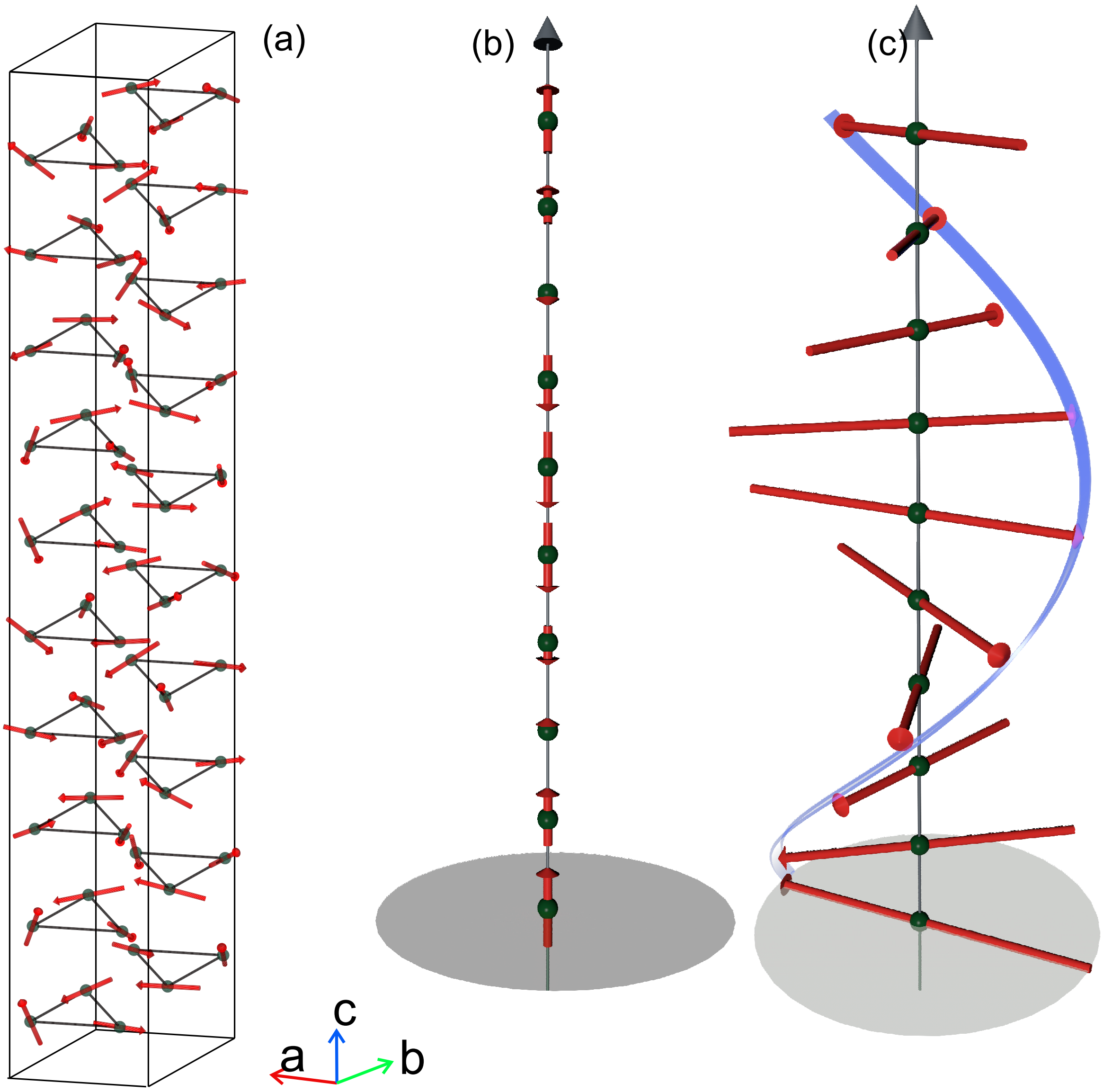

Figure 4.18: Refined magnetic structure from single crystal neutron diffraction data of Mn$_3$Sn at 225 K collected at HEiDi at MLZ. (a) Superstructure of Mn$_3$Sn with ten Mn$_3$Sn unit cells, where only Mn atoms are plotted. Magnetic structure model is plotted by Vesta [62]. (b) The magnetic components along c direction are a longitudinal spin density wave, which are measured in $znsf$ channels. (c) The magnetic components lying in ab plane are a helix, which are measured in zsf channels.

Table 4.5: Refined parameters of the topological semimetal Mn$_3$Sn at 225 K based on the magnetic superspace model $P6_322.1'(00g)$-$h00s$ from single crystal neutron diffraction data collected at HEiDi at MLZ.

Atom	Site	x	y	z	$Occ.$	U_{iso} (Å^2)
Mn	$6h$	0.8383(2)	0.6766(2)	0.25	1.016	0.0050(3)
Sn	$8j$	0.3333	0.6667	0.25	0.3333	0.0040(5)

Refined magnetic parameters for waves in Bohr magnetons:

Waves	length (μ_B)
0	0.0(0)
sin	3.0(5)
cos	2.7(3)

$R(obs)$ = 3.43%, $R_w(obs)$ = 5.27%, $R_w(all)$ = 5.49%

The observed reflections are those reflections with $I/sigma \geq 3$.

$Occ.$: atom occupation;

U_{iso}: isotropic atomic displacement parameters.

4.7 Discussion

4.7.1 Sample comparison between the samples in this work and old Bridgmann samples

Fig.4.19 shows the **Q**-scan along [$\bar{1}$,0,**L**] (r.l.u) in the flux grown sample (a-b) and **Q**-scan along [1,0,**L**] (r.l.u) in an old Bridgman sample (c) and (d) [161] respectively. It is clear that at 260 K ($\bar{1}$,0,0) peak in the sample in this work is about 11300 cts/s and the intensity for the modulated peak is 4000 cts/s, leading to a ratio about 2.82, while for the Bridgman sample, the intensities for (1,0,0) and the modulated peak are 71000 ct/min, 700ct/min, leading to a ratio of 101.43 at 260 K. Apparently, the phase transition in the old Bridgman sample pertains only to a very small part of the sample and most of it remains in the room temperature triangular inverse antiferromagnetic order. In addition, in the sample in this work the polarised neutron diffraction has proven the complete disappearance of the antiferromagnetic ($\bar{1}$,0,0), indicating the intrinsic nature of this transition in the sample. Besides, a latest resistivity study of Mn$_3$Sn has demonstrated that only when the composition of the sample is close to stoichiometry, this magnetic phase transition at ~280 K will not be suppressed [162].

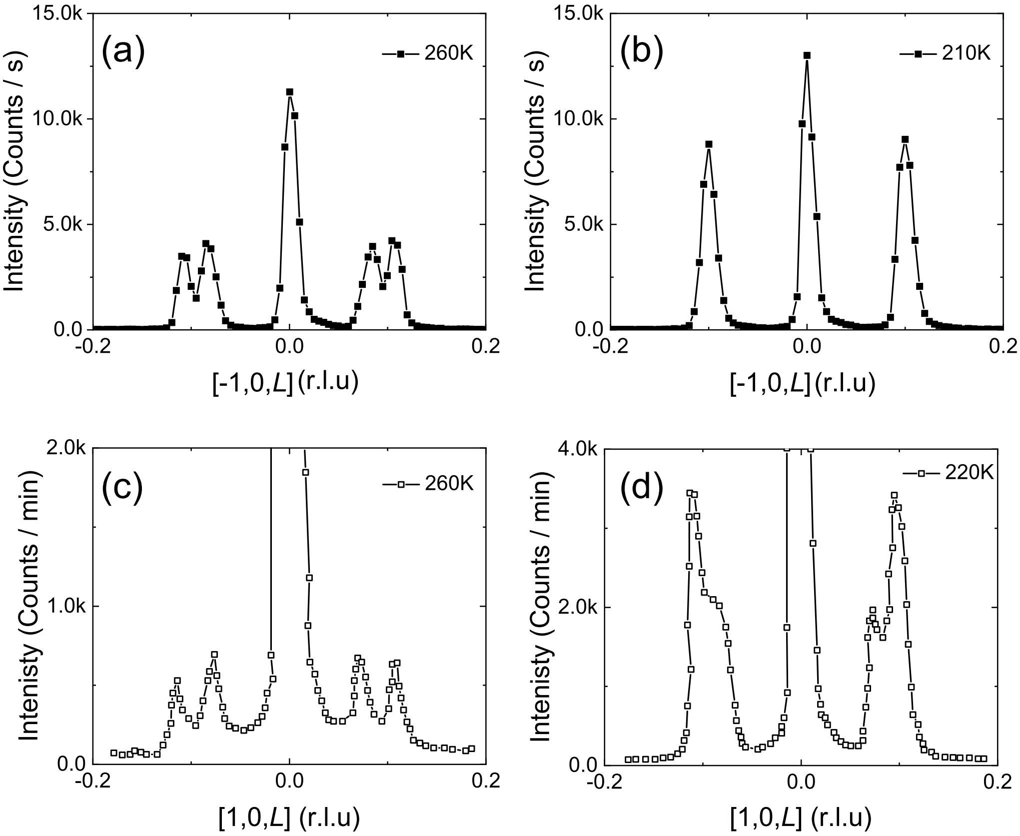

Figure 4.19: Comparison of the **Q**-scan along [$\bar{1}$,0,**L**] (r.l.u) direction in the flux grown sample in this work and **Q**-scan along [$\bar{1}$,0,**L**] (r.l.u.) direction in an old Bridgman sample from [161]. (a)-(b): The sample in this work measured at 260 K and 210 K. (c-d) The Bridgman sample measured at 260 K and 220 K. The cut-off peak (1,0,0) in (c) and (d) has an intensity of ~ 71000 Counts/min.

4.7.2 Reasons for non-coplanar order

The possible reasons for the non-coplanar magnetic order in Mn_3Sn are discussed from the crystal structure and Dzyaloshinskii–Moriya (DM) interaction.

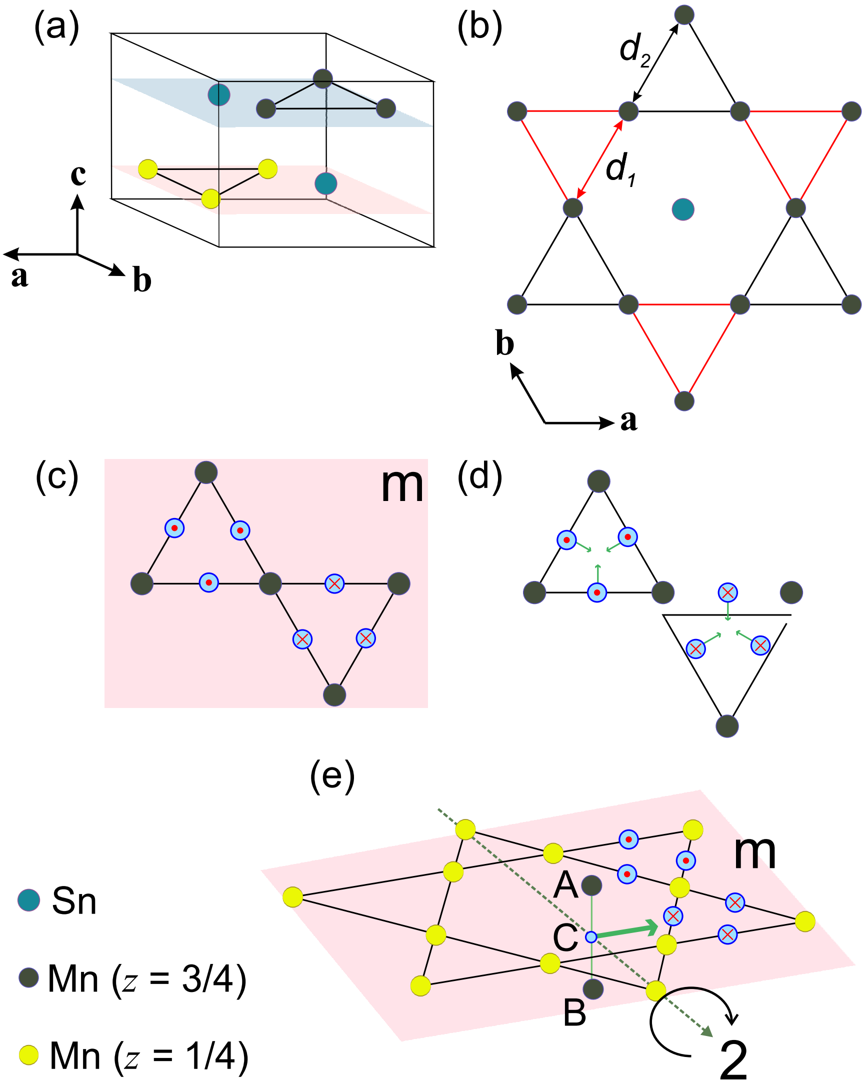

Figure 4.20: (a-b) Crystal structure of Mn_3Sn. The unit cell of Mn_3Sn and a kagomé lattice in crystallographic *ab* plane. In the kagomé plane, the length of the nearest triangles d_1 and d_2 has a breathing amplitude of 0.18 Å, giving a ratio of 1.066. (c)-(d) DM interactions in a kagomé plane with and without a mirror plane: (c) The DM interaction vectors (red dots and green arrows) are perpendicular to the kagomé plane. (d) When the mirror plane of the kagomé is broken, there are in plane DM interaction vectors. (e) The interlayer DM interaction vectors which are perpendicular to the two fold rotation symmetry in the kagomé plane lie in the *ab* plane. This in-plane DM interactions could drive the magnetic moments to tilt out of the *ab* kagomé plane.

The slight distortion of the kagomé lattice could be one of the reasons for the non-coplanar magnetic order. As mentioned before, for an ideal kagomé lattice formed by Mn-atoms, the six triangles in kagomé plane have the same bond length. In Mn$_3$A materials, the Wyckoff position for Mn is 6h (x, $2x$, $1/4$), only when $x = 5/6$ (0.8333) the kagomé plane is perfect, otherwise it develops into the breathing type with unequal bond length between two nearest triangles as shown in Fig.4.20. In Mn$_3$Sn, the refined x is 0.8386(1) in the flux grown crystal in this work, close to a recent Bridgman grown crystal, where the refined x is 0.8385(1), which also shows a similar transition at $\sim$ 260 K [167]. The slight change in the atom positions of Mn-atoms results in a non-negligible breathing amplitude as large as 0.16 Å with a 6.6% difference in ratio between two nearest triangles as shown in Fig.4.20. Whereas for Mn$_3$Ge, it is quite close to a perfect kagomé lattice with only 0.007 Å breathing amplitude. Similar to the negligible breathing difference, there is no report about sample dependence or phase transition in Mn$_3$Ge to the knowledge. The small in-plane distortion of Mn$_3$Sn may cause this non-coplanar magnetic order since frustrated magnets are very sensitive to these delicate interactions.

In addition, as shown in Fig.4.20 (c)-(e), three kinds of DM interaction are considered in Mn$_3$Sn from the viewpoint of Moriya's law [169]. For a kagomé plane the middle of the connection of two nearest Mn atoms is not on an inverse centre. Besides, if this kagomé plane is a mirror plane, the direction of DM interaction will be perpendicular to the kagomé plane at this position, which is the case (c). In case (d), if the mirror plane is broken, then there will be in-plane DM interactions, which will drive the magnetic moments from in-plane to out of plane. The crystal structure of Mn$_3$Sn was checked at 210 K by single crystal neutron diffraction and there is no structural transition, which means the kagomé plane is a mirror plane so that there will not be any in-plane DM interaction arising from the nearest interaction in kagomé plane. However, if the next nearest interlayer interaction of Mn$_3$Sn is considered, as shown in case (e), there is a two fold rotation symmetry crossing the kagomé plane, the middle point C of the connection the two atoms A and B is located in kagomé plane, which has the in-plane direction for the DM interaction. This in-plane DM interaction may cause the magnetic moment tilted from ab plane to c direction.

4.7.3 Reasons for absence of AHE in the low temperature

In order to understand the absence of anomalous Hall effect below T_1 = 280 K, first consider the $\mathbf{q}_T = \mathbf{q}_L$ phase. In the low temperature modulated phases, the mirror symmetry in the inverse triangular structure has been broken by the non-coplanar order so it is not expected any contribution from non-vanishing Berry curvature. From the viewpoint of symmetry analysis, a general property of incommensurate magnetic modulation with single modulated wave vector is the existence of a spatial translation time-reversal symmetry in the superspace group, where there is a time-reversal operator combined a lattice translation of one half for the magnetic superspace [130]. In this case for the $\mathbf{q}_T = \mathbf{q}_L$ phase, since the period is $10c$, the magnetic moments at "$l_i c$" and "$(l_i+5)c$" are related by the time-reversal symmetry in the superspace. In addition, as mentioned before, for a non-coplanar magnetic structure, the non-vanishing scalar spin chirality can generate AHE and it is defined as

$$\kappa_{\mathrm{ijk}} = \boldsymbol{s}_{\mathrm{i}} \cdot (\boldsymbol{s}_{\mathrm{j}} \times \boldsymbol{s}_{\mathrm{k}})$$

, where s_{i}, s_{j}, s_{k} are the spins. This result is further confirmed by the online magnetic space group model analysis on Bilbao Crystallographic Server [129, 136, 170] and the single crystal neutron diffraction result. To integrate the scalar spin chirality of the $\mathbf{q}_T = \mathbf{q}_L$ phase in a superspace structure, the summation will readily be zero due to the existence of the spatial translation time-reversal symmetry. In this regard, it is anticipated that the AHE in the $\mathbf{q}_T = \mathbf{q}_L$ phase would vanish since there will be no contribution from either the non-vanishing Berry curvature or the scalar spin chirality. For the $\mathbf{q}_T \neq \mathbf{q}_L$ phases, the magnetic structure could be described by a double-**q** magnetic structure of a superposition of two single-**q** magnetic structures which describe the magnetic moments in *ab* plane and *c* direction by $\mathbf{q}_T$ and $\mathbf{q}_L$, respectively. The scalar spin chirality is still zero because $\mathbf{q}_T$ and $\mathbf{q}_L$ are orthogonal to each other. That is the reason that AHE from 280 K to 2 K is not observed.

4.8 Conclusion

In this chapter, the high quality single crystal growth, magnetic phase transition and magnetic structures of the topological Weyl semimetal Mn$_3$Sn are systematically studied. The following important results are obtained:

1. There is a magnetic phase transition around $\sim$ 280 K in the self-flux grown sample in this work, which is a transition from coplanar inverse triangular magnetic structure to a novel double-$\mathbf{q}$ non-coplanar incommensurate magnetic structure.
2. The large AHE has completely disappeared after the magnetic phase transition because of the broken symmetry.
3. In the experiments of the polarised neutron scattering study at DNS and high resolution neutron diffraction at D23, the temperature dependence of this double-$\mathbf{q}$ magnetic structure has successfully been revealed .
4. Single crystal neutron diffraction experiment on Mn$_3$Sn at 225 K was performed and the magnetic structure in the $\mathbf{q}_T = \mathbf{q}_L$ phase was successfully determined.

This work is of great research importance because it is the first time to reveal the nature of low temperature magnetic structure of Mn$_3$Sn. Since materials with multiple-$\mathbf{q}$ magnetic order are fertile playgrounds to study the topological textures and novel electrical properties, it is anticipated that Mn$_3$Sn may become a new prototype material to study the relationship between magnetic order and topological properties in antiferomagnets.

5

α-RuCl$_3$

5.1 Single crystal growth of α-RuCl$_3$

Single crystals of α-RuCl$_3$ were grown by the chemical vapour transport method in a three-zone furnace. The principles and methods of chemical vapour transport have been discussed in Sec.3.1.2. As discussed before, the greatest challenge in the growth of α-RuCl$_3$ is to minimize the stacking faults density, since stacking faults are inevitable for the growth of Van der Waals materials by chemical vapour transport methods. By optimising the crystal growth condition, controlling the crystal growth speed and improving the purity of starting materials, the density of stacking faults has been reduced substantially in this work.

The stacking faults in α-RuCl$_3$ will introduce some magnetic orders from different stacking sequences at low temperature, which could be observed in the heat capacity with several small anomalies between 10 K and 15 K along with the main zigzag magnetic anomaly around 7.5 K [92, 171, 172]. Fig.5.1 compares the heat capacity of α-RuCl$_3$ single crystal samples grown from different batches. The heat capacity of WX009, WX011 and WX031 shows several kinks at $\sim$10 K, $\sim$14 K, which are signatures of the magnetic order from different stacking sequences [92], while in the heat capacity of samples from WX086, only a sharp λ-shape peak is observed, proving high quality of this sample.

The final optimised growth procedure is as following: The raw materials α-RuCl$_3$ powders ($\sim$3-5 g) are sealed in a silica ampoule with 12 cm in length and 2 cm in diameter in vacuum. Then the ampoule is put in the three zones furnace, where the middle point temperature is set as 700 °C, and 780 °C for the source part, 680 °C for the sink part. Depending on the amount of the raw materials, it takes 4 days for 3 g starting materials for the growth. After growth, the ampoule is taken out from the furnace directly without cooling down the furnace. This procedure is very important because it avoids the formation of small crystals during the cooling of ampoule in the furnace. It also should be mentioned here, that the quality of the raw material is essential to grow large crystals with minimised stacking fault density. The raw materials with high quality are black powders and that in this PhD work is bought from **Furuya** metal, which has 49.37 wt..% Ru in α-RuCl$_3$ without containing any water or RuOCl. A typical picture of an as-grown α-RuCl$_3$ single crystal is shown in Fig.5.2.

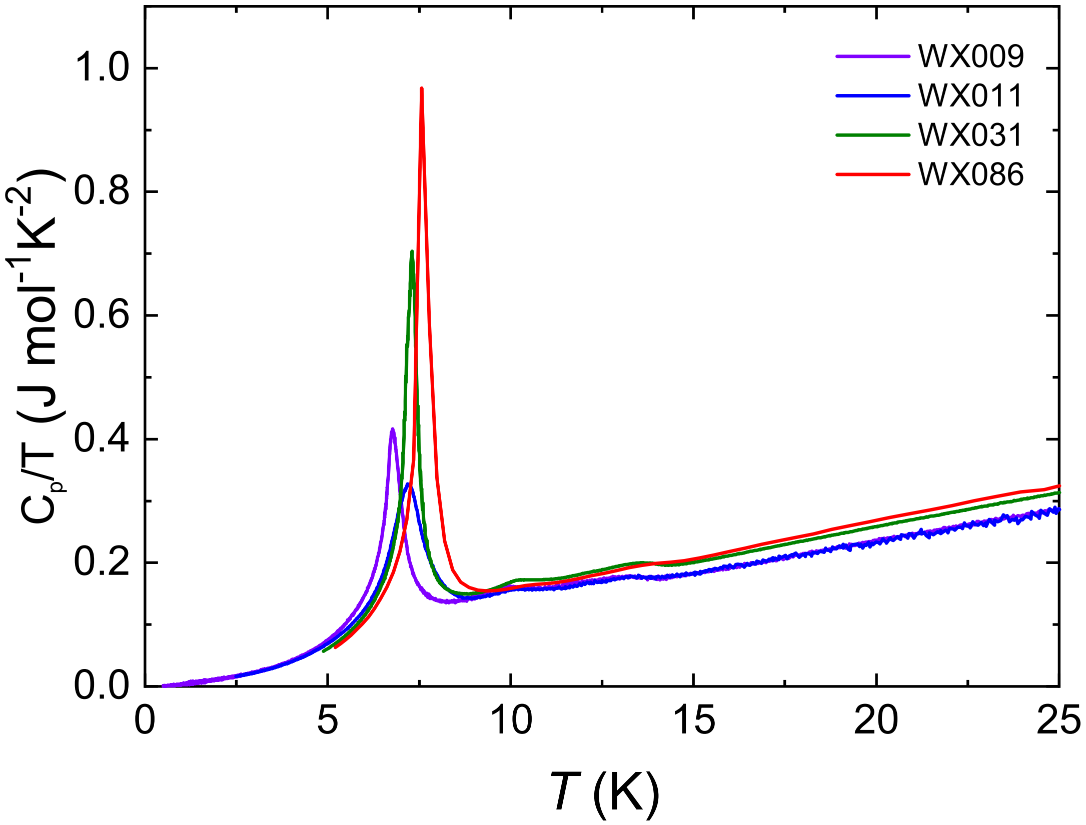

Figure 5.1: Comparison of heat capacity among different crystal growth batches measured on PPMS. The sample quality of WX086 is best as there is only one sharp transition peak at 7.5 K.

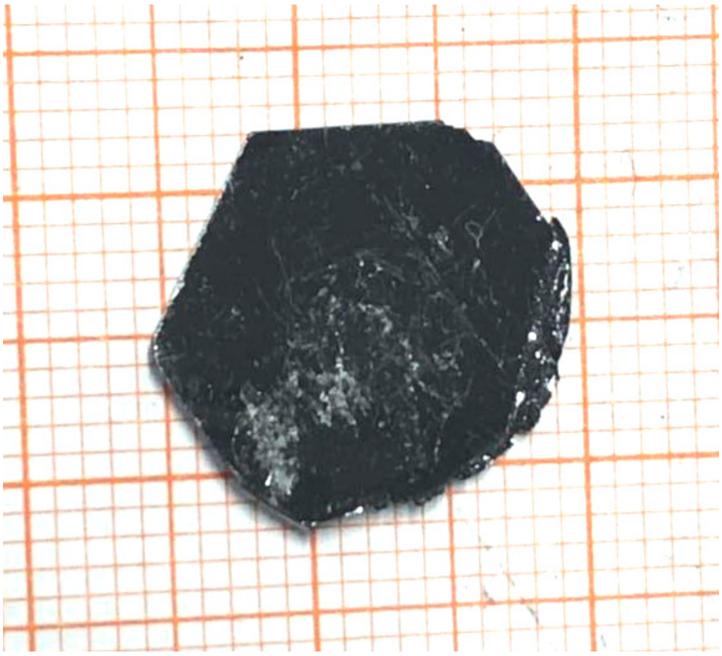

Figure 5.2: Picture of an α-RuCl$_3$ as-grown single crystal (~540 mg) on the millimetre paper.

5.2 Heat capacity

As mentioned before, α-RuCl$_3$ shows a zigzag type antiferromagnetic order at ∼8 K. For the antiferromagnetic order, an effective way to suppress the magnetic order is applying a magnetic field. In α-RuCl$_3$ there have been been a vast number of studies about its behaviour under magnetic fields [171, 173–175], and we also check this in our as-grown sample. Consistent with previous reports, when the magnetic field is applied along the *ab* plane, the antiferromagnetic order is gradually suppressed and when the magnetic field reaches 10 T, it is fully suppressed . By contrast, when the magnetic field is applied along *c* direction, it will not suppress the magnetic order until ∼ 60 T [176].

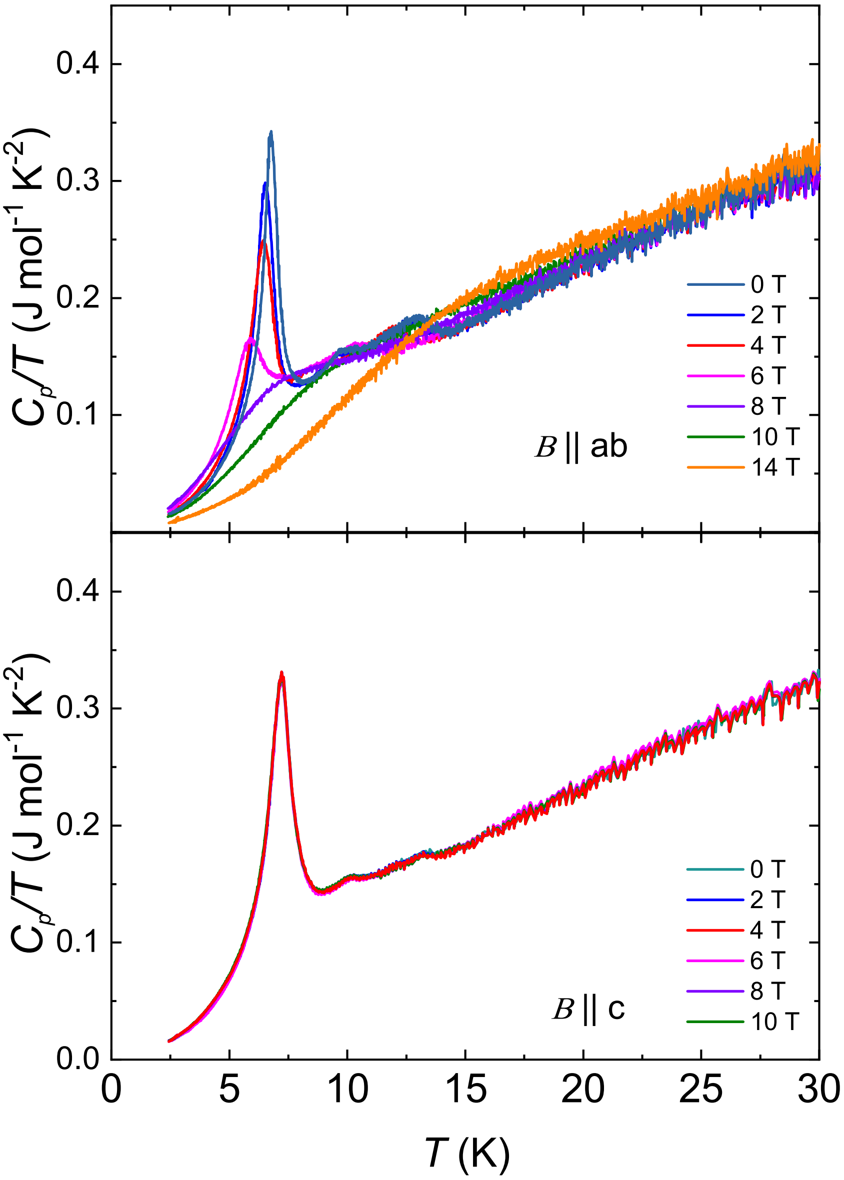

Figure 5.3: Field dependence of heat capacity of α-RuCl$_3$ measured under magnetic fields along *ab* basal plane and crystallographic *c* directions. The α-RuCl$_3$ sample is from WX011 batch.

5.3 Crystal structure and magnetic structure determination

5.3.1 Structural transition in α-RuCl$_3$

The real crystal structure of α-RuCl$_3$ at low temperature is still under debate. For the room temperature, it has been proved to be the monoclinic $C2/m$ as shown in Fig.5.4, while for the low temperature (below 50 K) crystal structure, there are several proposed models such as $C2/m$, $R\overline{3}$, $P3_112$ [92, 177]. If the low temperature crystal structure is not $C2/m$, which means there is a structural transition. Actually, many techniques like magnetization measurement, thermal expansion, infrared spectroscopy measurement reveal a first order phase transition by observing a hysteresis from 50 K to 200 K, which is the signature of the structural transition [178–181]. However, the structural transition temperatures reported from different groups are quite different, which are from 200 K to 50 K. Up to now, there is not a systematic study of this phase transition and the crystal structure below this transition by neutron scattering technique. One big challenge is the stacking faults in the samples as discussed before, thus in order to solve the crystal structure in the low temperature, the first step is to grow high quality α-RuCl$_3$ single crystal.

From previous X-ray synchrotron study, the low temperature crystal structure of α-RuCl$_3$ is rhombohedral $R\overline{3}$ instead of the monoclinic crystal structure $C2/m$ [177]. Besides, previous neutron scattering experiment on our α-RuCl$_3$ single crystals at IN12 and D23 have demonstrated the systematic disappearance of reflections and the emergence of many additional reflections below 50 K. These new peaks could be indexed with a rhombohedral unit cell and reflection conditions: Reflections (hkl) observed only if $-h+k+l=3n$ or $h-k+l=3n$. Therefore, the low temperature structure of α-RuCl$_3$ should be rhombohedral.

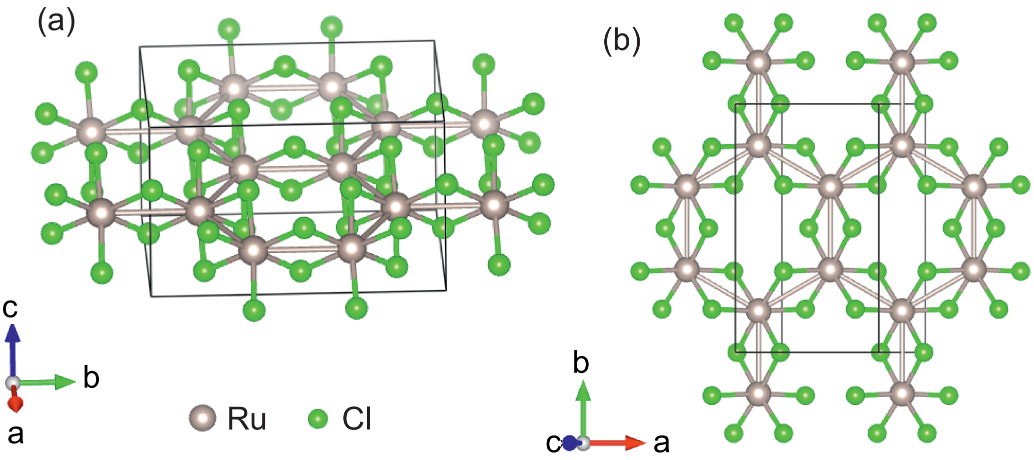

Figure 5.4: Crystal structure of α-RuCl$_3$ at room temperature. (a) The monoclinic $C2/m$ unit cell, where Ru-atoms are in a Cl-atoms Octahedron. (b) The each layer, Ru-atoms from a honeycomb lattice. Crystal structure model is plotted by Vesta [62].

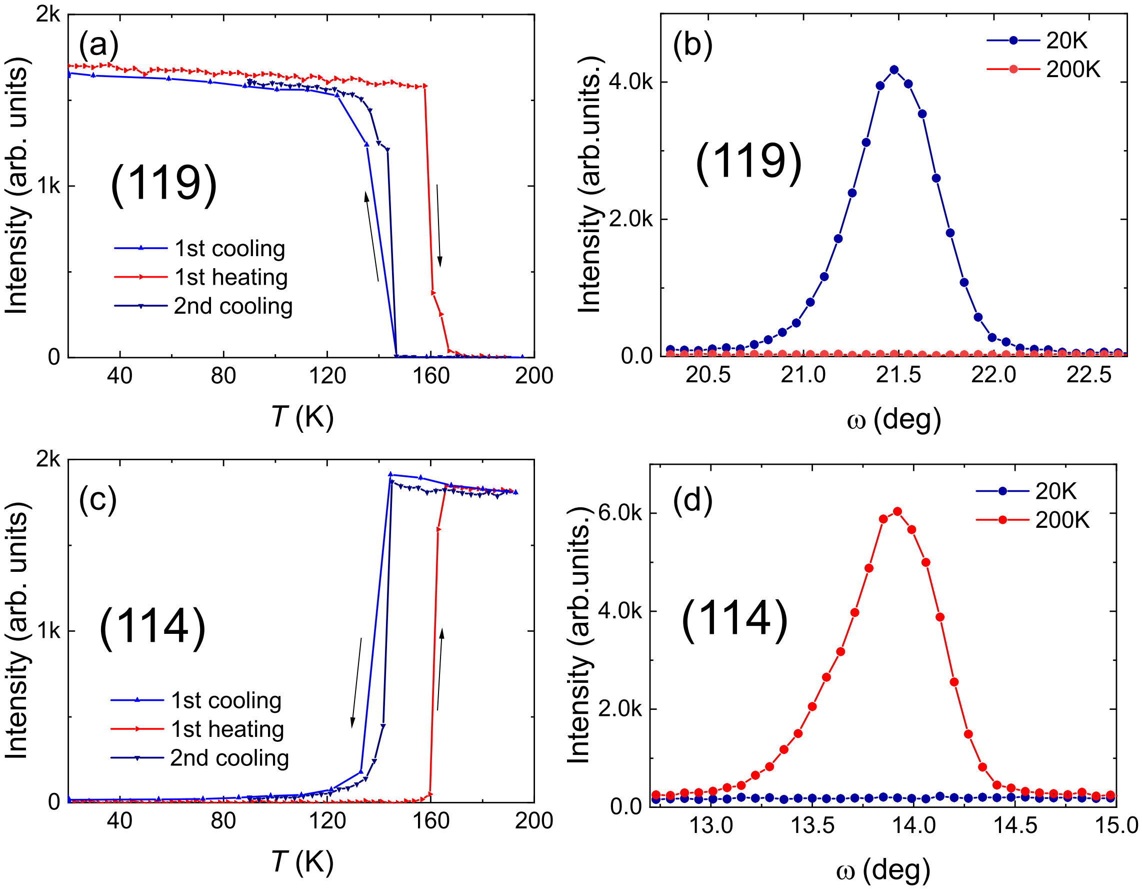

Figure 5.5: Temperature dependence of the intensity of reflections (1,1,9), (1,1,4) and the related rocking curve scans at 200 K and 20 K, respectively measured at HEiDi at MLZ. Reflection (1,1,9) is forbidden in the monoclinic structure model and (1,1,4) is forbidden in the rhombohedral structure model. The disappearance of (1,1,4) reflection and the appearance of (1,1,9) reflection indicate the low temperature crystal structure of α-RuCl$_3$ is rhombohedral.

In order to study the structure transition, a high quality α-RuCl$_3$ single crystal with a mass of $\sim$30 mg was selected for the single crystal neutron diffraction experiment. The heat capacity measurement of this sample showed only one strong anomaly at 8 K, indicating a low stacking fault density.

The structural transition was firstly studied at the single crystal diffractometer HEiDi. By following the intensity of (1,1,9) and (1,1,4) reflections during cooling and heating, a structural transition hysteresis loop was traced as shown in Fig.5.5. The (1,1,9) reflection cannot be indexed by a $C2/m$ structural model, while for (1,1,4) reflection which is forbidden in the rhombohedral structure model can be indexed the $C2/m$ model. In this case, it it evident that there is a structural phase transition from $C2/m$ to $R\bar{3}$ and the rocking curves of (1,1,9) and (1,1,4) reveal the complete phase transition in this sample. During cooling, the intensity of (1,1,9) increases from $\sim$145 K and saturates at 130 K while the intensity of (1,1,4) decreases dramatically to zero in this temperature range. With heating up the sample, the onset transition temperature shifts up to 160 K with a $\sim$15 K temperature hysteresis compared with cooling. The large temperature hysteresis of the intensity of (1,1,4) and (1,1,9) upon cooling and heating heating clearly shows that this transition is of first order.

5.3.2 Structure determination at low temperature

Single crystal neutron diffraction was performed on the same crystal which was used for the study of phase transition on HEiDi at MLZ. 601 neutron single crystal reflections were collected based on the primitive hexagonal setting below the magnetic phase transition at at 2 K. The crystal structure refinement was performed on the crystallographic computing system Jana2006. In Jana2006, the crystal domains or twins could be introduced into the refinement manually with a transformation matrix, which describes the symmetry relationship between the main refined crystal structure model and the domains or twins. The $R\bar{3}$ structure model is refined with two rhombohedral twins: reverse and obverse and the reflections from them are related by the following twin law matrix:

$$\begin{bmatrix} -1 & 0 & 0 \\ 0 & -1 & 0 \\ 0 & 0 & 1 \end{bmatrix}$$

In order to refine the $C2/m$ structure model, three domains related by a pseudo three fold symmetry operator along c^* directions are introduced according to a previous report [92].

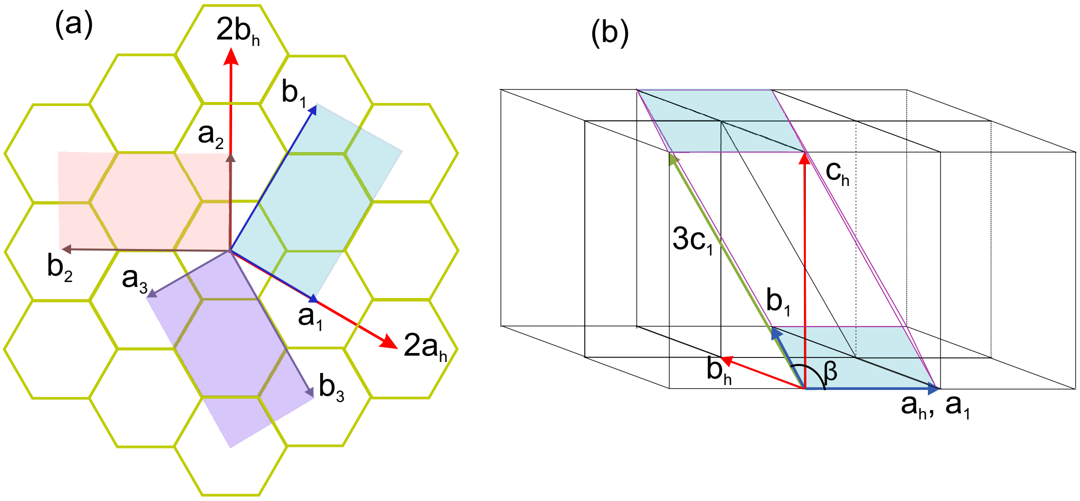

Figure 5.6: Construction of three monoclinic domains from the hexagonal unit cell. (a) Three monoclinic domains and their unit cell axis projected on the *ab* basal plane. (b) The relationship of the hexagonal unit cell and the unit cell of monoclinic domain 1, where $\mathbf{a}_1 = \mathbf{a}_h$; $\mathbf{b}_1 = \mathbf{a}_h + 2\mathbf{b}_h$; $\mathbf{c}_1 = (-\mathbf{a}_h + \mathbf{c}_h)/3$.

Since the reflections were collected in a hexagonal setting, in order to refine the crystal structure in a monoclinic structure, these reflections should be converted to a monoclinic setting. Firstly, the monoclinic unit cell on the hexagonal unit cell is constructed. According to previous report [92], there are three 120° structure domains in the $C2/m$ structure, so they have to be included in refinement. The relationship between three monoclinic domains and hexagonal unit cell is plotted in Fig.5.6. The unit cell of the three monoclinic domains is constructed by the following cell transformation matrices:

$$\textbf{domain}\quad 1: \qquad \begin{aligned} \mathbf{a}_1 &= \mathbf{a}_h \\ \mathbf{b}_1 &= \mathbf{a}_h + 2\mathbf{b}_h \\ \mathbf{c}_1 &= (-\mathbf{a}_h + \mathbf{c}_h)/3 \end{aligned}$$

$$\textbf{domain}\quad 2: \qquad \begin{aligned} \mathbf{a}_2 &= \mathbf{b}_h \\ \mathbf{b}_2 &= 2\mathbf{a}_h - \mathbf{b}_h \\ \mathbf{c}_2 &= (-\mathbf{b}_h + \mathbf{c}_h)/3 \end{aligned}$$

$$\textbf{domain}\quad 3: \qquad \begin{aligned} \mathbf{a}_3 &= -\mathbf{a}_h - \mathbf{b}_h \\ \mathbf{b}_3 &= \mathbf{a}_h - \mathbf{b}_h \\ \mathbf{c}_3 &= (\mathbf{a}_h + \mathbf{b}_h + \mathbf{c}_h)/3 \end{aligned}$$

where $\mathbf{a}_i$, $\mathbf{b}_i$, $\mathbf{c}_i$, $i = 1,2,3$ are the unit cell axis for three monoclinic domains and $\mathbf{a}_h$, $\mathbf{b}_h$, $\mathbf{c}_h$ are the unit cell axis for rhombohedral structure in a hexagonal setting. Based on the unit cell relationship, the reflections should be converted to a monoclinic setting. In order to convert the observed reflections (h,k,l) from a hexagonal cell to monoclinic unit cell, the following matrices based on the unit cell transformation matrices are used to index them in three $C2/m$ domains:

$$\textbf{domain}\quad 1: \qquad \begin{bmatrix} 1 & 1 & -1/3 \\ 0 & 2 & 0 \\ 0 & 0 & 1/3 \end{bmatrix}$$

$$\textbf{domain}\quad 2: \qquad \begin{bmatrix} 0 & -2 & 0 \\ 1 & -1 & -1/3 \\ 0 & 0 & 1/3 \end{bmatrix}$$

$$\textbf{domain}\quad 3: \qquad \begin{bmatrix} -1 & -1 & 1/3 \\ -1 & -1 & 1/3 \\ 0 & 0 & 1/3 \end{bmatrix}$$

It should be mentioned here that there exists 122 reflections that could be not indexed by any of the monoclinic domains, for instance (1,1,9) reflection, which highly suggests the low temperature space group is not $C2/m$. In order to compare these two models, a test refinement of these reflections that could be indexed by $C2/m$ model was also performed. The refinement of these two structure models was also performed in Jana2006.

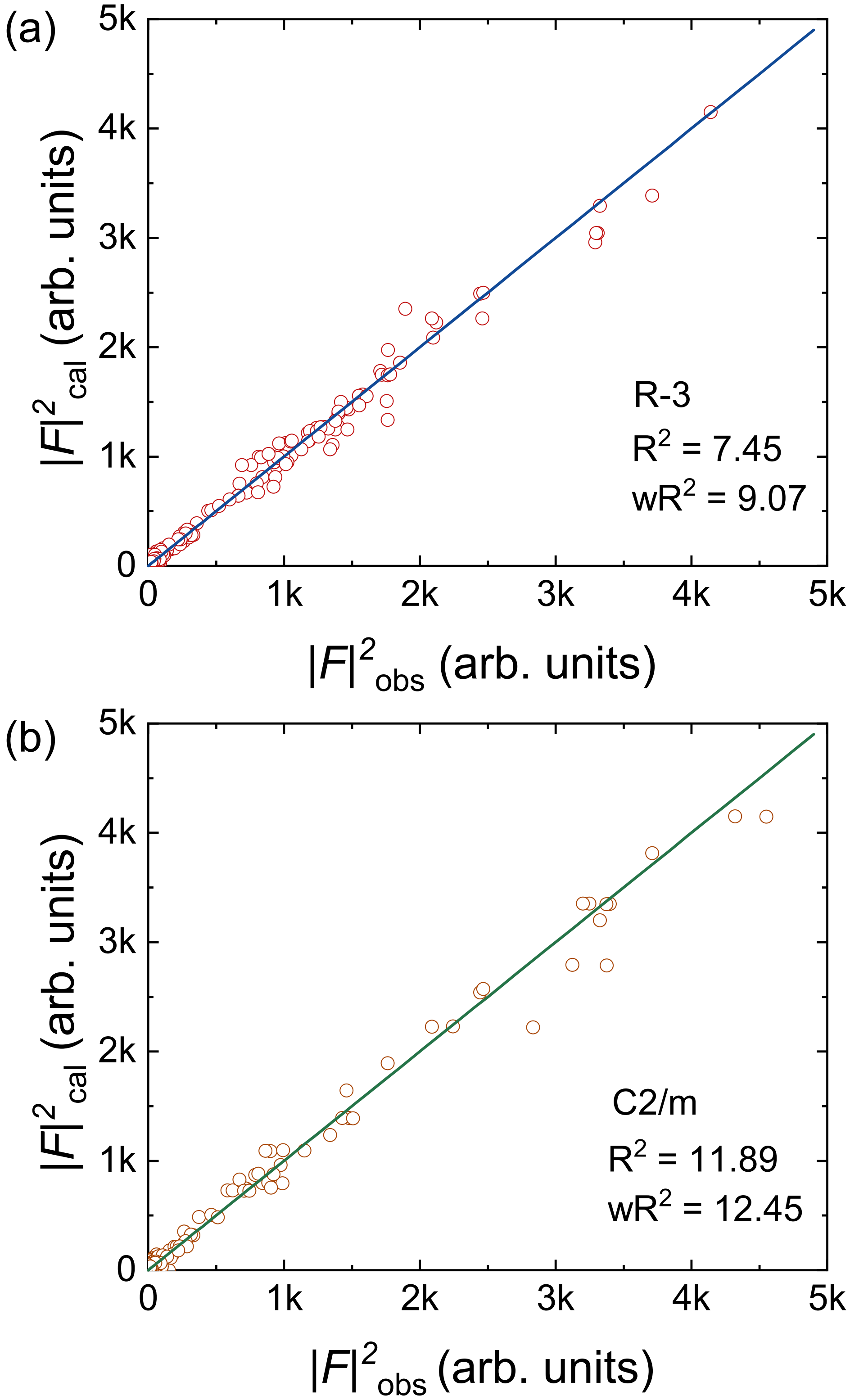

Figure 5.7: Calculated square of structure factors $|F|^2_{cal}$ versus observed square of structure factors $|F|^2_{obs}$ in $R\overline{3}$ in $C2/m$ and $R\overline{3}$ models. $|F|^2_{obs}$ was obtained from the single crystal neutron diffraction measurements at T = 2 K. (a) Observed square of structure factor square $|F|^2_{obs}$ versus calculated ones for $R\overline{3}$ structure model. (b) Observed square of structure factor square $|F|^2_{obs}$ versus calculated $|F|^2_{cal}$ for $C2/m$ structure model.

In Jana2006, all the reflections (h, k, l) are firstly indexed by the domain 1 and then reflections from the left two domains are calculated by the following domain laws in Jana2006:

$$\textbf{domain} \quad 2: \quad \begin{bmatrix} -1/2 & -3/2 & 1/2 \\ 1/2 & -1/2 & -1/6 \\ 0 & 0 & 1 \end{bmatrix}$$

and

$$\textbf{domain} \quad 3: \quad \begin{bmatrix} -1/2 & 3/2 & 1/2 \\ -1/2 & -1/2 & 1/6 \\ 0 & 0 & 1 \end{bmatrix}$$

.

Table 5.1: α-RuCl$_3$ structure refinement results from neutron single crystal diffraction data collected at HEiDi at MLZ based on $R\overline{3}$ structure model at 2 K.

Atom	Site	x	y	z	*Occ.*
Ru	$6c$	0	0	0.3332(3)	1
Cl	$18f$	0.3203(4)	0.3356(4)	0.4114(8)	1
Occ. is atom occupation:					
ADP harmonic parameters:					
	U_{11} (Å^2)	U_{22} (Å^2)	U_{33} (Å^2)		
Ru	0.0033(10)	0.0033(10)	0.0107(14)		
Cl	0.0063(9)	0.0040(8)	0.0069(5)		
	U_{12} (Å^2)	U_{13} (Å^2)	U_{23} (Å^2)		
Ru	0.0016(5)	0	0		
Cl	0.0029(7)	0.0021(5)	-0.0007(4)		
twin populations for reverse and obverse twins: 0.44(4)					
lattice parameters: $a = b = 5.97(3)$ Å, $c = 16.93(6)$ Å					
$R(obs) = 7.45\%$, $R_w(obs) = 9.07\%$, $R_w(all) = 9.46\%$					
The observed reflections are those reflections with $I/sigma \geq 3$.					

Table 5.2: α-RuCl$_3$ structure refinement results from neutron single crystal diffraction data collected at HEiDi at MLZ based on $C2/m$ structure model at 2 K.

Atom	Site	x	y	z	$Occ.$	U_{iso} (Å^2)
Ru	$4g$	0	0.3343(5)	0	1	0.0057(9)
Cl1	$8j$	0.7447(10)	0.1748(3)	0.7643(4)	1	0.0062(7)
Cl2	$4i$	0.7278(11)	0	0.2348(5)	1	0.0062(7)
three monoclinic domain populations: 0.319(5); 0.302(2)						
a = 5.97(3) Å, b = 10.34(6) Å, c = 5.98(3) Å, β = 109.4(3)°						
$R(obs)$ = 11.89%, $R_w(obs)$ = 12.45%, $R_w(all)$ = 12.98%						
The observed reflections are those reflections with $I/sigma \geq 3$.						

Since some of the reflections like (0,0,3n), (3n,0,0) and (3n,0,3n) belong to multiple domains, with these reflections the domain population can be well refined. The calculated square of structure factors versus observed square of structure factors are shown in Fig.5.7 and the refined parameters are summarised in Tab.5.1 and Tab.5.2. The refined R value for $R\overline{3}$ is 7.45%, much better than 11.89% for $C2/m$ model. The refined twin population is 0.44(4) for $R\overline{3}$, which is close to 0.5, the theoretical ratio for obverse and reverse twins in rhombohedral structure. The result demonstrates that even for these reflections could be indexed in the monoclinic model, their calculated intensities do not match with the observed ones. The results strongly prove that the low temperature crystal structure is $R\overline{3}$ for α-RuCl$_3$.

5.3.3 Spherical neutron polarisation analysis of magnetic structure

In order to reveal the direction of the ordered magnetic moments of α-RuCl$_3$, spherical neutron polarised study was performed. The principles of the spherical neutron polarised experiment are introduced in Sec.3.2.1. Spherical neutron polarisation analysis was performed on the cold three axis spectrometry IN12 in the Institut Laue Langevin, Grenoble. The zero field polarimeter Croypad was installed on IN12 for the collection of polarisation analysis data. A 100 mg high quality α-RuCl$_3$ single crystal grown by chemical vapour transport method was mounted on the ($h0l$) scattering plane. According to previous reports [92, 177], α-RuCl$_3$ orders antiferromagnetically at ∼8 K. There are two proposed magnetic strictures, and both magnetic moments are parallel to the crystallographic axis a or b but tilted from ab basal plane by 35° and 48°, respectively. Here they are denoted as model II and model III, and model I is for the magnetic structure in this work. The propagation vector is $\boldsymbol{k} = (0, 0.5, 1)$, and by performing irreducible representation analysis, the star of the $\boldsymbol{k}$ contains three arms: $\boldsymbol{k}_1 = (0, 0.5, 1)$, $\boldsymbol{k}_2 = (0.5, \overline{0.5}, 1)$ and $\boldsymbol{k}_3 = (\overline{0.5}, 0, 1)$, which will give rise to separate magnetic reflections from every configuration magnetic domain. Besides, since the magnetic reflections are also totally separated from nuclear reflection, the nuclear-magnetic interference effect is not considered. Therefore, the magnetic reflections (±0.5,0,±L) in this experiment come from one single domain and their polarisation matrix can be calculated from the formula in matrix 5.1.

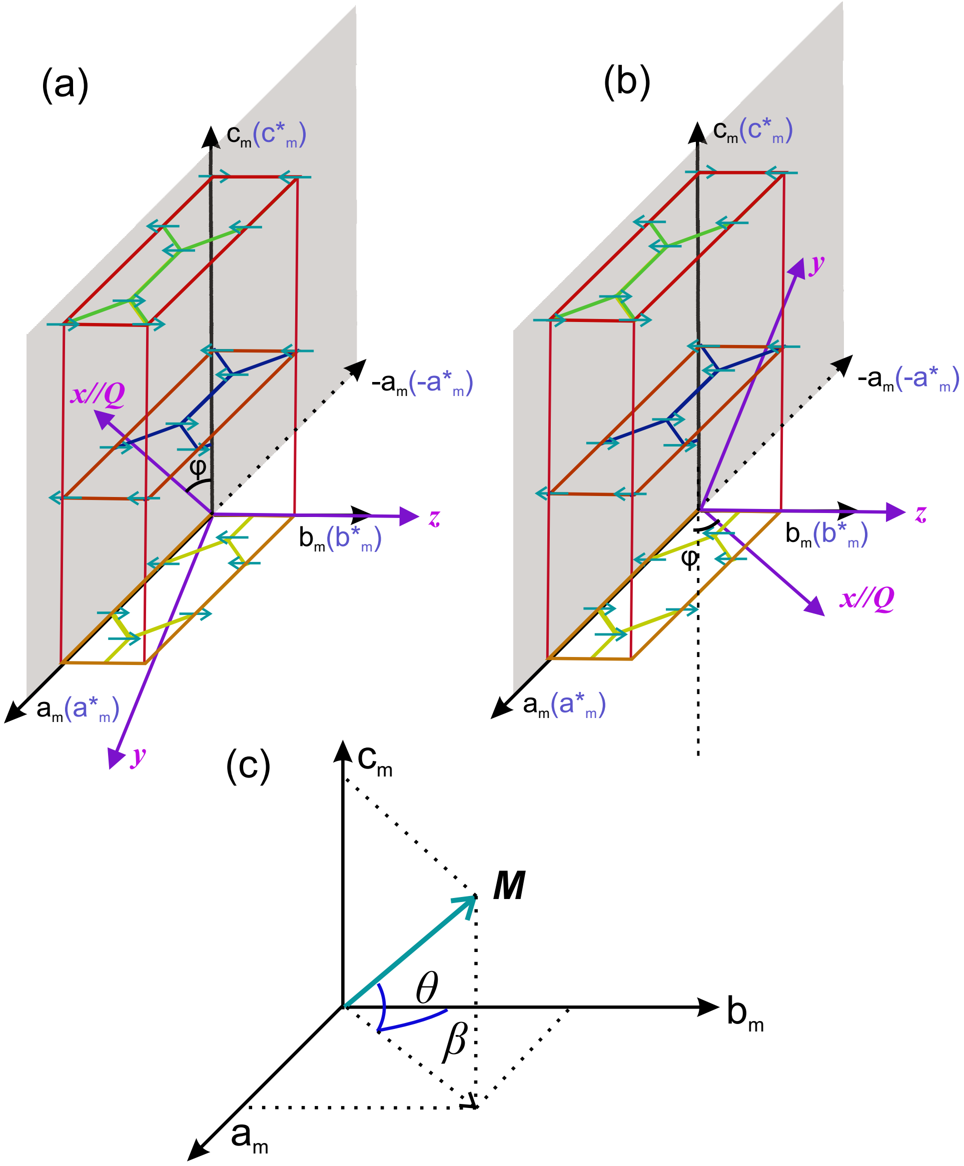

Figure 5.8: (a) and (b) Scattering geometry of the experiment for the magnetic reflections (+0.5,0,+L) and (-0.5,0,-L). An auxiliary magnetic unit cell is built from the $R\bar{3}$ parent structure with $\mathbf{a}_m = 2\mathbf{a}_h + \mathbf{b}_h$, $\mathbf{b}_m = \mathbf{b}_h$, $\mathbf{c}_m = \mathbf{c}_h$ and $\alpha = \beta = \gamma = 90°$. The scattering plane is $(h0l)$, where the polarisation direction x is parallel to scattered vector $\mathbf{Q}$ and the polarisation direction z which is along $\mathbf{c}_m$ is perpendicular to the scattering plane. φ is the angle between x and c^*. (c) The direction of the magnetic moment of Ru^{3+} in the auxiliary unit cell is plotted with assuming that the magnetic moment $\mathbf{M}$ is inclined from the c_m axis by angle $(90 - \theta)$ and the b_m axis by angle β.

$$\begin{pmatrix} \frac{p_0\mathbf{M}_\perp^2 - J_{yz}}{I_x} & \frac{-J_{yz}}{I_y} & \frac{-J_{yz}}{I_z} \\ 0 & \frac{p_0\left(\mathbf{M}_{\perp y}^2 - \mathbf{M}_{\perp z}^2\right)}{I_y} & \frac{p_0 R_{yz}}{I_z} \\ 0 & \frac{p_0 R_{yz}}{I_y} & \frac{p_0\left(-\mathbf{M}_{\perp y}^2 + \mathbf{M}_{\perp z}^2\right)}{I_z} \end{pmatrix} \tag{5.1}$$

In order to analyse the data, an auxiliary magnetic unit cell is setup for assistance. This auxiliary magnetic unit cell is constructed based on our new refined crystal structure and the magnetic unit cell. The scattering geometry in our experiment can be summarized in Fig.5.8, where in the auxiliary magnetic unit cell, the base is defined as: $\mathbf{a}_m = 2\mathbf{a}_h + \mathbf{b}_h$, $\mathbf{b}_m = \mathbf{b}_h$, $\mathbf{c}_m = \mathbf{c}_h$ and $\alpha = \beta = \gamma = 90°$. The magnetic reflections (0.5,0,L) are indexed by (1,0,L) in the auxiliary magnetic unit cell, but for convenience, the (0.5,0,L) index in the hexagonal cell is still used in this thesis.

The scattering plane is ($h0l$), and as shown in Fig.5.8 (a) and (b) the polarisation direction x is parallel to scattering vector $\mathbf{Q}$ strictly. z is perpendicular to the scattering plane and y is the third direction in a right-handed orthogonal coordinate system as mentioned before. The magnetic components projection along different polarised directions are calculated. First, the magnetic moment in a spherical coordinates is defined. For each magnetic reflection, φ is the angle between x polarisation direction or $\mathbf{Q}$ and c_m^* in Fig.5.8 (c). The direction of magnetic moment of Ru^{3+} in the auxiliary unit cell is shown in Fig.5.8(a), assuming that the magnetic moment $\mathbf{M}$ is inclined from the c_m axis by angle $(90° - \theta)$ and the b_m axis by angle β. Apparently in model II and model III, β equals 0°. For a magnetic reflection (0.5,0,L), the expressions for the components of the magnetic interaction vectors $\mathbf{M}_\perp$ along each polarisation axis are summarized in Tab.5.3.

Table 5.3: Components of the magnetic interaction vectors $\mathbf{M}_\perp$ on three polarisation axes for (0.5,0,L) magnetic reflection.

	Magnetic components
$\mathbf{M}_{\perp x}$	0
$\mathbf{M}_{\perp y}$	$-\mathbf{M}_\perp sin(\theta) sin(\varphi) + \mathbf{M}_\perp cos(\theta) sin(\beta) cos(\varphi)$
$\mathbf{M}_{\perp z}$	$\mathbf{M}_\perp cos(\theta) cos(\beta)$

For the experiment, the strong magnetic reflections were firstly checked for the measurement of the polarisation matrix. Since the propagation vector is $\mathbf{k} = (0, 0.5, 1)$, the magnetic reflection will appear at (0.5,0,L) (L $\neq$ 3n) positions. The rocking curves (A3 scan, A3 is the sample rotation at IN12) of each reflection is depicted in Fig.5.9 (a). The low $\mathbf{Q}$ magnetic reflection (0.5,0,1) is very strong and the (0.5,0,4) reflection is relatively weak due to the strong magnetic form factor fall-off at large $\mathbf{Q}$. In this regard, four peaks (0.5,0,1), ($\overline{0.5}$,0,$\bar{1}$), (0.5,0,2), (0.5,0,4) are chosen for this measurement. To take data of each term in the polarised matrix, firstly move the instrument to the peak maximum and count 10 min. After that rotate the sample by

±5° and measure 5 mins for (A3 + 5)° and (A3 - 5)° for background (A3 is sample rotation at IN12).

The real intensity could be calculated by subtracting the background from the intensity of the peak maximum. After measurement of each term of matrix 5.1, one can fit the value of θ and β by the the least squares method. It should be mentioned here that because the magnetic reflections do not coincide with the nuclear reflections, the amplitude of the magnetic moment cannot be decided but the relationship between ordered magnetic moment and crystallographic axis could be measured precisely. Fig.5.9 (b-f) also summarizes the **Q**-scan of magnetic refection ($\overline{0.5}$,0,$\overline{1}$) in xx, yx, yy, yz and zz channels at 2 K. The magnetic reflections have different intensity in xx, yy, yz and zz channels for spin up and spin down states of the scattered polarised neutron beams, and for yx channel the intensities for spin up and and spin down states of the scattered polarised neutron beam are same because there is no nuclear and magnetization interaction.

The calculated polarisation $\mathcal{P}_{ij}$ versus measured ones are illustrated in Fig.5.10. The best fitting result with $\chi^2 = 0.127$ is shown in Tab.5.4, where $\beta = -12(2)^\circ$ and $\theta = 17(3)^\circ$.

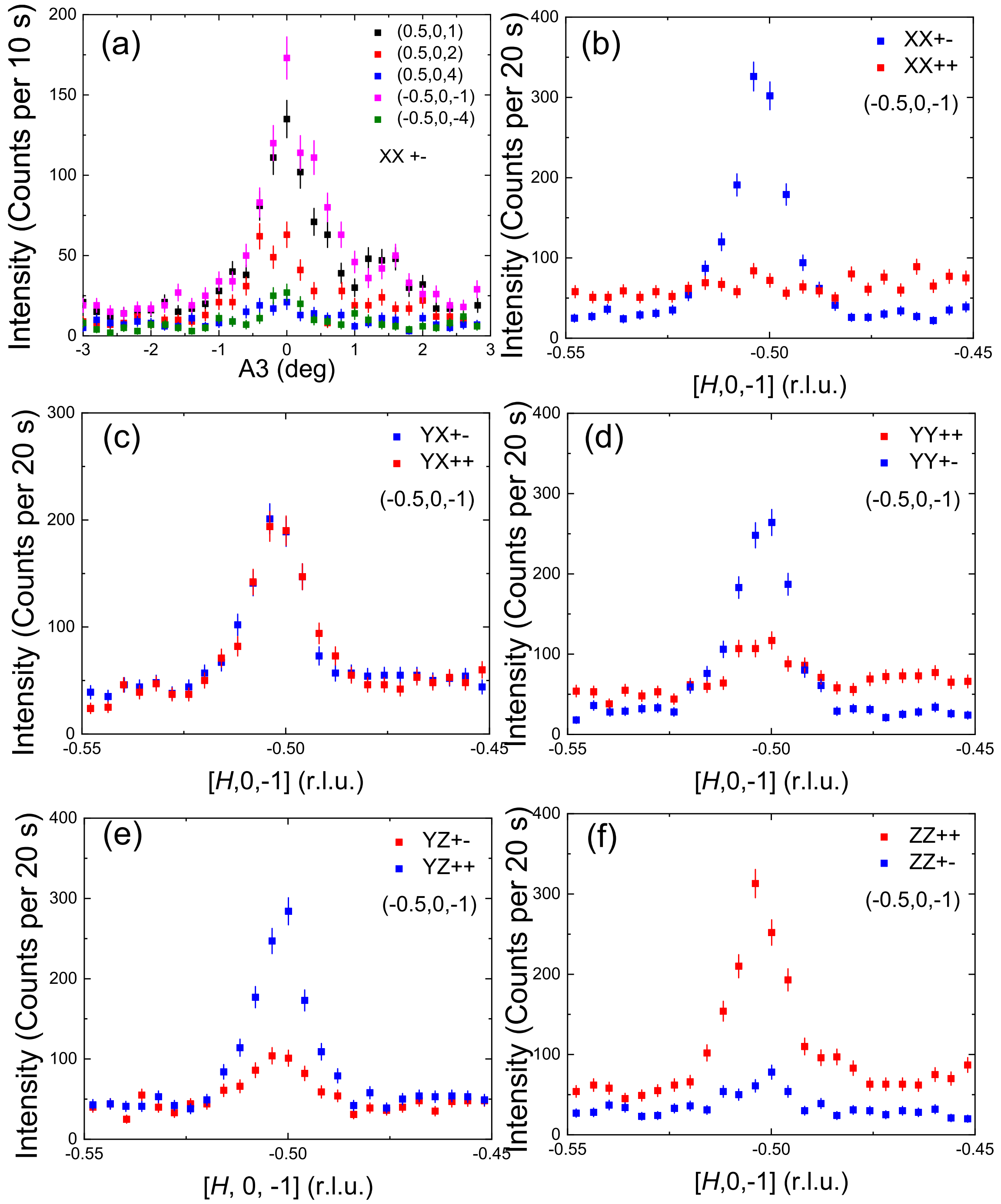

Figure 5.9: Raw data of the A3 scans of the magnetic reflections in different channels. (a) A3 scan of magnetic reflections (0.5,0,1), (0.5,0,2), (0.5,0,4), ($\overline{0.5}$,0,$\bar{1}$) and ($\overline{0.5}$,0,$\bar{4}$) at XX+- channel. (b)-(f) **Q**-scan along [**H**,0,$\bar{1}$] (r.l.u) in various spin polarised channels at 1.5 K measured at IN12.

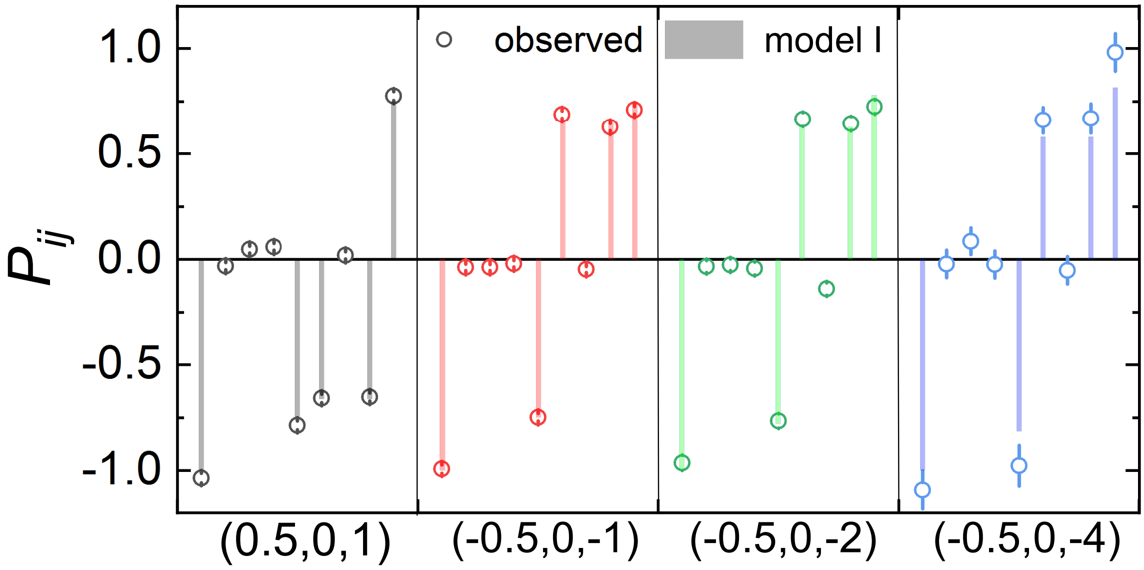

Figure 5.10: Comparison between calculated polarisation elements $\mathcal{P}_{ij}$ (dashes) based on Model I and measured ones (circles with error bars) for magnetic reflections (0.5,0,1), ($\overline{0.5}$,0,$\bar{1}$), ($\overline{0.5}$,0,$\bar{2}$) and ($\overline{0.5}$,0,$\bar{4}$) at IN12 at 1.5 K. From left to right, for each reflection the polarisation terms are in the following sequence: $\mathcal{P}_{xx}$, $\mathcal{P}_{xy}$, $\mathcal{P}_{xz}$, $\mathcal{P}_{yx}$, $\mathcal{P}_{yy}$, $\mathcal{P}_{yz}$, $\mathcal{P}_{zx}$, $\mathcal{P}_{zy}$ and $\mathcal{P}_{zz}$. Data was obtained at 1.5 K at IN12 at ILL, Grenoble.

Table 5.4: The χ^2 is defined as $\chi^2 = \sum_{ij} \left(\mathcal{P}_{ij}\left(calculated\right) - \mathcal{P}_{ij}\left(measured\right)\right)^2$ in this experiment. Comparison of refined χ^2 for three magnetic structure models with different β and θ [92, 177]. The minus sign of β indicates it has opposite rotation direction compared to the assuming value. Model I in this work was obtained at 1.5 K at IN12 at ILL, Grenoble.

	Model I (our work)	Model II	Model III
$\beta(°)$	-12(2)	0	0
$\theta(°)$	17(3)	35	48(3)
χ^2	0.127	0.686	3.168

Details of the tilted magnetic moment in the honeycomb lattice of α-RuCl$_3$ are shown in Fig.5.11 (a). This result indicates the magnetic moment does not only tilt from the hexagonal ab basal plane but also tilts from the crystallographic axis a or b. The χ^2 for model II and model III is calculated, which are 0.686 and 3.168, respectively (see Tab.5.4). Besides, assuming the value of β is zero, the best fitted θ is 27°, with a large $\chi^2 = 0.294$. Fig.5.11 (b) shows the direction of the magnetic moment in the local xyz orthogonal coordination system. According to theoretical calculation, the tilt of the magnetic moment is probably as a result of the large off-diagonal exchange term in the spin Hamiltonian [182, 183] and the result in this work calls for further quantum chemistry calculation for a better understanding of the Kitaev physics in α-RuCl$_3$.

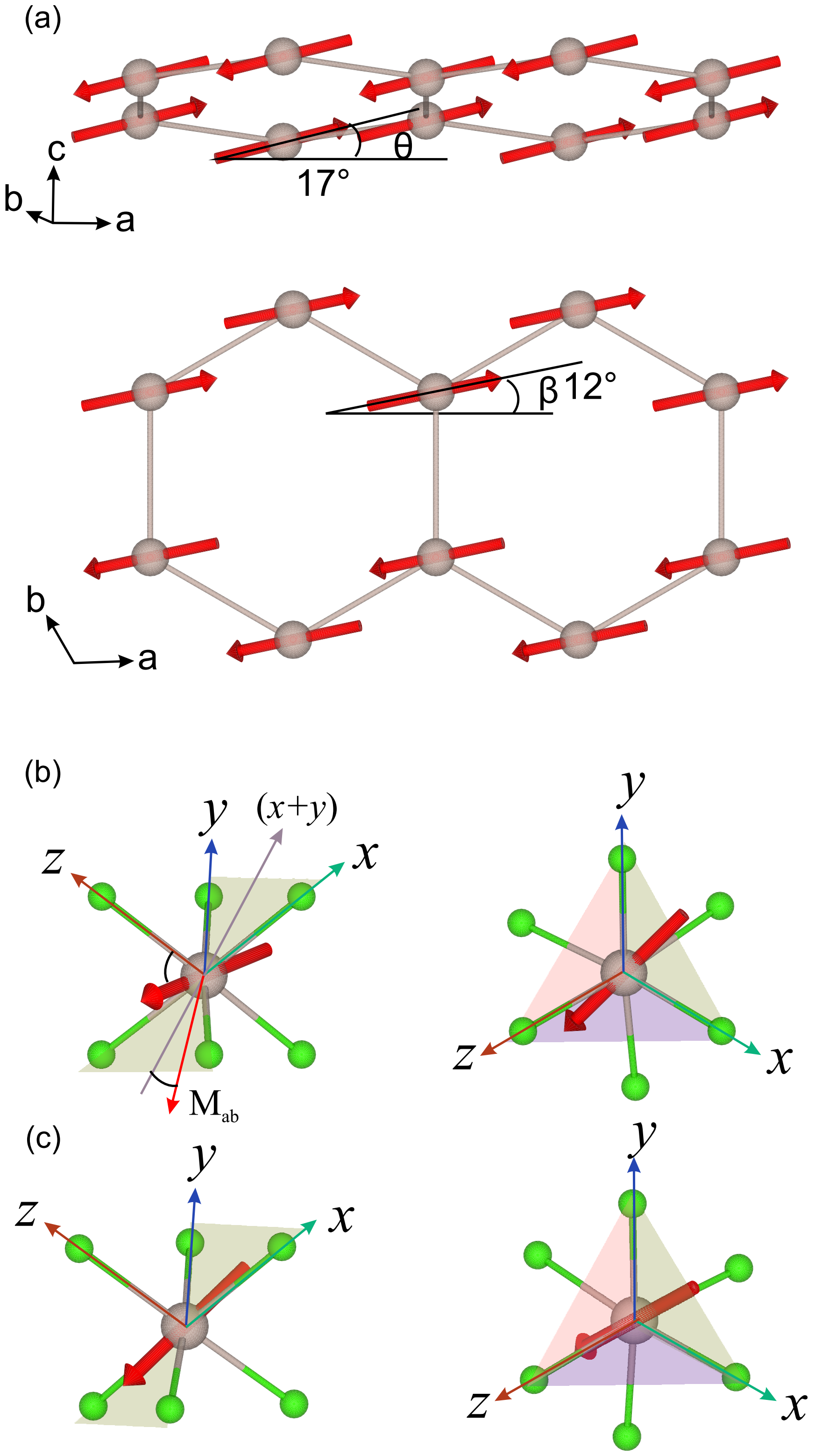

Figure 5.11: (a) Illustration of magnetic structure refined from the spherical neutron polarisation data at 1.5 K obtained from IN12. (b) and (c) the direction Magnetic moment of Ru^{3+} are depicted in a local rectangular coordination xyz for model I and model II and III. This local coordinate system has been introduced in Fig.2.13.

5.4 Neutron diffraction study of α-RuCl$_3$ under isostatic pressures

It has been well proved that pressure is an effective way to tune the magnetic order in Kitaev materials by previous experiments since it changes the lattice parameter directly [184, 185]. In case of α-RuCl$_3$, there has been many studies of its magnetic order under isostatic pressures [178, 181, 186–194]. Heat capacity measurements show that the zigzag order transition temperature increases slowly under quasi-isostatic pressures and suddenly disappears at 1 GPa. The magnetization and NMR studies on a AB stacking reveal the phase transition temperature experiences a concave shape in which the phase transition decreases below 0.5 GPa and then grows up till 1.05 GPa. A phase separation happens at 0.5 GPa and the magnetic volume fraction is completely suppressed at 1.05 GPa. This result is similar to the magnetization measurements on a ABC stacking α-RuCl$_3$ sample where the zigzag order keeps constant up to about 0.2 GPa and then it undergoes a pressure induced phase transition into a non-magnetic state. Besides, a symmetry-breaking is observed by optical studies, which is forbidden for the realisation of Kitaev physics.

Up to now, the questions that arise, from an experimental point of view, are:

(a) what is the effect of pressure on the magnetic transition in the low pressure range, and what is the critical pressure for the structural separation in α-RuCl$_3$ if it exists?

(b) In addition, a structural phase transition is found in α-RuCl$_3$ at ambient condition from $\sim$50 K to $\sim$200 K (see Sec.5.3.1). If one applies pressures at room temperature, it means the pressures are applied on another phase (high temperature phase) initially, after the structural transition the pressure will be passed to the phase (low temperature phase) that hosts the antiferromagnetic order. Since the pressure dependence of the structural transition in α-RuCl$_3$ is still unknown and in order to avoid the effects of this structural transition, it will be better to apply the pressure below the structural transition. In order to shed lights on these questions, single crystal neutron diffraction experiment was performed at D10 at ILL, Grenoble to study the *in situ* pressure dependence of magnetic order of α-RuCl$_3$ with isostatic pressures applied at 30 K.

5.4.1 Experiment preparation and setup

A 60 mg high quality α-RuCl$_3$ single crystal sample was prepared for the experiment as shown in Fig.5.12.

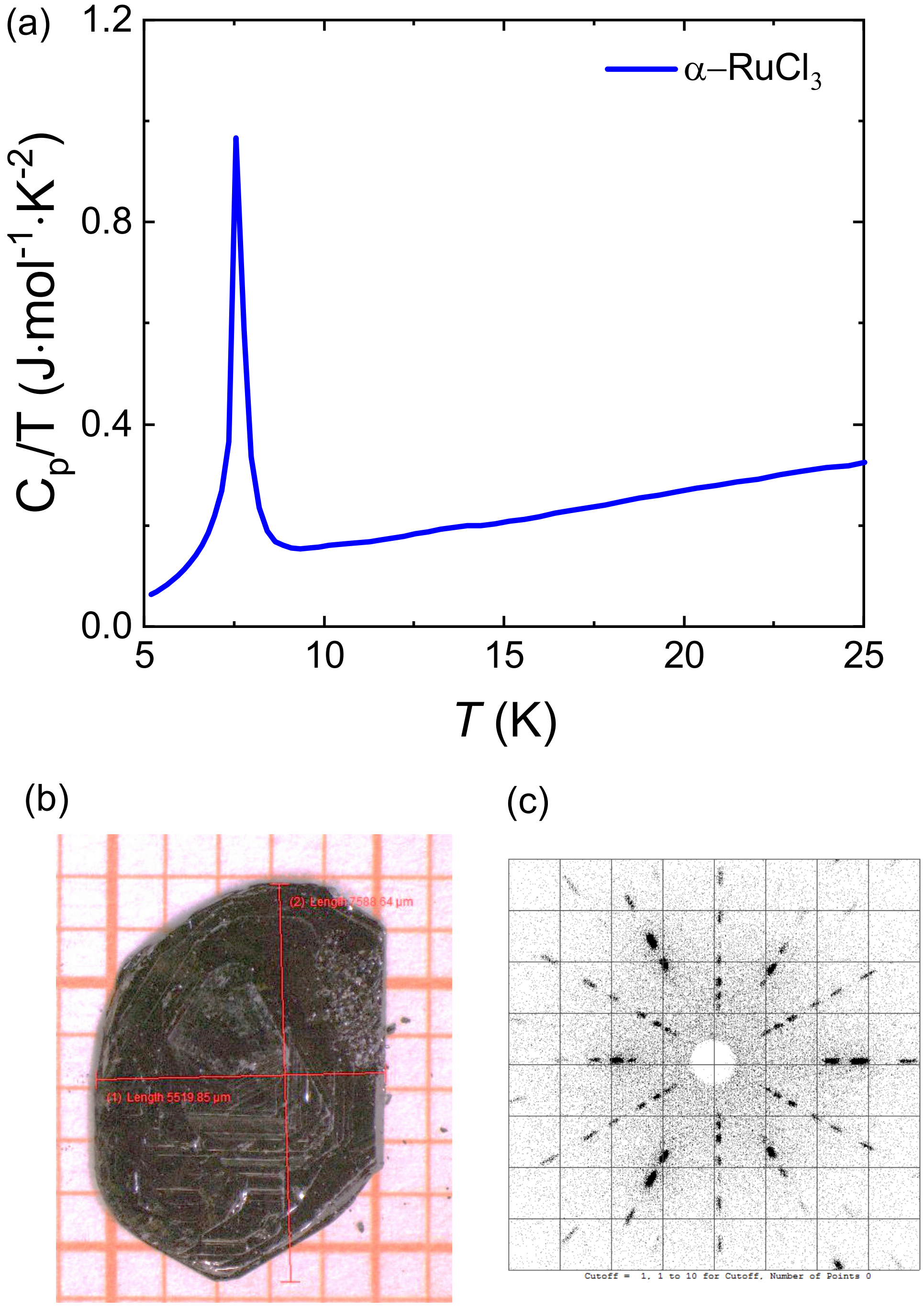

Figure 5.12: (a) Heat capacity of the α-RuCl$_3$ single crystal for the neutron diffraction experiment. There is no obvious anomaly between ∼10 K and ∼ 14 K, proving the high quality of our sample [92] (see sec.5.1). (b) and (c) Picture of the sample and its X-ray Laue diffraction result. The Laue picture shows sharp peaks and the three-fold symmetry.

In Fig.5.12 (a), the heat capacity of a cleaved small part of the sample demonstrates there is only one sharp magnetic phase transition at T_N = ∼8 K, proving there is a low stacking fault density in the sample. The quality of the sample was also checked by X-ray Laue by scanning the surface of the crystal and a typical picture of the sample shows sharp peaks and three-fold symmetry. Single Crystal neutron diffraction experiment was carried out on the four cycle diffractometer D10 at Institut Laue-Langevin, Grenoble.

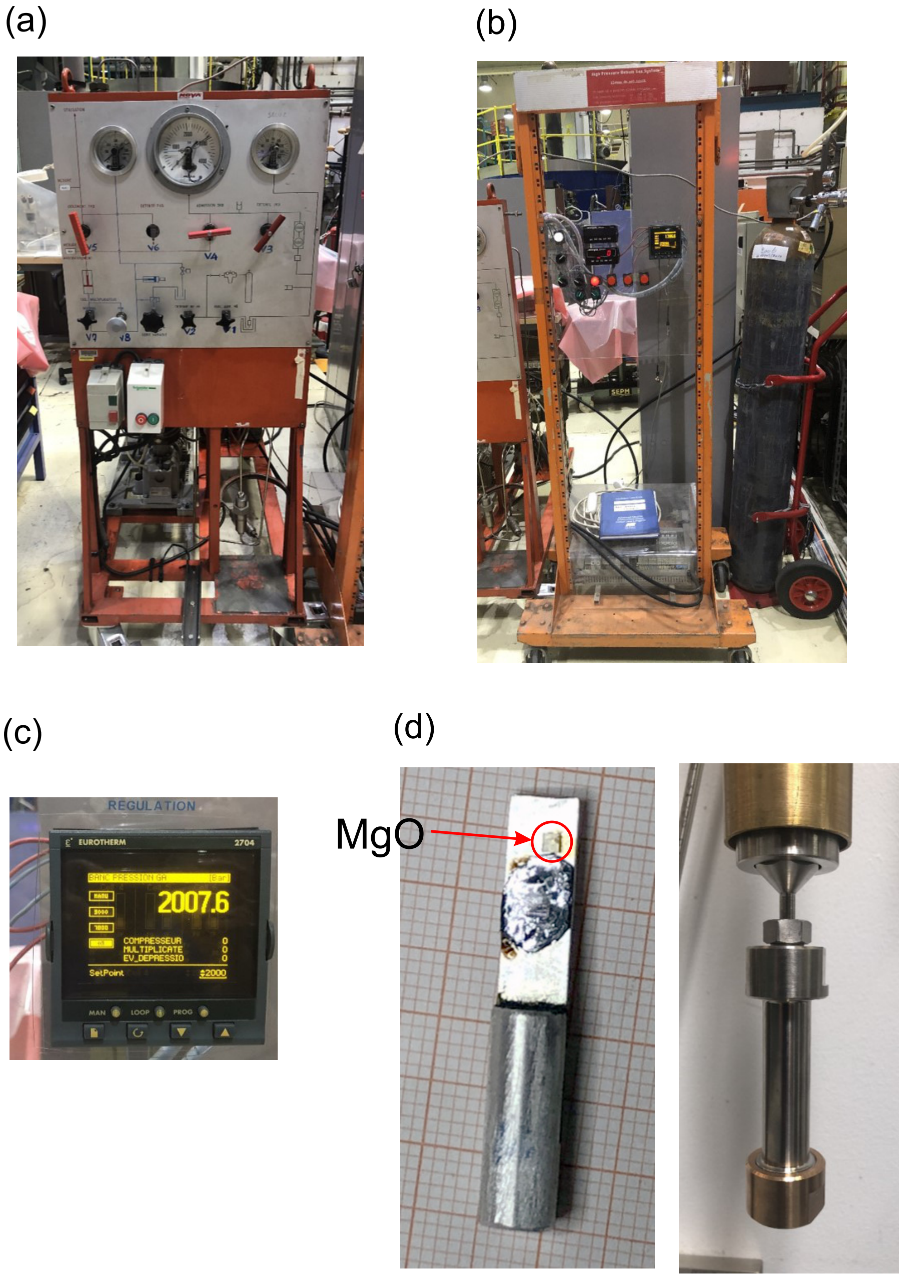

Figure 5.13: Experiment equipments for the isostatic pressure experiment at D10 at ILL, Grenoble. (a) Controller of pressure of the helium compressor. (b) and (c) Gauge of helium pressure. (d) Samples and the sample holder, where an additional MgO single crystal was glued next to the sample for the pressure calibration.

The isostatic pressure was generated with a gas compressor with helium gas acting as a pressure medium. A gaseous pressure transmit would ensure the pressure applied on the sample was always isostatic. As shown in Fig.5.13 (a) and (b), the pressure could be adjusted continuously by the valves. There was a pressure gauge close to the sample, which measured the gas pressure in the sample chamber and displayed it on the digital monitor in Fig.5.13 (c). In order to monitor the pressures in the sample chamber, a gas pressure gauge was also installed on the top of the Orange cryostat to measure the pressure of the helium gas. As illustrated in Fig.5.13 (d), the α-RuCl$_3$ single crystal sample was glued to the holder by GE varnish (type GE 7031) and a MgO single crystal was also mounted close to the sample to measure the pressure near the sample.

5.4.2 Magnetic phase transition under isostatic pressures

First the sample was cooled down to base temperature 1.5 K and the intensity of the magnetic reflections were checked. At D10, there were two detectors, one was a 2D detector which had relatively large detecting area, and another one was a point detector with the analyser, which would help reduce the background. For alignment, the nuclear reflections were collected by the 2D detector. After that, the magnetic reflections were measured by the point detector with analyser. Four magnetic reflections were found at 1.5 K as plotted in Fig.5.14, in which the magnetic reflection (0.5,0,1) was strongest, so the intensity of this peak was measured to study the magnetic order of α-RuCl$_3$ under various isostatic pressures.

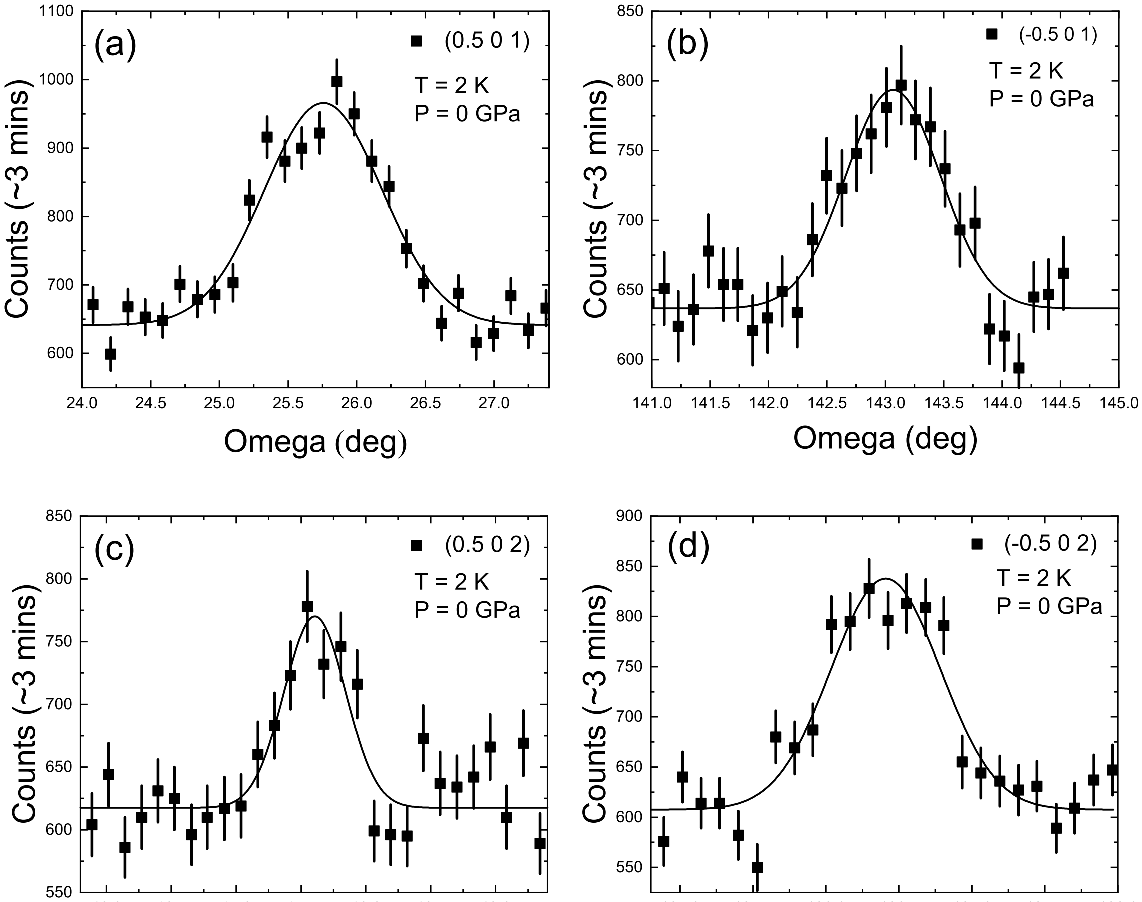

Figure 5.14: Rocking curves of magnetic reflections (0.5,0,1), ($\overline{0.5}$,0,1),(0.5,0,2) and ($\overline{0.5}$,0,2) under zero pressure measured at 2 K at D10 at ILL, Grenoble.

For the study of the pressure dependence of the transition temperature, the sample was first cooled down to 1.5 K with pressure applied and the temperature dependence of the intensity (peak maximum) of the magnetic peak (0.5,0,1) was measured during heating up the sample step by step. In order to make sure the temperature was stable at the sample, 1 minute before collecting data was waited. After finishing the measurement at one pressure, the sample was warmed up to 30 K slowly and the pressure increased by the external helium gas compressor gradually and slowly. This ensured the pressure was applied in the paramagnetic state of α-RuCl$_3$ and also far below the structural transition. For each pressure, the sample was re-aligned individually to ensure the sample was always in the scattering centre.

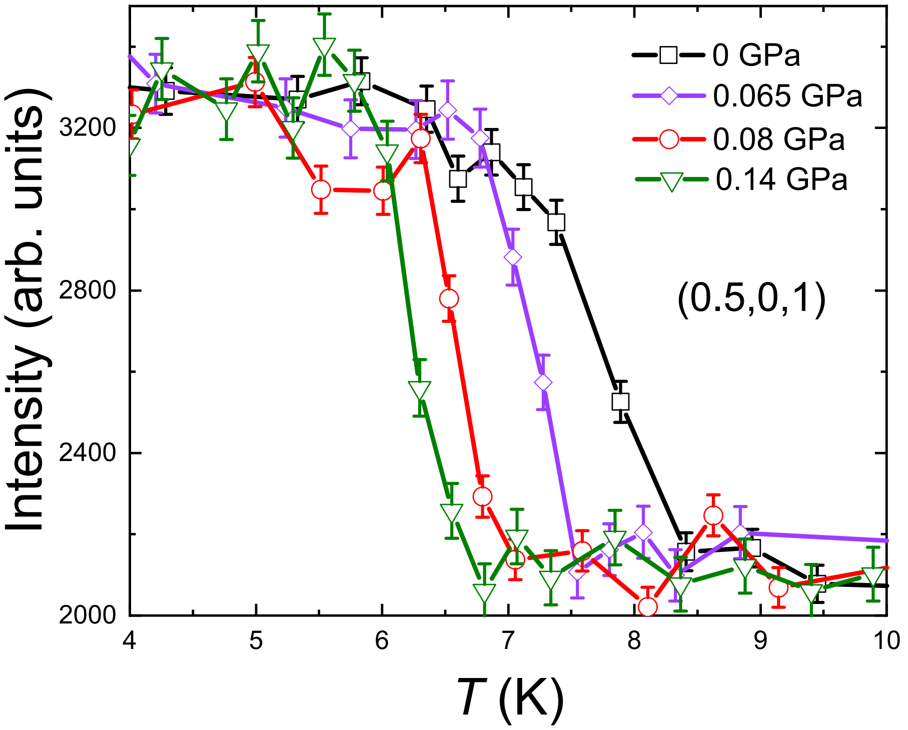

Figure 5.15: Temperature dependence of peak intensity of magnetic Bragg reflection (0.5,0,1) under various isostatic pressures obtained at D10 at ILL, Grenoble.

The temperature dependence of the peak intensity of magnetic reflection (0.5,0,1) under different pressures is depicted in Fig.5.15. The temperature dependence curve can be fitted by the power critical law:

$$I = A\left(\frac{T_N - T}{T_N}\right)^{2\beta} + bg, \tag{5.2}$$

where T_N, β is magnetic phase transition temperature and fitted critical exponent; bg is background.

At zero pressure the zigzag antiferromagnetic transition happens at 7.91(5) K consistent with our heat capacity measurement and similar experiment on other samples with ABC stacking sequence [92, 177]. It is evident that the antiferromagnetic transition temperature decreases systematically as a function of increasing pressures in Fig.5.15. This can be further confirmed by the comparison of **Q**-scan along [1,0,0] (r.l.u.) direction (**H** scan) and [0,0,1] (r.l.u) direction (**L** scan) for the magnetic reflection (0.5,0,1) under 0.065 GPa and 0.14 GPa at 7 K in Fig.5.16. The (0.5,0,1) magnetic reflection can be clearly observed at 0.065 GPa while it is completely suppressed at 0.14 GPa at 7 K because the transition temperature has been shifted from 7.29(5) K at 0.065 GPa to 6.30(3) K at 0.14 GPa. Fig.5.17 presents the rocking curves of (0.5,0,1) magnetic reflection at 10 K and 2 K for 0.065 GPa, 0.14 GPa and 0.16 GPa, respectively. The left picture is the nuclear reflection ($\overline{3}$,0,0) measured by the 2D detector. As for 0.065 GPa and 0.14 GPa, the data was collected by the high resolution analyser at D10. For a good counting statistics, each point was measured 6 minutes and the zigzag magnetic order was observed for both pressures at 2 K. And for the pressure 0.16 GPa, every point was measured about 20 minutes by integrating the intensities from the 2D detector. It is clear that there is no evidence for the appearance of the magnetic reflection (0.5,0,1) of the zigzag order at 2 K under 0.16 GPa. This result is quite inspiring because following the large linear slope of -11.5 K/GPa from 0 GPa to 0.14 GPa, it can be deduced that the antiferromagnetic order could be fully suppressed by a small pressure $\sim$0.7 GPa and the sample may attain a quantum spin liquid state. However this is not realised in this experiment because a pressure induced structural transition occurs at a larger pressure.

In addition, from the 2D data, it is clear that reflection ($\overline{3}$,0,0) is quite sharp and strong for 0.065 GPa and 0.14 GPa, but at 0.16 GPa this reflection has become quite broad and fuzzy as shown in Fig.5.17. The evolution of ($\overline{3}$,0,0) reflection under pressures implies crystal structure of α-RuCl$_3$ gradually becomes another phase at the high pressure.

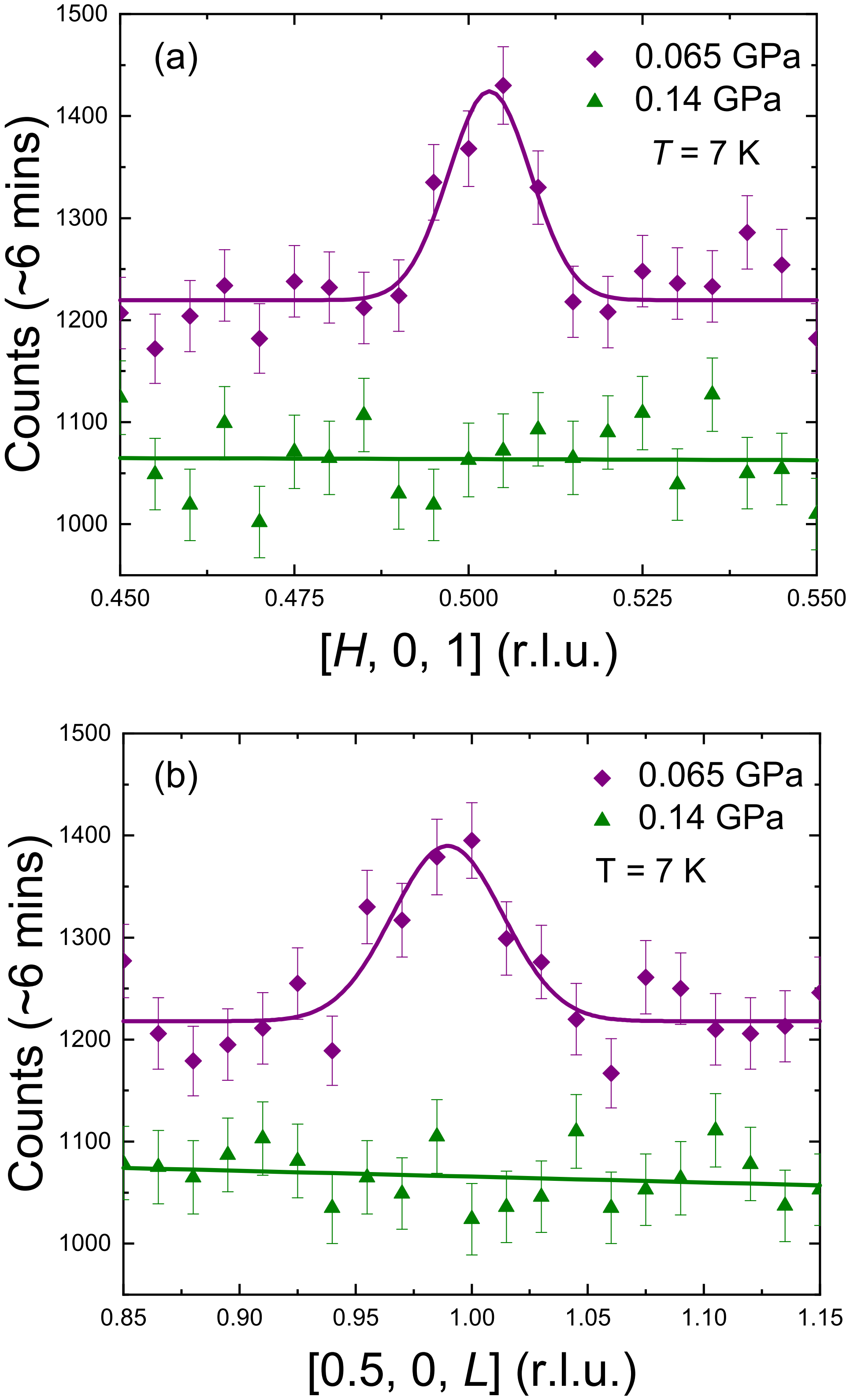

Figure 5.16: (a) and (b) **H** and **L** scans for magnetic Bragg reflection (0.5,0,1) under 0.065 GPa and 0.14 GP at 7 K obtained at D10 at ILL, Grenoble. The data for 0.065 GPa is raised by 200 counts.

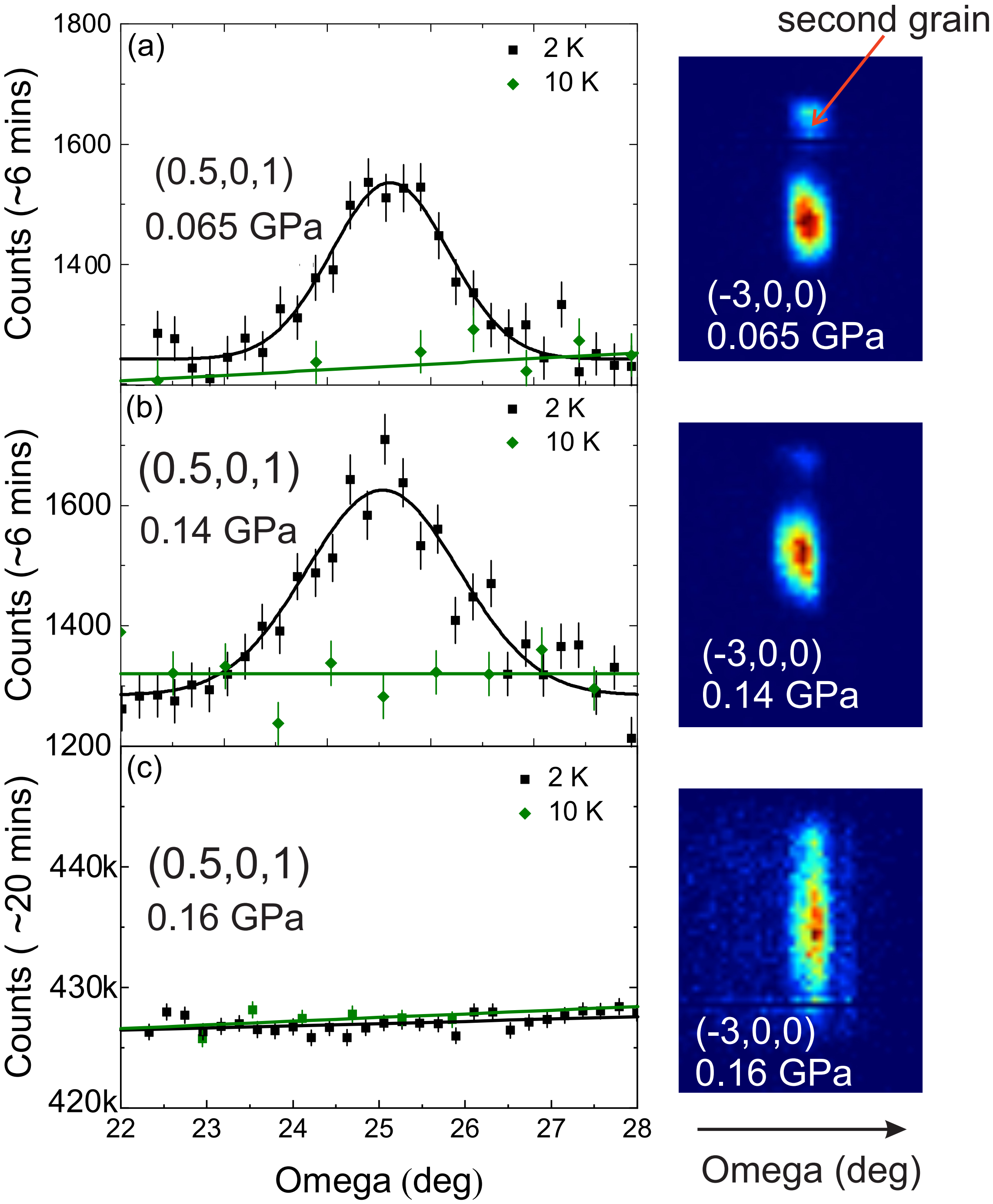

Figure 5.17: Rocking curves of magnetic Bragg reflection (0.5,0,1) under (a) 0.065 GPa , (b) 0.14 GPa, (c) 0.16 GPa for 2 K and 10 K, respectively collected at D10 at ILL, Grenoble. Left: 2D contour maps of nuclear reflection ($\overline{3}$,0,0) under these pressures at 10 K.

In order to reveal the pressure dependence of the structural transition and its critical pressure, the integrated intensity of ($\overline{3}$,0,0) as a function of temperatures and pressures has been studied. The critical pressure test was carried out by increasing pressures gradually at 30 K and monitoring the intensity of nuclear reflection ($\overline{3}$,0,0) at the same time. The result is summarized in

Fig.5.18 (a) by normalising the integrated intensity of each peak with the zero pressure data. It is clear that a drastic drop of the integrated intensity happens at 0.14 GPa. Here the critical pressure P_d is defined as the critical pressure where the ($\bar{3}$,0,0) reflection has the half intensity compared to 0 GPa, which is 0.15 GPa at 30 K.

Fig.5.18 (b) illustrates the temperature dependence of normalised integrated intensity of ($\bar{3}$,0,0) under various pressures. The pressure is loaded at 100 K and after applying the pressures the sample is cooled down slowly along with monitoring the integrated peak intensity of ($\bar{3}$,0,0) by the 2D detector. When the phase transition finishes, the intensity of ($\bar{3}$,0,0) becomes less temperature dependent. The sample is then warmed up again to measure its pressure dependence upon heating. A giant hysteresis loop is found during cooling and warming in the measurement as a signature of the first order transition.

In addition, as shown in Fig.5.18 (b) even at very high pressure the intensity of ($\bar{3}$,0,0) does not completely disappear and the residual intensity decreases upon increasing pressure. For instance, under 0.165 GPa there is still 11% residual intensity at 45 K while under 0.26 GPa it decreases to 8%. Despite that a phase separation picture can explain the residual intensity in this measurement but indeed there is no any indication of the long range magnetic order at 0.16 GPa where the zigzag magnetic reflection is supposed to still have at least 10% intensity. This means as soon as the occurrence of the pressure induced structural transition, the long range zigzag magnetic order has been broken. The result in this work is different from other macroscopic studies where they have observed the coexistence of the magnetic order phase and the pressure induced phase. This may result from the difference in the experiment setup. For all the macroscopic measurement the pressure was applied at room temperature while in this experiment the pressure was applied at 30 K to the magnetic phase that hosts the antiferromagnetic order. Therefore, the sample states will not be affected by any structural transition upon cooling in this measurement.

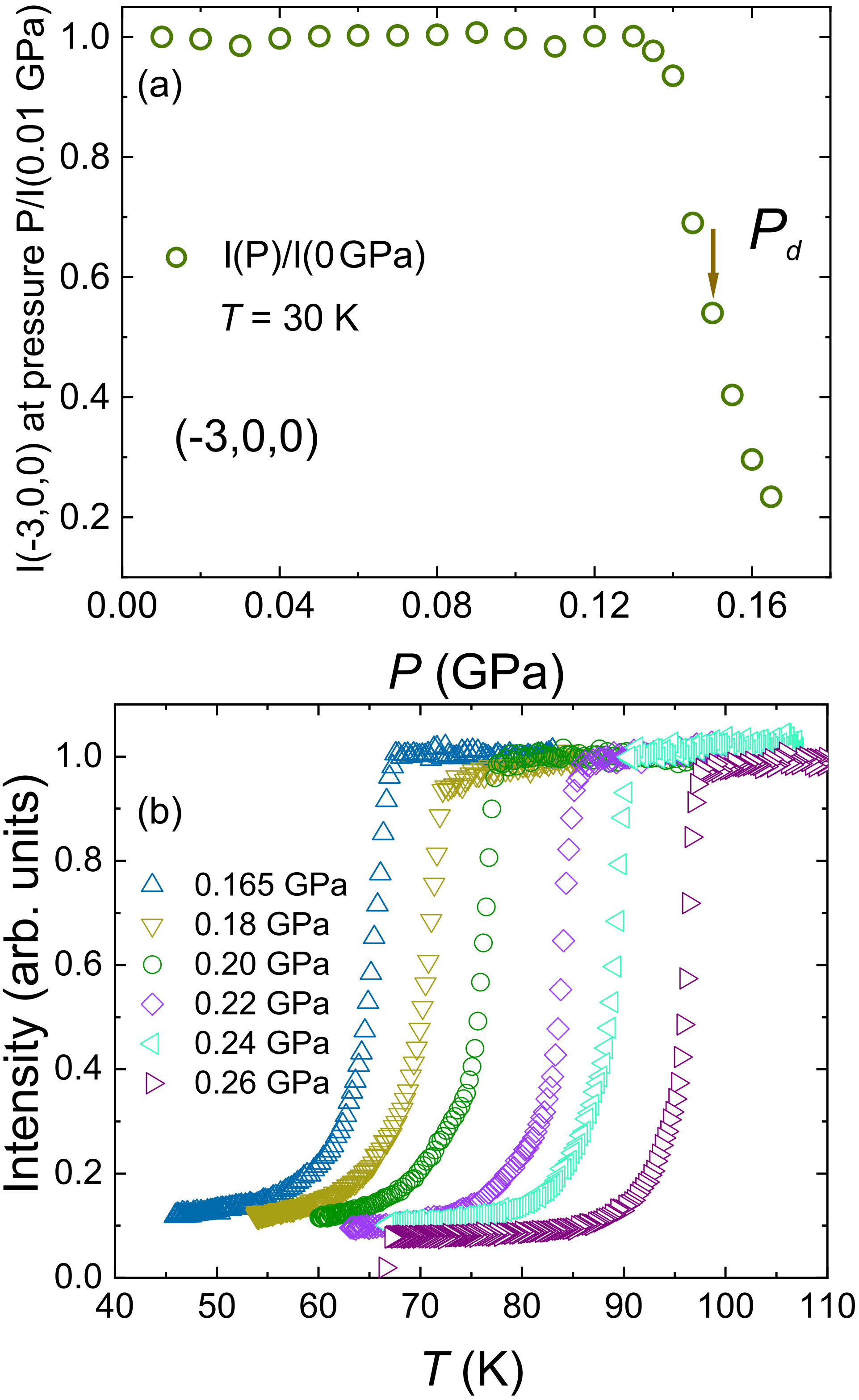

Figure 5.18: (a) Critical pressure test for the nuclear Bragg peak ($\bar{3}$,0,0) at 30 K. The integrated intensity is normalised by the data at 0 GPa obtained at D10 at ILL. (b) Temperature dependence of peak intensity of nuclear reflection ($\bar{3}$,0,0) normalised to the zero pressure value under various isostatic pressures upon cooling obtained at D10 at ILL, Grenoble.

The compared **Q**-scan curves for (0,0,3) and (3,0,0) nuclear reflections under 0.14 GPa and 0.26 GPa are shown in Fig.5.19 (c) and (d). It is anticipated that under 0.14 GPa the peaks of both (0,0,3) and (3,0,0) are sharp and strong, but for 0.26 GPa the peaks become much broader and weaker. Besides, the peak maximum moves to high **Q** position for both reflections at 0.26 GPa, implying the shrinkage of lattice parameters and distortion in the structure. Thus, the residual intensities of ($\overline{3}$,0,0) we have measured at different pressures come from the broadening peaks in the distorted lattice. Due to the limit of the instrument, the maximum pressure is 0.3 GPa at 30 K. It is also clear that 0.26 GPa is not large enough to drive α-RuCl$_3$ into the high pressure phase and that's the reason it is called distorted phase since it is in the intermediate range between the ambient structure and the high pressure structure.

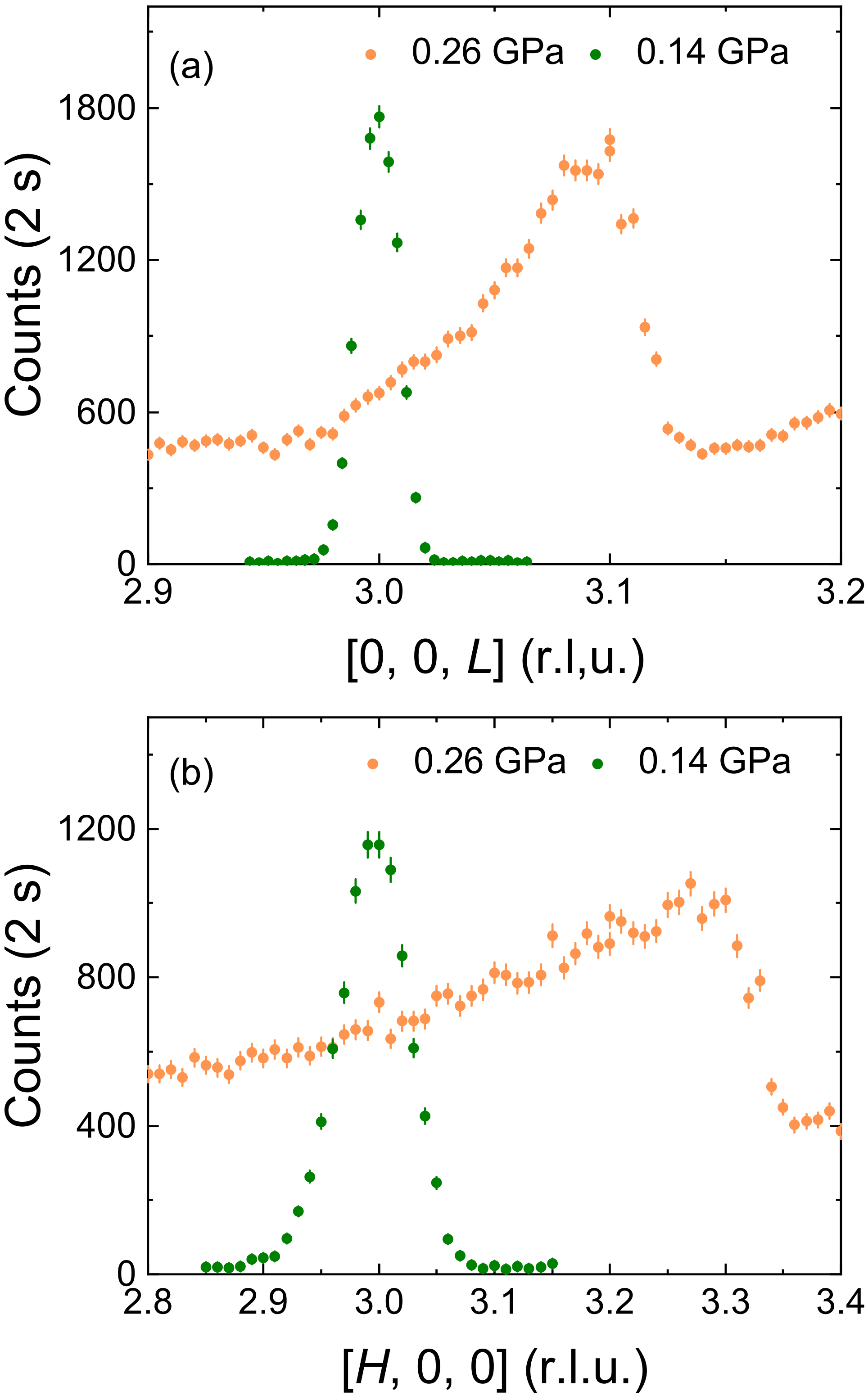

Figure 5.19: **Q**-scans for (0,0,3) and (3,0,0) reflections at (a) 0.14 GPa and (b) 0.26 GPa were measured at D10 at ILL, Grenoble. At 0.14 GPa, **Q**-scan curves were obtained by the point detector with the analyser, so the background is very low. At 0.14 GPa, **Q**-scan curves were obtained by integrating the intensity measured from 2D detector, so the background is very high.

A phase diagram could be constructed based on the neutron diffraction results as depicted in Fig.5.20(a), where the left axis represents the antiferromagnetic zigzag order transition temperature and the right axis represents the transition temperature of the distorted phase. The antiferromagnetic transition temperatures below P_d are fitted from the temperature dependence by the critical power law equation in Equ.5.2, where β is the critical exponent. And for the pressure induced distorted phase, the transition temperatures T_d are assigned by cooling and warming processes separately. At low pressure regime ($P < P_d$), it has been demonstrated that the zigzag phase transition could be well suppressed with the increase of isostatic pressures, while when $P > P_d$ a pressure induced structural transition happens along with the totally disappearance of the zigzag order. The obtained critical exponent β from the power law for each pressure is 0.12(3) at 0 GPa, 0.12(4) at 0.065 GPa, 0.14(4) at 0.1 GPa and 0.11(4) at 0.14 GPa, close to the ideal 2D Ising model where β is 0.125. If it is assumed the magnetic pressure dependence of phase transition temperature under different pressures also follows 2D Ising, it is easy to estimate the critical pressure P_{c1} = 0.255 GPa.

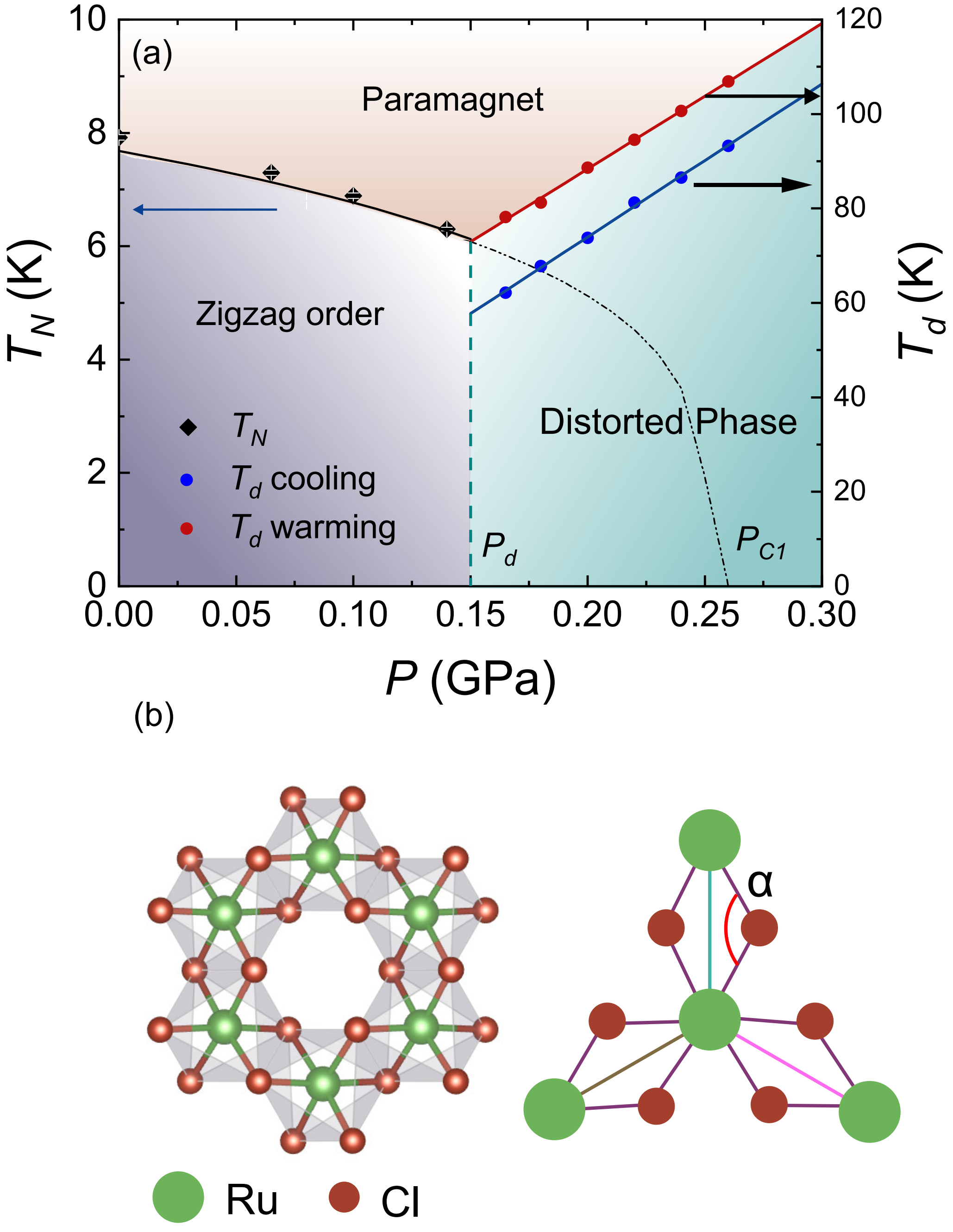

Figure 5.20: (a) Phase diagram of α-RuCl$_3$ under isostatic pressures constructed from single crystal neutron diffraction data collected at D10 at ILL. The left axis represents the transition temperature of the antiferromagnetic zigzag order and the right axis represents the transition temperature of the distorted phase upon cooling and warming. P_d is the critical pressure of distorted phase. P_{c1} is the estimated critical pressure when the magnetic pressure dependence of phase transition temperature is 2D Ising type type if the structural transition would be absent. (b) The honeycomb plane of α-RuCl$_3$ and the Ru-Cl-Ru angle is marked.

In order to understand the pressure effects in α-RuCl$_3$ under different pressures, several structure reflections were also collected at 0 GPa and 0.14 GPa. Due to the limit of D10, only the reflections in the ($h0l$) plane could be collected. 12 reflections were measured and all of them could be indexed by a rhombohedral unit cell. Based on the crystal structure determined in this PhD work in Sec.5.3.1, the crystal structure of α-RuCl$_3$ under pressures were refined in the $R\overline{3}$ space group by Jana2006.

Table 5.5: Compared refined structures of α-RuCl$_3$ at 2 K under 0 GPa and 0.14 GPa.

	0 GPa	0.14 GPa	ratio
Ru-Ru (c) (Å)	5.648(5)	5.633(4)	-0.266%
Ru-Ru (ab nearest) (Å)	3.446(3)	3.443(3)	-0.087%
Ru-Ru (ab next nearest) (Å)	5.968(4)	5.964(5)	-0.067%
∠Ru-Cl-Ru (α) (deg)	93(3)	94(2)	1%

From the refined results, there is no structural transition or distortion between 0 GPa and 0.14 GPa. Besides, the change in the coordination of Ru atoms is also compared between 0 GPa and 0.14 GPa as shown in Tab.5.5. For the distance between Ru atoms in ab basal plane, there is no significant change. For the distance between two Ru atoms in different layers, the distance has decreased -0.266% which is about 3 times larger than the lattice change in ab basal plane. This is easily understood because the layers in α-RuCl$_3$ are connected by the Van der Waals force, which is a very weak force, leading to a larger compressibility along c direction. Another change occurs in the angle Ru-Cl-Ru (α) shown in Fig.5.20 (b), which has a significant change of 1% from 0 GPa to 0.14 GPa. According to a previous quantum chemistry computation result [189, 195], with increasing the Ru-Cl-Ru angle, the Kitaev interaction reaches its peak at 94° and the Heisenberg interaction changes its sign at about 92.5°. This calculation is based on varying the Ru-Cl-Ru angles with fixed Ru-Ru distance at 3.44 Å. In the refinement results the Ru-Ru distance is 3.446(3) Å and 3.443(3) Å for 0 GPa and 0.14 GPa, respectively. When increasing isostatic pressure, the Ru-Cl-Ru angle (α) increases gradually, leading to the increase of Kitaev interaction from 93(3)° to 94(2)°. As a result, the magnetic order is suppressed by the enhancement of the Kitaev exchange.

5.5 Conclusion

In this chapter, the following important results are obtained:
1. The optimised method to prepare high quality and sizeable α-RuCl$_3$ single crystals for neutron scattering study was found.
2. Neutron diffraction study was performed at 2 K on α-RuCl$_3$ and the crystal structure of α-RuCl$_3$ was successfully determined.
3. Using spherical neutron polarisation analysis, a tilted zigzag magnetic ground state was revealed in α-RuCl$_3$, which will contribute to a better understanding interactions in Kitaev materials.
4. The phase diagram of α-RuCl$_3$ under isostatic pressures was successfully determined. In contrast to the initial anticipation, α-RuCl$_3$ could not be driven into the quantum spin liquid state by external pressure because of pressure induced structural transition, but it has been demonstrated that pressure indeed affects the transition temperature greatly. This experimental finding will also be helpful for the future study of Kitaev physics.

6

Summary and Outlook

In this PhD work, a series of high quality single crystals have been successfully grown by molten flux method or chemical vapour transport method. Along with that, a comprehensive study of crystal structure, magnetic structure of the topological semimetal Mn_3Sn and Kitaev quantum spin liquid candidate α-$RuCl_3$ by means of both in-house characterizations and neutron scattering techniques is presented. The focus is to study the relationship among crystal structure, magnetic order and physical properties. This chapter is dedicated to a summary of some essential results and gives a perspective discussion of further studies.

6.1 Summary

Employing cutting-edge crystal growth methods, series of quantum materials have been grown successfully, such as CeSb, PrSb, NdSb, $Cr_2Ge_2Te_6$, $Cr_2Si_2Te_6$, $CeZn_3As_3$, $PrZn_3As_3$, $EuMnBi_2$, $YbMnBi_2$, $PtBi_2$, $ZrTe_5$, α-$RuCl_3$ and Mn_3Sn. The topological Weyl semimetal Mn_3Sn has been an active study topic since the discovery of the large anomalous Hall effect, large Nernst effect at room temperature, magnetic Weyl fermions and magnetic inverse spin Hall effects. Its large AHE arising from non trivial band structure is connected to the inverse triangle magnetic structure at room temperature. Almost 30 years ago, a magnetic phase transition was found in a Bridgman grown Mn_3Sn single crystals characterised along the emergence of a pair of modulated reflections around (1,0,0.1). The magnetic ground state was claimed as the double spiral magnetic structure. Very recently the large AHE was found to be completely suppressed in the modulated phases along with a great change in the magnetic anisotropies in the flux grown single crystal samples. With the Sn self-flux method, large high quality Mn_3Sn single crystals were successfully grown for physical properties study and neutron scattering experiments. The electrical resistivity measurement revealed that in the sample there was a jump at 280 K, which was consistent with the magnetic phase transition detected in magnetic susceptibilities. After this magnetic phase transition, the AHE also completely disappeared in the sample in this work.

With polarised neutron scattering at DNS and IN12, the magnetic phase transition was confirmed to be intrinsic in the samples which was signified by the complete vanishing of the magnetic reflection (1,0,0) and (1,1,0) of the room temperature $\mathbf{k}$ = (0,0,0) magnetic structure.

Besides, it is surprising that the modulated reflections below 280 K could be well separated by zsf channel and $znsf$ channel respectively, which indicates they should come from different magnetic components. Each magnetic component for the modulated reflection was identified and the results show the modulated reflection in zsf channel from the magnetic components along c direction, while the modulated reflection in $znsf$ channel was from the contribution of magnetic components in ab plane, denoted as $\mathbf{q}_T$ and $\mathbf{q}_L$, respectively. With the high resolution diffraction experiment at two axis diffractometer D23, the temperature dependence of the modulated phases was mapped out and a higher order harmonic, $\mathbf{q}_3$ was found, which was considered as the third order of the modulated reflection $\mathbf{q}_T$ in the previous report. However, $\mathbf{q}_3$ could not be indexed by the three times of $\mathbf{q}_T$ or $\mathbf{q}_L$. By trials with the combination of $\mathbf{q}_L$ and $\mathbf{q}_T$, $\mathbf{q}_3$ was successfully indexed by $(2\mathbf{q}_L + \mathbf{q}_T)$, which is a solid evidence of the emergence of a double-$\mathbf{q}$ magnetic modulation at low temperature. The temperature dependence of $\mathbf{q}_T$, $\mathbf{q}_L$ and $\mathbf{q}_3$ revealed the existence of single-$\mathbf{q}$ magnetic structure in the temperature range between 250 K and 200 K, when $\mathbf{q}_T = \mathbf{q}_L$. Single crystal neutron diffraction was performed at Heidi to collect the satellite reflections with $\mathbf{k}$ = (0,0,1/10) at 225 K. The result is consistent with the polarisation neutron analysis since the magnetic structure at 225 K can be decomposed into a longitudinal spin density wave along c direction and a helix magnetic structure in ab basal plane. The longitudinal spin density wave along c direction is consistent with the jump in electric resistivity at 280 K because an energy gap will be formed when the spin density wave emerges.

Based on the magnetic structure, the disappearance of AHE could be explained by the breaking of the mirror symmetry in ab basal plane. In addition, the formation of this non-coplanar magnetic order could result from the magnetic frustration and the next nearest interlayer DM interactions.

The study of Kitaev quantum spin liquid candidate α-RuCl$_3$ arises as a fertile playground to search exotic excitations and Majorana Fermions. However, there still exist some fundamental questions to be answered, for instance the crystal structure and magnetic structure of α-RuCl$_3$ at the low temperature. The big challenge is the sample quality because α-RuCl$_3$ is a Van de Waals material and stacking fault is easily introduced during crystal growth, which makes it difficulty to solve the crystal structure. Large α-RuCl$_3$ single crystals were successfully grown up to 670 mg per crystal in This PhD work. The heat capacity measurement reveals that there was low stacking fault density in the sample since there was only one sharp antiferromagnetic peak at ~7.5 K. A structural phase transition was clearly found in the sample and a single crystal neutron diffraction experiment at 2 K has proved the low temperature crystal structure is $R\overline{3}$ instead of $C2/m$ as previously reported. In addition,spherical polarisation neutron scattering experiment was carried out to study the direction of the ordered magnetic moment of α-RuCl$_3$. The results showed that the ordered magnetic moment did not only tilt from ab basal plane but also inclined from the crystallographic a axis, which could be a result from the large off-diagonal interaction term in α-RuCl$_3$. In addition, neutron diffraction experiment under isostatic pressures was also carried out at D10 at ILL. It was clear that the zigzag magnetic order at ~7.5 K under ambient condition was suppressed gradually with the increase of the pressure. When the pressure come to 0.15 GPa, a pressure induced structural transition was found and the zigzag magnetic order also disappeared. As a result of this pressure induced structural transition, a pressure induced quantum spin liquid state could not be realised in α-RuCl$_3$. However this result reveals a great pressure effect towards a suppression of the magnetic order with a slope of -11.5 K/GPa which sheds lights on the possibility of studying pressure-tuned magnetic order in other Kitaev materials.

6.2 Outlook

Among the current study topics of quantum materials, the coupling of magnetism and topology stands out because of the novel physical phenomena, such as the magnetic topological insulators and magnetic Weyl fermions. By doping $3d$ magnetic ions Mn or Cr into topological insulators like Bi_2Te_3, one has already observed the quantum anomalous Hall effect in the antiferromagnetic $MnBi_2Te_4$ at low temperature and the next step is to realise the quantum anomalous Hall effect at room temperature in a ferromagnetic material. Frustration, which is another parameter to tune quantum materials, is now studied extensively in kagomé lattices or triangular lattices. Recent discovery of antiferromagnetic Skyrmions in the geometrically frustrated kagomé compound Gd_2PdSi_3 has demonstrated that frustration could also give rise to topological textures. Mn_3Sn which now has been proven in this thesis to experience a non coplanar magnetic in the kagomé plane at low temperature is a promising candidate to study the correlation between topological magnetic order and external fields or pressures. In addition, other Mn-based materials with incommensurate magnetic order such as RMn_6Sn_6 (R is the rare earth element) also have a Mn kagomé plane, and would constitute another set of candidate compounds to study the topological magnetic orders. To search for the Kitaev quantum spin liquid, the two dimensional halides of general formula RX_3 would be good candidates since some of them have similar crystal structure as α-$RuCl_3$. In addition, the rare earth faced centred double perovskite, which has three orthogonal interaction exchange paths for rare earth could also be materials hosting Kitaev physics.

An essential prerequisite for such studies is always the successful growth of sufficiently large, high quality single crystals.

Bibliography

[1] B. Keimer and J. E. Moore, “The physics of quantum materials”, Nat. Phys. **13**, 1045 (2017) (cited on page 1).

[2] Y. Tokura, M. Kawasaki, and N. Nagaosa, “Emergent functions of quantum materials”, Nat. Phys. **13**, 1056 (2017) (cited on pages 1, 3, 4).

[3] D. N. Basov, R. D. Averitt, and D. Hsieh, “Towards properties on demand in quantum materials”, Nat. Mater. **16**, 1077 (2017) (cited on page 1).

[4] M. den Nijs, “Quantized Hall conductance in a two dimensional periodic potential”, Phys. A Stat. Mech. its Appl. **124**, 199 (1984) (cited on page 1).

[5] M. Kohmoto, “Topological invariant and the quantization of the Hall conductance”, Ann. Phys. (N. Y). **160**, 343 (1985) (cited on page 1).

[6] C. L. Kane and E. J. Mele, “Z_2 topological order and the quantum spin hall effect”, Phys. Rev. Lett. **95**, 3 (2005) (cited on page 1).

[7] C. L. Kane and E. J. Mele, “Quantum Spin hall effect in graphene”, Phys. Rev. Lett. **95**, 1 (2005) (cited on page 1).

[8] N. P. Ong and W. L. Lee, “Geometry and the anomalous hall effect in ferromagnets”, Proc. 8th Int. Symp. Found. Quantum Mech. Light New Technol. ISQM-Tokyo 2005 **3**, 121 (2006) (cited on page 1).

[9] J. E. Moore and L. Balents, “Topological invariants of time-reversal-invariant band structures”, Phys. Rev. B - Condens. Matter Mater. Phys. **75**, 3 (2007) (cited on page 1).

[10] L. Fu and C. L. Kane, “Topological insulators with inversion symmetry”, Phys. Rev. B - Condens. Matter Mater. Phys. **76**, 1 (2007) (cited on page 1).

[11] M. Z. Hasan and C. L. Kane, “Colloquium: Topological insulators”, Rev. Mod. Phys. **82**, 3045 (2010) (cited on page 1).

[12] J. E. Moore, “The birth of topological insulators”, Nature **464**, 194 (2010) (cited on pages 1, 5).

[13] Y. Ando, “Topological insulator materials”, J. Phys. Soc. Japan **82**, 1 (2013) (cited on page 1).

[14] B. A. Bernevig, “It’s been a Weyl coming”, Nat. Phys. **11**, 698 (2015) (cited on pages 1, 7).

[15] S. Y. Xu et al., “Discovery of a Weyl fermion semimetal and topological Fermi arcs”, Science (80-.). **349**, 613 (2015) (cited on pages 1, 7, 8).

[16] S. Jia, S. Y. Xu, and M. Z. Hasan, “Weyl semimetals, Fermi arcs and chiral anomalies”, Nat. Mater. **15**, 1140 (2016) (cited on pages 1, 7).

[17] A. Burkov, “Topological semimetals”, Nat. Mater. **15**, 1145 (2016) (cited on page 1).

[18] J. Wang and S. C. Zhang, “Topological states of condensed matter”, Nat. Mater. **16**, 1062 (2017) (cited on page 1).

[19] M. Sato and Y. Ando, “Topological superconductors: A review”, Reports Prog. Phys. **80**, aa6ac7 (2017) (cited on page 1).

[20] Y. Tokura, K. Yasuda, and A. Tsukazaki, “Magnetic topological insulators”, Nat. Rev. Phys. **1**, 126 (2019) (cited on pages 1, 6).

[21] “The rise of quantum materials”, Nat. Phys. **12**, 105 (2016) (cited on page 3).

[22] Y. L. Chen, J. G. Analytis, J.-H. Chu, Z. K. Liu, S.-K. Mo, X. L. Qi, H. J. Zhang, D. H. Lu, X. Dai, Z. Fang, S. C. Zhang, I. R. Fisher, Z. Hussain, and Z.-X. Shen, “Experimental Realization of a Three-Dimensional Topological Insulator, Bi_2Te_3”, Science (80-.). **325**, 178 (2009) (cited on page 5).

[23] H. Zhang, C. X. Liu, X. L. Qi, X. Dai, Z. Fang, and S. C. Zhang, “Topological insulators in Bi_2Se_3, Bi_2Te_3 and Sb_2Te_3 with a single Dirac cone on the surface”, Nat. Phys. **5**, 438 (2009) (cited on page 5).

[24] D. Hsieh, Y. Xia, D. Qian, L. Wray, J. H. Dil, F. Meier, J. Osterwalder, L. Patthey, J. G. Checkelsky, N. P. Ong, A. V. Fedorov, H. Lin, A. Bansil, D. Grauer, Y. S. Hor, R. J. Cava, and M. Z. Hasan, “A tunable topological insulator in the spin helical Dirac transport regime”, Nature **460**, 1101 (2009) (cited on page 5).

[25] Y. Xia, D. Qian, D. Hsieh, L. Wray, A. Pal, H. Lin, A. Bansil, D. Grauer, Y. S. Hor, R. J. Cava, and M. Z. Hasan, “Observation of a large-gap topological-insulator class with a single Dirac cone on the surface”, Nat. Phys. **5**, 398 (2009) (cited on page 5).

[26] X. Kou, Y. Fan, M. Lang, P. Upadhyaya, and K. L. Wang, “Magnetic topological insulators and quantum anomalous hall effect”, Solid State Commun. **215-216**, 34 (2015) (cited on page 6).

[27] C. Z. Chang and M. Li, “Quantum anomalous Hall effect in time-reversal-symmetry breaking topological insulators”, J. Phys. Condens. Matter **28** (2016) (cited on page 6).

[28] K. He, Y. Wang, and Q. K. Xue, “Topological Materials: Quantum Anomalous Hall System”, Annu. Rev. Condens. Matter Phys. **9**, 329 (2018) (cited on page 6).

[29] C. Liu, Y. Wang, H. Li, Y. Wu, Y. Li, J. Li, K. He, Y. Xu, J. Zhang, and Y. Wang, “Robust axion insulator and Chern insulator phases in a two-dimensional antiferromagnetic topological insulator”, Nat. Mater. **19**, 522 (2020) (cited on page 6).

[30] H. Fu, C. X. Liu, and B. Yan, “Exchange bias and quantum anomalous nomalous Hall effect in the $MnBi_2Te_4/CrI_3$ heterostructure”, Sci. Adv. **6**, 1 (2020) (cited on page 6).

[31] Y. Deng, Y. Yu, M. Z. Shi, Z. Guo, Z. Xu, J. Wang, X. H. Chen, and Y. Zhang, “Quantum anomalous Hall effect in intrinsic magnetic topological insulator MnBi2Te4”, Science (80-.). **367**, 895 (2020) (cited on page 6).

[32] B. Yan and C. Felser, “Topological Materials: Weyl Semimetals”, Annu. Rev. Condens. Matter Phys. **8**, 337 (2017) (cited on pages 7, 8).

[33] B. Q. Lv, H. M. Weng, B. B. Fu, X. P. Wang, H. Miao, J. Ma, P. Richard, X. C. Huang, L. X. Zhao, G. F. Chen, Z. Fang, X. Dai, T. Qian, and H. Ding, “Experimental discovery of weyl semimetal TaAs”, Phys. Rev. X **5**, 1 (2015) (cited on page 8).

[34] S. Y. Xu et al., “Experimental discovery of a topological Weyl semimetal state in TaP”, Sci. Adv. **1** (2015) (cited on page 8).

[35] N. Xu, H. M. Weng, B. Q. Lv, C. E. Matt, J. Park, F. Bisti, V. N. Strocov, D. Gawryluk, E. Pomjakushina, K. Conder, N. C. Plumb, M. Radovic, G. Autès, O. V. Yazyev, Z. Fang, X. Dai, T. Qian, J. Mesot, H. Ding, and M. Shi, “Observation of Weyl nodes and Fermi arcs in tantalum phosphide”, Nat. Commun. **7**, 1 (2016) (cited on page 8).

[36] S. M. Huang, S. Y. Xu, I. Belopolski, C. C. Lee, G. Chang, B. Wang, N. Alidoust, G. Bian, M. Neupane, C. Zhang, S. Jia, A. Bansil, H. Lin, and M. Z. Hasan, “A Weyl Fermion semimetal with surface Fermi arcs in the transition metal monopnictide TaAs class”, Nat. Commun. **6** (2015) (cited on page 8).

[37] H. Weng, C. Fang, Z. Fang, B. Andrei Bernevig, and X. Dai, “Weyl semimetal phase in noncentrosymmetric transition-metal monophosphides”, Phys. Rev. X **5**, 1 (2015) (cited on page 8).

[38] P. G. Labarre, L. Dong, J. Trinh, T. Siegrist, and A. P. Ramirez, “Evidence for undoped Weyl semimetal charge transport in $Y_2Ir_2O_7$”, J. Phys. Condens. Matter **32** (2020) (cited on page 8).

[39] S. K. Jian and H. Yao, “Correlated double-Weyl semimetals with Coulomb interactions: Possible applications to $HgCr_2Se_4$ and $SrSi_2$”, Phys. Rev. B - Condens. Matter Mater. Phys. **92**, 1 (2015) (cited on page 8).

[40] P. Li, Y. Wen, X. He, Q. Zhang, C. Xia, Z. M. Yu, S. A. Yang, Z. Zhu, H. N. Alshareef, and X. X. Zhang, “Evidence for topological type-II Weyl semimetal WTe_2”, Nat. Commun. **8**, 8 (2017) (cited on pages 8, 53).

[41] J. Jiang, Z. K. Liu, Y. Sun, H. F. Yang, C. R. Rajamathi, Y. P. Qi, L. X. Yang, C. Chen, H. Peng, C. C. Hwang, S. Z. Sun, S. K. Mo, I. Vobornik, J. Fujii, S. S. Parkin, C. Felser, B. H. Yan, and Y. L. Chen, “Signature of type-II Weyl semimetal phase in $MoTe_2$”, Nat. Commun. **8**, 1 (2017) (cited on page 8).

[42] N. Morali, R. Batabyal, P. K. Nag, E. Liu, Q. Xu, Y. Sun, B. Yan, C. Felser, N. Avraham, and H. Beidenkopf, “Fermi-arc diversity on surface terminations of the magnetic Weyl semimetal $Co_3Sn_2S_2$”, Science (80-.). **365**, 1286 (2019) (cited on page 8).

[43] Z. K. Liu, B. Zhou, Y. Zhang, Z. J. Wang, H. M. Weng, D. Prabhakaran, S. Mo, Z. X. Shen, Z. Fang, X. Dai, Z. Hussain, and Y. L. Chen, “Topological Dirac Semimetal , Na_3Bi”, Science (80-.). **343**, 864 (2014) (cited on page 9).

[44] M. Neupane, S. Y. Xu, R. Sankar, N. Alidoust, G. Bian, C. Liu, I. Belopolski, T. R. Chang, H. T. Jeng, H. Lin, A. Bansil, F. Chou, and M. Z. Hasan, “Observation of a three-dimensional topological dirac semimetal phase in high-mobility Cd_3As_2”, Nat. Commun. **5**, 1 (2014) (cited on page 9).

[45] K. Kuroda et al., “Evidence for Magnetic Weyl Fermions in a Correlated Metal”, Nat. Mater. **16**, 1090 (2017) (cited on pages 9, 53).

[46] E. H. Hall, “On a New Action of the Magnet on Electric Currents”, Am. J. Math. **2**, 287 (1879) (cited on page 10).

[47] E. M. Pugh, “Hall effect and the magnetic properties of some ferromagnetic materials”, Phys. Rev. **36**, 1503 (1930) (cited on page 10).

[48] E. M. Pugh and T. W. Lippert, “Hall e.m.f. and Intensity of Magnetization”, Phys. Rev. **42**, 709 (1932) (cited on page 10).

[49] D. J. Thouless, M. Kohmoto, M. P. Nightingale, and M. den Nijs, “Quantized Hall Conductance in a Two-Dimensional Periodic Potential”, Phys. Rev. Lett. **49**, 405 (1982) (cited on page 10).

[50] R. E. Prange and S. M. Girvin, eds., “The Quantum Hall Effect”, Graduate Texts in Contemporary Physics (Springer New York, New York, NY, 1990) (cited on page 10).

[51] M. C. Chang and Q. Niu, “Berry phase, hyperorbits, and the Hofstadter spectrum”, Phys. Rev. Lett. **75**, 1348 (1995) (cited on page 10).

[52] P. Bruno, V. K. Dugaev, and M. Taillefumier, “Topological Hall effect and Berry phase in magnetic napostructures”, Phys. Rev. Lett. **93**, 1 (2004) (cited on pages 10, 16).

[53] N. Nagaosa, J. Sinova, S. Onoda, A. H. MacDonald, and N. P. Ong, “Anomalous Hall effect”, Rev. Mod. Phys. **82**, 1539 (2010) (cited on pages 10, 11, 53).

[54] R. Karplus and J. M. Luttinger, “Hall effect in ferromagnetics”, Phys. Rev. **95**, 1154 (1954) (cited on pages 10, 11).

[55] J. Smit, “The spontaneous hall effect in ferromagnetics I”, Physica **21**, 877 (1955) (cited on page 11).

[56] J. Smit, “The spontaneous hall effect in ferromagnetics II”, Physica **24**, 39 (1958) (cited on page 11).

[57] L. Berger, “Side-jump mechanism for the hall effect of ferromagnets”, Phys. Rev. B **2**, 4559 (1970) (cited on page 11).

[58] J. Sinova, D. Culcer, Q. Niu, N. A. Sinitsyn, T. Jungwirth, and A. H. MacDonald, “Universal intrinsic spin Hall effect”, Phys. Rev. Lett. **92**, 1 (2004) (cited on page 11).

[59] J. Sinova, T. Jungwirth, and J. Černe, “Magneto-transport and magneto-optical properties of ferromagnetic (III,Mn)V semiconductors: A review”, Int. J. Mod. Phys. B **18**, 1083 (2004) (cited on page 11).

[60] N. Nagaosa, “Anomalous hall effect - A new perspective”, J. Phys. Soc. Japan **75**, 1 (2006) (cited on page 11).

[61] M. T. Suzuki, T. Koretsune, M. Ochi, and R. Arita, “Cluster multipole theory for anomalous Hall effect in antiferromagnets”, Phys. Rev. B **95**, 1 (2017) (cited on pages 13, 14, 16, 53).

[62] K. Momma and F. Izumi, “VESTA3 for three-dimensional visualization of crystal, volumetric and morphology data”, J. Appl. Crystallogr. **44**, 1272 (2011) (cited on pages 14, 78, 88).

[63] S. Nakatsuji, N. Kiyohara, and T. Higo, “Large anomalous Hall effect in a non-collinear antiferromagnet at room temperature”, Nature **527**, 212 (2015) (cited on pages 14, 53, 54, 61, 62).

[64] A. K. Nayak, J. E. Fischer, Y. Sun, B. Yan, J. Karel, A. C. Komarek, C. Shekhar, N. Kumar, W. Schnelle, J. Kübler, C. Felser, and S. S. Parkin, “Large anomalous Hall effect driven by a nonvanishing Berry curvature in the noncolinear antiferromagnet Mn_3Ge”, Sci. Adv. **2**, 1 (2016) (cited on pages 14, 53).

[65] H. Yang, Y. Sun, Y. Zhang, W.-J. Shi, S. S. P. Parkin, and B. Yan, “Topological Weyl semimetals in the chiral antiferromagnetic materials Mn_3Ge and Mn_3Sn”, New J. Phys. **19**, 015008 (2017) (cited on pages 14, 15, 53, 54, 64).

[66] J. Kübler and C. Felser, “Weyl fermions in antiferromagnetic Mn_3Sn and Mn_3Ge”, Epl **120** (2017) (cited on pages 14, 53).

[67] P. J. Brown, V. Nunez, F. Tasset, J. B. Forsyth, and P. Radhakrishna, “Determination of the magnetic structure of Mn_3Sn using generalized neutron polarization analysis”, J. Phys. Condens. Matter **2**, 9409 (1990) (cited on pages 14, 53, 64).

[68] H. Chen, Q. Niu, and A. H. Macdonald, “Anomalous hall effect arising from non-collinear antiferromagnetism”, Phys. Rev. Lett. **112**, 1 (2014) (cited on pages 16, 53).

[69] A. Neubauer, C. Pfleiderer, B. Binz, A. Rosch, R. Ritz, P. G. Niklowitz, and P. Böni, “Topological hall effect in the a phase of MnSi”, Phys. Rev. Lett. **102**, 1 (2009) (cited on page 16).

[70] T. Kurumaji, T. Nakajima, M. Hirschberger, A. Kikkawa, Y. Yamasaki, H. Sagayama, H. Nakao, Y. Taguchi, T. hisa Arima, and Y. Tokura, “Skyrmion lattice with a giant topological Hall effect in a frustrated triangular-lattice magnet”, Science (80-.). **365**, 914 (2019) (cited on page 16).

[71] S. Wang, Q. Zeng, D. Liu, H. Zhang, L. Ma, G. Xu, Y. Liang, Z. Zhang, H. Wu, R. Che, X. Han, and Q. Huang, “Giant Topological Hall Effect and Superstable Spontaneous Skyrmions below 330 K in a Centrosymmetric Complex Noncollinear Ferromagnet $NdMn_2Ge_2$”, ACS Appl. Mater. Interfaces **12**, 24125 (2020) (cited on page 16).

[72] S. Mühlbauer, “Skyrmion lattice in a chiral magnet ”, Science (80-.). **333**, 1381 (2011) (cited on page 16).

[73] L. Balents, “Spin liquids in frustrated magnets”, Nature **464**, 199 (2010) (cited on pages 17, 19, 20).

[74] A. A. Zvyagin, “New physics in frustrated magnets: Spin ices, monopoles, etc. (Review Article)”, Low Temp. Phys. **39** (2013) (cited on page 17).

[75] D. S. Inosov, “Quantum magnetism in minerals”, Adv. Phys. **67**, 149 (2018) (cited on page 17).

[76] I. Rousochatzakis, Y. Sizyuk, and N. B. Perkins, “Quantum spin liquid in the semiclassical regime”, Nat. Commun. **9**, 1 (2018) (cited on page 17).

[77] J. Knolle and R. Moessner, "A field guide to spin liquids", Annu. Rev. Condens. Matter Phys. **10**, 451 (2019) (cited on page 17).

[78] G. Misguich and C. Lhuillier, "Two-dimensitional quantum antiferromagnets", in *Frustrated spin syst.* Vol. c (World Scientific, Jan. 2005), pp. 229–306 (cited on page 17).

[79] H. Takagi, T. Takayama, G. Jackeli, G. Khaliullin, and S. E. Nagler, "Concept and realization of Kitaev quantum spin liquids", Nat. Rev. Phys. **1**, 264 (2019) (cited on page 19).

[80] L. Savary and L. Balents, "Quantum spin liquids: A review", Reports Prog. Phys. **80** (2017) (cited on page 19).

[81] P. W. Anderson, "Resonating valence bonds: A new kind of insulator?", Mater. Res. Bull. **8**, 153 (1973) (cited on page 19).

[82] P. W. Anderson, "The Resonating Valence Bond State in La_2CuO_4 and Superconductivity", Science (80-.). **235**, 1196 (1986) (cited on page 19).

[83] M. Noga and J. Milko, "The resonating valence bond state and high temperature superconductivity", Czechoslov. J. Phys. **39**, 90 (1989) (cited on page 19).

[84] T. H. Han, J. S. Helton, S. Chu, D. G. Nocera, J. A. Rodriguez-Rivera, C. Broholm, and Y. S. Lee, "Fractionalized excitations in the spin-liquid state of a kagome-lattice antiferromagnet", Nature **492**, 406 (2012) (cited on page 20).

[85] A. Kitaev, "Anyons in an exactly solved model and beyond", Ann. Phys. (N. Y). **321**, 2 (2006) (cited on page 22).

[86] B. J. Kim, H. Jin, S. J. Moon, J. Y. Kim, B. G. Park, C. S. Leem, J. Yu, T. W. Noh, C. Kim, S. J. Oh, J. H. Park, V. Durairaj, G. Cao, and E. Rotenberg, "Novel j_{eff} = 1/2 mott state induced by relativistic spin-orbit coupling in Sr_2IrO_4", Phys. Rev. Lett. **101**, 1 (2008) (cited on page 23).

[87] C. H. Sohn, H. S. Kim, T. F. Qi, D. W. Jeong, H. J. Park, H. K. Yoo, H. H. Kim, J. Y. Kim, T. D. Kang, D. Y. Cho, G. Cao, J. Yu, S. J. Moon, and T. W. Noh, "Mixing between J_{eff} = 1/2 and 32 orbitals in Na_2IrO_3: A spectroscopic and density functional calculation study", Phys. Rev. B - Condens. Matter Mater. Phys. **88**, 1 (2013) (cited on page 23).

[88] A. Koitzsch, C. Habenicht, E. Müller, M. Knupfer, B. Büchner, H. C. Kandpal, J. Van Den Brink, D. Nowak, A. Isaeva, and T. Doert, "Jeff Description of the Honeycomb Mott Insulator α-$RuCl_3$", Phys. Rev. Lett. **117**, 1 (2016) (cited on page 23).

[89] N. Read and D. Green, "Paired states of fermions in two dimensions with breaking of parity and time-reversal symmetries and the fractional quantum Hall effect", Phys. Rev. B **61**, 10267 (2000) (cited on page 23).

[90] A. Banerjee, P. Lampen-Kelley, J. Knolle, C. Balz, A. A. Aczel, B. Winn, Y. Liu, D. Pajerowski, J. Yan, C. A. Bridges, A. T. Savici, B. C. Chakoumakos, M. D. Lumsden, D. A. Tennant, R. Moessner, D. G. Mandrus, and S. E. Nagler, "Excitations in the field-induced quantum spin liquid state of α-$RuCl_3$", npj Quantum Mater. **3**, 8 (2018) (cited on page 24).

[91] Y. Kasahara, T. Ohnishi, Y. Mizukami, O. Tanaka, S. Ma, K. Sugii, N. Kurita, H. Tanaka, J. Nasu, Y. Motome, T. Shibauchi, and Y. Matsuda, “Majorana quantization and half-integer thermal quantum Hall effect in a Kitaev spin liquid”, Nature **559**, 227 (2018) (cited on page 24).

[92] H. B. Cao, A. Banerjee, J.-Q. Yan, C. A. Bridges, M. D. Lumsden, D. G. Mandrus, D. A. Tennant, B. C. Chakoumakos, and S. E. Nagler, “Low-temperature crystal and magnetic structure of α-$RuCl_3$”, Phys. Rev. B **93**, 134423 (2016) (cited on pages 27, 85, 88, 90, 94, 99, 102, 106).

[93] B. M. Wanklyn, “Flux growth of some complex oxide materials”, J. Mater. Sci. **7**, 813 (1972) (cited on page 28).

[94] P. C. Canfield and Z. Fisk, “Growth of single crystals from metallic fluxes”, Philos. Mag. B Phys. Condens. Matter; Stat. Mech. Electron. Opt. Magn. Prop. **65**, 1117 (1992) (cited on page 28).

[95] P. C. Canfield and I. R. Fisher, “High-temperature solution growth of intermetallic single crystals and quasicrystals”, J. Cryst. Growth **225**, 155 (2001) (cited on page 28).

[96] W. R. Gemmill, M. D. Smith, R. Prozorov, and H.-C. zur Loye, “Crystal Growth and Magnetic Properties of Lanthanide-Containing Osmium Double Perovskites, Ln_2NaOsO_6 (Ln = La, Pr, Nd)”, Inorg. Chem. **44**, 2639 (2005) (cited on page 28).

[97] P. C. Canfield, “Solution Growth of Intermetallic Single Crystals: a Beginner’S Guide”, 93 (2009) (cited on page 28).

[98] S. J. Mugavero, W. R. Gemmill, I. P. Roof, and H. C. zur Loye, “Materials discovery by crystal growth: Lanthanide metal containing oxides of the platinum group metals (Ru, Os, Ir, Rh, Pd, Pt) from molten alkali metal hydroxides”, J. Solid State Chem. **182**, 1950 (2009) (cited on page 28).

[99] C. Krellner, S. Taube, T. Westerkamp, Z. Hossain, and C. Geibel, “Single-crystal growth of $YbRh_2Si_2$ and $YbIr_2Si_2$”, Philos. Mag. **92**, 2508 (2012) (cited on page 28).

[100] E. D. Bauer, P. H. Tobash, J. N. Mitchell, and J. L. Sarrao, “Single crystal growth of plutonium compounds from molten metal fluxes”, Philos. Mag. **92**, 2466 (2012) (cited on page 28).

[101] D. E. Bugaris and H. C. Zur Loye, “Materials discovery by flux crystal growth: Quaternary and higher order oxides”, Angew. Chemie - Int. Ed. **51**, 3780 (2012) (cited on page 28).

[102] A. Jesche and P. C. Canfield, “Single crystal growth from light, volatile and reactive materials using lithium and calcium flux”, Philos. Mag. **94**, 2372 (2014) (cited on page 28).

[103] I. R. Fisher, M. C. Shapiro, and J. G. Analytis, “Principles of crystal growth of intermetallic and oxide compounds from molten solutions”, Philos. Mag. **92**, 2401 (2012) (cited on page 28).

[104] P. C. Canfield, T. Kong, U. S. Kaluarachchi, and N. H. Jo, “Use of frit-disc crucibles for routine and exploratory solution growth of single crystalline samples”, Philos. Mag. **96**, 84 (2016) (cited on page 28).

[105] M. C. Hatnean, C. Decorse, M. R. Lees, O. A. Petrenko, and G. Balakrishnan, “Zirconate pyrochlore frustrated magnets: Crystal growth by the floating zone technique”, Crystals **6**, 1 (2016) (cited on page 28).

[106] J. Li, C. J. Tilbury, S. H. Kim, and M. F. Doherty, “A design aid for crystal growth engineering”, Prog. Mater. Sci. **82**, 1 (2016) (cited on page 28).

[107] S. M. Koohpayeh, “Single crystal growth by the traveling solvent technique: A review”, Prog. Cryst. Growth Charact. Mater. **62**, 22 (2016) (cited on page 28).

[108] J. Q. Yan, B. C. Sales, M. A. Susner, and M. A. McGuire, “Flux growth in a horizontal configuration: An analog to vapor transport growth”, Phys. Rev. Mater. **1**, 1 (2017) (cited on page 28).

[109] D. Elwell and H. J. Scheel, “Crystal growth from high-temperature solutions”, English (Academic Press, 1975) (cited on pages 29, 30).

[110] T. Wolf, “Flux separation methods for flux-grown single crystals”, Philos. Mag. **92**, 2458 (2012) (cited on pages 30, 31).

[111] M. Binnewies, R. Glaum, M. Schmidt, and P. Schmidt, “Chemical vapor transport reactions - A historical review”, Zeitschrift fur Anorg. und Allg. Chemie **639**, 219 (2013) (cited on page 32).

[112] H. Schäfer, “Bemerkungen zur Entstehung höhermolekularer Siliciumchloride im Abschreckrohr”, Zeitschrift für Anorg. und Allg. Chemie **274**, 265 (1953) (cited on page 34).

[113] H. Schäfer, H. Jacob, and K. Etzel, “Chemische Transportreaktionen. II. Die Verwendung der Zerfallsgleichgewichte der Eisen(II)- und Nickel(II)-halogenide zum Metalltransport im Temperaturgefälle”, Zeitschrift für Anorg. und Allg. Chemie **286**, 42 (1956) (cited on page 34).

[114] A. Furrer, J. Mesot, and T. Strässle, “Neutron Scattering in Condensed Matter Physics”, Vol. 04, Series on Neutron Techniques and Applications (WORLD SCIENTIFIC, May 2009) (cited on page 36).

[115] S. R. Spurgeon, “Experimental Neutron Scattering, by B.T.M. Willis and C.J. Carlile”, Vol. 55, 3 (July 2014), pp. 250–251 (cited on page 36).

[116] P. J. Brown, “Polarised neutrons and complex antiferromagnets: An overview”, Phys. B Condens. Matter **297**, 198 (2001) (cited on pages 39, 72).

[117] E. Ressouche, “Polarized neutron diffraction”, École thématique la Société Française la Neutron. **13**, 02002 (2014) (cited on page 39).

[118] P. J. Brown, “Spherical Neutron Polarimetry”, Neutron Scatt. from Magn. Mater., 215 (2006) (cited on page 39).

[119] N. Terada, N. Qureshi, L. C. Chapon, and T. Osakabe, “Spherical neutron polarimetry under high pressure for a multiferroic delafossite ferrite”, Nat. Commun. **9**, 1 (2018) (cited on page 39).

[120] N. Qureshi, E. Ressouche, A. Mukhin, M. Gospodinov, and V. Skumryev, “Proof of the elusive high-temperature incommensurate phase in CuO by spherical neutron polarimetry”, Sci. Adv. **6**, eaay7661 (2020) (cited on page 39).

[121] W. Schweika, “XYZ-polarisation analysis of diffuse magnetic neutron scattering from single crystals”, J. Phys. Conf. Ser. **211** (2010) (cited on page 42).

[122] Y. Su, K. Nemkovskiy, and S. Demirdiş, “DNS: Diffuse scattering neutron time-of-flight spectrometer”, J. large-scale Res. Facil. JLSRF **1**, A27 (2015) (cited on page 42).

[123] M. Meven and A. Sazonov, “HEiDi: Single crystal diffractometer at hot source”, J. large-scale Res. Facil. JLSRF **1**, A7 (2015) (cited on pages 44, 64).

[124] N. Qureshi, “Instrumental aspects”, EPJ Web Conf. **155**, 1 (2017) (cited on page 44).

[125] A. Janner and T. Janssen, “Symmetry of incommensurate crystal phases. I. Commensurate basic structures”, Acta Crystallogr. Sect. A **36**, 399 (1980) (cited on page 47).

[126] V. Petříček, J. Fuksa, and M. Dušek, “Magnetic space and superspace groups, representation analysis: Competing or friendly concepts?”, Acta Crystallogr. Sect. A Found. Crystallogr. **66**, 649 (2010) (cited on pages 47, 77).

[127] T. Janssen, “Development of symmetry concepts for aperiodic crystals”, Symmetry (Basel). **6**, 171 (2014) (cited on page 47).

[128] M. S. Groups and D. B. Litvin, “Magnetic Group Tables” (2013) (cited on page 47).

[129] S. V. Gallego, E. S. Tasci, G. De La Flor, J. Manuel Perez-Mato, and M. I. Aroyo, “Magnetic symmetry in the Bilbao Crystallographic Server: A computer program to provide systematic absences of magnetic neutron diffraction”, J. Appl. Crystallogr. **45**, 1236 (2012) (cited on pages 47, 83).

[130] J. M. Perez-Mato, J. L. Ribeiro, V. Petricek, and M. I. Aroyo, “Magnetic superspace groups and symmetry constraints in incommensurate magnetic phases”, J. Phys. Condens. Matter **24** (2012) (cited on pages 47, 82).

[131] J. M. Perez-Mato, J. L. Ribeiro, V. Petricek, and M. I. Aroyo, “Magnetic superspace groups and symmetry constraints in incommensurate magnetic phases”, J. Phys. Condens. Matter **24** (2012) (cited on pages 47, 52).

[132] H. T. Stokes, B. J. Campbell, and S. Van Smaalen, “Generation of (3 + d)-dimensional superspace groups for describing the symmetry of modulated crystalline structures”, Acta Crystallogr. Sect. A Found. Crystallogr. **67**, 45 (2011) (cited on page 47).

[133] S.J. Joshua, “Symmetry Principles and Magnetic Symmetry In Solid State Physics” (A. Hilger, Bristol, England, 1991), pp. 115–134 (cited on page 47).

[134] J. Rodríguez-Carvajal and F. Bourée, “Symmetry and magnetic structures”, EPJ Web Conf. **22**, 00010 (2012) (cited on page 47).

[135] V. Petříček, M. Dušek, and L. Palatinus, “Crystallographic Computing System JANA2006: General features”, Zeitschrift für Krist. - Cryst. Mater. **229**, 345 (2014) (cited on pages 48, 57, 77).

[136] J. Perez-Mato, S. Gallego, E. Tasci, L. Elcoro, G. de la Flor, and M. Aroyo, “Symmetry-Based Computational Tools for Magnetic Crystallography”, Annu. Rev. Mater. Res. **45**, 217 (2015) (cited on pages 48, 64, 83).

[137] S. Alexander, “Symmetry Considerations in the Determination of Magnetic Structures”, Phys. Rev. **127**, 420 (1962) (cited on page 48).

[138] E. F. Bertaut, “Representation analysis of magnetic structures”, Acta Crystallogr. Sect. A Cryst. Physics, Diffraction, Theor. Gen. Crystallogr. **24**, 217 (1968) (cited on page 48).

[139] E. Ascher, “Permutation representations, epikernels and phase transitions”, J. Phys. C Solid State Phys. **10**, 1365 (1977) (cited on page 48).

[140] V. Petříček and P. Coppens, “Structure analysis of modulated crystals. III. Scattering formalism and symmetry considerations: extension to higher-dimensional space groups”, Acta Crystallogr. Sect. A Found. Crystallogr. **44**, 235 (1988) (cited on page 48).

[141] B. Grenier and R. Ballou, “Crystallography: Symmetry groups and group representations”, EPJ Web Conf. **22**, 00006 (2012) (cited on page 48).

[142] J. Rodríguez-Carvajal, “Recent advances in magnetic structure determination by neutron powder diffraction”, Phys. B Condens. Matter **192**, 55 (1993) (cited on page 52).

[143] A. S. Wills, “A new protocol for the determination of magnetic structures using simulated annealing and representational analysis (SARAh)”, Phys. B Condens. Matter **276-278**, 680 (2000) (cited on page 52).

[144] M. Onoda and N. Nagaosa, “Topological Nature of Anomalous Hall Effect in Ferromagnets”, J. Phys. Soc. Japan **71**, 19 (2002) (cited on page 53).

[145] T. Jungwirth, Q. Niu, and A. H. MacDonald, “Anomalous Hall Effect in Ferromagnetic Semiconductors”, Phys. Rev. Lett. **88**, 4 (2002) (cited on page 53).

[146] Y. MacHida, S. Nakatsuji, S. Onoda, T. Tayama, and T. Sakakibara, “Time-reversal symmetry breaking and spontaneous Hall effect without magnetic dipole order”, Nature **463**, 210 (2010) (cited on page 53).

[147] J. Kübler and C. Felser, “Non-collinear antiferromagnets and the anomalous Hall effect”, Epl **108** (2014) (cited on pages 53, 54, 64).

[148] X. Li, L. Xu, L. Ding, J. Wang, M. Shen, X. Lu, Z. Zhu, and K. Behnia, “Anomalous Nernst and Righi-Leduc Effects in Mn_3Sn: Berry Curvature and Entropy Flow”, Phys. Rev. Lett. **119**, 1 (2017) (cited on page 53).

[149] S. Nakatsuji, T. Higo, M. Ikhlas, T. Tomita, and Z. Tian, “Large spontaneous Hall effects in chiral topological magnets”, Philos. Mag. **97**, 2815 (2017) (cited on pages 53, 54).

[150] M. Ikhlas, T. Tomita, T. Koretsune, M. T. Suzuki, D. Nishio-Hamane, R. Arita, Y. Otani, and S. Nakatsuji, “Large anomalous Nernst effect at room temperature in a chiral antiferromagnet”, Nat. Phys. **13**, 1085 (2017) (cited on page 53).

[151] Y. Zhang, Y. Sun, H. Yang, J. Železný, S. P. Parkin, C. Felser, and B. Yan, "Strong anisotropic anomalous Hall effect and spin Hall effect in the chiral antiferromagnetic compounds Mn_3X (X=Ge, Sn, Ga, Ir, Rh, and Pt)", Phys. Rev. B **95**, 1 (2017) (cited on pages 53, 65).

[152] G. Y. Guo and T. C. Wang, "Large anomalous Nernst and spin Nernst effects in the noncollinear antiferromagnets Mn_3X (X=Sn,Ge,Ga)", Phys. Rev. B **96**, 1 (2017) (cited on pages 53, 65).

[153] M. Kimata, H. Chen, K. Kondou, S. Sugimoto, P. K. Muduli, M. Ikhlas, Y. Omori, T. Tomita, A. H. MacDonald, S. Nakatsuji, and Y. Otani, "Magnetic and magnetic inverse spin Hall effects in a non-collinear antiferromagnet", Nature **565**, 627 (2019) (cited on page 53).

[154] J. Yan, X. Luo, H. Y. Lv, Y. Sun, P. Tong, W. J. Lu, X. B. Zhu, W. H. Song, and Y. P. Sun, " Room-temperature angular-dependent topological Hall effect in chiral antiferromagnetic Weyl semimetal Mn_3Sn ", Appl. Phys. Lett. **115**, 102404 (2019) (cited on pages 53–55).

[155] E. Krén, J. Paitz, G. Zimmer, and É. Zsoldos, "Study of the magnetic phase transformation in the Mn_3Sn phase", Phys. B+C **80**, 226 (1975) (cited on pages 53, 54, 64).

[156] S. Tomiyoshi and Y. Yamaguchi, "Magnetic Structure and Weak Ferromagnetism of Mn_3Sn Studied by Polarized Neutron Diffraction", J. Phys. Soc. Japan **51**, 2478 (1982) (cited on pages 53, 75).

[157] T. Nagamiya, S. Tomiyoshi, and Y. Yamaguchi, "Triangular spin configuration and weak ferromagnetism of Mn_3Sn and Mn_3Ge", Solid State Commun. **42**, 385 (1982) (cited on page 53).

[158] S. Tomiyoshi, S. Abe, Y. Yamaguchi, H. Yamauchi, and H. Yamamoto, "Triangular spin structure and weak ferromagnetism of Mn_3Sn at low temperature", J. Magn. Magn. Mater. **54-57**, 1001 (1986) (cited on pages 53, 75).

[159] T. F. Duan, W. J. Ren, W. L. Liu, S. J. Li, W. Liu, and Z. D. Zhang, "Magnetic anisotropy of single-crystalline Mn_3Sn in triangular and helix-phase states", Appl. Phys. Lett. **107**, 082403 (2015) (cited on pages 54, 55, 60).

[160] N. H. Sung, F. Ronning, J. D. Thompson, and E. D. Bauer, "Magnetic phase dependence of the anomalous Hall effect in Mn_3Sn single crystals", Appl. Phys. Lett. **112** (2018) (cited on pages 54, 55).

[161] J. Cable, N. Wakabayashi, and P. Radhakrishna, "A neutron study of the magnetic structure of Mn_3Sn", Solid State Commun. **88**, 161 (1993) (cited on pages 54, 71, 80).

[162] M. Ikhlas, T. Tomita, and S. Nakatsuji, "Sample Quality Dependence of the Magnetic Properties in Non-collinear Antiferromagnet Mn_3Sn", **011177**, 1 (2020) (cited on pages 54, 80).

[163] P. Villars and H. Okamoto, eds., “Mn-Sn binary phase diagram 0-100 at.% Sn: datasheet from “pauling file multinaries edition – 2012” in springermaterials”, accessed 2020-10-12 (cited on pages 54, 56).

[164] J. S. Kouvel, “Exchange anisotropy and long-range magnetic order in the mixed intermetallic compounds, (Mn, Fe)$_3$Sn”, J. Appl. Phys. **36**, 980 (1965) (cited on pages 59, 60).

[165] G. J. Zimmer, E. Kren, C. D. Graham, and J. J. Rhyne, “Invsetigation of the magnetic phase transition in Mn$_3$Sn”, in , Vol. 513 (1972), pp. 513–516 (cited on pages 59, 60).

[166] J.-R. Soh, F. de Juan, N. Qureshi, H. Jacobsen, H.-Y. Wang, Y.-F. Guo, and A. T. Boothroyd, “Ground-state magnetic structure of Mn$_3$Ge”, Phys. Rev. B **101**, 140411 (2020) (cited on page 65).

[167] P. Park, J. Oh, K. Uhlířová, J. Jackson, A. Deák, L. Szunyogh, K. H. Lee, H. Cho, H. L. Kim, H. C. Walker, D. Adroja, V. Sechovský, and J. G. Park, “Magnetic excitations in non-collinear antiferromagnetic Weyl semimetal Mn$_3$Sn”, npj Quantum Mater. **3**, 1 (2018) (cited on pages 66, 71, 82).

[168] N. Kiyohara, T. Tomita, and S. Nakatsuji, “Giant Anomalous Hall Effect in the Chiral Antiferromagnet Mn$_3$Ge”, Phys. Rev. Appl. **5**, 1 (2016) (cited on page 66).

[169] T. Moriya, “Anisotropic Superexchange Interaction and Weak Ferromagnetism”, Phys. Rev. **120**, 91 (1960) (cited on page 82).

[170] M. I. Aroyo, J. M. Perez-Mato, C. Capillas, E. Kroumova, S. Ivantchev, G. Madariaga, A. Kirov, and H. Wondratschek, “Bilbao Crystallographic Server: I. Databases and crystallographic computing programs”, Zeitschrift für Krist. - Cryst. Mater. **221**, 15 (2006) (cited on page 83).

[171] R. D. Johnson, S. C. Williams, A. A. Haghighirad, J. Singleton, V. Zapf, P. Manuel, I. I. Mazin, Y. Li, H. O. Jeschke, R. Valentí, and R. Coldea, “Monoclinic crystal structure of α-RuCl$_3$ and the zigzag antiferromagnetic ground state”, Phys. Rev. B **92**, 235119 (2015) (cited on pages 85, 87).

[172] A. Glamazda, P. Lemmens, S. H. Do, Y. S. Kwon, and K. Y. Choi, “Relation between Kitaev magnetism and structure in α-RuCl$_3$”, Phys. Rev. B **95**, 1 (2017) (cited on page 85).

[173] J. A. Sears, M. Songvilay, K. W. Plumb, J. P. Clancy, Y. Qiu, Y. Zhao, D. Parshall, and Y.-J. Kim, “Magnetic order in α-RuCl$_3$: A honeycomb-lattice quantum magnet with strong spin-orbit coupling”, Phys. Rev. B **91**, 144420 (2015) (cited on page 87).

[174] J. A. Sears, Y. Zhao, Z. Xu, J. W. Lynn, and Y. J. Kim, “Phase diagram of α-RuCl$_3$ in an in-plane magnetic field”, Phys. Rev. B **95**, 1 (2017) (cited on page 87).

[175] S.-H. Baek, S.-H. Do, K.-Y. Choi, Y. S. Kwon, A. U. B. Wolter, S. Nishimoto, J. van den Brink, and B. Büchner, “Evidence for a Field-Induced Quantum Spin Liquid in α-RuCl$_3$”, Phys. Rev. Lett. **119**, 037201 (2017) (cited on page 87).

[176] Y. Kubota, H. Tanaka, T. Ono, Y. Narumi, and K. Kindo, "Successive magnetic phase transitions in α-$RuCl_3$: XY-like frustrated magnet on the honeycomb lattice", Phys. Rev. B **91**, 094422 (2015) (cited on page 87).

[177] S. Park, S.-H. Do, K. Choi, D. Jang, T.-H. Jang, J. Schefer, C. Wu, J. Gardner, J., M. S. Park, J. Park, and S. Ji, "Emergence of the Isotropic Kitaev Honeycomb Lattice with Two-dimensional Ising Universality in α-$RuCl_3$", in (2016) (cited on pages 88, 94, 99, 106).

[178] M. He, X. Wang, L. Wang, F. Hardy, T. Wolf, P. Adelmann, T. Brückel, Y. Su, and C. Meingast, "Uniaxial and hydrostatic pressure effects in α-$RuCl_3$ single crystals via thermal-expansion measurements", J. Phys. Condens. Matter **30** (2018) (cited on pages 88, 101).

[179] B. Zhou, Y. Wang, G. B. Osterhoudt, P. Lampen-Kelley, D. Mandrus, R. He, K. S. Burch, and E. A. Henriksen, "Possible structural transformation and enhanced magnetic fluctuations in exfoliated α-$RuCl_3$", J. Phys. Chem. Solids **128**, 291 (2019) (cited on page 88).

[180] S. Reschke, F. Mayr, S. Widmann, H. A. K. Von Nidda, V. Tsurkan, M. V. Eremin, S. H. Do, K. Y. Choi, Z. Wang, and A. Loidl, "Sub-gap optical response in the Kitaev spin-liquid candidate α-$RuCl_3$", J. Phys. Condens. Matter **30** (2018) (cited on page 88).

[181] S. Gass, P. M. Cônsoli, V. Kocsis, L. T. Corredor, P. Lampen-Kelley, D. G. Mandrus, S. E. Nagler, L. Janssen, M. Vojta, B. Büchner, and A. U. Wolter, "Field-induced transitions in the Kitaev material α-$RuCl_3$ probed by thermal expansion and magnetostriction", Phys. Rev. B **101**, 1 (2020) (cited on pages 88, 101).

[182] J. Chaloupka and G. Khaliullin, "Magnetic anisotropy in the Kitaev model systems Na_2IrO_3 and $RuCl_3$", Phys. Rev. B **94**, 1 (2016) (cited on page 99).

[183] L. Janssen and M. Vojta, "Heisenberg-Kitaev physics in magnetic fields", **277202** (2019) (cited on page 99).

[184] S. Nishimoto, V. M. Katukuri, V. Yushankhai, H. Stoll, U. K. Rößler, L. Hozoi, I. Rousochatzakis, and J. Van Den Brink, "Strongly frustrated triangular spin lattice emerging from triplet dimer formation in honeycomb Li_2IrO_3", Nat. Commun. **7**, 1 (2016) (cited on page 101).

[185] T. Takayama, A. Krajewska, A. S. Gibbs, A. N. Yaresko, H. Ishii, H. Yamaoka, K. Ishii, N. Hiraoka, N. P. Funnell, C. L. Bull, and H. Takagi, "Pressure-induced collapse of the spin-orbital Mott state in the hyperhoneycomb iridate β-Li_2IrO_3", Phys. Rev. B **99**, 1 (2019) (cited on page 101).

[186] Y. Cui, J. Zheng, K. Ran, J. Wen, Z. X. Liu, B. Liu, W. Guo, and W. Yu, "High-pressure magnetization and NMR studies of α-$RuCl_3$", Phys. Rev. B **96**, 1 (2017) (cited on page 101).

[187] K. Hu, Z. Zhou, Y. W. Wei, C. K. Li, and J. Feng, "Bond ordering and phase transitions in Na_2IrO_3 under high pressure", Phys. Rev. B **98**, 1 (2018) (cited on page 101).

[188] T. Biesner, S. Biswas, W. Li, Y. Saito, A. Pustogow, M. Altmeyer, A. U. B. Wolter, B. Büchner, M. Roslova, T. Doert, S. M. Winter, R. Valentí, and M. Dressel, "Detuning the honeycomb of α-$RuCl_3$: Pressure-dependent optical studies reveal broken symmetry", Phys. Rev. B **97**, 220401 (2018) (cited on page 101).

[189] R. Yadav, S. Rachel, L. Hozoi, J. Van Den Brink, and G. Jackeli, "Strain- and pressure-tuned magnetic interactions in honeycomb Kitaev materials", Phys. Rev. B **98**, 1 (2018) (cited on pages 101, 116).

[190] Z. Wang et al., "Pressure-induced melting of magnetic order and emergence of a new quantum state in α-$RuCl_3$", Phys. Rev. B **97**, 1 (2018) (cited on page 101).

[191] G. Simutis, N. Barbero, K. Rolfs, P. Leroy-Calatayud, K. Mehlawat, R. Khasanov, H. Luetkens, E. Pomjakushina, Y. Singh, H. R. Ott, J. Mesot, A. Amato, and T. Shiroka, "Chemical and hydrostatic-pressure effects on the Kitaev honeycomb material Na_2IrO_3", Phys. Rev. B **98**, 1 (2018) (cited on page 101).

[192] G. Bastien et al., "Pressure-induced dimerization and valence bond crystal formation in the Kitaev-Heisenberg magnet α-$RuCl_3$", Phys. Rev. B **97**, 1 (2018) (cited on page 101).

[193] G. Li, X. Chen, Y. Gan, F. Li, M. Yan, F. F. F. Ye, S. Pei, Y. Zhang, L. Wang, H. Su, J. Dai, Y. Chen, Y. Shi, X. Wang, L. Zhang, S. Wang, D. Yu, F. F. F. Ye, J. W. Mei, and M. Huang, "Raman spectroscopy evidence for dimerization and Mott collapse in α-$RuCl_3$ under pressures", Phys. Rev. Mater. **3**, 51 (2019) (cited on page 101).

[194] V. Hermann, J. Ebad-Allah, F. Freund, A. Jesche, A. A. Tsirlin, P. Gegenwart, and C. A. Kuntscher, "Optical signature of the pressure-induced dimerization in the honeycomb iridate α-Li_2IrO_3", Phys. Rev. B **99**, 1 (2019) (cited on page 101).

[195] R. Yadav, N. A. Bogdanov, V. M. Katukuri, S. Nishimoto, J. Van Den Brink, and L. Hozoi, "Kitaev exchange and field-induced quantum spin-liquid states in honeycomb α-$RuCl_3$", Sci. Rep. **6**, 1 (2016) (cited on page 116).

A

Appendix

A.1 Summary of crystal growth experiments

In this PhD work, more than 200 batches of crystal growth experiments have been performed for my study and a summary of them is shown in Tab A.1, Tab. A.2, Tab. A.3 and Tab. A.4. The tables only list experiments that I carry out individually at MLZ in Garching. For those not in the list, batches WX001-WX028 have been done with **Dr. Thomas Wolf** at Institut für Festkörperphysik (IFP) in Karlsruher Institut für Technologie (KIT) during January to March 2017 and batches WX054-WX080 are carried out with the assistance of **Dr. Changjiang Y**i and **Prof. Dr. Youguo Shi** at Institute of Physics, Chinese Academy of Sciences. In addition, these experiments only for the feasibility test are also excluded.

Table A.1: Summary of crystal growth experiments (I).

Batch number	Date	Crystals to grow	Methods	Duration / day	Results
WX029	05.05.2017	α-RuCl$_3$	CVT	4	Crystals size < 5mg
WX030	10.05.2017	α-RuCl$_3$	CVT	4	failed
WX031	18.05.2017	α-RuCl$_3$	CVT	5	Crystals size < 5 mg
WX032	24.05.2017	α-RuCl$_3$	CVT	3	Crystals size < 10 mg
WX033	01.06.2017	α-RuCl$_3$	CVT	1	Crystals size < 5 mg
WX034	03.06.2017	α-RuCl$_3$	CVT	1	failed
WX035	09.06.2017	α-RuCl$_3$	CVT	6	Crystals size < 20 mg
WX036	11.06.2017	α-RuCl$_3$	CVT	1	Crystals size < 5 mg
WX037	15.06.2017	α-RuCl$_3$	CVT	1	failed
WX038	22.06.2017	α-RuCl$_3$	CVT	5	failed
WX039	23.06.2017	α-RuCl$_3$	CVT	0	ampoule sealed failed
WX040	03.07.2017	α-RuCl$_3$	CVT	1.5	Crystals size < 5 mg
WX041	09.07.2017	α-RuCl$_3$	CVT	1.5	Crystals size < 3 mg
WX042	13.07.2017	α-RuCl$_3$	CVT	1	Crystals size < 5 mg
WX043	16.07.2017	α-RuCl$_3$	CVT	2	Crystals size < 5 mg
WX045	20.07.2017	PrSb	Flux	10	Crystals size < 200 mg
WX046	21.07.2017	α-RuCl$_3$	CVT	3	Crystals size < 10 mg
WX047	09.06.2017	NdSb	Flux	10	Crystals size < 300 mg
WX048	27.07.2017	PrSb	Flux	10	Crystals size < 400 mg
WX049	01.08.2017	α-RuCl$_3$	CVT	6	Crystals size < 5 mg
WX050	08.08.2017	α-RuCl$_3$	CVT	6	Crystals size < 5 mg
WX052	23.08.2017	α-RuCl$_3$	CVT	6	Crystals size < 10 mg
WX053	29.07.2017	α-RuCl$_3$	CVT	6	Crystals size < 20 mg
WX081	25.01.2018	α-RuCl$_3$	CVT	5	Crystals size < 5 mg
WX082	31.01.2018	α-RuCl$_3$	CVT	2	Crystals size < 10 mg
WX083	02.02.2017	α-RuCl$_3$	CVT	5	Crystals size < 100 mg
WX084	05.02.2018	α-RuCl$_3$	CVT	6	failed
WX085	10.02.2018	α-RuCl$_3$	CVT	9	failed
WX086	12.02.2018	α-RuCl$_3$	CVT	3	failed
WX087	16.02.2018	α-RuCl$_3$	CVT	3	Crystals size < 20 mg
WX088	19.02.2018	α-RuCl$_3$	CVT	1	Crystals size < 5 mg
WX089	20.02.2018	α-RuCl$_3$	CVT	3	Crystals size < 50 mg

Table A.2: Summary of crystal growth experiments (II).

Batch number	Date	Crystals to grow	Methods	Duration / day	Results
WX090	20.02.2018	α-$RuCl_3$	CVT	1	Power failed
WX091	01.03.2018	α-$RuCl_3$	CVT	3	failed
WX092	01.03.2018	α-$RuCl_3$	CVT	0	Oxided
WX093	02.03.2018	α-$RuCl_3$	CVT	5	No trasfer.
WX094	09.05.2018	α-$RuCl_3$	CVT	6	Crystals size < 20 mg
WX095	23.05.2018	α-$RuCl_3$	CVT	5	Crystals size < 50 mg
WX096	27.06.2018	Na_2IrO_3	Flux	10	failed
WX097	28.06.2018	α-$RuCl_3$	CVT	5	Crystals size < 5 mg
WX098	11.07.2018	Mn_3Sn	Flux	5	Crystals size < 100 mg
WX099	16.07.2018	Na_2IrO_3	Flux	10	failed
WX100	19.07.2018	Mn_3Sn	Flux	5	Crystals size < 20 mg
WX101	27.07.2018	$EuMnBi_2$	Flux	6	Crystals size < 200 mg
WX102	30.07.2018	Mn_3Sn	Flux	6	Crystals size < 50 mg
WX103	02.08.2018	YbPtBi	Flux	8	Crystals size < 20 mg
WX104	05.08.2018	$YbMnBi_2$	Flux	8	Crystals size < 300 mg
WX105-1	09.08.2018	CeSb	Flux	13	Crystals size < 400 mg
WX105-2	16.10.2018	CeSb	Flux	15	failed
WX106	22.08.2017	α-$RuCl_3$	CVT	8	Crystals size < 15 mg
WX107-1	29.08.2018	$Cr_2Ge_2Te_6$	Flux	11	Crystals size < 50 mg
WX107-2	29.08.2018	$Cr_2Ge_2Te_6$	Flux	11	Crystals size < 20 mg
WX108-1	28.08.2018	YbPtBi	Flux	9	Crystals size < 30 mg
WX108-2	28.08.2018	YbPtBi	Flux	8	Crystals size < 100 mg
WX109	05.09.2018	Fe_3Sn_2	Powders	7	failed
WX110	12.09.2018	$Cr_2Ge_2Te_6$	Flux	7	Crystals size < 30 mg
WX111-1	11.10.2018	Mn_3Sn	Flux	11	Ampoule broken
WX111-2	11.10.2018	Mn_3Sn	Flux	6	Ampoule broken
WX112-1	19.09.2018	$Cr_2Ge_2Te_6$	Flux	6	Flux separated failed
WX112-2	19.09.2018	$Cr_2Ge_2Te_6$	Flux	6	Crystals size < 10 mg
WX116-1	20.09.2018	α-$RuCl_3$	CVT	4	Crystals size < 75 mg
WX116-2	20.09.2018	α-$RuCl_3$	CVT	8	Crystals size < 70 mg
WX117-1	07.11.2018	$Cr_2Ge_2Te_6$	Flux	14	Crystals size < 10 mg

Table A.3: Summary of crystal growth experiments (III).

Batch number	Date	Crystals to grow	Methods	Duration / day	Results
WX117-2	07.11.2018	$Cr_2Ge_2Te_6$	Flux	7	Crystals size < 10 mg
WX118-1	08.11.2018	$Cr_2Si_2Te_6$	Flux	6	Crystals size < 1500 mg
WX118-2	08.11.2018	$Cr_2Si_2Te_6$	Flux	7	Crystals size < 1000 mg
WX119-1	09.11.2018	Mn_3Sn	Flux	10	Crystals size < 50 mg
WX119-2	09.11.2018	Mn_3Sn	Flux	10	Crystals size < 50 mg
WX121-1	09.11.2018	α-$RuCl_3$	CVT	6	failed
WX121-2	16.11.2018	α-$RuCl_3$	CVT	3	Crystals size < 170 mg
WX121-3	19.11.2018	α-$RuCl_3$	CVT	3	Crystals size < 100 mg
WX122-1	22.11.2018	YbPtBi	Flux	9	Crystals size < 30 mg
WX122-2	22.11.2018	YbPtBi	Flux	8	Crystals size < 20 mg
WX124	15.11.2018	α-$RuCl_3$	CVT	1	Crystals size < 50 mg
WX125	16.11.2018	α-$RuCl_3$	CVT	4	failed
WX127	23.11.2018	α-$RuCl_3$	CVT	5	Crystals size < **610 mg**
WX128-1	21.11.2018	Mn_3Sn	Flux	10	Crystals size < 50 mg
WX128-2	21.11.2018	Mn_3Sn	Flux	10	Crystals size < 50 mg
WX129	21.11.2018	CeSb	Flux	14	Crystals size < 300 mg
WX131	26.11.2018	Mn_3Sn	Flux	9	Crystals size < 30 mg
WX132-1	28.11.2018	Mn_3Sn	Flux	8	Crystals size < 10 mg
WX132-2	28.11.2018	Mn_3Sn	Flux	8	Crystals size < 10 mg
WX134	04.12.2018	$Cr_2Ge_2Te_6$	Flux	14	Crystals size < 30 mg
WX135	04.12.2018	$Cr_2Ge_2Te_6$	Flux	15	Crystals size < 100 mg
WX136	03.12.2018	α-$RuCl_3$	CVT	3	failed
WX137	07.12.2018	α-$RuCl_3$	CVT	4	Crystals size < 200 mg
WX138	15.12.2018	α-$RuCl_3$	CVT	7	Crystals size < **720 mg**
WX139-1	06.12.2018	Mn_3Sn	Flux	12	Crystals size < **2000 mg**
WX139-2	06.12.2018	Mn_3Sn	Flux	12	Crystals size < **1000 mg**
WX139-3	06.12.2018	Mn_3Sn	Flux	12	Crystals size < **1000 mg**
WX140	05.02.2019	α-$RuCl_3$	CVT	5	Crystals size < 200 mg
WX142	12.02.2019	$PtBi_2$	Flux	8	Crystals size < 30 mg
WX148	15.02.2019	α-$RuCl_3$	CVT	7	failed
WX150	28.02.2019	α-$RuCl_3$	CVT	7	Crystals size < 50 mg
WX151	07.03.2019	α-$RuCl_3$	CVT	4	Crystals size < 100 mg

Table A.4: Summary of crystal growth experiments (IV).

Batch number	Date	Crystals to grow	Methods	Duration / day	Results
WX152	11.03.2019	α-$RuCl_3$	CVT	6	Crystals size < 150 mg
WX153-1	15.03.2019	Mn_3Sn	Flux	10	Crystals size < 50 mg
WX153-2	15.03.2019	Mn_3Sn	Flux	10	failed
WX155	18.03.2019	Mn_3Sn	Flux	4	Crystals size < 150 mg
WX156-1	22.03.2019	Mn_3Sn	Flux	11	Centrifuging failed
WX156-2	22.03.2019	Mn_3Sn	Flux	12	Mn oxidised
WX162	23.04.2019	α-$RuCl_3$	CVT	5	Crystals size < 200 mg
WX176	21.07.2019	$ZrTe_5$	Flux	12	No crystals
WX181	30.09.2019	$ZrTr_5$	CVT	25	Crystals size < 20 mg

A.2 Glossary

AFM	Antiferromagnetic
AHE	Anomalous Hall effect
ARPES	Angle-resolved photoemission spectroscopy
B	Magnetic induction
CVT	Chemical vapour transport
Δ_{cubic}	Cubic crystal field
DM	Dzyaloshinskii-Moriya interaction
DNS	Diffuse scattering neutron time of flight spectrometer
EDX	Energy-dispersive X-ray spectroscopy
f	Frustration index
FC	Field cooling
$\mathbf{G}$	Crystallographic group
$\mathbf{G_k}$	Little group
H	Hamiltonian
$\mathbf{H}$	Subgroup of index 2
$\hbar\omega$	Energy transfer of neutrons in neutron scattering experiment
I	Electrical current
$Irreps$	Irreducible representation
J_{eff}	Effective total angular momentum operator
$\mathbf{k}$	Propagation wave vector
K_x, K_y, K_z	Bond dependent Kitaev Hamiltonian
$\boldsymbol{k}_f$	Scattered neutron wave vector
$\boldsymbol{k}_i$	Incident neutron wave vector
κ_{xy}	Thermal Hall conductance
κ_{xy}^{2D}	Two dimensional thermal Hall conductance
K_0	Quantum thermal conductance
λ	Spin orbit coupling
$\mathbf{M}$	Magnetic group
m	Mirror plane
m'	Mirror plane plus time-reversal symmetry
$M_\perp$	Magnetic interaction
MSG	Magnetic space group
MSSG	Magnetic superspace group
N	Nuclear structure factor

NSF	Non spin flip
$Occ.$	Atoms occupation
1D	One dimensional
$\mathcal{P}$	Neutron beam polarisation states tensor
$\mathbf{P}$	Polarisation of a neutron beam
P_f	Polarisation of a scattered neutron beam
PPMS	Quantum Design Physical Properties Measurement Systems
P_i	Polarisation of an incident neutron beam
$\mathbf{Q}$	Neutron scattering wave vector
QAHE	Quantum anomalous Hall effect
QHE	Quantum Hall effect
QSL	Quantum spin liquid
$\mathbf{R}$	Time reversal symmetry group
ρ_H	Hall electrical resistivity
ρ_{xx}	Longitudinal electric resistivity
SF	Spin flip
RVB	Resonating valence bond
3D	Three dimensional
THE	Topological Hall effect
TI	Topological insulator
2D	Two dimensional
ZFC	Zero field cooling

Acknowledgments

This PhD research would not have been possible without the help of my friends and colleagues in Jülich Centre for Neutron Science (JCNS) at Heinz Maier-Leibnitz Zentrum (MLZ), and I would like to thank everyone for their kind help and support over the years. Here I would like to express my sincere gratitude in particular to the following people:
Dr. Yixi Su, **Prof. Dr. Georg Roth** and **Prof. Dr. Thomas Brückel** for their great support, mentoring in this fascinating project and invaluable help in this PhD work.
Dr. Thomas Wolf for teaching me the knowledge of single crystal growth in Karlsruhe Institute of Technology (KIT).
Dr. Changjiang Yi, **Dayu Yan** and **Prof. Dr. Youguo Shi** for their kind help of crystal growth at Institute of Physics (IOP), China.
Dr. Mingquan He for his help for the measurement of heat capacity at high fields.
Dr. Min Kai Lee, **Yusheng Chen** and **Prof. Dr. Lieh-Jeng Chang** for their assistance of measurement of heat capacity at National Cheng Kung University.
Dr. Fengfeng Zhu for his participation and support in the neutron scattering experiments as well as data reduction.
Dr. Meng Yang, **Cuixiang Wang** and **Dr. Junda Song** for their assistance in the sample preparation.
Instrument scientists for on-site user support:
Dr. Schmalzl Karin and **Dr.Schmidt Wolfgang F** (IN12, IN22, D23 @ ILL)
Dr. Beauvois Ketty and **Dr. Navid Qureshi** (D10 @ ILL)
Dr. Martin Meven (Heidi @ FRM2)
Dr. Yixi Su and **Dr. Thomas Müller** (DNS @ FRM2)
And the following people who have helped me in the sample preparation, physical catheterisation and neutron scattering experiments:
Dr. Wilhelm Klein, Susanne Mayr, Michael Stanger, Dr. Jianhui Xu, Dr. Hao Deng, Dr. Erxi Feng, Dr. Oleg Petracic , Dr. Xiao Sun, Dr. Liming Wang, Dr. Wenhai Ji, Dr. Lei Cao, Patrick Schöffmann, Dr, Wentao Jin, Dr. Zhendong Fu, Dr. Sultan Demirdis, Dr. Rui Wang.